ACOUSTIC MONITORING OF HYDRAULIC RESISTANCE IN PARTIALLY FULL PIPES

Anna ROMANOVA

Submitted for the degree
of Doctor of Philosophy

School of Engineering, Design and Technology

University of Bradford

2013

Abstract

Hydraulic losses in sewer pipes are caused by wall roughness, blockages and in-pipe sedimentation. Hydraulic resistance is a key parameter that is used to account for the hydraulic energy losses and predict the sewer system propensity to flood. Unfortunately, there are no objective methods to measure the hydraulic resistance in live sewers. A common method to estimate the hydraulic resistance of a sewer is to analyse collected CCTV images and then to compare them against a number of suggested hydraulic roughness values published in the Sewer Rehabilitation Manual.

This thesis reports on the development of a novel, non-invasive acoustic method and instrumentation to measure the hydraulic roughness in partially filled pipes under various structural and operational conditions objectively. This research presents systematic laboratory and field studies of the hydraulic and surface water wave characteristics, of shallow water flows in a sewer pipes with the presence of local and distributed roughness, in order to relate them to some fundamental properties of the acoustic field measured in the vicinity of the flow surface. The results of this thesis indicate that for the local roughness the energy content of the reflected acoustic signal is an indicator of the pipe head loss and hydraulic roughness. In the case of the distributed roughness, the variation in the temporal and frequency characteristics of the propagated sound wave can be related empirically to the mean flow depth, mean velocity, wave standard deviation and hydraulic roughness.

Acknowledgement

The author would like to express gratitude to Prof. Kirill V. Horoshenkov and Prof. Simon J. Tait for outstanding supervision and support provided through all the years of the study.

Also, the author is thankful to Hydraulic Laboratory technicians Nigel Smith and Antony J.F. Daron, technical support of Ian B. MacKay, workshop technicians Ken B. Howell, Stephen D. Robinson, Lee Thomas and Joanna Wood for technical assistance and design advice. Furthermore, author expresses admiration to Thomas Ertl, Hanns Plihal, Erwin Pamperl and Josef Siligan for provided opportunity and assistance in the field surveys.

The author would like to thank all members of the Acoustics & Hydraulics research group which was a pleasure to work with during all these years.

A deep appreciation is expressed to husband Yury, who provided constant comfort and care. As well as the author would like to thank parents Ludmila and Vjacheslav, grandma Margarita and sister Kate for support they always give.

Publications

Journal papers:

[1] Romanova, A., Tait, S.J. and Horoshenkov, K.V. (2012) Sewer inspection and comparison of acoustic and CCTV methods. *Proceedings of the ICE - Water Management*, online print, DOI: 10.1680/wama.11.00039.

[2] Romanova, A., Tait, S.J. and Horoshenkov, K.V. (2012) Local head loss monitoring using acoustic instrumentation in partially full sewer pipes. *Water Science and Technology*, 65(9), pp. 1639-1647.

[3] Romanova, A., Bin Ali, M.T. and Horoshenkov K.V. (2011) A non-intrusive acoustic method of sewer pipe survey: A novel, inexpensive and rapid primary survey technique. *AWA, Water Journal, Asset Management*, 38(4), pp. 103-105.

Conference papers:

[1] Romanova, A., Tait, S.J. and Horoshenkov, K.V. (2012) Sound characteristics of a pipe with dynamically rough boundary. *Proceedings of Acoustics 2012, 11th Congress of Acoustics 2012*, Annual IOA Meeting, Nantes, France, 23-27 April 2012, Paper No. 000035. ISBN: 978-2-919340-01-9.

[2] Romanova, A., Horoshenkov, K.V. and Tait, S.J. (2011) Sound propagation in a pipe with dynamically rough boundary. *Proceedings of 162th Meeting of Acoustics Society of America* (ASA162), San Diego, CA, USA.

[3] Romanova, A., Tait, S.J. and Horoshenkov, K.V. (2011) Using Rapid, Non-intrusive Methods to Measure Hydraulic Roughness in Partially Filled Pipes. *Proceedings of 12th International Conference on Urban Drainage* (ICUD12), Porto Alegre, Brazil.

[4] Romanova, A., Tait, S.J. and Horoshenkov, K.V. (2010) Hydraulic head loss monitoring and roughness determination by acoustic instrumentation in partially full sewers. *Proceedings of 6th International Conference on Sewer Processes and Networks* (SPN6), Surfers Paradise, Gold Coast, Australia.

[5] Romanova, A. and Horoshenkov, K.V. (2010) Acoustic method of sewer inspection and pipe roughness estimation. *Proceedings of a Conference on the Kanalmanagement 2010, Grundlagen der Kamalsanierung*, Austria, Wiener Mitteilungen, Band 220, pp. C1-10.

Awards:

[1] “Young Water Professional” prize at SPN6 conference (Surfers Paradise, Australia, Nov 2010).

Nomenclature

A_a	*area of air in pipe's cross-section*	[m^2]
A_b	*blockage area in pipe's cross-section*	[m^2]
A_c	*critical flow area*	[m^2]
A_{h_1}	*flow area at* h_1	[m^2]
A_h	*pipe's cross-sectional area occupied by uniform flow*	[m^2]
A_p	*pipe's cross-sectional area*	[m^2]
A_λ	*total bed area*	[m^2]
$\tilde{A}$	*signal envelope*	[V]
a	*boils / roughness radius*	[m]
a_b	*pipe's cross-sectional area occupied by blockage*	[%]
a_h	*pipe's cross-sectional area occupied by uniform flow*	[%]
a_{h_1}	*pipe's cross-sectional area occupied by flow at* h_1	[-]
a_λ	*roughness upstream projected area*	[m^2]
$\overline{a_b}$	*pipe's cross-sectional area occupied by blockage*	[-]
B	*envelope amplitude limit*	[V]
ΔB	*envelope bin width*	[-]
β	*acoustic admittance*	[-]
C	*constant*	[-]
CF	*pulse maximum mean correlation function*	[-]
$[CF]^{**}$	*pulse maximum mean CF normalised by the ratio of flow free surface width to pipe's dry perimeter in c-s*	[-]
c	*speed of sound in air*	[m/s]
c_w	*recorded filtered continuous sine wave*	[V]
c_{w_a}	*signal envelope in analytical form*	[V]
$\widehat{c_w}$	*Hilbert transform of a continuous sine wave*	[V]
D	*sphere diameter*	[m]
D_c	*pipe diameter*	[m]
D_r	*roughness particle diameter*	[m]
$\overline{D_c}$	*pipe diameter factor*	[-]
d	*distance from pipe inlet*	[m]
d_r	*radial distance*	[m]
E	*specific energy*	[m]
E_j	*expected value operator*	[-]

E_{min}	*minimal specific energy*	[m]
$[E]^*$	*acoustic energy content ET_n further normalised by area of flow to area of block*	[-]
ET	*reflected acoustic energy content*	[-]
ET_d	*acoustic energy content normalised by pipe distance*	[-]
ET_n	*acoustic energy content normalised by energy content of clean pipe and flow depth to pipe diameter ratio*	[-]
ET_0	*acoustic energy content for clean pipe*	[-]
Fr	*Froude number*	[-]
F_j	*frequency indices*	[-]
F_s	*force attained by the speaker*	[N]
f	*friction factor*	[-]
f_c	*cut-on or resonance frequency*	[Hz]
f_e	*frequency of sound*	[Hz]
f_s	*sampling frequency*	[Hz]
$\bar{f}$	*friction factor due to the blockage*	[-]
g	*Gaussian pulse signal*	[Pa]
g_a	*acceleration due to gravity*	[m/s^2]
$\langle g \rangle$	*mean absolute relative pulse signal*	[-]
$\widetilde{g_{y_i}}$	*filtered pulse signal*	[Pa]
$\widetilde{g_{y_i}}$	*pulse signal normalised by maximum pulse signal*	[-]
$[\langle g \rangle]^{**}$	*mean absolute relative pulse signal normalised by ratio of flow free surface width to pipe's dry perimeter*	[-]
H_n	*dimensionless hydraulic parameter*	[-]
H_r	*bed form height*	[m]
$[H]^*$	*hydraulic parameter normalised by shear velocity to velocity ratio and area of pipe occupied by blockage*	[-]
h	*time-averaged uniform flow depth*	[m]
h_L	*head loss due to pipe length*	[m]
h_b	*blockage model sample height*	[m]
h_c	*critical flow depth*	[m]
h_f	*head loss due to friction*	[m]
h_m	*mean time averaged flow depth*	[m]
$h_{1,2}$	*mean flow depth between points 1 & 2*	[m]
$[h_f]^*$	*head loss due to friction normalised by shear velocity to velocity ratio, pipe diameter and area of pipe*	[-]

	occupied by blockage	
I	*acoustic intensity*	[W/m²]
$I(\omega)$	*transformed input pulse*	[V]
$\dot{I}(\omega)$	*complex conjugate of duct reflection*	[V]
$\tilde{I}(t)$	*instantaneous acoustic intensity*	[W/m²]
$\vec{I}(t)$	*active part of the instantaneous acoustic intensity*	[V]
IIR	*input impulse response*	[-]
iir	*Butterwort filter of 3rd kind*	[-]
i, j	*microphone index number*	[-]
$\vec{J}(t)$	*reactive part of the instantaneous acoustic intensity*	[W/m²]
K	*Karman's coefficient*	[-]
K_c	*resistance coefficient*	[-]
K_F	*length of Fourier transform*	[s]
K_N	*Karman's coefficient defined by Nikuradse*	[-]
k	*wavenumber*	[m^{-1}]
k_b	*side wall correction*	[m]
k_h	*mean roughness height*	[m]
k_s	*hydraulic roughness height*	[m]
k_w	*wall roughness due to bottom roughness*	[m]
k_s^r	*estimated hydraulic roughness height, WRc*	[m]
$[k_s]$	*hydraulic roughness normalised by pipe diameter factor*	[m]
$[k_s]^*$	*hydraulic roughness height normalised by shear velocity to velocity ratio, pipe diameter and area of pipe occupied by blockage*	[-]
L	*pipe length*	[m]
L_b	*blockage model sample length*	[m]
L_r	*ripple / dune length*	[m]
L_s	*streamwise spacing between roughness*	[m]
L_w	*flow free surface width in pipe's cross-section*	[m]
l	*distance from the boundary*	[m]
l_a	*mean spacing between the boils*	[m]
l_c	*correlation radius length*	[m]
M	*total number of wave probes*	[-]
m	*wave probe number*	[-]
N	*total length of wave probe time series*	[-]

N_a	*mean density of boils (ratio of boils area to bed area)*	[-]
n	*sample number of wave probe time series*	[-]
n_i	*number of flow regime*	[-]
n_λ	*roughness elements number present on the bed area*	[-]
P_a	*dry perimeter of air in pipe's cross-section*	[m]
p_a	*atmospheric pressure*	[Pa]
p_{n_i}	*measured acoustic pressure in the dry area of pipe*	[Pa]
p_s	*sound / acoustic pressure*	[Pa]
p_{00}	*acoustic pressure in the fundamental mode*	[Pa]
$p_1(t)$	*time-dependent acoustic pressure recorded on mic 1*	[Pa]
$p_2(t)$	*time-dependent acoustic pressure recorded on mic 2*	[Pa]
Q	*flow discharge*	[l/s]
q	*flow rate*	[m^3/s]
q_{mn}	*eigen value*	[-]
$\bar{q}$	*conditioning factor*	[-]
R	*hydraulic radius*	[m]
R_b	*bed hydraulic radius*	[m]
R_w	*wall hydraulic radius*	[m]
$R_{1,2}$	*average hydraulic radius between points 1 & 2*	[m]
Re	*Reynolds number*	[-]
$Re_{1,2}$	*Reynolds number averaged between points 1 & 2*	[-]
$R(\omega)$	*transformed duct reflection*	[V]
r	*pipe radius*	[m]
S	*piezometric gradient*	[-]
S_0	*hydraulic / pipe gradient*	[-]
s	*continuous sinusoidal wave envelope*	[V]
s_V	*fluid shear velocity*	[m/s]
s_f	*friction slope / pipe bed slope*	[-]
$[s]^{**}$	*CW envelope normalised by ratio of flow free surface width to pipe's dry perimeter in c-s*	[V]
T^o	*temperature*	[C^0, K]
T_e	*time window of signal envelope*	[s]
T_s	*time shift*	[s]
T_w	*time window of pulse tail*	[s]
t	*time*	[s]
t_0	*time series for Fourier analysis*	[s]
Δt	*time step*	[s]

u	*acoustic particle velocity*	[m/s]
V	*mean flow velocity*	[m/s]
V_c	*critical flow velocity*	[m/s]
V_l	*velocity at specific distance from the boundary*	[m/s]
$V_{1,2}$	*average velocity between points 1 & 2*	[m/s]
W	*mean wave peak-to-peak amplitude*	[m]
$\overline{W_c}$	*uniform mean c-s wave peak-to-peak amplitude*	[m]
w	*wave probe data*	[m]
w_s	*spatial correlation function*	[-]
$\overline{w}_m$	*wave probe reading fluctuations from the mean*	[m]
$\widetilde{w}_m$	*probability density function of the flow depth variation*	[m]
X	*total number of microphones*	[-]
x	*coordinate*	[-]
x_s	*normalised argument in spatial correlation function*	[-]
x_i	*microphone number*	[-]
x_j	*microphone number different from* x_i	[-]
Y	*total number of pulses*	[-]
y	*coordinate*	[-]
y_i	*pulse sequential number*	[-]
Z	*elevation head*	[m]
Z_f	*total energy line or energy slope*	[m]
Z_{kin}	*kinetic energy slope*	[m]
z	*coordinate*	[-]
z_h	*height above the bed*	[m]
β	*acoustic admittance*	[-]
θ	*azimuthal angle in polar coordinates of a pipe center*	[rad]
θ_i	*incident wave angle*	[rad]
θ_k	*transitional changing roughness parameter*	[m]
θ_r	*reflected wave angle*	[rad]
λ	*wavelength*	[m]
λ_r	*roughness concentration*	[-]
λ_s	*roughness wavelength - element separation*	[m]
μ	*fluid dynamic viscosity*	[kg/sm]
$\mu_{1,2}$	*mean value between two wave probes*	[m]
ρ	*fluid density*	[kg/m^3]
ρ_0	*air density*	[kg/m^3]
σ	*mean STD of all WP / mean roughness height*	[m]

σ_{CF}	*mean STD of pulse maximum CF*	[-]
σ_{g}	*mean STD of pulse tail peak*	[-]
σ_h	*mean STD of surface roughness height*	[m]
σ_l	*mean streamwise / longitudinal wave STD*	[m]
σ_m	*wave probe standard deviation*	[m]
σ_s	*mean STD of continuous sinusoidal wave envelope*	[V]
$\sigma_{1,2}$	*standard deviation of two wave probe data*	[m]
$\overline{\sigma_c}$	*uniform mean c-s wave STD*	[m]
$\overline{\sigma_l}$	*uniform mean streamwise / longitudinal wave STD*	[m]
$[\sigma]^*$	*mean wave roughness height normalised by the ratio of flow depth to flow free surface width*	[-]
$[\sigma_{CF}]^{**}$	*mean STD of pulse maximum CF normalised by ratio of flow free surface width to pipe's dry perimeter*	[-]
$[\sigma_s]^{***}$	*mean STD of CW envelope normalised by the ratio of pipe's c-s area to dry pipe's c-s area*	[V]
τ	*auxiliary integration variable*	[s]
τ_b	*bed shear stress*	[Pa]
τ_c	*critical bed shear stress*	[Ps]
$\Delta\phi$	*phase difference*	[-]
φ	*angle subtended at the pipe centre by free surface*	[rad]
ω	*angular frequency of the wave*	[rad/s]
Ψ_{mn}	*eigen-function, with modal indices m and n*	[-]
Ψ_{00}	*change in acoustic pressure in fundamental mode*	[Pa]

Abbreviations

AMP	*amplifier*
C	*clean pipe*
CCTV	*Closed-Circuit Television*
CF	*correlation function*
c-s	*cross-sectional*
DAC	*digital to analogue converter*
DAQ	*data acquisition system*
EU	*European Union*
FFT	*fast Fourier transform*
M	*mesh*
MAX	*maximum*
MIN	*minimum*
mic	*microphone*
RC	*roughness condition*
RMS	*root mean square*
RVI	*Laser Profiling*
PC	*personal computer*
PSD	*power spectral density*
PDF	*probability density function*
PVC	*polyvinyl chloride*
STD	*standard deviation*
WP	*wave probe*

Contents

List of Figures

List of Tables

Chapter 1 Introduction

1.1 Background

The combined sewer network in the UK includes more than 300,000km of pipes (OFWAT 2004). The majority of wastewater assets were installed after 1950's and many date back to the beginning of 20th century or earlier. The existing assets are deteriorating and their serviceability needs to be controlled and maintained. It has been estimated that in the last decade 30% of the sewer pipes per year caused severe problems. In 20% of cases the sewer pipes caused flooding incidents, which are referred to as 'critical hot-spots' (Great Britain, House of Commons 2004). Research by Blanksby et al. (2002) has shown that the majority of flooding incidents from sewers in the UK is caused by intermittent blockages occurring in pipes of smaller diameter, less than 300mm, rather than structural defects (which was the reason for flooding in only in 2% of cases). A study by Arthur et al. (2008) has identified that 13% of all sewer flooding incidents in England and Wales caused property internal damage. These flooding incidents in majority appear from small sewer pipes, with low flow velocities. The analysis by Ugarelli et al. (2007, 2008) has shown that chronic blockages tend to appear in foul water sewer pipes 20% more often than in combined sewers and 70% more often than in storm water pipes (Oslo data, Ugarelli et al. 2008 and Ugarelli and Di Federico 2010). Also, it was shown that in years 1991 - 2006, on average at least 1 blockage occurred in every 150 sewer sections. Also, the statistical analysis has proved that the blockages tend to form in the pipe of smaller diameters (150 - 300mm) and in pipes with a slope less than 10% which represent a majority of sewer pipes. The blockages or

obstructions, either local or distributed were reported to form from excess sedimentation, hard compacted solids, buildup of slit and fats, root intrusion, buildup of roots, choking associated with siltation, poor gradient design, low velocities, displaced joints and structural problems.

Until recently, most water companies in the UK had a tactics of post-reacting to the problematic pipes. This attitude has raised major public and governmental health and safety concerns as there is a lack of information on the sewer conditions to enable efficient pro-active management. As a result of this pressure, water companies are now more willing to move into pro-active management by preventing sewer failure early, so preventing flooding, and as such a range of sewer monitoring systems are implied.

One obstacle to more pro-active management is the cost and efficiency of the current sewer inspection technologies, which include CCTV, laser profiling and zoom camera methods of inspection. These techniques provide a relatively good resolution but they are slow and relatively expensive. The video data obtained as a result of these surveys are difficult to interpret automatically and a human intervention is required to prepare subsequent inspection reports.

More recently, acoustic reflectometry survey techniques have been developed (Bin Ali 2010). These techniques cost considerably less than the visual inspection techniques, they are quicker and more objective. There are evidence that acoustic field in the pipe can be related to the hydraulic roughness (Horoshenkov et al. 2004). The hydraulic roughness value is of great interest to the water companies as it controls the pipe flow capacity and overall hydraulic

performance. This topic has not been examined in detail and it will be the focus of this study.

1.2 Hypothesis

The author of this work believes that the pipe wall roughness in shallow water flows influences the water surface texture and pattern. Also, the pipe wall geometrical properties in combination with flow regime provide a unique water surface pattern. If this pattern can be measured then the hydraulic resistance and afterwards the hydraulic roughness can be determined. In this project a non-contact acoustic method was investigated to examine the feasibility of measuring the water surface pattern and hence determining resistance and then the pipe wall roughness.

1.3 Work focus

This work focuses on the development and application of a novel acoustic methodology and instrumentation that aims to estimate the pipe hydraulic roughness caused by the submerged pipe wall roughness conditions. This project is split into two studies (see Figure 1.1): local pipe roughness (i.e. blockage / obstruction) and distributed roughness (i.e. sedimentation, continuous pipe wall roughness). For both of these problems a method of measuring either the reflections or propagation of guided sound waves and linking this information to the hydraulic and structural characteristics of the sewer pipe will be proposed.

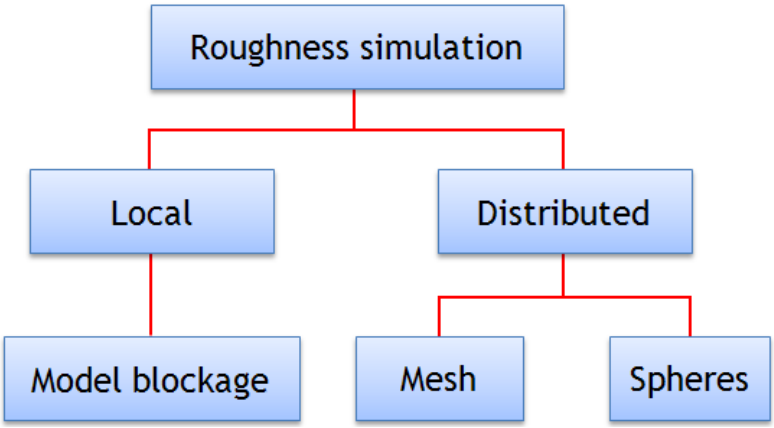

Figure 1.1 Local and distributed roughness simulation.

For this purpose, the internal conditions of the pipe will be altered by adding local (by the use of model blockages shaped to fit pipe internal geometry) or distributed (by the use of continuous mesh type grid and spheres arranged continuously in a number of patterns) roughness to simulate variable pipe wall roughness conditions.

Currently an acoustic based instrumentation (Bin Ali 2010) exists that is capable of identifying the location of a sewer pipe blockage and its geometrical extent. Novel approaches will be applied to analyse the signals recorded with this instrument in order to determine the pipe hydraulic roughness and energy head loss due to the presence of local roughness. In the case of a distributed pipe roughness a novel acoustic instrumentation and sound analysis techniques will be developed to relate the water surface fluctuations due to distributed roughness to pipe flow roughness and pipe bed roughness pattern. The obtained methodology will be validated in the field.

1.4 Aims and objectives

The aim of this research is to obtain a representative set of hydraulic and acoustic data for a sewer pipe with turbulent flow under steady and uniform and non-uniform flow conditions. The data will be gathered using experimental laboratory setup.

The objectives of this study are:

I. Develop a new laboratory pipe facility for acoustic and hydraulic analysis of the flow characteristics associated with partially filled pipes.

II. Use this laboratory facility to measure the hydraulic and acoustical characteristics of a sewer pipe in the presence of turbulent flow with and without local roughness.

III. Develop acoustic instrumentation to measure the propagating sound characteristics in a pipe with distributed roughness.

IV. Use this laboratory facility to measure the hydraulic and acoustical characteristics of a sewer pipe in the presence of turbulent flow with and without distributed roughness.

V. Develop unambiguous relations between the acoustical and hydraulic characteristics in a sewer for a range of hydraulic regimes and pipe bed conditions.

VI. Develop relationship between the pipe wall roughness and acoustic data recorded in field trials for pipes with no flow.

1.5 Structure of thesis

This thesis is organised as follows: Chapter 1 provides the overall background information leading to project focus, aims and objectives. Chapter 2 presents the relevant acoustics and hydraulics literature review and also formulates the challenges. Chapter 3 describes the experimental set up, hydraulic regimes and acoustic instrumentation for the experiments with local roughness. This chapter also presents the results obtained from the described experiments. Chapter 4 presents the novel acoustic instrumentation, overall experimental setup, conditions for experiments with distributed roughness and the results obtained from these experiments. Chapter 5 describes the field trials carried out in live sewers, presents the acoustic results and explains the novel findings. Chapter 6 summarises the findings and achievements of the work and recommends future strategy to improve the proposed acoustic technology.

Chapter 2 Literature review

This work focuses on pipes with free surface flows in the presence of significant roughness, which in real word application is found in sewer pipes. This chapter will give an overview of the key fundamental elements and characteristics of the hydraulic flow in pipes and pipe wall roughness.

The work considers two conceptual types of possible pipe roughness: (i) isolated or local and (ii) distributed roughness.

Followed from the above, a review of the influence of the pipe bed and wall roughness type, size and concentration on hydraulic roughness and energy losses will be discussed.

The research of this work is turned toward the examination of the sewer pipe roughness. As part of their life cycle, sewer pipe lines are affected by continuous deterioration, buildup of sediment and potential blockage formation. All of the above cause extra pipe bed and wall roughness, which leads to changes in pipe flow capacity and pipe line extra energy loses. Therefore, in cases when the problematic pipe line sections are not identified in a timely manner, severe pipe flow transportation delays and on land flooding may occur. The last can be a serious threat to public health. Statistics show that there are more than 300,000km of sewer pipes in the UK, where on average 20% of sewer pipes are found partially or fully blocked and causing problems each year (Arthur et al. 2008). Current inspection technologies are expensive, time consuming and require special training, hence only the problematic pipes are examined post factum.

2.1 Introduction to sewer problems

Traditionally, wastewater collection and drainage collection transport in urban areas is carried out using an extensive and complex system of underground pipes. In the UK the underground water mains and sewers has developed rapidly over many years, so that now there are over 668,000km of pipes (OFWAT 2010).

Water companies need information on sewers to manage efficiently their day-to-day and long term performance. The operational condition of sewer systems can change over time due to the deterioration of pipe wall surfaces and blockages caused by sediment and fats. The incidence of pipe deterioration and blockage has been linked to flooding and other service failures (Ugarelli et al. 2007). Currently, it is very difficult to gather sufficient information on the condition of a sewer pipe, often enough so as to pro-actively prevent hydraulic failure due to deterioration or blockage.

In the UK flooding caused by hydraulic overload has been progressively tackled through capital investment. Analysis by Arthur et al. (2008) showed that 'flooding other causes' has become an increasingly significant service failure. In England and Wales, there were around 25,000 sewer blockages of which 13% resulted in internal property flooding. Water companies are therefore now looking for new ways of reducing the frequency of these incidents through means such as CCTV inspection to locate developing blockage problems, the statistical analysis of historical blockage data or modeling the hydraulic performance of systems to identify potential blockage 'hot-spots'.

In contrast to flooding due to hydraulic overload 'flooding other causes' problems commonly exist on small diameter local sewers, which make up by far the largest part of the sewer network (Ugarelli et al. 2008). No longer will it be

sufficient to focus attention on the 20% or so of large ‘critical’ sewers as has been the case in the past. Current technologies are limited by cost and time, therefore quick and economical technology is needed that will identify the wall roughness due to pipes deterioration and the presence of blockages, which then can be used to predict changes to flow capacity of individual pipes. Furthermore, the required inspection is not a one-off activity. Having identified areas at risk it is important to regularly check for progressive roughness increase and intervene at the right time, before flow capacity deteriorates to a level that flooding occurs.

Blanksby et al. (2002) carried out an analysis of historical water company customer complaints and CCTV records to examine the causes of flooding incidents over a range of sewer sizes. Their study indicated that the majority of flooding incidents were in smaller sewers, and that the majority of these were caused by intermittent blockages rather than structural failures. The analysis also indicated that collapses were proportionately more prevalent in smaller sewers, but that the incidence of structural problems was low with around only 2% of the CCTV surveyed lengths showing signs of structural deterioration.

They concluded that it would be difficult to generate a pro-active cleaning routine based on prior predictions as the data indicated that the location of blockages generally could not be linked to a structural defect and so it was thought to be linked with either the local hydraulic conditions, or local sources of slit and fat inputs. It appears that continual measurement or monitoring may provide an answer to manage sewer performance rather than some predictive tool due to the intermittent nature of the processes that are involved in pipe deterioration and blockage formation.

2.1.1 Estimation of roughness in sewers

Live sewers contain pipe wall roughness. This roughness comes in the form of coarse wall finish, sedimentation, local obstructions and poorly connected joints. These result in an increase in vicious friction, flow detachment and turbulence which cause a proportion of the energy in the hydraulic flow to be lost. The pipe roughness needs to be estimated and quantified so that the flow capacity of the underground sewer network can be correctly estimated. Combined sewers are designed to be only partially filled a majority of the time to provide the additional capacity for conveying any extra discharge caused by heavy rainfall events or to accommodate the additional sources of foul water which can be created as the population continues to grow. Sewer pipe condition assessment is important in sewer management as it is strongly linked to sewer hydraulic performance.

Currently, the most commonly used sewer pipe inspection techniques are classified as Closed-Circuit Television (CCTV). This type of technology consists of a pushed or motorised trolley with camera to capture a series of images and a computer based remote control situated on a ground level (Figure 2.1).

Figure 2.1 Example of CCTV (MiniCam 2010).

The images (Figure 2.2) recorded by the camera are then visually assessed by an operator to estimate the roughness based on classification system used in

the UK (WRc 2004) and the European classification system (CEN 2002) which is adopted in most other EU countries. This method fully depends upon the pipe line image/video quality i.e. resolution, local illumination, in-sewer physical conditions as obstructions or humidity and operator competency (Fischer et al. 2007). To produce high quality pipe survey reports, competent and consistent in decision making operators are required. Several EU countries require operators to be trained and certified. Even then, the analysis of the CCTV images can misidentify defects and general pipe condition with an error of 20 - 30% (Korving and Clemens 2005, Dirksen et al. 2007, Dirksen et al. 2011). From the above it can be concluded that a better alternatives of pipe inspection techniques are required, which could provide an objective measure of in-sewer roughness.

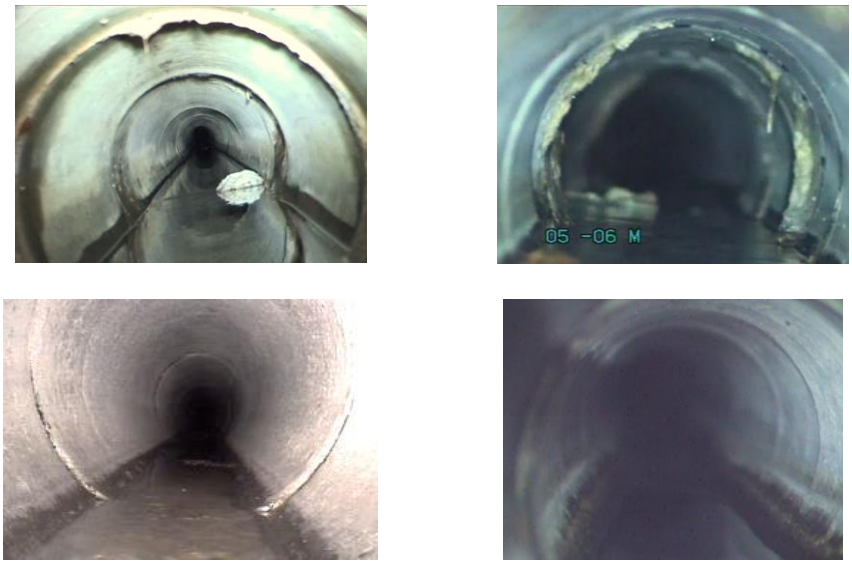

Figure 2.2 CCTV produced images of a sewer pipe (IKB 2009).

Considering the above, the supporting hardware and software was developed to facilitate CCTV to enable pipe wall equivalent roughness automated estimation (Dirksen et al. 2011, Hao et al. 2012, Rogers et al. 2012). One of the supportive techniques (Figure 2.3) is called Laser Profiling (RVI), which mounts on top of

the existing CCTV cameras, and created a circle type laser beam which projected to the pipe wall some distance away from the camera so that it shape can be fully captured (Maverick Inspection 2010).

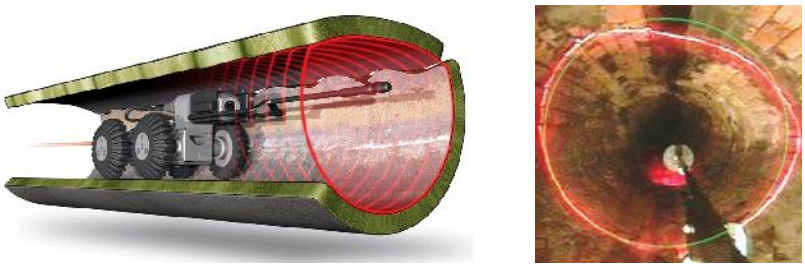

Figure 2.3 Light Line equipment example with projected laser beam (MiniCam 2010).

Further, RVI collects survey data and creates automated pipeline reports based on laser circle boundary discrepancy from the original pipe diameter. The following reports also include fault measurements and internal pipeline features as pipe size, laterals and flow depths. The automated visual performance of pipe cross-sectional area estimates pipe ovality, corrosion, material loss, sediment depth (in water absence). And three - dimensional (3D) image can be produced using additional software utilities (Figure 2.4).

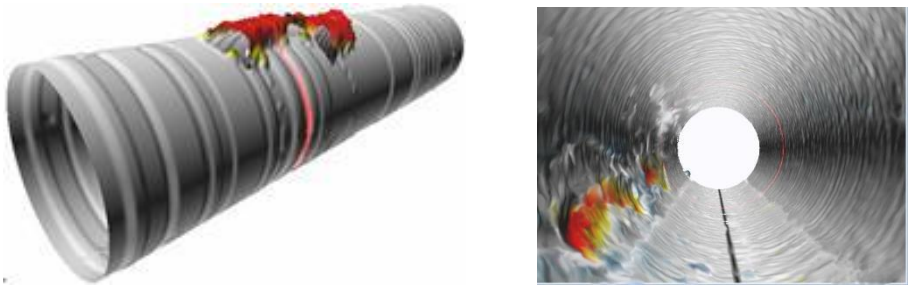

Figure 2.4 Light line computer based 3D interpretation of laser beam, with colored areas identifying pipe wall damage (Maverick Inspection 2010).

The automated RVI system with additional analysis software performs detailed analysis of the pipe profile, however it fundamentally depends on CCTV machine movement ability and can easily be terminated in front of a large

obstacle, pipe misalignment, or increased water level. Furthermore, CCTV and RPI equipment sets start at £2000 for simple crawler cameras and exceed £20,000 for full van equipment (Scanprobe 2001, OurProperty 2012). As such, contractor companies are charging at least £2 per meter of pipe survey (Baur and Herz 2002). Also, additional costs are involved if automated computer based analysis software is chosen to analyse pipe condition, which is expensive and time consuming (Baur and Herz 2002, Ugarelli et al. 2010).

Currently, a number of other automatic image analysis systems for CCTV systems are being developed as Sewer Scanning Evaluation Technology (SSET) by Iseley (1999), laser light projector automated defect classification system by Duran et al. (2007), or semi-automated system that extracts historical CCTV condition data and compares them against new CCTV data proposed by Sarshar et al. (2009). However, these analysis methods do not provide information whereby the pipe roughness condition can be extracted.

2.2 Hydraulic overview

Pipe flow has certain characteristics that can be defined as steady or unsteady, uniform or non-uniform, laminar or turbulent, and subcritical or supercritical. A brief explanation of the following is summarized below.

2.2.1 Steady, uniform and critical flow

A flow can be classified as steady, where the flow condition is constant with time. Otherwise the flow is classified as unsteady (CAHE 2002).

The hydraulic condition of the flow can be considered uniform if the given flow discharges and the cross-sectional area of occupation are constant with streamwise distance. For flow in a pipe with a uniform cross-section the flow rate and water depth inside the pipe are constant with distance. Otherwise flow condition has non-uniform characteristics.

Critical depth is used to understanding the flow characteristics:

(i) If the actual flow depth is greater than the critical depth, then the flow is considered "subcritical". Subcritical flow is characterised as a "slow flow" and the streamwise water depth profile is governed by downstream conditions.

(ii) If the actual flow depth is less than the critical depth, then the flow is "supercritical". Supercritical flow has a characteristic of a "fast flow" and is impacted by the upstream conditions. It flows faster than the wave speed and is independent from downstream conditions. With supercritical flow there is a high probability that a hydraulic jump will occur at some point downstream when the flow is unable to lose sufficient energy with streamwise distance.

It should be noted that the critical flow depth (h_c) is achieved at a point of minimal specific energy (E_{min}). The above is illustrated in Figure 2.5 below.

The specific energy (E) can be found from the equation below, (Chow 1959):

$$E = h + \frac{q^2}{2g_a {A_h}^2} \quad \textbf{(2.1)}$$

where h is the flow depth, q is the flow rate, g_a is the acceleration due to gravity and A_h is the flow area in pipe's cross-section.

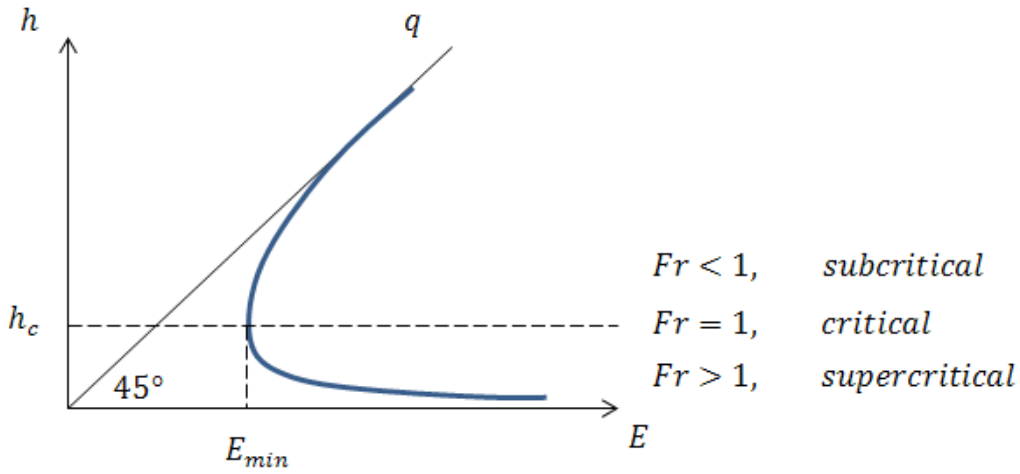

Figure 2.5 Specific energy as a function of flow depth.

The Froude number (Fr) is used to define the type of experimental flow:

$$Fr = \frac{V}{\sqrt{\frac{g_a A_h}{L_w}}} \tag{2.2}$$

where V is the flow velocity and L_w is the free surface width in pipe's cross-section. For critical flow the $Fr = 1$, the subcritical flow is defined at $Fr < 1$ and the supercritical flow is achieved at $Fr > 1$, which is illustrated in Figure 2.5.

The critical flow velocity (V_c) for a given condition can be defined from ratio of flow rate to critical flow area in pipe's cross-section (q/A_c), which occurs at critical flow depth where the $Fr = 1$. As such, the critical flow velocity can also be defined from acceleration due to gravity, critical flow area and free surface width (Chow 1959):

$$V_c = \frac{q}{A_c} = \sqrt{\frac{g_a A_c}{L_w}} \tag{2.3}$$

where at $Fr = 1$ the above equation can be rearranges as (Smith 2004):

$$1 = \frac{q L_w}{g_a {A_c}^3} \tag{2.4}$$

The above equation can be solved as a function of critical depth (h_c) by interval halving procedure:

$$f(h_c) = \frac{{A_c}^3}{L_w} - \frac{q^2}{g_a} = 0 \quad \textbf{(2.5)}$$

where from pipe geometry the critical flow area, is expressed as:

$$A_c = \frac{{D_c}^2}{8}[\varphi - \sin\varphi] \quad \textbf{(2.6)}$$

where D_c is the pipe diameter and φ is the angle subtended at the pipe centre by the flow free surface width in pipe's cross-section. As such, the critical flow area is determined from combining equations (2.7) and (2.8).

$$L_w = 2\sqrt{\left(D_c h_c - {h_c}^2\right)} \quad \textbf{(2.7)}$$

$$\varphi = 2\tan^{-1}\left(\frac{L_w}{D_c - 2h_c}\right) \quad \textbf{(2.8)}$$

Finally the critical flow depth is obtained by substituting equations (2.6), (2.7) and (2.8) into equation (2.5), (Smith 2004).

2.2.2 Laminar or turbulent flow

Laminar flow is characterized by flow with smooth flow stream lines, with no eddies, so that momentum is transferred within the fluid solely by friction. Whereas in the turbulent flow the velocity pattern had a chaotic behavior which is caused by the presence of eddies within the flow. Eddies are the resulting factors from flow and wall boundary conditions, which cause continuous transfer of fluid momentum so creating the loss of energy due to internal fluid mixing and also mixing close to the wall.

To characterize the flow type a Reynolds number (Re) is used, which for the flow with the presence of free surface is defined as:

$$Re = \frac{\rho V R}{\mu} \quad \textbf{(2.9)}$$

where ρ is fluid density, μ is the dynamic viscosity of the fluid, V is flow velocity and R is the hydraulic radius, which is found as a ratio of flow area to flow wetted perimeter.

For circular pipes, if $Re < 2300$ the flow is considered to be laminar, in the range of $2300 < Re < 4000$ the flow is transitional, and usually avoided in the analysis due to a high level of complication, and at $Re > 4000$ the flow is considered to be turbulent (White 2006).

2.2.3 Flow resistance, friction factor and roughness

Flow hydraulic resistance is a measure of the resistance that the flow experiences when moving down the pipe caused by the boundary condition. The hydraulic resistance is expressed through a coefficient (K_c), which shows the amount of fluid energy loss per unit length of a conduit for a particular hydraulic regime and can be expressed as:

$$K_c = \frac{h_L 2 g_a}{V^2} \quad \textbf{(2.10)}$$

where h_L is the head loss due to pipe length, g_a is the acceleration due to gravity and V is the flow velocity.

Often the flow resistance coefficient is described by an empirical friction factor in hydraulic roughness calculations (Morvan et al. 2008). Flow resistance coefficients often reflects an equivalent measure of pipe condition and so do not reflect the actual physical size and shape of pipe wall roughness. Whereas the roughness reflects the pipe / bed shape geometrical properties, which can be physically measured.

Friction in a pipe occurs when a fluid travels over a solid boundary, and momentum and energy is lost due to frictional and pressure drag effects. Among the factors that determine the amount of friction caused include the viscosity and velocity of the fluid and the surface texture of the pipe. Change in any of these parameters influences the increase or decrease of the friction factor which affects the performance of the fluid.

In general, friction factor is empirically determined and has been shown to depends on the Reynolds Number of the pipe flow and the relative roughness (k_s/D_c) of the pipe wall, where k_s is the equivalent roughness height, which is a measure of average particle grain size inside the pipe (Nikuradse 1933). The equivalent roughness height is also called the hydraulic roughness. Usually, it is assumed that the hydraulic roughness is equally distributed along the length of the pipe.

Most of the friction factor calculations presented in this section correspond to pipes running full, where it is assumed that the equations are appropriate for partially filled pipes by substituting the pipe diameter (D_c) with four times the hydraulic radius ($4R$).

Early studies of Darcy and Weisbach back in the 19th century have established a strong correlation of energy loss in liquid flowing through pipes due to the flow velocity, pipe diameter and wall condition (Weisbach 1845 and Darcy 1857). The equation is empirical and expressed as follows:

$$h_f = f\frac{L}{D_c}\frac{V^2}{2g_a} \quad \textbf{(2.11)}$$

where h_f is the head loss due to friction, f is the dimensionless Darcy - Weisbach friction factor coefficient, L is the pipe length, V is flow velocity and g_a is the acceleration due to gravity.

$$f = \frac{8Rg_a s_f}{V^2} \quad \textbf{(2.12)}$$

For the partially full pipes (pipes with free surfaces) the Darcy - Weisbach friction factor (f) can be presented in terms of hydraulic radius (R) instead of pipe diameter (equation 2.12), where s_f is the pipe bed slope.

In late 1930's Colebrook and White introduced an implicit equation to solve for Darcy - Weisbach friction factor (f) using iteration. The equation was developed by the combination of theoretical and experimental studies of turbulent flows in smooth and rough pipes (Colebrook 1939). The equation is appropriate for full-flowing conduit with relative roughness (k_s/D_c) values up to 0.05:

$$\frac{1}{\sqrt{f}} = -2\log_{10}\left(\frac{k_s/D_c}{3.7} + \frac{2.51}{Re\sqrt{f}}\right) \quad \textbf{(2.13)}$$

The above equation can be rearranged for the pipe with free surface flow using four hydraulic radius ($4R$) instead of pipe diameter:

$$\frac{1}{\sqrt{f}} = -2\log_{10}\left(\frac{k_s}{14.8R} + \frac{2.51}{Re\sqrt{f}}\right) \quad \textbf{(2.14)}$$

The equation can be rearranged to solve for the pipe hydraulic roughness (k_s):

$$k_s = 14.8R\left(10^{\frac{-1}{2\sqrt{f}}} - \frac{2.51}{Re\sqrt{f}}\right) \quad \textbf{(2.15)}$$

The above equation will be used to calculate the hydraulic roughness in experiments carried out in this work, where the friction factor is obtained using equation (2.12). It should be noted that this equation will provide a roughness value which will reflect the equivalent physical roughness associated with the specific pipe flow and resistance. For a given pipe section this may not reflect the actual physical size of the roughness height.

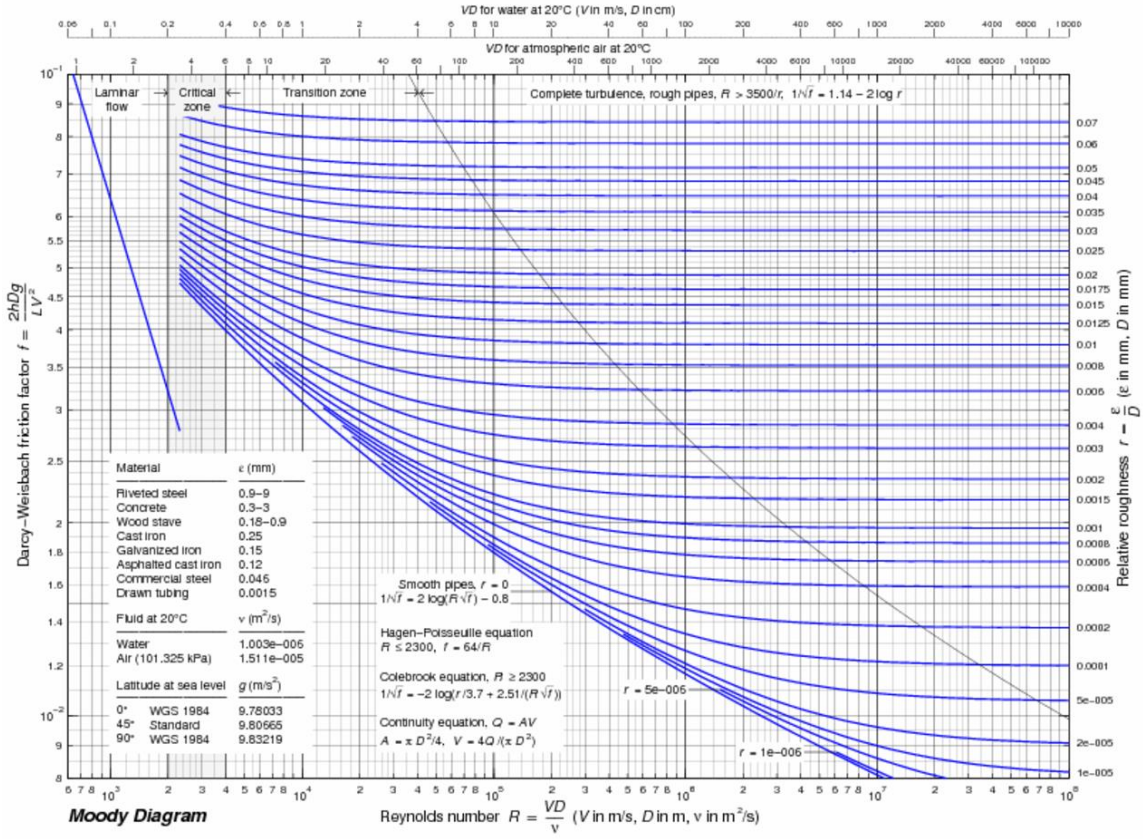

Figure 2.6 Moody diagram (Softpedia 2012).

Moody has used Darcy - Weisbach expression of friction factor and created a chart of relative values (Figure 2.6, where $\varepsilon = k_s$). This work of Moody (1944) generalised common experimental results for finding friction factor for different pipe diameters, roughness and flow regimes. With above findings, Moody proposed an empirical equation for the friction factor (Moody 1944):

$$f = 0.0055\left(1 + \left(2 \times 10^4 \frac{k_s}{D_c} + \frac{10^6}{Re}\right)^{1/3}\right) \quad \textbf{(2.16)}$$

This equation is applicable for Reynolds number greater than 4000 and relative roughness of up to 0.01.

Barr has published tables (Barr and Wallingford 1998) with proposed discharge, velocity and roughness calculations for part-full circular pipes (Barr 1981).

Based on experimental data, Barr has proposed an equation of proportional flow variation to pipes' cross-section with changing roughness parameter:

$$\theta_k = \left\{ \frac{k_s}{D_c} + \frac{1}{3600 D_c S^{\frac{1}{3}}} \right\}^{-1} \quad \textbf{(2.17)}$$

where θ_k is the so called transitioning parameter, D_c is the pipe diameter and S is the piezometric gradient.

The tables created by Barr provide values of θ_k for a range of proportional pipe depth to discharges for circular pipes. Which further substituted into equation (2.17) will provide an estimate of the hydraulic roughness (k_s).

2.2.4 Hydraulic parameter variation with water depth

The geometry of a circular pipe is such that the volumetric flow rate (q) increases with the increase in the cross-sectional flow area (A_h) and hence the flow depth (h). The same happens with the flow discharge (Q), however both the velocity (V) and discharge (equation 2.18) have different curve geometry (Figure 2.7). This occurs as the flow wetted perimeter changes more rapidly compared to the area of flow. The V_{max} and Q_{max} are defined by computation for $A_{h,max}$ which corresponds to pipe running full.

$$V = \frac{Q}{A_h}, \qquad V_{max} = \frac{Q_{max}}{A_{h,max}} \quad \textbf{(2.18)}$$

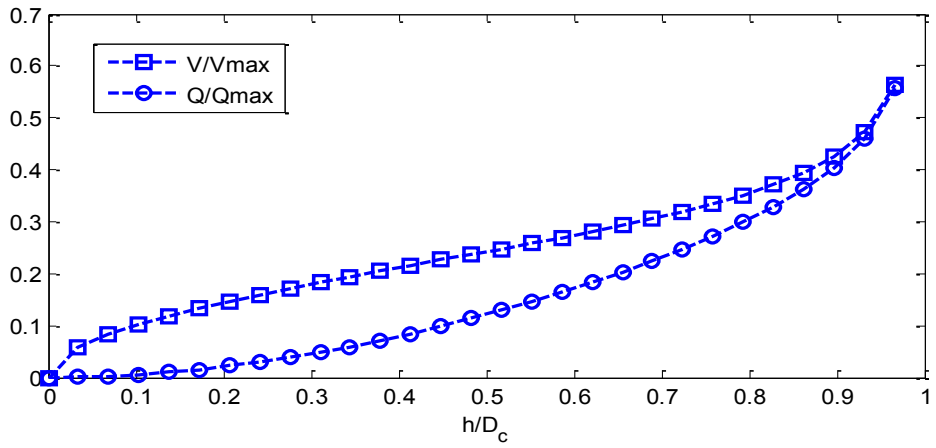

Figure 2.7 Velocity and discharge as a function of flow depth in partially filled pipe.

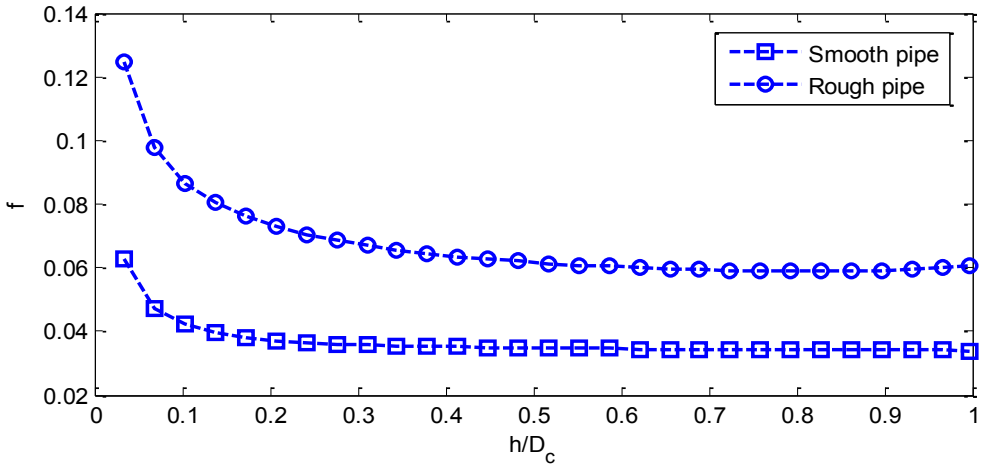

Figure 2.8 Friction factor as a function of flow depth in partially filled pipe.

On the other hand, the frictional resistance increases when in contact with pipe walls. However, as the friction factor is dependent upon the hydraulic radius (flow area / wetted perimeter), in pipe with free flow, and velocity squared (which increases rapidly with flow area), the friction factor does decrease with the increasing flow depth. Figure 2.8 demonstrates the change in the friction factor with non-dimensional water depth for a pipe with free flow (under uniform conditions). The graph illustrates the friction curve for smooth pipe (PVC pipe with pipe material roughness of 0.02mm) and rough pipe with roughness value of 5mm.

Similar as for the friction, the hydraulic roughness values (k_s), calculated from Colebrook - White equation, decrease with increasing flow depth. Figure 2.9 demonstrates the data for smooth and rough pipe condition (as per friction factor). For the rough pipe the k_s values are expectedly higher than for smooth pipe. Also, in the rough pipe regime, when the flow depth reaches full pipe the roughness increases slightly, hence it is more efficient to run the pipe just few percent's below the full water depth.

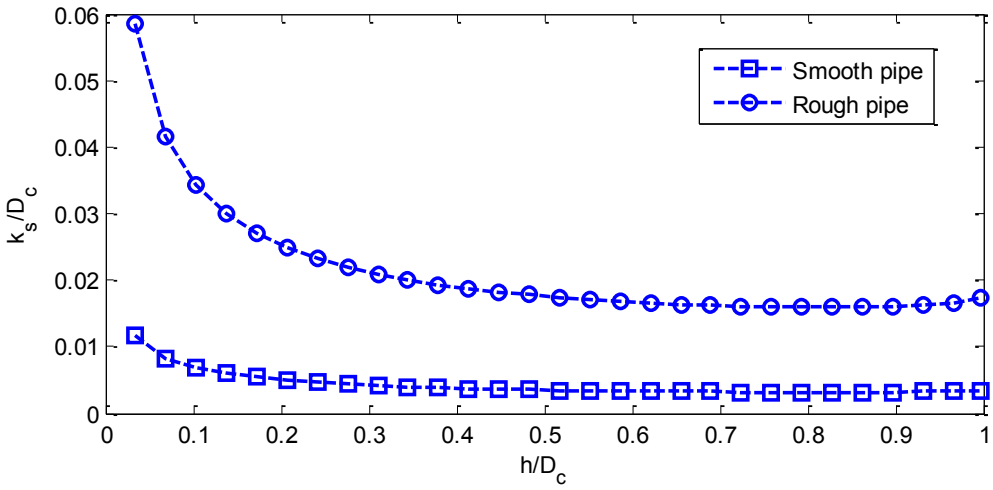

Figure 2.9 Roughness as a function of flow depth in partially filled pipe.

In the presence of physical pipe wall roughness, or some physical roughness on the pipe bed (i.e. sediment, hard compacted solids build up and random blocks in sewer pipes), the friction and hydraulic roughness parameters of the pipe are predicted to be much higher and decrease more rapidly with the increase in water flow depth.

2.2.5 Roughness concentration and pattern

O'Loughlin and MacDonald (1964) with the use of roughness concentration described the variation of the resistance coefficient. The authors used sand grains and aluminum cast cubes as a roughness equivalent, which were organised randomly and in a fixed pattern, respectively.

The 13mm cubes were used to simulate roughness concentration (λ_r) of 0.11 - 0.70 according to Schlichting's (1936) definition:

$$\lambda_r = \frac{n_\lambda a_\lambda}{A_\lambda} \quad \textbf{(2.19)}$$

Where n_λ is the number of elements present on the area of the bed, a_λ is the upstream projected area from the particles and A_λ is the total area of the bed.

Sand grains with mean height (k_h) of 2.9mm were used to achieve a 0.0077 - 0.64 of roughness concentration.

From the experimental data it was possible to note that any relative roughness to resistance coefficient curve can be expressed by the following equation:

$$\frac{1}{\sqrt{f}} = \frac{C}{K}\log_{10}\left(\frac{\lambda_r h}{k_h}\right) \quad \textbf{(2.20)}$$

Where K is the Karman's coefficient, C is a constant, λ_r is roughness concentration, h is the uniform flow depth and k_h is the mean roughness height.

The equivalent sand roughness can be computed, assuming that the resistance equation can be written for flat surfaces roughness with Nikuradse (1933) type uniform sand. Hence the following resistance equation can be obtained by integrating the experimental velocity distribution observed by Nikuradse in pipes:

$$\frac{\mathrm{V}_l}{\mathrm{s_V}} = \frac{2.3}{K_N}\log_{10}\left(\frac{30l}{k_s}\right) \quad \textbf{(2.21)}$$

where V_l is the velocity at distance l from the boundary, $\mathrm{s_V}$ is the shear velocity and K_N is the Karman's number defined by Nikuradse. The integration of the above equation (2.21) over flow depth gives the following:

$$\frac{1}{\sqrt{f}} = \frac{0.81}{K_N}\log_{10}\left(2.75\frac{4h}{k_s}\right) \quad \textbf{(2.22)}$$

And by comparing equations (2.20) and (2.22) the same equivalent sand roughness is achieved for the same resistance coefficient:

$$\frac{k_s}{k_h} = \frac{11}{\lambda_r(C_{K_N}/0.81K)}\left(\frac{h}{k_h}\right)^{1-(C_{K_N}/0.81K)} \quad \textbf{(2.23)}$$

Combining the above methodology with experimental data it was found:

In terms of concentration, when $\lambda_r = 0$ the sand roughness also was zero, i.e. the surface was smooth. At low concentration a one-to-one correspondence

between k_s and λ_r was established regardless the shape of roughness element. For medium values, the wave behind each element is not diffused before the flow reached the next one. At high concentration values, the individual element influence on the boundary resistance diminishes due to sheltering effect of the neighboring elements. Also, it was noted that the regularity of the cubes allows for a skimming flow development over the cube smooth surface when the spacing between cubes is small enough. This fact influences the drop of effective resistance.

The change of cubes pattern can have the same effect as the change of cubes regularity or shape. And again the effect of the skimming flow can be observed. For low cube concentration or pattern no viscous effects were observed. The data was also found to dependent upon the reference of bed elevation.

Chow (1959), summarized roughness element density on the conduit bed under three groups, 'k-type', transitional and 'd-type', where λ_s is the roughness wavelength (element separation) and k_h is the roughness height. This classification is based on a theory that the loss of energy in turbulent flow is mainly caused by the formation of wakes behind each of the roughness elements.

$$\lambda_s/k_h > 4 \quad - \quad \text{'k-type'}$$

$$2 < \lambda_s/k_h < 4 \quad - \quad \text{transitional}$$

$$\lambda_s/k_h < 2 \quad - \quad \text{'d-type'}$$

First is the 'k-type' roughness where each roughness element acts as an individual (isolated) roughness component. According to the Perry et al. (1969), in this type of roughness, eddies of the flow structures which are generated between the roughness elements are affecting the flow above the crests of the

roughness elements. At higher water depth eddies effect dissipated in the boundary layer, however can be pronounced on water surface in shallow water flows (unfortunately no ratio of k_h/h has been provided). Second is ‘d-type’ roughness where the bed roughness elements are more closely spaced. Here, eddies of the flow structures which are generated between the roughness elements are isolated by the roughness element walls and they do not contribute to the flow above the roughness element, such that the outer flow is considered to be undistracted (Chow 1959). Also, beds with ‘d-type’ roughness tend towards a smooth pipe condition with constant drag coefficient (Perry et al. 1969, Wood and Antonia 1975). With ‘k-type’ roughness there is an apparent link between hydraulic roughness and roughness element height, which is not true for the ‘d-type’ (Perry et al. 1969).

An experimental and numerical study (Lyn 1993, Yoon and Patel 1996) have suggested that for large roughness (with small spatial distribution) to flow depth ratios the periodic roughness elements (dynes, ripples, cubes) can be considered as distributed roughness, however for small roughness (with large spatial distribution) to flow depth ratio the periodic roughness elements are considered to be local (i.e. isolated from each other).

Further, the PhD thesis of Kleijwegt (1992) has some very interesting studies on the relation of grain roughness to the bed from dimensions and flow resistance for the circular sewer pipes with sediment. Although, the sediment is not used in our work, Kleijwegt (1992) developed results that can still be of interest.
For the roughness determination of pipe wall, with the presence of some sort of flat bed, the author used side-wall correction procedure.

$$k_w = \frac{R_w^4}{R_b^4} k_b \quad \textbf{(2.24)}$$

Here k_w is the wall roughness due to bottom roughness, R_b is the bed hydraulic radius (calculated from mean flow data), R_w is the wall hydraulic radius and k_b is the side wall correction and it was confirmed that the values of $2.5D_{r,90}$ and $3D_{r,90}$ provide the best accuracy, where D_r is the diameter of particle such that n % of sample is finer. Further, the author describes the prediction of bed-form dimensions and compares to the experimental data. The bed forms were describes as: continuous, flat motion bed, bed with forms (dunes or ripples), discontinuous and isolated object bed. Dune is a regular bed form with straight crest and maximum length of larger than flow depth. Ripple is an irregular shape and with maximum length equal to flow depth. We are mostly interested in the last bed form.

It was suggested that the Froude number should be used to predict the bed form, i.e. for $Fr < 0.6$ bed form occurs and at $Fr > 0.7$ flat bed takes place.
Also, the Gill's (1971) bed-form height predictor was applied, and concluded that the following formulae gives acceptable results for continuous bed:

$$H_r = \frac{1}{3} R_b (1 - Fr^2) \left(1 - \frac{\tau_c}{\tau_b}\right) \quad \textbf{(2.25)}$$

where H_r is the bed-form height, R_b is the hydraulic radius of the bed, τ_b is the bed-shear stress and τ_c is the critical bed-shear stress for particle motion. However, this formulae underestimates the height for dunes bed form, hence a correction of 3.36 instead of 3 in this case is applied.
Though, a more simple formula was calibrated from the experimental data that is capable of detecting ripple height:

$$H_r = 0.015(1 - Fr^2) \quad \textbf{(2.26)}$$

The bed form length can be predicted by simple two formulas, one developed by Gill (1971) and other by Yalin (1992):

$$\frac{H_r}{L_r} = 0.06 \ and \ \ L_r = 1000 D_{r,50} \quad \textbf{(2.27)}$$

Both of the formulas predict better for the ripples length (L_r), whereas the Yalin's method can be also used for the dunes, however the results are not great. Hence, the prediction of Van Rijn (1984) is advised for dunes length $L_r = 7.3h$, where h is the depth of flow.

Next, this work describes the study of flow resistance which depends on bed (continuous element) and wall roughness and is an important factor in flow characteristics. The author has confirmed that the methods for rectangular channels are not acceptable to sewers as shape-educed energy losses should be considered.

However, an interesting study of Manes et al. (2009) commenced in rectangular channels have suggested that due to the bed with the presence of some roughness element pattern the flow resistance can be significantly affected. Moreover, for this bed conditions, the friction factor increases with the increasing Reynolds number.

Whereas, Sterling and Knight (2000), Knight and Sterling (2000) and Berlamont et al. (2003) have found (during experimental trials and computer simulations) that for circular pipes with free flow with the presence of sediment, the shear stress distribution is significantly affected, with maximum occurring at pipe's cross-sectional hydraulic center and different depth for different h/D_c runs. The

shear stress turned out to be extremely sensitive to pipe bed and wall geometry (Knight and Sterling 2000). However, if the roughness height (k_s) of the sediment bed equals the roughness of the pipe wall, there is little effect on shear stress distribution. For increasing depth of flow (Knight and Sterling 2000) and low flow velocities (Berlamont et al. 2003) the shear stress is more uniformly distributed along the pipe's cross-section. Experiments have revealed that the shear stress is the same for supercritical and subcritical flow regimes (Knight and Sterling 2000). Also, it was confirmed that these are complex secondary structures present in the flow and that the nature of the flow in such pipes has a pronounced three dimensional nature (Sterling and Knight 2000).

Thus it may be argued that with the presence of roughness elements on the pipe walls the shear stress pattern will also be highly affected. Hence the friction at those points may be higher than the average and this phenomenon will contribute to the increase in the overall hydraulic roughness.

Some further works of Yalin (1992) and Krogstad and Antonia (1999) have confirmed that the large scale roughness can have a major effect on the instantaneous flow field where time and space averaged properties may change. Whereas it was suggested that due to the bed large enough size roughness elements the structure of the outer layer of the flow (surface flow) may be unique and correspond to a particular roughness structure and pattern and flow characteristics (Krogstad 1991, Djenidi at al. 1999).

2.2.6 Bed induced surface wave forms

The studies of pipe bed roughness concentration and pattern lead to an assumption, that the pipe bed topography has a measurable influence on the flow surface structures (when in turbulent flow regime) in shallow water flows.

The works of Smith and McLean (1977), Nelson et al. (1993), Pokrajac and Manes (2009) and Pokrajac (2010) examined double-averaged velocity profiles due to rough beds which has shown that there are two distinct behaviors present. First, a near-wall zone (very near to rough bed) of irregularity was observed which produced a significant form-induced stress. This is due to the strong influence of roughness element on the flow structure. Second, further from the wall all parameters are roughly equal and hence the form-induced stress is negligible. Further, it was noted (Pokrajac and Manes 2009) that the irregular zone takes up less of the flow depth than the second one, and the maximum form-induced stress occurs in the plane near the roughness crest at $z_h/k_h = 1.15$ where z_h is the height above the bed and k_h is the roughness height. It should be noted, that above this point the velocities are still under the influence of roughness element, but the flow has minimized the form-induced stress. This pattern continues only some distance further down the flow from roughness element. This study confirms that the bed roughness elements that have a smaller h/k_h ratio (i.e. shallow flow regime) and/or are located closer to the flow free surface (i.e. on the pipe wall curvature just below the flow surface, rather than in the center of pipe bed) have a stronger influence on pipe flow friction and hydraulic roughness.

A number of studies have been made in the channels for turbulent flows in the presence of rough bed (Raupach et al. 1991, Patel 1998, Nikora et al. 2001, Nikora et al. 2004 and Jimenez 2004), which confirmed that the mean velocity profiles in these channels vary significantly from those with a smooth bed as the flow bottom drag increases considerably with the presence of roughness. Work of Polatel (2006) confirms experimentally that shape and magnitude of surface

waves in channels is governed by the roughness bed shape and pattern. Further, it has also been suggested that that the surface water pattern of turbulent free surface flows in rivers and rectangular channels can carry information of the flow characteristics such as hydraulic roughness (Cooper et al. 2006). For example, the work of Julien et al. (2010) states that there is a relation between the channel slope, discharge and hence the Froude number with the surface wave amplification. This work also identifies that different wave lengths are present at the same time and concludes that the shorter wave lengths have a greater amplification over time and hence carry more information. Other tests conducted in the rectangular channels suggest that the water surface pattern carries information on the overall hydraulic losses (Cooper et al. 2006). It is known that the secondary flow pattern in circular pipes is very different from that in rectangular channels (Cieslik 2009), however it seems reasonable that the surface water waves in turbulent flow in a partially filed pipe would also carry sufficient information on the flow so that hydraulic parameters such as the pipe wall roughness can be determined.

2.3 Acoustics overview

Pipe survey technologies based on acoustic instrumentation and signal processing are extensively used by the water industry. The advantages of acoustic inspection methods are the speed of inspection and the ability to analyse data objectively with automatic classification systems (El-Ghamry et al. 2003, Dhanalakshmi et al. 2011). The methodology of a majority of acoustic methods is based on pulse reflectometry (Sharp 2001), sound transmission techniques (Yin and Horoshenkov 2006) and signal correlation techniques

(Fuchs and Riehle 1991). There are models for sound propagation in a pipe with a static wall roughness Yin and Horoshenkov (2006). However, there are models which can be used to predict the effect of the dynamic roughness generated on the water surface by the flow turbulence in the pipe. The purpose of this section is to review the literature which report on the models for and experiments which can be used to study the effects of the wall roughness on the acoustic field in a pipe. This will be followed by the models for sound attenuation which account for a statistically rough surface.

2.3.1 Sound propagation in pipes

Low-frequency sound wave propagation in a narrow duct of uniform cross-section is often modelled as a 2-dimensional problem. In this model, it is assumed that the wavelength (λ) of the transmitted sound should be much longer than the diameter of the pipe, and that the acoustical impedance of the wall is much greater than the impedance of air. In a case when the wavelength is smaller than the pipe diameter, a number of higher-order modes can be excited. These modes travel in various directions and at group velocities which are lower than sound speed in air. Normal modes combine in a complex sound pressure pattern which is hard to analyse and extract information from. In order to ensure that the sound field in the pipe is not multimodal, the frequency of sound (f_e) should not exceed the cut-on frequency (f_c) of the first cross-sectional mode, which for a 2-D case can be estimated from

$$f_c \approx 0.5c/D_c \tag{2.28}$$

where c is the speed of sound in air and D_c is the pipe diameter. For a 2-D pipe case it can be summarized that: (i) in the plane wave regime, when $\lambda \gg D_c$, or $f_e < f_c$, sound waves travel along the central axis of the pipe at the speed close

to the speed of sound in air and any waves traveling in other directions are evanescent and their amplitude attenuates exponentially with the pipe distance; (ii) in the case, when $\lambda < D_c/2$, the sound waves can propagate in directions other than along the central axis of the pipe. The above two phenomenon's are illustrated in Figure 2.10.

Figure 2.10a demonstrates the propagation of an acoustic wave along the central axis of a 2-D duct. Figure 2.10b shows the multimodal nature of sound propagation in a 2-D duct.

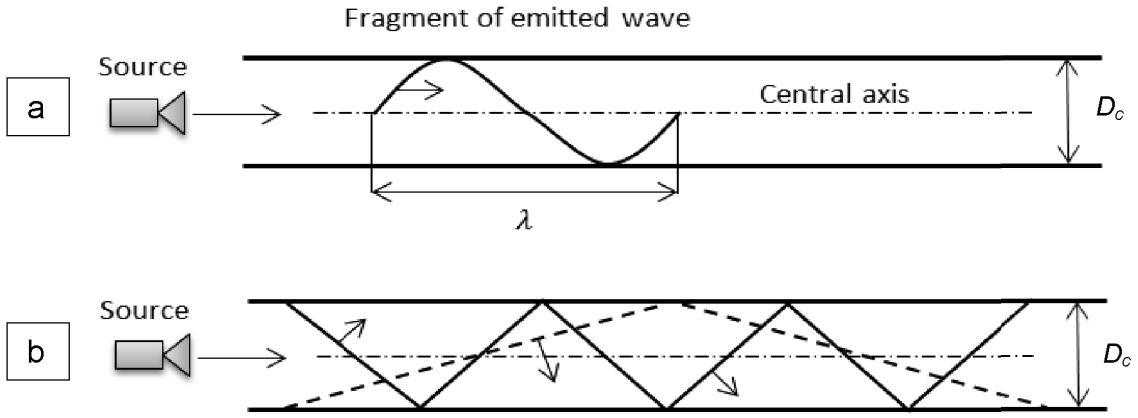

Figure 2.10 Wave propagation in a pipe, 2-D case.

For a more realistic case is when sound propagates in a round 3-dimensional pipe. This case is illustrated in Figure 2.11.

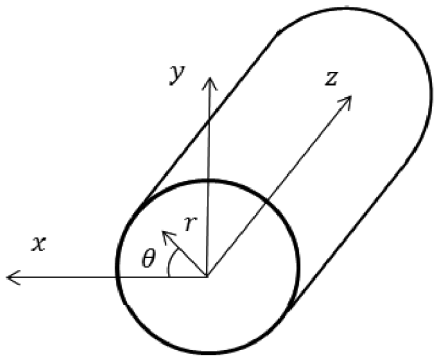

Figure 2.11 Coordinate system of a 3-D pipe.

A typical way to represent the sound field in a 3-D pipe is to use the method of normal model decomposition (Morse and Ingard 1968) according to which the sound pressure is given by

$$p_s(d_r, \theta, z) = \sum \Psi_{mn} e^{ik_{mn}z}. \quad \textbf{(2.29)}$$

In the above equation, d_r and θ are the radial distance and azimuthal angle in the polar coordinates (x, y, z) about the central axis of a pipe (see Figure 2.11), Ψ_{mn} is the eigen-function, m and n are the modal indices, k is the wavenumber. In the case of a round pipe, the eigen-function are a combination of a Bessel and cosine functions, i.e.

$$\Psi_{mn} = \cos(m\theta) J_m(X_{mn} d_r). \quad \textbf{(2.30)}$$

The pipe radius is denoted as r, and the eigen-values for this equation can be found as shown below.

$$X_{mn} = \frac{\pi q_{mn}}{r} \quad \textbf{(2.31)}$$

$$k_{mn} = \sqrt{k^2 - X_{mn}^2} \quad \textbf{(2.32)}$$

In the case of the fundamental mode $(m, n = 0,0)$, the eigen-function is independent of the coordinates and the sound pressure distribution across the pipe section is constant. Similarly, to the 2-D case, this is true when $\lambda \gg D_c$. In the case, when $\lambda < D_c$, several modes can propagate in the pipe and the sound pressure distribution depends strongly on the cross-sectional coordinate. In the case of a circular pipe, the plane wave regime is achieved when the frequency of sound $f_e \ll f_{10}$, where $f_{10} = 0.5861c/D_c$. This regime is mostly suitable for the development of robust acoustic instrumentation because the sound field registered with the microphones is relatively unaffected when the microphones are misplaced from their assumed position in the pipe.

2.3.2 Scattering from rough surface

In nature, all surfaces are inherently rough. The surface roughness can be either small or large depending on the surface material, texture and pattern. This condition affects the propagation and scattering characteristics of a wave which is reflected by a rough surface. A plane wave which is incident on a perfectly smooth, flat surface is reflected only in the specular direction. However, if this wave is reflected from a rough surface it is scattered in all possible directions. An additional complexity here is when the surface roughness is not stationary, but changes with time. In this case, the dynamic changes in the roughness statistics and spectral characteristics will affect the temporal characteristics of the scattered sound field.

The scattering of sound from a rough surface depends on the wavelength and the direction of sound propagation (Ishimary 1978). In the case of a smooth, acoustically rigid surface, there is no shift in the phase between the incident and reflected waves. The angles for the incident and reflected waves are equal (Figure 12a). In case of a rough surface, there is some phase shift between the reflected and incident waves and the angles at which these waves propagate can be radically different (Figure 12b). The phase difference ($\Delta\phi$) depends on roughness height and can be expressed as follows (Ishimaru 1978):

$$\Delta\phi = 2k\sigma_h \cos\theta_i \qquad \textbf{(2.33)}$$

For σ_h the standard deviation of the height variation of the rough surface should be considered. Hence: $smooth\ surface, \sigma_h > \lambda/(8\cos\theta_i) > \sigma_h, rough\ \ surface.$

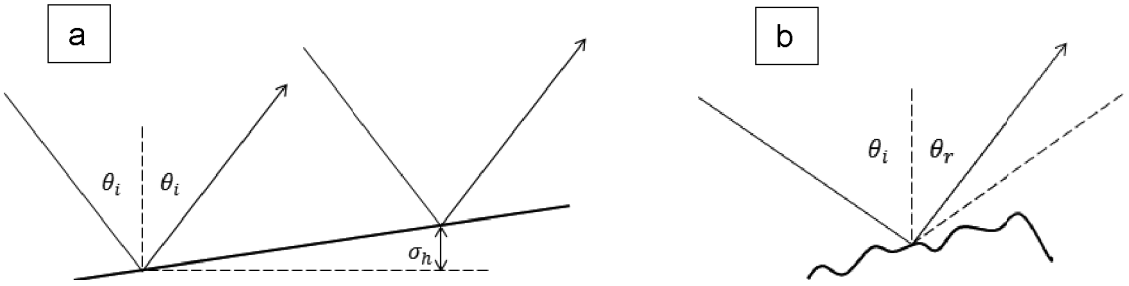

Figure 2.12 Wave reflection from any surface (Ishimaru 1978).

Shenderov (1989) review of the Rayleigh hypothesis of sound reflection due to roughness, suggests that it is true for the shallow surfaces with the surface roughness equation similar to $z = \sigma_h \cos(2\pi x/l_c)$, hence roughness with sinusoidal shape (see Figure 2.11 for x and z, and l_c is the correlation radius length). In such cases, the theory is true where the $2\pi x/l_c \ll 0.448$ or $\sigma_h/l_c < 1/14$, which is independent of the wave length and is defined only by the geometric roughness parameters.

The power of the transmitted wave reflected in the specular direction is called the specular or coherent component, and the scattered power is referred to as diffused or incoherent component. For rougher surfaces, the coherent (specular) field diminishes and the incoherent (diffused) field becomes to dominate.

A simple way to account for a small surface roughness is to introduce the notion of equivalent acoustic admittance. This procedure is well described in the work by (Bass and Fuks 1972). In one particular case, when the wavelength is much greater than the spatial correlation radius for the surface roughness $kl_c \ll 1$, the equivalent acoustic admittance of the rough surface can be given by the following expression:

$$\beta \approx -i\frac{k\sigma^2}{l_c}\int_0^{\infty}\frac{1}{x_s}\frac{dw_s}{dx_s}dx_s \qquad \textbf{(2.34)}$$

where $k = 2\pi/\lambda$ is the wavenumber in air, σ is the mean roughness height and $w_s(x)$ is the spatial correlation function for the surface roughness with the normalised argument $x_s = \rho_0/l_c$. We note that the value of the equivalent admittance is purely imaginary so that the admittance itself is purely reactive causing no energy loss in the pipe as the wall being perfectly rigid.

More recently, Boulanger et al. (1998) calculated the effective impedance of a rough surface using the Twersky boss theory (Twersky 1983). This study revealed that the obtained effective acoustic impedance differ considerably when measured on a surface with periodic or random roughness elements of same density. For the roughness with periodic arrangement the sound pressure levels are higher and more sensitive to small changes in roughness geometry. This model has been developed further (Boulanger et al. 2005) to predict the reflection from surfaces with more random roughness distributions. The results revealed that the element distribution has a large effect on relative sound pressure level, hence to obtain meaningful surface roughness result, element roughness distribution should be normalised over an examination area.

2.3.3 Acoustic field in the presence of roughness

A number of studies have been carried out to examine the effect of surface roughness on sound propagation in an underwater. The works of Kryazhev and Kudryashov (1976 - 1984) are focused on the sound field in a waveguides with irregular boundaries. The experiments and the numerical model have been conducted in and prepared for the Arctic sea with the continuous ice cover surface which was statistically rough.

In one particular model, (Kryazhev et al. 1976), the effect of multiple scattering due to the irregularly rough surface is successfully described through the coherent component of the acoustic field. The work concludes that the surface ice cover, i.e. the irregular rough boundary causes considerable attenuation of the sound field at frequencies greater than 30Hz as well as modifying the field structure. At these frequencies the attenuation increases with the increase in mean roughness height.

In their later works, Kryazhev and Kudryashov (1978) have investigated the spatial and temporal correlation function for the diffused component of the sound field in a waveguide with statically rough boundaries. Along with the usual coherent component, the diffused component of the sound field is formed from the sound scattering due to the irregular boundaries. The surface roughness results in the redistribution of the energy in the coherent component of the sound field into the diffused (stochastic) component. As such, sound field spatial correlation decreases with the increase in frequency and distance in the presence of roughness.

The results of another study by the same authors suggests Kryazhev and Kudryashov (1984) that in the presence of continuously rough boundary the multimodal sound field in the waveguide rapidly looses its coherence with the increasing distance and the scattering component begins to dominate. The coherence here depends on the number of normal modes excited in the waveguide and on the parameters of the roughness.

More recent work by Attenborough and Taherzadeh (1995), Umnova et al. (2002) and Qin et al. (2008) concerns with the reflections of sound radiated with a point source in the presence of a rough surface. In these studies

predominantly pulse signals were used. The work of Qin et al. (2008) investigates the reflections from the sound propagating over a dynamically rough water surface. The results have shown that the secularly reflected component of the sound decreases with the increasing mean roughness height, while the fluctuations in the waveform of the pulse tail increase. This suggests that the acoustic energy in the incident sound wave is multiply scattered by the surface roughness pattern resulting in the extended tail in the reflected pulse.

2.3.4 Attenuation of sound due to pipe roughness

Some previous studies which are reviewed in the previous section, suggest that the acoustic effect of a static surface roughness can be expressed via the equivalent surface admittance. It is known from the basic theory of waveguides that the effect of the small wall admittance (i.e. $kr\beta \ll 1$) on the acoustic pressure the fundamental mode in a round pipe can be expressed as (Morse and Ingad 1986, p.512):

$$p_{00} \approx 1 + i\beta \frac{k{d_r}^2}{4r} \qquad \textbf{(2.35)}$$

where k is the wavenumber, d_r is the radial distance and r is the pipe radius.

If the surface is dynamically rough, then the admittance and pressure in expression (2.31) are time-dependent functions. In this case, the value of the admittance in the above expression should depend on the spatial correlation function $w_s(x_s, t)$ and on the mean roughness height σ (see equation 2.31), both of which can undergo temporal variations. Here, an apparent increase in the mean roughness height results in the apparent increase in the acoustic pressure in the fundamental mode due to the multiple scattering effects.

A simple way to account for the surface roughness with a pronounced geometrical pattern is to use the acoustic admittance model suggested by Attenborough and Taherzadeh (1995). Their work links the geometrical properties and statistical distribution of the rigid hemispherical scatterers to the imaginary part of the effective surface admittance, i.e.

$$\beta(t) \approx -ik\frac{\pi N_a(t)a(t)^3}{3}\left(1-\frac{\pi^2 a(t)^3}{4l_a(t)^3}\right)\left(1+\frac{\pi^2 a(t)^3}{4l_a(t)^3}\right), \quad \textbf{(2.36)}$$

where N_a is the mean density of boils per unit area, l_a is the mean spacing between the boils and a is the boils radius.

2.3.5 Acoustic intensity relations in a pipe

The traditional definition of the acoustic intensity is a measure of the time averaged power per unit area at which the acoustic energy is transmitted in space. Hence, the intensity is a vector quantity which describes the amount of energy and the direction (indicated by the sign) in which this energy propagates. More generally, the acoustic intensity can be defined as a product of the sound pressure (p_s) and particle velocity vector ($\vec{u}$):

$$\vec{I} = p_s\vec{u}, \quad \textbf{(2.37)}$$

where the sound pressure and velocity can be time-dependent. The measure of the instantaneous acoustic intensity in a pipe is very useful as it can provide information on the temporal variations in the incident and reflected sound energies.

The instantaneous acoustic intensity can be measured with a pair of microphones which are separated by some short distance Δ, so that the time-dependent acoustic pressures $p_1(t)$ and $p_2(t)$ can be recorded. In this case,

the instantaneous intensity can be given by the following approximate expression

$$\tilde{I}(t) = p_s(t)\vec{u}(t) \approx \vec{n}\frac{p_1(t) + p_2(t)}{2\Delta\rho_0}\int [p_1(\tau) - p_2(\tau)]dt \quad \textbf{(2.38)}$$

$$\vec{u}(t) = -\frac{1}{\rho_0}\int \frac{\partial p_s}{\partial \vec{n}}d\tau \approx \frac{1}{\Delta\rho_0}\int [p_1(\tau) - p_2(\tau)]dt \quad \textbf{(2.39)}$$

$$\rho_0 = 3.432 \times 10^{-3\frac{p_a}{T^0}} \quad \textbf{(2.40)}$$

$$c = 343.2\sqrt{T^0/293} \quad \textbf{(2.41)}$$

where equation (2.38) gives the amplitude of the projection of the acoustic velocity vector in the direction defined by the orientation of the pair of microphones. Here the normal, $\vec{n}$, is oriented in the direction of identical to the direction of sound propagation. In the above equations, τ is an auxiliary integration variable that correspond to time delay, p_a is the current atmospheric pressure, T^0 is the temperature in Kelvin (experimentally measured with the help of thermometer), where $1(C^o) = -273.15\ (K)$.

A general assumption is that the instantaneous acoustic intensity is a real. However, the work of Heyser (1986) suggests that it can be convenient to present the instantaneous acoustic intensity as a complex quantity, i.e. a quantity which contains the real (active) and the imaginary (reactive):

$$\tilde{I}(t) = \vec{I}(t) + i\vec{J}(t) \quad \textbf{(2.42)}$$

$$\vec{I}(t) = [p_s(t)\vec{u}(t) + \hat{p}_s(t)\hat{u}(t)]/2 \quad \textbf{(2.43)}$$

$$\vec{J}(t) = [\hat{p}_s(t)\vec{u}(t) - p_s(t)\hat{u}(t)]/2 \quad \textbf{(2.44)}$$

Equations (2.43) and (2.44) define the active and reactive part of the instantaneous acoustic intensity respectively. In these equations $\hat{p}$ and $\hat{u}$ are the Hilbert transform ($\hat{f}(t)$) values of sound pressure and particle velocity, respectively. The Hilbert transform for each of the parameters is found from

$$\hat{f}(t) = \frac{1}{\pi} \Pr \int_{-\infty}^{+\infty} \frac{f(\tau)}{t-\tau} d\tau \qquad \textbf{(2.45)}$$

where the $\Pr$ is the principal value of the integral. The active ($\tilde{I}(t)$) part of the instantaneous intensity accounts for the magnitude of the local energy flow, and the reactive ($\tilde{J}(t)$) part accounts for the local oscillatory transport of the energy associated with the sudden changes in the direction of sound wave propagation.

2.3.6 Pulse reflectometry

Pulse reflectometry methods are based on measuring the impulse response of the pipe, either with the use of transmitted or reflected signal. The success of the method is predominantly dependent upon the quality of our knowledge about the emitted pulse and boundary conditions which exist around the source when this signal was emitted.

The early studies of pulse reflectometry go to Mermelstein (1967) who described the reconstruction of the vocal-tract shape by the used of measured resonate frequencies using spark discharge. Further investigation of Sondhi and Gopinath (1971) revealed that the airway profile area of a vocal-tract can be described by the recording of a pulse reflection. Jackson et al. (1977), Goodwin (1981) and Duffield (1984) described reflectometers which were able to detect pipe segment areas. Deane (1986) took it further and replaced spark source by the loudspeaker, which meant that the pulse waveform was more reproducible. Hence consistent, and the signal-to-noise ratio could now be reduced by the means of averaging.

Currently, acoustic pulse reflectometry is known as a non-invasive technique for measuring pipe internal conditions. Works of Sharp and Campbell (1997) and Sharp (2001) discuss this technique in sufficient detail and explain its practical limitations.

A typical reflectometry method makes used of a source tube, where at the inlet a loudspeaker is placed. A microphone is attached to this tube some distance away near the place where this outlet is connected to the pipe. This arrangement allows the entire reference (emitted) pulse to pass the microphone before first reflection from the pipe discontinuities will reaches the microphone. The method then works from the basic principles on sound reflection and transmission through a duct with variable cross-section. In this way, the recorded reflections together with the emitted pulse provide the acoustic data (equation 2.46) from which the cross-sectional area can be deconvolved as a input impulse response of the pipe, i.e.

$$IIR(\omega) = \frac{R(\omega)\dot{I}(\omega)}{I(\omega)\dot{I}(\omega) + \bar{q}} \qquad \textbf{(2.46)}$$

where ω is the angular frequency, $R(\omega)$ is the transformed duct reflections, $I(\omega)$ is the transformed input pulse, $\dot{I}(\omega)$ is the complex conjugate of duct reflection and $\bar{q}$ is the conditioning factor. The method works very well if the quality of data is good and if the plane wave approximation is satisfied. There are some limitations which mainly relate to the finite width of the spectrum for which the plane wave approximation is satisfied. The spatial resolution reduces with the reduced frequency range.

2.3.7 Obstacle and roughness detection in pipes

Any type of change in the pipes cross-section will result in the variance of the acoustic signal response from that pipe. This basic principle was used to develop sensors which were capable of detecting such pipe diameter changes, which could either be general roughness or blockage.

The pioneering study of pipes obstacle sensing via acoustics was described by Antonopoulos-Domis (1980). The developed methodology used an eigen-frequency shift analysis, where fist two frequencies of the pipe shifted with the presence of obstacle. However, the method could not reveal the exact location along the pipe. Continuing the study, Qunli and Fricke (1990) revealed that the eigen-frequency shift pattern is unique for the blockage location inside the pipe. Whereas, the amplitude of the eigen-frequency shift can be used to define the obstacle size. Their developed method could also be applied in pipes with closed ends, however the method is only relevant for larger pipes. The above studies were followed by the important founding of DeSalis and Oldham (1999), where they reveal the blockage area function reconstruction from the pipe by the use of eigen-frequency and anti-resonance frequency shifts. In this method a single pressure response measurement from pipe of any length is used. A high noise immunity maximum length sequence technique was applied to identify anti-resonance residual pressure location in the measured frequency response.

Currently a robust method, developed by Horoshenkov et al. (2004, 2008) and Bin Ali (2010), of identifying obstacle location inside the pipes, as well as classifying blockage type exists. The method is based on response signal

complex analysis Bin Ali et al. (2010). The method is capable of detecting small obstacles as cracks, encrustation and joints defect to full pipe blockage.

However, it should be noted that none of the existing acoustic methods (known to the author of this work) are capable of detecting the hydraulic properties of the pipe as a result of the present obstacles (i.e. the hydraulic roughness).

2.4 Conclusions

This chapter provides information on general sewer problems related to increasing roughness and conventional methods of pipe roughness investigation. Further this chapter summarises previous important hydraulic and acoustic study foundings relevant to this thesis:

A number of studies undertaken in channels provide few definitions of roughness concentration types, situated on conduit, and propose equations which in turns divide the roughness in three groups, ‘k’- type, transitional and ‘d’-type. However, none of these are mentioned to be relevant to similar problem in the circular pipe. Further studies of channel bed roughness concentration provide evidence that the roughness concentration, shape, pattern, and submergence ratio depending on type, cause significant change in flow resistance, shear stress and secondary flow structures. Experiments conducted in pipes revealed that the same phenomenon as per channel is observed with magnifying effect due to pipe wall shape induced forces. Examination of rough beds in pipes concluded that roughness structure and pattern affects uniquely flow surface which has a 3-D characteristics. Although, some fundamental understanding of roughness effect on flow surface is

provided, no clear relations between bed shape roughness parameters and general hydraulic properties for pipes were found.

The acoustic review provided theoretical model of sound propagation in pipes with complex pipe boundary conditions that can be successfully applied to the purpose of this study. A number of key works are presented which step-by-step developed reflectometry techniques for acoustic detection of pipe conditions. Both sound propagation and reflectometry techniques will be applied in this work to determine the flow characteristics. A method of reflected signal analysis in terms of instantaneous acoustic intensity and further determination of the energy field is presented. Two mathematical theories are presented which suggest that the change in surface roughness should result in apparent change in reflected acoustic field, which will be investigated practically in current study. During broad literature search, no attempts by other authors to measure acoustically pipe hydraulic conditions in a pipe, rather than detect flow level, were identified by the author of this thesis.

Chapter 3 Local roughness experiments

In order to establish a link between the hydraulic characteristics of a pipe and the recorded acoustic field with and without the presence of local pipe roughness, a number of controlled experiments were carried out in the Hydraulic Laboratory of University of Bradford. Two different full scale sewer pipes, a 150mm diameter clay pipe and a 290mm diameter perspex pipe were used. This chapter provides information on the experimental facilities, measurement equipment and experimental conditions for which the local roughness and energy losses were measured directly and then deduced from the acoustic data. The acoustic data were analysed in terms of temporal frequency dependent composition of the energy reflected from the local roughness. These data were related to the hydraulic data obtained directly from independent measurements. The final part of this chapter presents a novel method of measuring acoustically the hydraulic performance of a sewer pipe.

3.1 Laboratory facilities

In the UK, the majority of problematic sewer pipes, where blockages are found, are of a small diameter, 300mm and less (Blanksby et al. 2002). These pipes make up to around 40% of the UK sewer network (OFWAT 2004). Hence the laboratory experiments will be conducted in two pipes, one clay pipe of 150mm in diameter and one perspex pipe of 290mm in diameter. The experiments will be conducted in these pipes with flow running partially full as this condition is commonly found in combined sewers. These conditions were selected so as to simulate representative full scale small diameter sewers.

3.1.1 150mm diameter clay pipe

A circular clay pipe of 150mm in diameter was used. It is 14.3m long and consists of 23 equal sections (each is 621mm long). The pipe sections were interconnected by a socket type arrangement and sealed with a rubber gasket. The pipe slope was set at 1:100, which is typical for small diameter pipes in sewer networks. The pipe rested on two interconnected steel beams which were supported by a number of adjustable, titling platforms as shown in Figure 3.1. The clay pipe had a small entry chamber (Figure 3.2) at section 12 which center was 7.1m away from the pipe inlet. This chamber was used to insert different types of blockages into the pipe (see section 3.1.4).

Figure 3.1 Arrangement of 150mm diameter clay pipe.

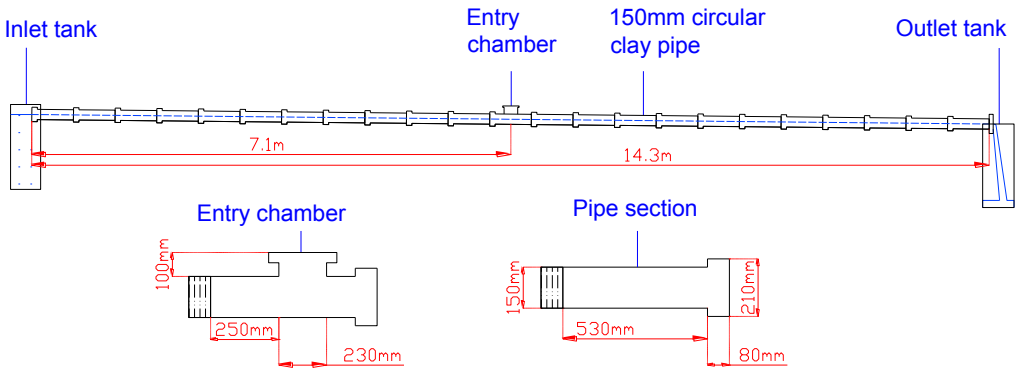

Figure 3.2 Side view of 150mm diameter pipe arrangement in the laboratory.

3.1.2 290mm diameter perspex pipe

The second circular pipe was made of transparent perspex material. The internal diameter of this pipe was 290mm. The pipe was 20m long and it was constructed from 10 equal 2m long sections that were sealed with connecting rings lined with external rubber gaskets (Figures 3.3 and 3.4). The pipe joints were carefully machined to provide little or no disturbance to the free flow. Pipe bed slope was fixed at a gradient of 1:100. This pipe had a rectangular entry slot cut in the pipe top, which center was 9.1m away from the pipes upstream end. The dimensions of this entry slot were 200 x 400mm (plan view dimensions) and it had a lid which was made to fit firmly sealing the gap. This entry was used to insert blockages and to install the measurement equipment.

Figure 3.3 Arrangement of 290mm diameter perspex pipe.

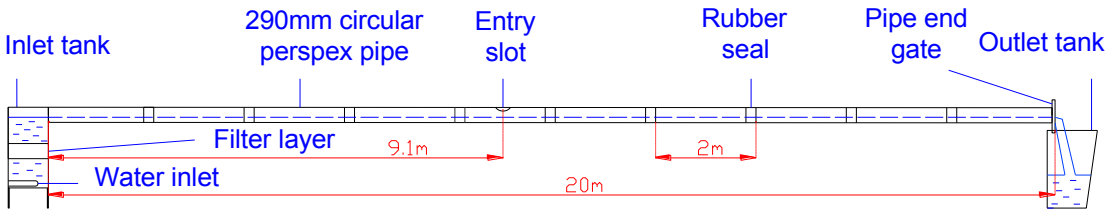

Figure 3.4 Side view of 290mm diameter pipe arrangement in the laboratory.

3.1.3 Flow regime control

Each of the two pipes had an inlet tank (see Figures 3.2 and 3.4) in which the inlet flow rate was controlled with a butterfly valve by changing the valve setting. The water was discharged into the pipe and collected in the outlet tank as shown in Figures 3.2 and 3.4. The water from the outlet tank was collected in a volumetric measurement tank located below the laboratory floor. In this way the volumetric flow rate delivered by the valves to the test pipe was determined by timing the collection of a known water volume in the volumetric measurement tank. The calibrated end gate located at the downstream end of the pipe was used to help to control the depth of flow in the pipe so as to achieve a uniform flow depth for a given discharge (see Figure 3.5).

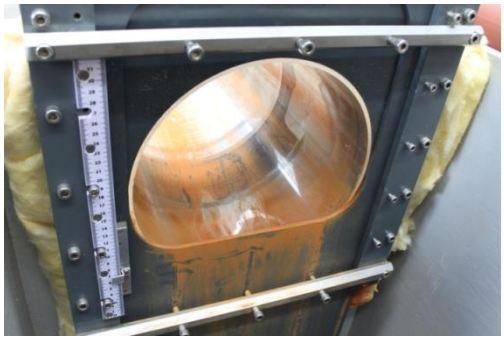

Figure 3.5 End gate of 290mm diameter perspex pipe which was used for uniform water depth control.

The water level measurements and uniform flow regime were monitored via the readings from the manometers. For both of the pipes, the manometers were non-equidistantly spaced, having at least one point reading per meter. In the case of the 150mm diameter pipe 14 manometers were used. In the case of the 290mm diameter pipe 30 manometers were used and these manometers were spaced more densely in the vicinity of the entry slot located at 9.1m from the inlet of the pipe.

3.1.4 Local roughness simulation

The sand-cement mixture cast model of the pipe internal geometry was used as a blockage to simulate a local obstruction and introduce an isolated roughness to the flow. For this purpose a set of different model sizes were used (see Figures 3.6 and 3.7) for both of the pipes. In the case of the 150mm diameter pipe, the blockage models were 100mm long (L_b) and ranged in height (h_b) from 15 - 60mm to represent a percentage of the pipe's cross-sectional area occupied by blockage (a_b) in range of 10 - 40% of the original pipe's cross-sectional area.

Figure 3.6 Model blockage samples for 150mm diameter pipe.

Figure 3.7 Model blockage samples for 290mm diameter pipe.

In the case of the 290mm diameter pipe, the model samples were 200mm long and had heights of 20 - 110mm. This provided pipe's cross-sectional area occupied area by blockage from 7 - 38% of the original pipe's cross-sectional area. The blockage length was chosen such that it would be between the length of pipe radius and diameter. The blockage was placed in the pipe through the

entry chamber and slot, which for both pipes are shown in Figure 3.8. The center of the blockage was aligned with the middle of the entry chamber and slot (at 7.1m for 150mm diameter pipe and 9.1m for 290mm diameter pipe).

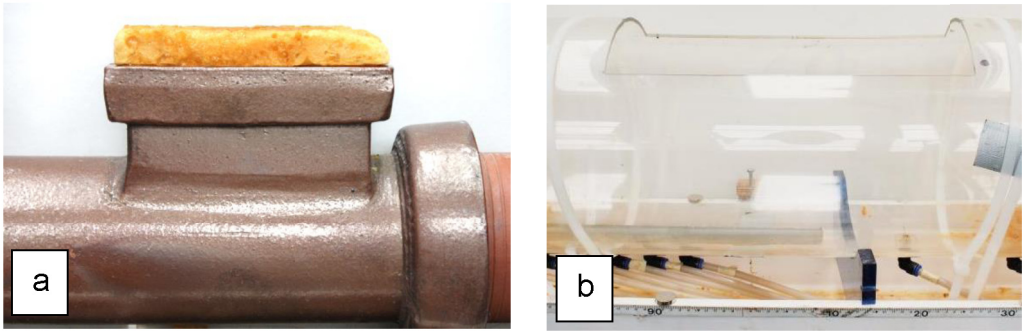

Figure 3.8 Entry chamber for 150mm diameter pipe (a) and entry slot for 290mm diameter pipe (b).

Table 3.1 presents the blockage dimensions and corresponding changes to pipe's cross-sectional area caused by the presence of the blockage.

Table 3.1 Blockage geometry and pipe's cross-section occupation.

Pipe diameter D_c [mm]	Blockage height h_b [mm]	Blockage length L_b [mm]	Pipe's cross-sectional occupation a_b [%]
150	15	100	10
150	30	100	20
150	40	100	27
150	55	100	37
150	60	100	40
290	20	200	7
290	30	200	10
290	40	200	14
290	50	200	17
290	60	200	21
290	70	200	24
290	90	200	31
290	110	200	38

3.2 Acoustic instrumentation

An acoustic based method of sewer pipe inspection was developed at the University of Bradford (Patent application: Horoshenkov et al. 2008). This method enables the detection of the location and extent of objects and defects which occur in sewer pipes (Horoshenkov et al. 2008, Bin Ali 2010). The instrumentation for the above acoustic method was used in this project to measure the acoustic response of the pipe in the presence of a local blockage. The acoustic response from the blockage was analysed and related to some hydraulic characteristics which were measured independently for a range of blockage dimensions and hydraulic regimes.

3.2.1 Acoustic Instrumentation

The acoustic instrumentation used in this work consisted of a sensor, electronic block and a laptop with software that controls the data acquisition and signal processing (Figure 3.9).

Figure 3.9 Acoustic equipment with large sensor.

The acoustic sensor comes in two sizes. The smaller sensor (Figure 3.10a) was used for the experiments in the 150mm diameter pipe, whereas the larger sensor (Figure 3.10b) was used in the 290mm diameter pipe. The smaller sensor is based on a speaker with a 64mm diaphragm (Visaton K64WP8OHM, see Appendix A1) which is capable of reproducing sounds in the 100Hz - 15kHz range. It is mounted in a 60mm long cylindrical enclosure. The larger sensor is based on a speaker with a 84mm diaphragm (Visaton FR84OHM, see Appendix A2) which is capable of reproducing sounds in the frequency range of 130Hz - 20kHz. It was mounted in a 114mm long cylindrical enclosure.

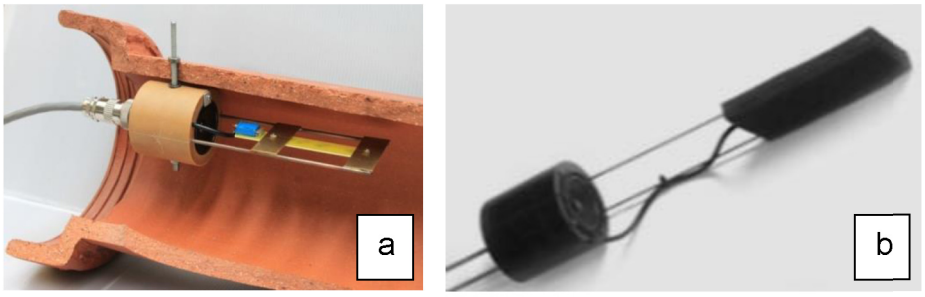

Figure 3.10 Small acoustic sensor in a 150mm diameter clay pipe (a) and free standing large acoustic sensor (b).

The small and large sensors used the same microphone array which was mounted in front of the speaker and aligned perpendicular with the speaker diaphragm. The microphone array was positioned at the distance of 75mm and 300mm in the small and large speakers, respectively. The microphone array consisted of four equidistantly spaced microphones (Knowles Acoustics SPM0208HE5), which had the sensitivity of 1V/Pa at 1KHz. The spacing between these microphones was chosen to be less than the wavelength (12.5mm, 17.5mm and 27mm) to enable the acoustic velocity measurement across the range of frequencies of interest (Bin Ali 2010).

During the experiment, the acoustic sensor was inserted in the pipe inlet above the pipe flow and attached to the top wall of the pipe (Figure 3.10a) with a screw. The sensor was positioned such that it was oriented towards the opposite end of the pipe (either upstream or downstream). The coaxial cable from the sensor was connected to the electronic block which was incorporated in an ultrabase of an IBM laptop. Matlab code was developed to control the data acquisition and processing. A chirp (sine sweep) signal with the frequency range of 50Hz - 20kHz was emitted through a 4-channel VX-Pocket soundcard. The top range of the chirp signal was chosen to be approximately half the sampling frequency ($f_s = 44.1kHz$) to eliminate the problem of poor conditioning during signal deconvolution. The chirp signal was amplified and transmitted via the loudspeaker. The reflected signals were detected with the 4-microphone array to be digitised using the sound card and deconvolved using Matlab code so that the acoustic pressure impulse response of the pipe could be determined (Horoshenkov et al. 2009). The average of all microphone pairs (six in total) was used to determine the acoustic intensity in accordance with the method described in (Horoshenkov et al. 2008). The acoustic experiment set up is illustrated in in Figure 3.11.

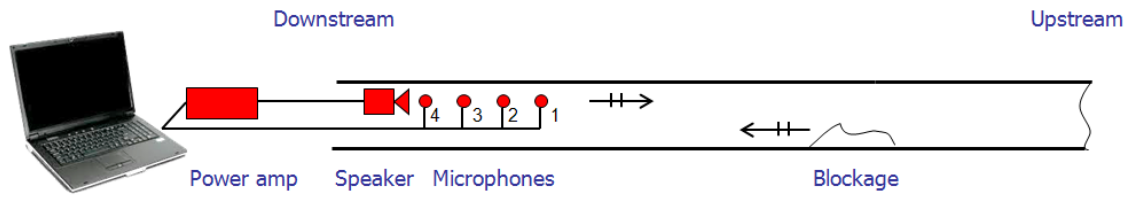

Figure 3.11 A schematic illustration of the acoustic experiment in the pipe.

The advantage of such a method is that: (i) it requires equipment only at one end of the pipe, (ii) it does not affect the flow, as the equipment is positioned above the flow free surface, (iii) and that the data collection and analysis is a

rapid process which can be completed within a 10 second period. The data processing method which was used in this work is described in section 3.2.2. It is based on impulse response, intensity and energy analysis of the recorded signal over specific distance and frequency range.

3.2.2 Signal processing

The acoustic intensity is known to be a vector quantity whose direction is identical to the sound wave propagation. The projection of the instantaneous intensity vector in the direction $\vec{n}$ is defined by the following equation:

$$I(t) = p_s(t)u(t) \approx \frac{p_1(t) + p_2(t)}{2\Delta\rho_0} \int [p_1(t) - p_2(t)]dt \qquad \textbf{(3.1)}$$

where $p_1(t)$ and $p_2(t)$ are time-dependent acoustic pressure responses that are recorded by a pair of microphones which are separated by a known distance Δ, $u(t) = -\frac{1}{\rho_0}\int \frac{\partial p_s}{\partial \vec{n}} dt$ is the acoustic velocity vector, where $\vec{n}$ is the normal with identical direction to sound propagation, $\rho_0 = 3.432 \times 10^{-3}\frac{p_a}{T^0}$ is the air density, p_a is the current atmospheric pressure, and T^0 is the air temperature in Kelvin.

The acoustic impulse responses which were recorded with a pair of microphones were used to calculate the instantaneous acoustic intensity as a function of the frequency and distance along the pipe. In the case of the 150mm diameter pipe, this intensity was filtered in a narrow frequency band of 150 - 750Hz using a 3rd order Butterworth filter and presented as a function of the distance $d = tc$, where t is the time and c is the sound speed in air. In the case of the 290mm diameter pipe the frequency range was 50 - 375Hz. The temperature inside the pipe was recorded and used to calculate the exact speed of sound propagation: $c = 343.2\sqrt{T^0/293}$.

Figure 3.12 presents a spectrogram for the acoustic intensity determined in the 150mm diameter with an open entry chamber. The darker areas on the graph show the frequency range at which the acoustic intensity was reflected from the open entry chamber (reflection starts at 7m) and the intensity reflected from the pipe end span (reflection starts at 14.3m).

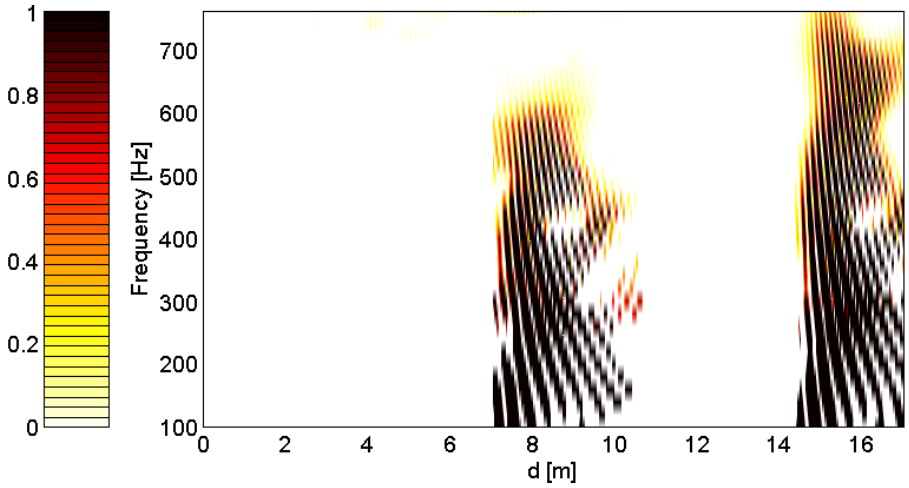

Figure 3.12 Example of frequency spectrogram as a function of pipe distance for 150mm diameter clay pipe with the open chamber entry at 7m and pipe end at 14.3m.

The total instantaneous intensity is obtained using equation (3.1). The instantaneous intensity can take negative and positive values. The sign here indicated the direction in which the sound energy propagates. In this work it was assumed that the negative sign of the intensity corresponds to the outgoing wave and positive sign relates to received reflections from the pipe.

The intensity data taken from the six microphone pairs were normalized to satisfy the following condition:

$$min\{I(t)\} = -1 \qquad \textbf{(3.2)}$$

These data were then used to estimate the reflected acoustic energy content (ET) which was calculated as:

$$ET = \frac{1}{2} \int_{t\,min}^{t\,max} \{|I(t)| + I(t)\} dt \qquad (3.3)$$

here t_{min} and t_{max} are the integration limits which define the distance interval (based on time) between the arrival of the reflected sound wave and the end of it, which is illustrated in Figure 3.13.

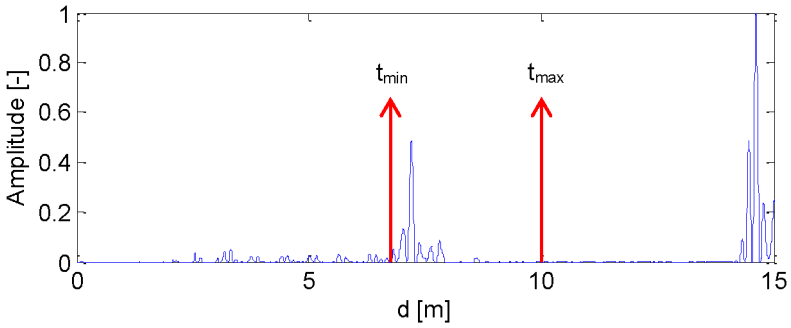

Figure 3.13 Integration limits, t_{min} and t_{max} for normalised my maximum acoustic intensity response from open chamber at 7m and end at 14.3m for 150mm diameter pipe.

Preliminary measurements have revealed that in the pipes with current blockage conditions the acoustic reflection caused by the blockage becomes negligible after 10ms which is approximately 3m. As such, for the experimental data the location of t_{min} and t_{max} were defined as 7m & 10m for the 150mm diameter pipe and as 9m & 12m for the 290mm diameter pipe. Where the start of the reflection, i.e. at 7m and 9m was governed by the blockage location inside each of the pipes.

Equation (3.3) accounts only for the reflections that occur from the local blockage which is introduced in the pipe and does not account for any other reflection which can include reflections from pipe joints and pipe end.

3.3 Experimental conditions

In each of the experiments a steady, uniform flow was achieved and maintained (for clean pipe conditions) using calibrated discharge values and pipe end gate position. In each pipe, three experimental regimes were set to deliver the discharge (Q) of 0.42 - 1.82l/s for 150mm diameter pipe and Q of 3.16 - 31.79l/s for 290mm diameter pipe.

Table 3.2 Experimental conditions for local roughness tests.

Pipe diameter	Discharge	Flow rate	Velocity	Uniform flow depth	Uniform flow occupation	Blockage height
D_c [mm]	Q [l/s]	q [m^3/s]	V [m/s]	h [mm]	a_h [%]	h_b [mm]
150	0.42	0.00042	0.38	17	11	0, 15, 30, 40, 50, 60
150	1.07	0.00107	0.58	23	15	0, 15, 30, 40, 50, 60
150	1.82	0.00182	0.65	32	21	0, 15, 30, 40, 50, 60
290	3.16	0.00316	0.80	31	11	0, 20, 30, 40, 50, 60
290	13.08	0.01308	1.21	63	22	0, 40, 50, 60, 70, 90, 110
290	31.79	0.03179	1.65	98	34	0, 60, 70, 90, 110

Table 3.2 summarizes 36 different conditions simulated during these experiments. Each of these experiments was repeated three times and the averages for the collected data were recorded. The flow depth (h) in all of three experiments for each flow regime had a variance of less than 2%. For each of the discharges a uniform flow depth and pipe's cross-sectional area occupied by uniform flow (a_h) is presented in Table 3.2. It was calculated in the clean pipe condition (without any blockage, where the flow regime was set to appear in supercritical zone for all experiments). The last column of Table 3.2 provides information on the blockages used for this particular flow regime (discharge and flow depth), where '0' blockage height indicates clean pipe condition.

In the experiments with the clean pipe (without any blockage) the uniform depth was determined when the water slope equaled the bed slope. In experiments

with blockages, the majority of the manometers readings were gathered before and after the blockage so as to provide accurate data on the streamwise water depth variation caused by the local obstruction. The local flow depth data were then used to calculate the local velocity given the measured flow rate and the geometry of each pipe.

Once the required hydraulic conditions had been achieved, the acoustic sensor, attached to the soffit of the pipe at either the upstream or downstream end, was used to measure the acoustic response of the pipe which was analysed according to equations (3.1) and (3.3). A previous study in 150mm clay pipe, using the same equipment, of Romanova (2009) and Bin Ali (2010) have shown that the direction from which the acoustic data was recorded does not play a major role in extracted acoustic results (the standard deviation of energy readings of no more than 3% was detected).

3.4 Experimental results

In these experiments the measured hydraulic data such as discharge and water level, was recorded which then was used to calculate flow depth, mean flow velocity, Reynolds number, Froude number, local head loss and pipe's cross-section occupied with the flow, and blockage-to-pipe cross-section ratio. The manometer data were used to plot the water surface variation due to the presence of a blockage of variable height. Also the flow depth and velocity data was used to calculate total and kinetic energy head loss for all pipe conditions. The experimentally measured hydraulic parameters for the 150mm and 290mm diameter pipes in the presence of the blockage are summarized in Table 3.3. In

the table h_b is the blockage height, h_1 and h_2 are water depths measured immediately upstream (location 1) of the blockage and downstream (location 2) of the blockage where the water returned to uniform flow condition for all flow regimes, respectively (Figure 3.14). In the case of the 150mm diameter pipe h_1 and h_2 were located at 7.1m and 8.5m respectively. Whereas in the case of 290mm diameter pipe h_1 and h_2 were located at 8.9m and 11.8m respectively. These depths were used to determine the Reynolds numbers (Re_1 and Re_2) and the local Froude Number (Fr_1 and Fr_2). The local head loss caused by the blockage (h_f) was estimated using equation (3.4), and the mean equivalent sand grain roughness (k_s) caused by the blockage between locations of h_1 and h_2, was estimated using equation (3.6). In the last column Table 3.3 presents the percentage of pipe's cross-sectional area occupied by blockage (a_b).

In the case of the clean pipe without any blockages, equations (2.11), (2.12) and (2.15) were used to calculate the head loss, friction factor and roughness parameters, respectively.

In the pipe with a blockage, non-uniform flow conditions were observed. In this case, the local head loss (specific energy loss) due to the blockage was calculated between points 1 and 2 as per equation (3.4), where Z is the elevation head:

$$h_f = \left(\frac{V_1^2}{2g_a} + h_1 + Z_1\right) - \left(\frac{V_2^2}{2g_a} + h_2 + Z_2\right) \quad \textbf{(3.4)}$$

The friction factor for the pipe with a blockage was determined from:

$$\bar{f} = \frac{g_a 8 R_{1,2}}{V_{1,2}^2} \frac{h_f}{L_{2-1}} \quad \textbf{(3.5)}$$

where $\bar{f}$ is the value of the average friction factor determined from the average hydraulic radius ($R_{1,2}$) and velocity ($V_{1,2}$) found between points 1 and 2.

Further, the hydraulic roughness parameter for the pipe with a blockage was also calculated as an average value between points 1 and 2:

$$k_s = 14.8\mathrm{R}_{1,2}\left(10^{\frac{-1}{2\sqrt{\bar{f}}}} - \frac{2.51}{Re_{1,2}\sqrt{\bar{f}}}\right) \quad \textbf{(3.6)}$$

where $Re_{1,2}$ is an average Reynolds number found between points 1 and 2.

Table 3.3 Measured hydraulic parameters for all experiments.

No.	D_c [mm]	Q [l/s]	h_b [mm]	h_1 [mm]	h_2 [mm]	Re_1 [-]	Re_2 [-]	Fr_1 [-]	Fr_2 [-]	h_f [m]	k_s [mm]	a_b [%]
1	150	0.42	0	17	17	14294	14294	1.13	1.13	0.056	15	-
2	150	0.42	15	32	17	10223	14294	0.32	1.13	0.065	59	10
3	150	0.42	30	44	17	8575	14294	0.17	1.13	0.076	98	20
4	150	0.42	40	51	17	7884	14294	0.13	1.13	0.083	120	27
5	150	0.42	55	66	17	6767	14294	0.08	1.13	0.098	164	37
6	150	0.42	60	73	17	6357	14294	0.07	1.13	0.105	182	40
7	150	1.07	0	23	23	29044	29044	1.48	1.48	0.056	9	-
8	150	1.07	15	35	23	23180	29044	0.65	1.48	0.056	28	10
9	150	1.07	30	52	23	18562	29044	0.30	1.48	0.069	69	20
10	150	1.07	40	60	23	17066	29044	0.23	1.48	0.078	90	27
11	150	1.07	55	74	23	15006	29044	0.15	1.48	0.091	125	37
12	150	1.07	60	80	23	14272	29044	0.13	1.48	0.098	139	40
13	150	1.82	0	32	32	43811	43811	1.39	1.39	0.056	6	-
14	150	1.82	15	34	32	42390	43811	1.23	1.39	0.055	15	10
15	150	1.82	30	64	32	29551	43811	0.36	1.39	0.068	77	20
16	150	1.82	40	73	32	27244	43811	0.28	1.39	0.077	100	27
17	150	1.82	55	87	32	24296	43811	0.20	1.39	0.090	133	37
18	150	1.82	60	94	32	23027	43811	0.17	1.39	0.096	147	40
19	290	3.16	0	31	31	54441	54441	1.74	1.74	0.056	3	-
20	290	3.16	20	62	31	37724	54441	0.44	1.74	0.060	23	7
21	290	3.16	30	75	31	33989	54441	0.31	1.74	0.072	45	10
22	290	3.16	40	81	31	32565	54441	0.26	1.74	0.077	56	14
23	290	3.16	50	94	31	29938	54441	0.20	1.74	0.089	84	17
24	290	3.16	60	102	31	28562	54441	0.17	1.74	0.097	102	21
25	290	13.08	0	63	63	162056	162056	1.86	1.86	0.056	2	-
26	290	13.08	40	123	63	110789	162056	0.51	1.86	0.052	19	14
27	290	13.08	50	147	63	99175	162056	0.36	1.86	0.072	48	17
28	290	13.08	60	157	63	95033	162056	0.32	1.86	0.081	63	21
29	290	13.08	70	167	63	91203	162056	0.28	1.86	0.090	79	24
30	290	13.08	90	188	63	83954	162056	0.23	1.86	0.109	114	31
31	290	13.08	110	210	63	77201	162056	0.18	1.86	0.130	149	38
32	290	31.79	0	98	98	311789	311789	1.94	1.94	0.056	1	-
33	290	31.79	60	205	98	193668	311789	0.47	1.94	0.050	15	21
34	290	31.79	70	222	98	181560	311789	0.40	1.94	0.063	27	24
35	290	31.79	90	250	98	162496	311789	0.31	1.94	0.088	51	31
36	290	31.79	110	276	98	143350	311789	0.22	1.94	0.112	70	38

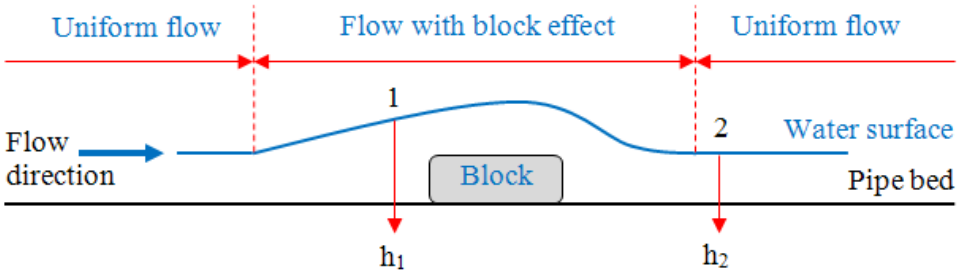

Figure 3.14 Location of h_1 and h_2 next to the block and flow distribution.

For all of the experiments the flow was in turbulent regime, with the Reynolds numbers in range from app. 6300 - 320000. The flow in pipe without the blockage was in supercritical flow regime. The Froude number at location h_1 shows that for the pipe with the blockage the flow was in the subcritical regime. This indicates a presence of hydraulic jump just before the blockage. Based on the experimental data as the Froude numbers were close to 1, the hydraulic jump is therefore very small. At the location of h_2 in all the experiments the flows downstream of the blockages were in the supercritical flow regime as it was located in uniform flow zone. The head loss was found to be in the range 0.05 - 0.13m. The roughness values for the clean pipe condition (no blockage) were in range 1 - 15mm. However, in the presence of a blockage the roughness increased to 15 - 182mm. It should be noted that the hydraulic roughness obtained in these tests represents the equivalent roughness height to create an equivalent resistance. Hence, the roughness values exceed the actual pipe diameter in some cases when the block is present in the pipe.

Table 3.4 presents measured hydraulic and acoustic parameters and their non-dimensional ratios. As per Table 3.3, first to third columns in Table 3.4 show experiment number, pipe diameter and flow discharge. Following columns show the pipe's cross-sectional area occupied by blockage (a_b), hydraulic roughness normalised by the pipe diameter factor ($\overline{D_c}$) as $[k_s] = k_s\overline{D_c}/10^2$ (where $\overline{D_c}$ takes

values of 15 and 29 for 150mm and 290mm pipes, respectively), the hydraulic roughness to flow area ratio ($[k_s]/a_{h_1}$), where the flow area at point 1 was used, and the head loss to pipe diameter ratio (h_f/D_c).

Table 3.4 Measured hydraulic and acoustic parameters for all experiments.

No.	D_c [mm]	Q [l/s]	a_b [%]	$[k_s]$ [mm]	$[k_s]/a_{h_1}$ [mm]	h_f/D_c [-]	ET [-]	ET_n [-]
1	150	0.42	-	2.18	0.3492	0.373	0.205	0
2	150	0.42	10	8.89	0.5694	0.433	0.593	11.6
3	150	0.42	20	14.76	0.6030	0.507	0.962	18.1
4	150	0.42	27	18.04	0.6015	0.553	1.300	23.5
5	150	0.42	37	24.54	0.5787	0.653	2.633	42.8
6	150	0.42	40	27.26	0.5640	0.700	3.371	51.4
7	150	1.07	-	1.31	0.1349	0.373	0.247	0
8	150	1.07	10	4.21	0.2371	0.374	0.789	11.3
9	150	1.07	20	10.38	0.3371	0.460	1.461	19.6
10	150	1.07	27	13.50	0.3612	0.520	1.991	25.5
11	150	1.07	37	18.73	0.3809	0.607	3.409	39.6
12	150	1.07	40	20.81	0.3834	0.653	4.518	50.3
13	150	1.82	-	1.12	0.0717	0.373	0.300	0
14	150	1.82	10	2.31	0.1359	0.367	1.284	14.9
15	150	1.82	20	11.60	0.2850	0.453	2.301	20.8
16	150	1.82	27	14.96	0.3096	0.513	2.840	24.2
17	150	1.82	37	19.88	0.3304	0.600	5.465	43.4
18	150	1.82	40	22.09	0.3347	0.640	6.436	48.7
19	290	3.16	-	0.43	0.0749	0.193	1.126	0
20	290	3.16	7	6.74	0.4299	0.207	2.950	10.1
21	290	3.16	10	12.92	0.6298	0.248	3.491	11.5
22	290	3.16	14	16.29	0.7129	0.266	4.068	13.5
23	290	3.16	17	24.33	0.8661	0.307	4.886	15.5
24	290	3.16	21	29.61	0.9423	0.334	6.348	20.2
25	290	13.08	-	0.39	0.0243	0.193	1.561	0
26	290	13.08	14	5.58	0.1381	0.179	7.578	12.0
27	290	13.08	17	13.93	0.2736	0.248	10.807	16.4
28	290	13.08	21	18.29	0.3308	0.279	12.047	17.7
29	290	13.08	24	22.95	0.3847	0.310	15.011	21.7
30	290	13.08	31	33.07	0.4818	0.376	28.041	32.1
31	290	13.08	38	43.19	0.5566	0.448	37.036	48.2
32	290	31.79	-	0.35	0.0119	0.193	2.005	0
33	290	31.79	21	4.29	0.0567	0.172	18.041	15.3
34	290	31.79	24	7.89	0.0960	0.217	22.087	18.1
35	290	31.79	31	14.90	0.1625	0.303	36.013	28.3
36	290	31.79	38	20.30	0.2066	0.386	44.072	37.6

The next to last column in Table 3.4 shows the normalised by the maximum acoustic energy of pipe (ET), and the last column shows the further normalised acoustic energy by the pipe geometry (ET_n), shown in equation (3.12).

3.4.1 Water depth distribution

In the absence of a blockage the flow depth distribution in the pipe was uniform, hence the flow depth and velocity at each given point along the pipe were the same. In the presence of the blockage the flow depth upstream and downstream of the blockage deviated from the uniform flow regime.

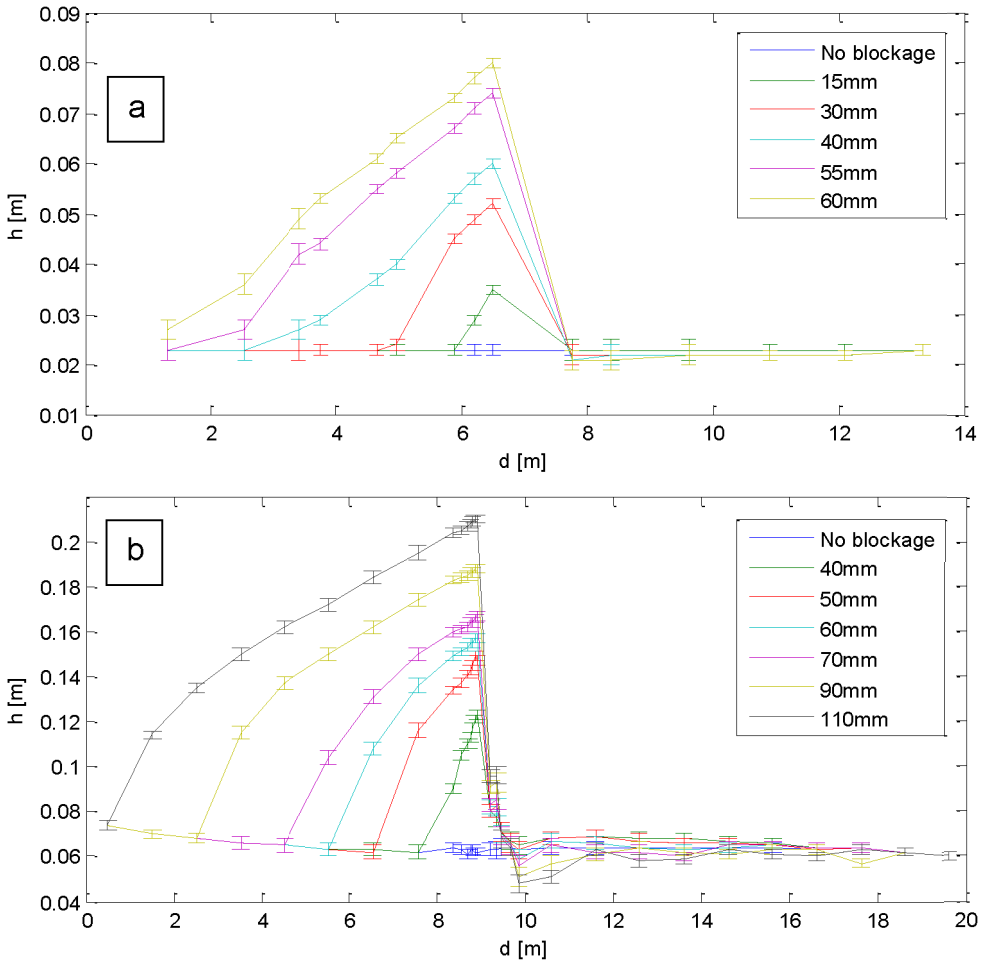

Figure 3.15 The flow depth distribution in the 150mm diameter pipe at 1.07l/s (a) and 290mm diameter pipe at 13.08l/s (b) with and without the presence of blockage.

Figure 3.15 presents the data for the flow depth in the 150mm diameter pipe (a) recorded at 1.07l/s and in the 290mm pipe (b) at 13.08l/s for the clean (without any blockage) and for the blocked conditions. The size of the blockage varied from 15 to 60mm in the case of the 150mm pipe and from 40 to 110mm in the case of the 290mm pipe. Noticeably, from Figure 3.15, prior to the obstacle the water level rises with the increasing blockage height (h_b). After the blockage, downstream, the water level falls dramatically. However, it recovers to become uniform within 1 - 3m from the end of the blockage for all the measured 36 conditions. Furthermore, remarkably for the greater blockage height the water level pass the blockage drops more than for smaller blockage height. This effect is clearly visible in Figure 3.15b. Figure 3.15 also shows error bars associated with water depth measurements, which were estimated from the standard deviation from the repeated water depth measurements. This indicated a maximum error of 4% of the measured water depth in the presence of blockage. In clean pipe condition water level estimation error was 0.5%, which at highest discharge in 290mm diameter pipe would give an error of 0.5mm, and cause a 0.2% error in velocity calculation.

3.4.2 Hydraulic energy slope and head loss

The total energy head loss was measured at three discharges in the both pipes with and without all the blockages. The effect of the blockage on the total hydraulic energy level (Z_f) was studied, which is a function of elevation head (Z) with respect to the pipe bed slope, flow depth (h), and mean flow velocity (V):

$$Z_f = Z + h + \frac{V^2}{2g_a} \quad \textbf{(3.7)}$$

The introduction of a blockage results in a lower energy loss per unit length in the upstream part of the pipe before the blockage, and the slope of the water surface becomes almost horizontal. Immediately after the blockage, the energy head is rapidly lost as a result of the non-uniform accelerating flow. Downstream of the blockage the flow settles, and the energy line tends towards the uniform flow conditions as it was observed in the case of clean pipe.

Figure 3.16 presents the total energy head data for the both pipes at one particular discharge, with error bars at each measured point.

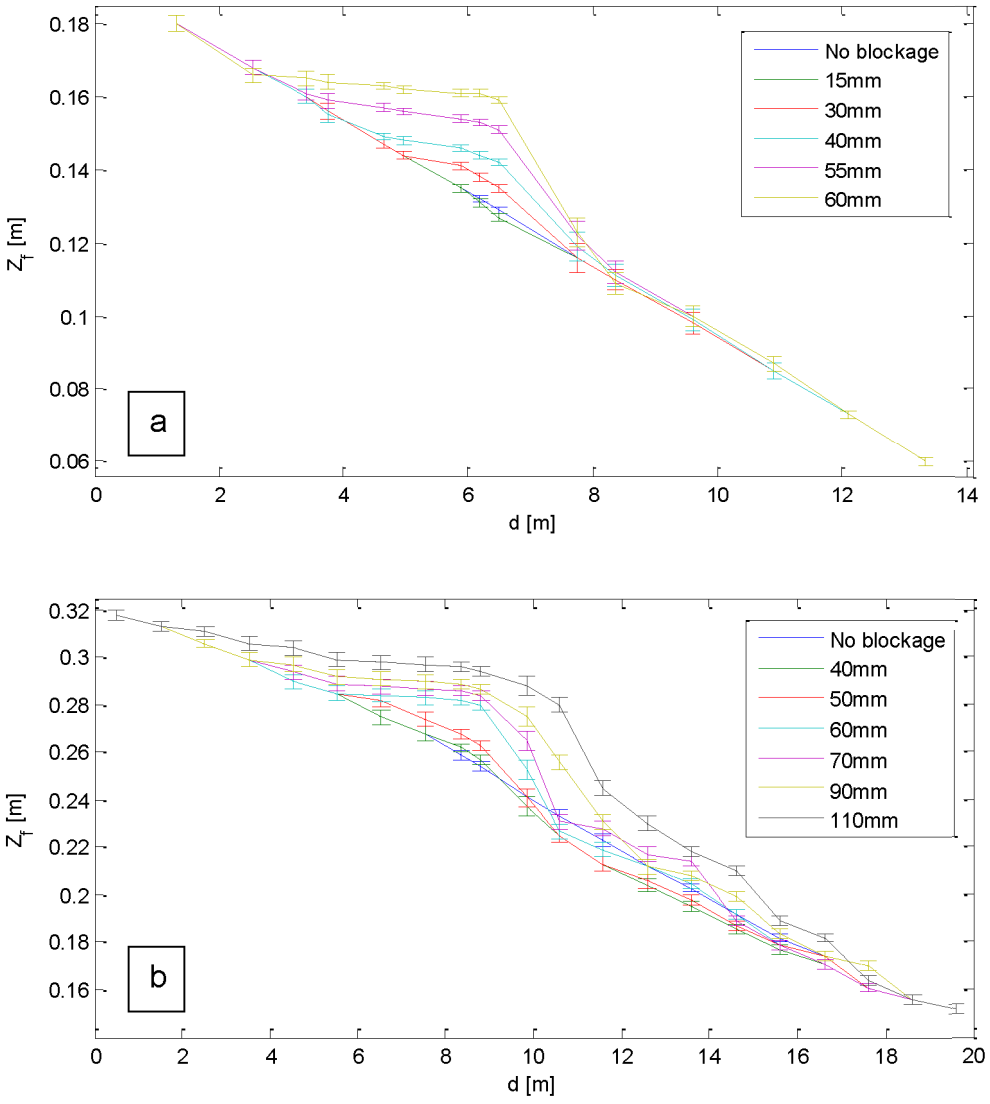

Figure 3.16 The total energy head for the 150mm diameter pipe at 1.82l/s (a) and 290mm diameter pipe at 13.08l/s (b) with and without the presence of blockage.

The total energy head is lost in two major steps as a result of the obstruction:

I. Before the small blockage, due to relatively small pipe wall roughness and low wetted perimeter the energy loss is steady and uniform (close to clean pipe condition). However with the increase in blockage size, the water backs up, increasing the wetted perimeter and slowing the flow velocity down so that the energy loss per streamwise length is comparably small.

II. For all cases, immediately after the blockage, the total energy head is lost more rapidly tending towards the loss as per clean pipe condition. The energy loss returns to stable and uniform within 3 to 9m for all experiment carried out in both pipes.

For all the blockages the hydraulic energy is rapidly lost over approximately the same distance, because the flow velocity is higher downstream of the block and the frictional loses are related to velocity square. The rate at which the energy is lost for all of the conditions stabilizes within the first 5m after the blockage, which is approximately equal to 33 pipe diameters. Generally, for all blockage conditions an equivalent amount of energy is lost over the whole length of the pipe. The only difference between these hydraulic regimes is the local estimation per unit length of the conduit. For increasing discharge the values of energy line are shifted upwards.

The kinetic energy head is a function of the mean flow velocity:

$$Z_{kin} = \frac{V^2}{2g_a} \quad \textbf{(3.8)}$$

The results for the kinetic energy measured in the two pipes for different blockage sizes are presented in Figure 3.17 together with error bars. Here, the impact of the obstruction on the velocity variation is well illustrated, i.e. the velocity is low before the blockage as the water builds up, and the velocity rapidly accelerates after the blockage. Hence, with an increasing model height, the kinetic energy is experiencing a more rapid loss before and an increase after the model.

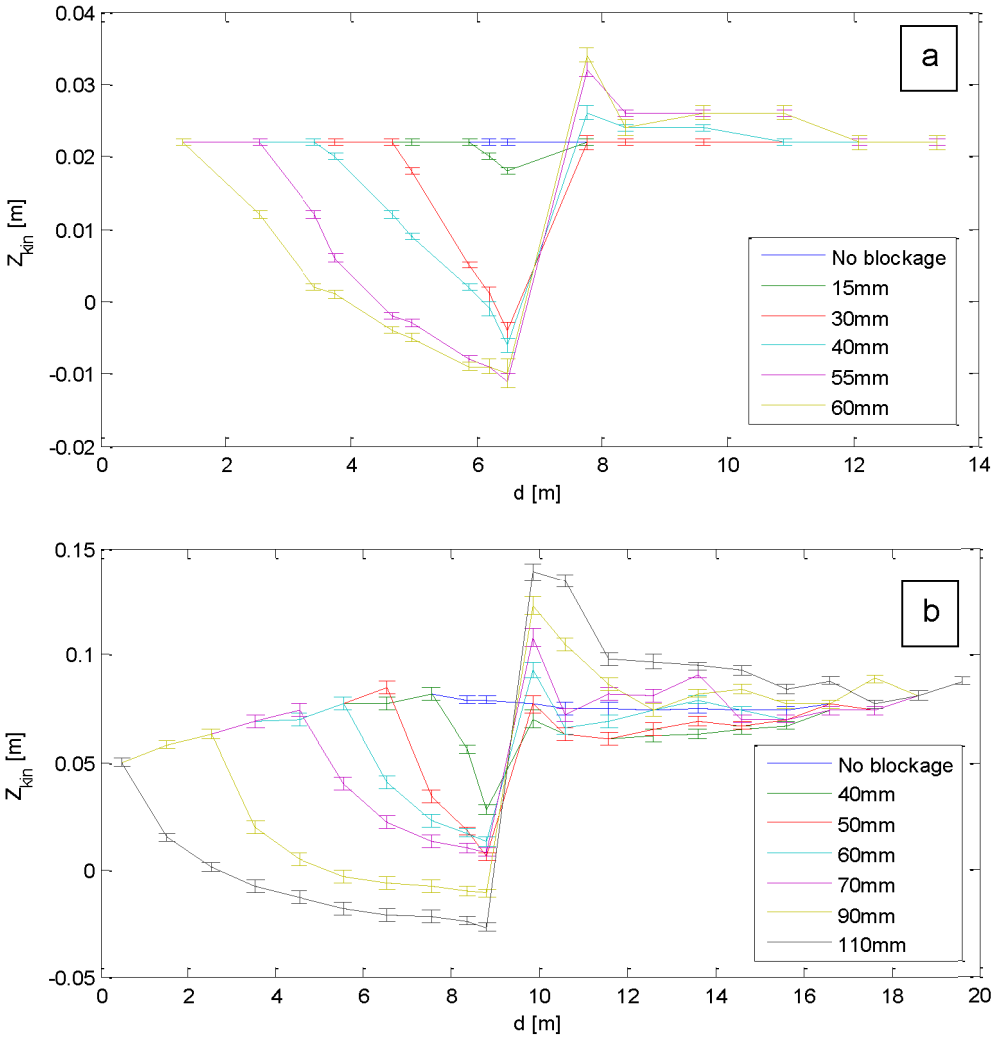

Figure 3.17 The kinetic energy head for the 150mm diameter pipe at 1.82l/s (a) and 290mm diameter pipe at 13.08l/s (b) with and without the presence of a blockage.

The behaviour of the kinetic energy is controlled by the mean flow velocity. Hence, from the above the following conclusions can be made:

I. For higher discharges, the effect of a small local roughness (a_b ≤ 10%) on the flow depth and, hence, on the mean flow velocity is relatively small. This fact indicates that the energy loss for a pipe with a relatively small local blockage (i.e. small blockage height to water depth ratio) is similar to that expected in the clean pipe with the equivalent wall roughness and uniform flow conditions.

II. For higher discharges and higher blockages, after the blockage the flow depth drops more significantly and thus the flow velocity increases. The velocity returns to that expected in the case of the uniform flow conditions within a short distance downstream of the blockage.

The obtained values for the head loss for each of the experimental discharges and blockage condition are shown in Table 3.3. The results suggest that the head loss is relatively constant in the pipe with no blockage for the all discharges considered here. For all tests, the head loss increases with increasing blockage height. To compare the head loss values between the pipe sizes, the values should be normalised by the pipe geometry (i.e. diameter) for conditions with the presence of block (Table 3.4), which is presented in Figure 3.18. The figure shows that the head loss is higher for smaller discharges, observed in smaller 150mm diameter clay pipe which walls were also rougher than for 290mm diameter perspex pipe. Also, the head loss for all tests increases with the increasing blockage occupation of pipe's cross-sectional area. From Figure 3.18 data it can be concluded that the head loss to pipe diameter ratio has a positive liner relationship with the increasing blockage size to pipe's cross-sectional area.

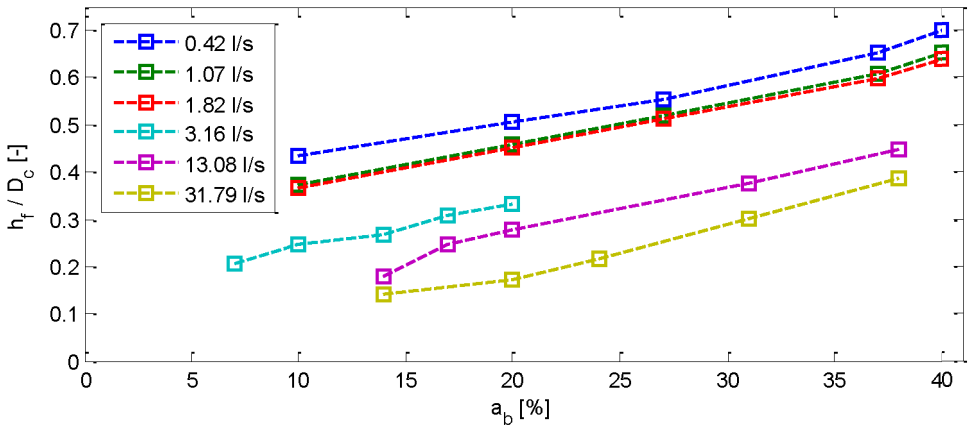

Figure 3.18 **The head loss to pipe diameter ratio as a function of pipe's cross-sectional area occupied by blockage.**

Figure 3.19 presents a non-dimensional relation between the head loss, for all the tests with the blockage, to pipe diameter ratio (h_f/D_c) and the normalised hydraulic parameter ($[H]^*$), where:

$$[H]^* = \frac{s_V}{V_1}\,\overline{a_b} \tag{3.9}$$

is dependent on ratio of shear velocity $s_V = \sqrt{S_0 g_a R}$ for point h_1 to velocity at that point V_1, and pipe area occupied by blockage used as $\overline{a_b} = a_b/100$.

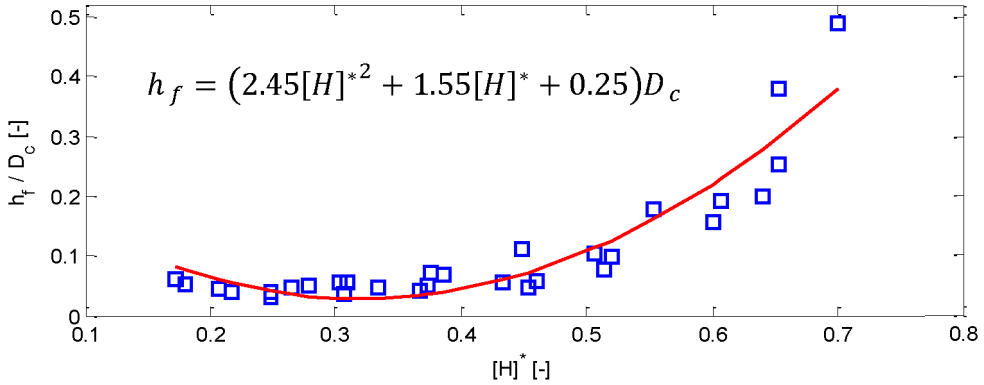

Figure 3.19 **The head loss to pipe diameter ratio as a function of the non-dimensional hydraulic parameter $[H]^*$ with a polynomial fit of R^2 = 0.86.**

The plot line on Figure 3.19 is the polynomial line of best fit, with accuracy of R^2 = 0.86, from which the head loss can be expressed as:

$$h_f = \left(2.45[H]^{*2} + 1.55[H]^{*} + 0.25\right)D_c \qquad \textbf{(3.10)}$$

This equation relates the non-dimensional parameter $[H]^{*}$ with the head loss in a pipe with diameter D_c. It is universal for a range of small pipes and block sizes and hydraulic flow conditions.

3.4.3 Hydraulic roughness estimation

The hydraulic roughness obtained from Colebrook-White equation for clean pipe and pipe with roughness is presented in Table 3.3. The roughness parameter to flow area ratio (Table 3.4) was used to compare the roughness values due to different blockage sizes in two pipes. It can be observed from the graph (Figure 3.20) that for all the discharges, above 0.42l/s, the Colebrook-White roughness as a ratio of pipe flow area increases with the increasing pipe's cross-sectional occupation by blockage.

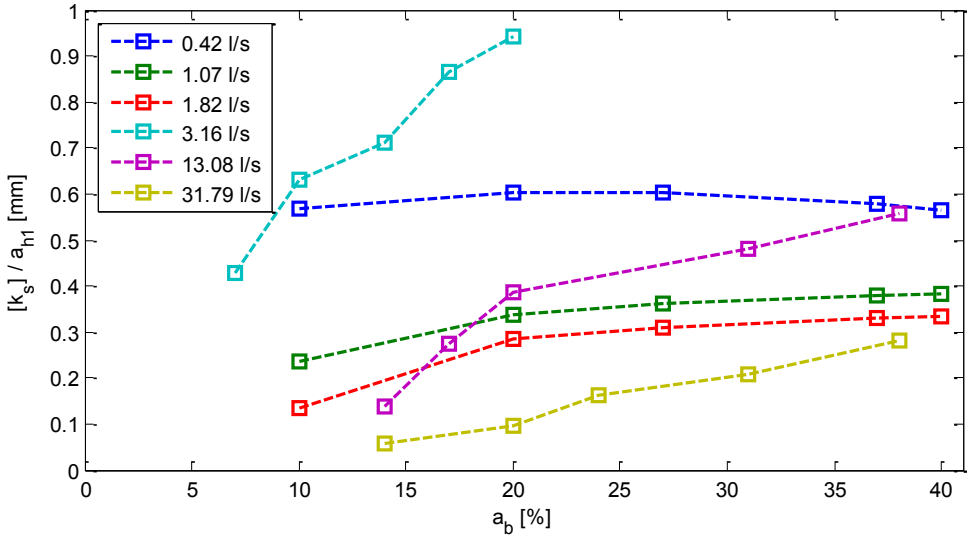

Figure 3.20 The hydraulic roughness to flow occupation area ratio as a function of blockage occupation of pipe area.

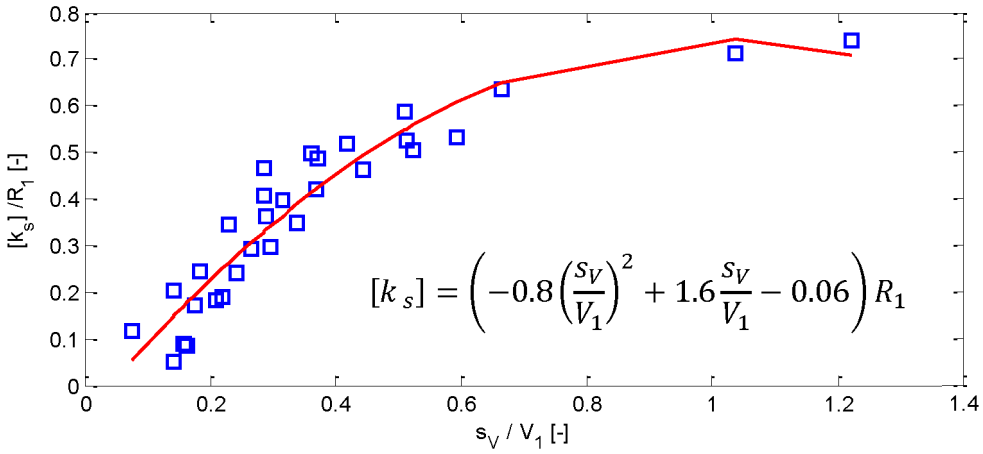

Figure 3.21 Hydraulic roughness to hydraulic radius ratio as a function of shear velocity to velocity ratio for all experiments with polynomial fit of R^2 = 0.90.

Figure 3.21 demonstrates a non-dimensional relation between the roughness to hydraulic radius ratio as a function of the shear velocity to the mean flow velocity ratio, for tests with blockage. The polynomial fit has an accuracy of R^2 = 0.90, where the hydraulic roughness can be expressed as:

$$[k_s] = \left(-0.8\left(\frac{s_V}{V_1}\right)^2 + 1.6\frac{s_V}{V_1} - 0.06\right)R_1 \qquad \textbf{(3.11)}$$

The above relation is independent of the blockage geometry, and it is universal for a pipe of any diameter and flow conditions.

3.4.4 Acoustic intensity spectrogram

The acoustic response was recorded in the clean pipes and in the pipes with a blockage for all the experimental conditions considered in this work. Figure 3.22 shows example spectrograms for the acoustic intensity recorded in the presence of a 15mm (a) and 55mm (b) blockage in the 150mm diameter clay pipe under the flow discharge of 1.07l/s.

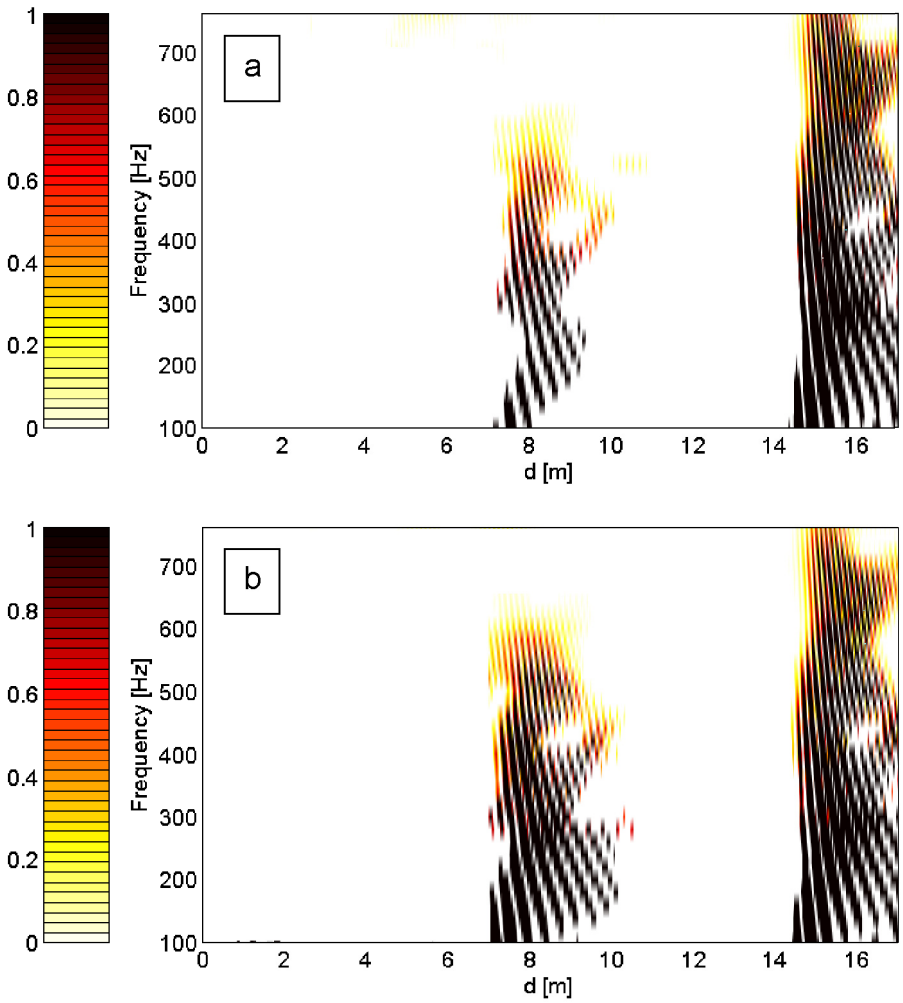

Figure 3.22 The acoustic intensity spectrograms recorded in the 150mm diameter pipe with a_b = 10% (a) and a_b = 37% (b) under the discharge of 1.07l/s.

Both blockages are identified at 7.05m, which correspond to the reflection from the blockage edge which was closest to the acoustic sensor. The strength of the reflection from the 15mm blockage is relatively small in comparison from that observed in the case of the 55mm blockage. The signals which are visible in the spectrograms at 14m correspond to the reflection from the open end of pipe. These signals were excluded from the analysis. These results illustrate that the reflection strength has a dependence on the blockage occupation ratio. Since the relative head loss also depends on the blockage occupation ratio (see Figure 3.18) as well as the flow rate (see Figure 3.19), there is an opportunity to relate the acoustic characteristics of the blockage in specific flow regime to

parameter of pipe area occupied by blockage. Figure 3.23 in comparison to Figure 3.22 shows the acoustic energy from 290mm pipe.

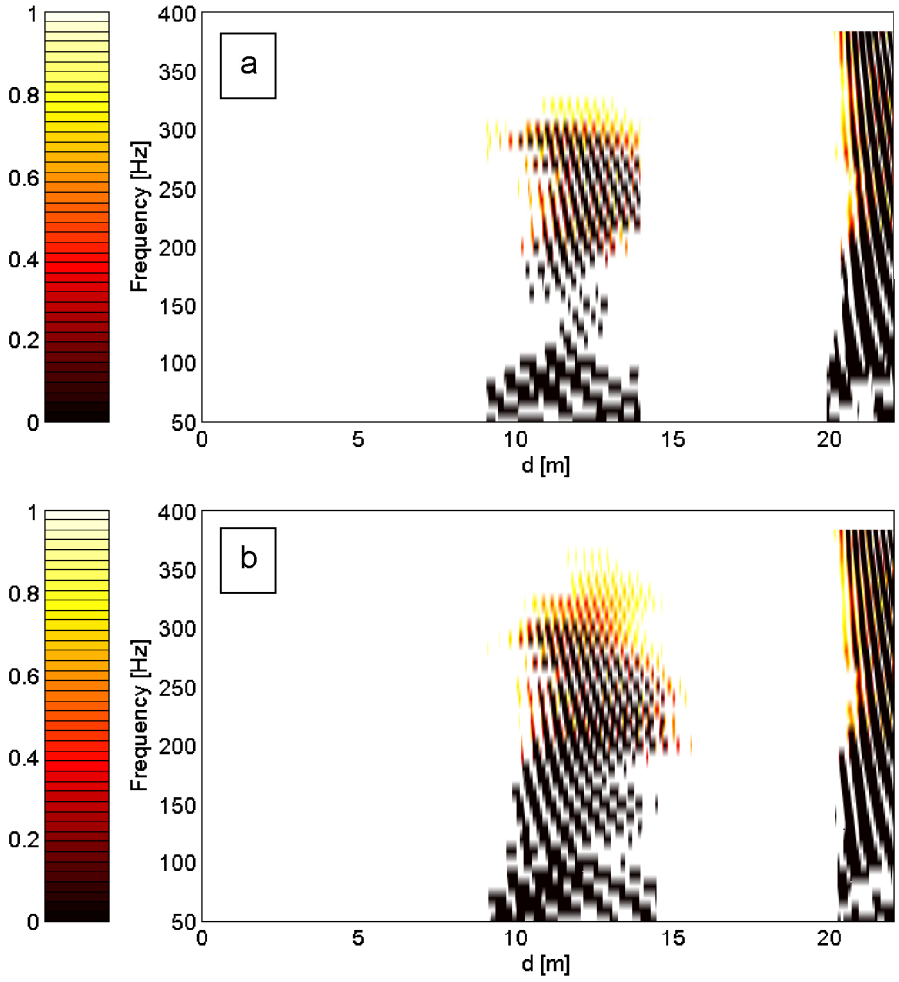

Figure 3.23 The acoustic intensity spectrograms recorded in the 290mm diameter pipe with a_b = 14% (a) and a_b = 37% (b) under the discharge of 13.08l/s.

By the method described in section 3.2.2, equation (3.3), the energy content (ET) was calculated as an average of the acoustic intensity from all the 6 microphone pairs in the 7 - 10m range for the 150mm diameter pipe and 9 - 12m range for the 290mm diameter pipe. The obtained acoustic energy results for all the discharges studied in this work are presented in Table 3.4. In order to compare the acoustic energy content between the two pipes, the values were normalised as demonstrated in equation (3.12):

$$ET_n = \left(\frac{ET - ET_0}{ET_0}\right) / \left(\frac{h_{1,2}}{D_c}\right) \quad \textbf{(3.12)}$$

where ET_0 is an energy content of clean pipe (no blockage) for a given discharge, $h_{1,2}$ is the mean flow depth between points h_1 and h_2, and D_c is the pipe diameter.

The following representation of the normalised acoustic energy content (ET_n) is very attractive as it is universal for any pipe dimension and flow condition. The following acoustic energy can be used to determine directly the percentage of area of pipe cross-section occupied by the blockage as shown in Figure 3.24. The red line on the graph shows a non-dimensional positive exponential relation that can be expressed as:

$$ET_n = 7.34e^{0.05a_b} \quad \textbf{(3.13)}$$

Equation (3.13) fits the experimental data well with R^2 = 0.97.

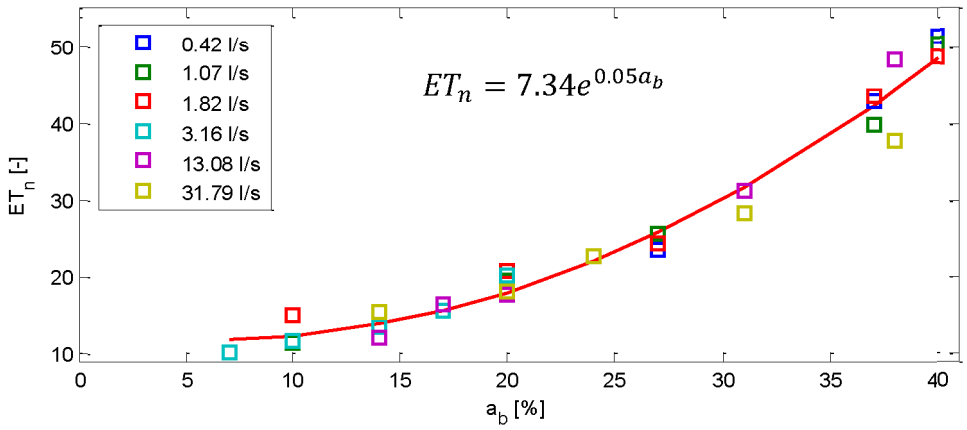

Figure 3.24 Acoustic energy content normalised by energy content of clean pipe and pipe geometry as a function of the pipe area occupied by blockage for all the hydraulic experiments, with a fit of R^2 = 0.97.

3.5 Acoustic estimation of hydraulic parameters

It is known that the acoustic response is sensitive to any changes in the boundary changes in the pipe. The introduction of a blockage in the pipe with a uniform flow results in a change in the boundary condition from which a proportion of the incident acoustic wave would inevitably reflect. The introduced blockage also influences the structure of the flow particularly in the vicinity of the blockage, which affects the hydraulic parameters such as the head loss and pipe roughness. Hence, it is attractive to establish links between the two major hydraulic parameters and the acoustic energy content in the signal reflected from this type of change.

Figure 3.25 presents the normalized acoustic energy content (see equation 3.12) as a function of the hydraulic head loss to pipe diameter ratio for a range of flow regimes simulated in two pipes. The acoustic energy content increases progressively with the increased ratio of h_f/D_c, also for a given ratio of h_f/D_c the acoustic energy content increases with the increased mean flow velocity. Therefore, it is desirable to combine the data obtained for the range of hydraulic regimes in the two pipes to derive a relation between the normalized acoustic energy content and some dimensionless hydraulic parameter.

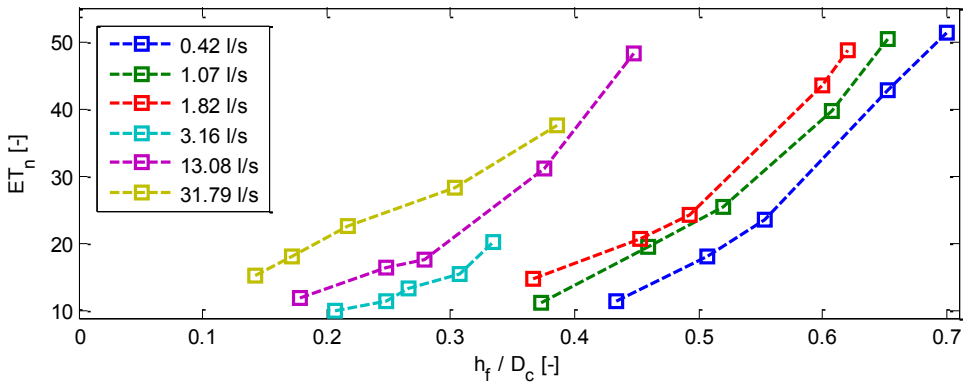

Figure 3.25 Normalised acoustic energy content as a function of hydraulic head loss to pipe diameter ratio for all experiments.

The hydraulic head loss was expressed in the following non-dimensional form:

$$[h_f]^* = \frac{s_V}{V_1}\frac{h_f}{D_c}\overline{a_b} \qquad \textbf{(3.14)}$$

where the area of pipe occupied by blockage is used in the non-percentage form as $\overline{a_b} = a_b/100$. The acoustic energy content was also normalised by further the use of hydraulic parameters (so that the energy content would be comparable between not only the pipes of different diameters, but also between pipes with different hydraulic conditions):

$$[E]^* = ET_n \frac{A_{h_1}}{A_b} \qquad \textbf{(3.15)}$$

where A_{h_1} is the area of flow in pipe's cross-section at location 1 in meters, and A_b is the area of block in meters.

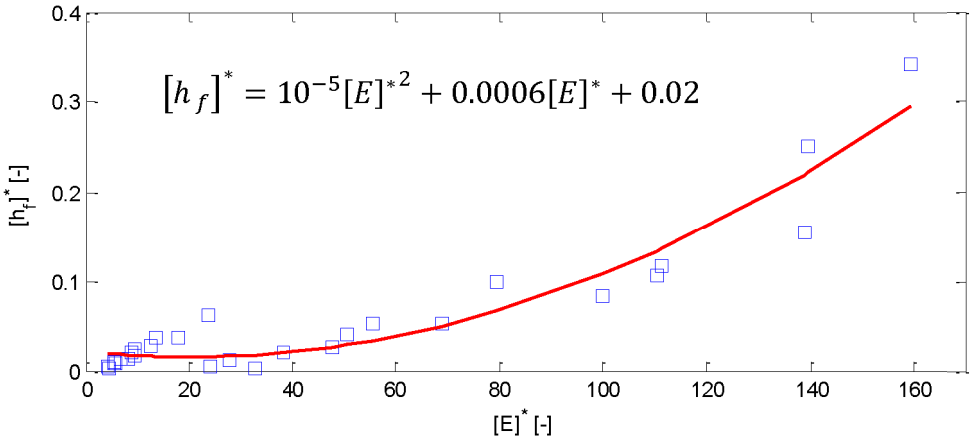

Figure 3.26 Non-dimensional relation between hydraulic head loss and acoustic energy for all experiments, with R^2 = 0.91.

The data shown in Figure 3.25 were then re-plotted as a function of these two dimensionless quantities (equations 3.14 and 3.15) and the result is shown in Figure 3.26. The plot line of the polynomial fit in Figure 3.26 shows a co-efficient of determination (R^2 = 0.91), where the head loss can be expressed as:

$$[h_f]^* = 10^{-5}[E]^{*2} + 0.0006[E]^* + 0.02 \qquad \textbf{(3.16)}$$

The above relation apart from the acoustic energy requires the knowledge of pipe diameter, velocity and water depth (from which shear velocity and hydraulic radius can be calculated), and area of pipe occupied by blockage (could be found from acoustic relation proposed in equation 3.13) to be applicable for a range of pipe sizes and conditions.

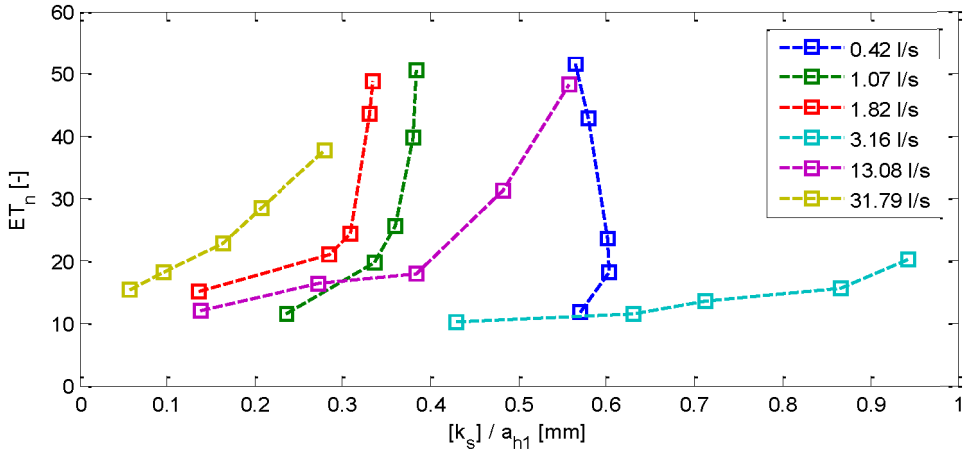

Figure 3.27 The normalised acoustic energy as a function of hydraulic roughness to area of flow ratio for all the hydraulic experiments.

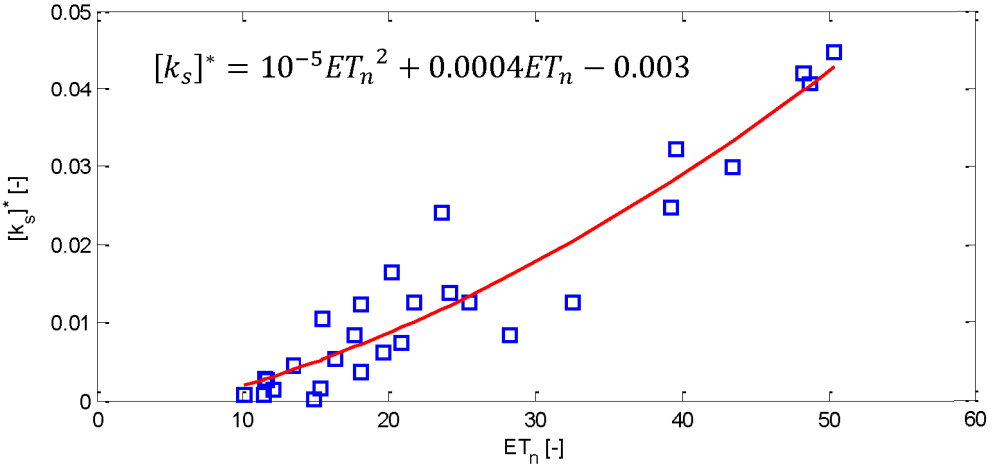

Figure 3.28 The relation between the non-dimensional hydraulic roughness and normalised acoustic energy for all experiments, with R^2 = 0.90.

Figure 3.27 presents the dependence of the normalized reflected acoustic energy on the hydraulic roughness to pipe's cross-section ratio for the 150mm pipe and 290mm pipes. The hydraulic roughness k_s was calculated from

Colebrook-White equation (equation 3.6). The behavior of the acoustic energy shown in Figure 3.27 suggests it increases with the increased $[k_s]/a_{h_1}$ ratio for regimes with flow higher than 0.42l/s. The hydraulic regimes with higher flow velocity correspond to the stronger dependence between the normalized acoustic energy and the roughness to area ratio.

Figure 3.28 presents the dependence between the non-dimensional hydraulic roughness and acoustic energy content (equation 3.15). The roughness used here was normalised as:

$$[k_s]^* = \frac{s_V}{V_1}\frac{[k_s]}{D_c}\overline{a_b} \quad \textbf{(3.17)}$$

Again, as per equation (3.14), here, the area of pipe occupied by blockage is used in the non-percentage form as $\overline{a_b} = a_b/100$. The red line of polynomial fit in Figure 3.28 shows the accuracy of R^2 = 0.90, where the hydraulic roughness can be expressed as:

$$[k_s]^* = 10^{-5}{ET_n}^2 + 0.0004ET_n - 0.003 \quad \textbf{(3.18)}$$

Relations proposed in equations (3.16) and (3.18) suggest that the hydraulic energy losses and hydraulic roughness can be determined non-invasively as function of the acoustic energy content in the signal reflected from the cross-sectional change in the pipe caused by the presence of a blockage (can be acoustically found from equation 3.13) and associated to local change in the hydraulic flow. This relation stands for all the hydraulic regimes simulated in the two pipe sizes and for all the blockage conditions considered in these experiments.

3.6 Conclusions

This chapter has described a number of controlled hydraulic and acoustic laboratory experiments in full scale sewer pipes with and without the presence of local roughness. The work demonstrates that acoustic methods can be used to measure non-invasively the hydraulic head losses and estimate the pipe roughness. More specifically, the results show that:

(i) The acoustic reflected energy can be used to predict geometrical parameters such as pipe area occupation by blockage (in range of 7 - 40%) for a range of flow discharges, in pipes with different diameters and joint conditions. An empirical equation has been proposed;

(ii) The normalised acoustic energy can be used to predict the hydraulic head loss and hydraulic roughness in a pipe due a local blockage. Non-dimensional empirical expressions have been proposed.

On top of original capabilities, the acoustic measurement method can therefore be used to estimate the size and location of a local energy loss and so with limited additional calculation this information can be used to determine the reduction in flow capacity in pipe caused by a single blockage. This information can also be imported into a sewer hydraulic network model to characterise a local energy loss so can aid the modeling of the impact of a real blockage on localised flooding. As it takes only few seconds to scan the pipe with such a method, it could be pro-actively used to monitor the developing blockages and so act in a timely fashion before such blockages causes serious damage to the pipe and flooding pipe to public health.

Chapter 4 Distributed roughness experiments

The work reported in this chapter has been carried out to verify the hypothesis that the water surface wave pattern and its statistical properties are influenced by the characteristics of the pipe wall roughness. This chapter describes the experimental methodology used and presents results of a number of controlled experiments which were carried out in the Hydraulic Laboratory of University of Bradford. The experiments were conducted in a pipe with different types of distributed wall roughness, and at a range of hydraulic conditions. The distributed roughness was simulated by the use of a square mesh with uniformly sized spheres arranged in different patterns and densities. Specially modified wave probes were used to capture accurately the dynamic behavior of the water surface. Acoustic measurements were also carried out to test the feasibility of measuring the water surface behavior using a non-contact measurement method.

This chapter provides information on experimental facilities, measurement equipment, data analysis methodology and presents results from preliminary experiments whose results governed the selection of the final experimental conditions. It is shown that there was a link between the statistics of the dynamic water surface, the wall roughness and the acoustic data. The final results propose a novel method of measuring acoustically surface water waves in the pipe. This method can be used in a number of practical applications whereby a non-invasive measurement technique is required. The results of these measurements can then be used to infer the hydraulic and wall roughness of the studied pipe.

4.1 Laboratory facilities

The experiments were carried out in a 290mm diameter transparent perspex pipe which was 20m long and set at a gradient of 1:2000 for all of the experiments (see section 3.1.2 for pipe detailed description). The pipe consisted of ten 2m long sections which were equipped with several wave probes (see section 4.2). These probes were used to record accurately the water level variations at several streamwise and lateral locations. Two phases of testing were carried out: a preliminary test phase, and final test phase the results of which were used in the final analysis. The wave probe number and arrangement varied between the preliminary and final test phases. The purpose and results of each testing phase are described in detail in sections 4.4 and 4.5 - 4.8. The pipe wall condition was altered by the use of mesh and patterns of uniformly sized spheres to simulated different pipe wall roughness (see section 4.1.1) in both testing phases.

4.1.1 Distributed roughness simulation

The distributed (continuous) roughness was simulated by the use of a square plastic mesh (Figure 4.1). The mesh was 250mm wide and 20m long. The mesh grid was 2mm thick and 4mm wide. The inside grid square length was 12mm. The mesh was forced to fit the inside curvature of the pipe bed by the use of tablet type magnets which had dimensions of 25mm in diameter and 4mm thick (Figures 4.1 and 4.2). Pairs of magnets, laterally spaced at 152mm from center to center, were glued to the mesh at a streamwise interval of 956mm (see Figure 4.2a). The second pair of magnets was applied to the outside of the pipe when the mesh was deposited in the pipe as shown in Figure 4.2b. This

ensured that the mesh followed accurately the natural curvature of the pipe and did not move during the experiments. The nature of this roughness experiment implied that the flow depth in all the experiments should be greater than 37mm to ensure that the mesh was fully submerged (see Figure 4.2b). The magnets had small contribution towards the overall pipe wall roughness as they were only 4mm thick. The edges of each section were carefully aligned and sealed with rubber gaskets from the outside. The contribution to hydraulic roughness from this type of pipe joint was considered negligible as the joints were machined and fitted to have a minimal gap.

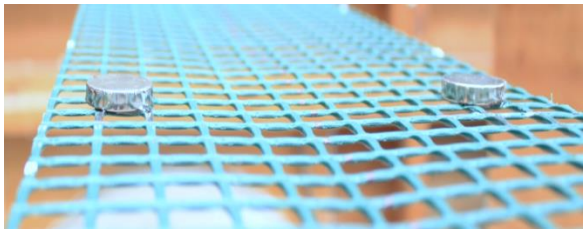

Figure 4.1 Plastic mesh with magnets.

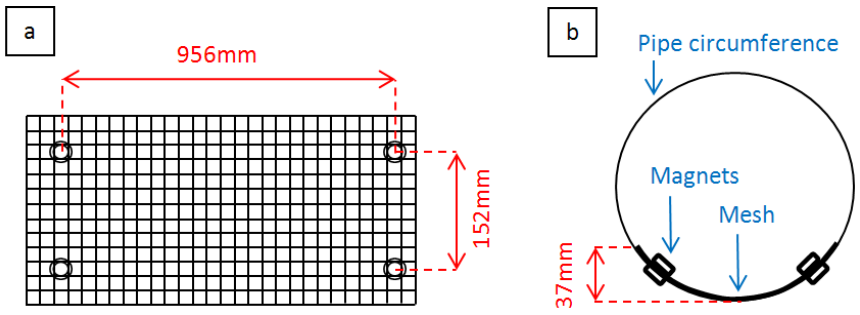

Figure 4.2 Pipe positioning diagram of plastic mesh with magnets.

To simulate some additional pipe bed roughness solid plastic spheres of 25.1mm in diameter (D) were attached to the mesh as shown in Figure 4.3. The spheres were firmly glued to the mesh in a hexagonal pattern. Figure 4.4 shows the general arrangement of spheres on the mesh in the pipe. The separation distance between the spheres (from center to center) was set in terms of the sphere diameter D as illustrated graphically in Figure 4.4a, where 'n' denotes

the separation in terms of number of sphere diameters. In the lateral direction the spheres had a 114mm separation from the center line of the mesh and a 228mm separation from sphere center to center for all conditions. Figure 4.4b shows that with the presence of these spheres the effective height of the rough section of the pipe increases to 55mm. As a result, the flow regimes simulated in these experiments were designed to have a flow depth that was able to fully submerge rough section of the pipe wall.

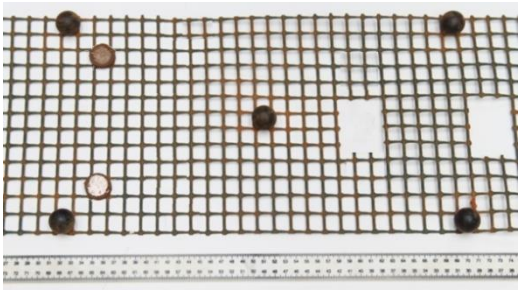

Figure 4.3 **Plastic mesh and sphere arrangement.**

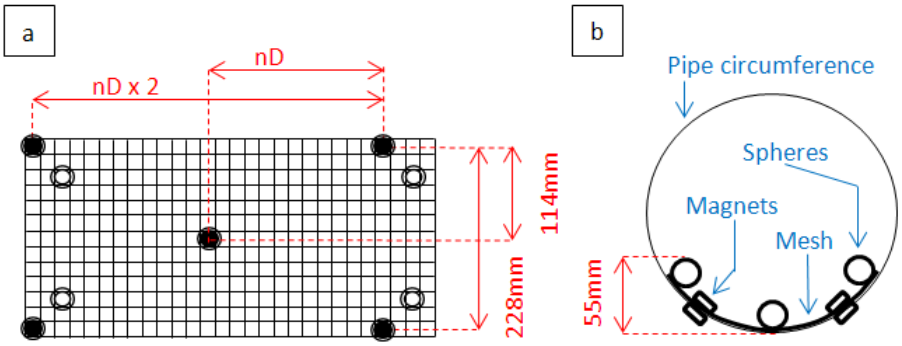

Figure 4.4 **Pipe positioning diagram of plastic mesh with spheres.**

In the streamwise direction the spheres were separated by the distance of 4D to 16D. Table 4.1 summarises the distributed roughness patterns, roughness element streamwise separation (L_s) and the roughness concentration (λ_r), which is presented using Schlichting's definition: $\lambda_r = n_\lambda a_\lambda / A_\lambda$, where n_λ is the number of elements present on the area of the bed, a_λ is the upstream projected area from the particles and A_λ is the total area of the bed (section 2.1.5). Figure 4.5 shows the range of roughness conditions studied in this work.

Table 4.1 **A summary of the distributed roughness patterns simulated in the pipe.**

Pattern No. -	Roughness type -	Roughness pattern -	Roughness element streamwise separation L_s [mm]	Roughness concentration λ_r [-]
1	Clean pipe	C	-	0.0001
2	Mesh	M	16	0.008
3	Spheres	4D	100	0.044
4	Spheres	6D	150	0.033
5	Spheres	8D	200	0.027
6	Spheres	10D	250	0.023
7	Spheres	12D	300	0.020
8	Spheres	16D	400	0.012

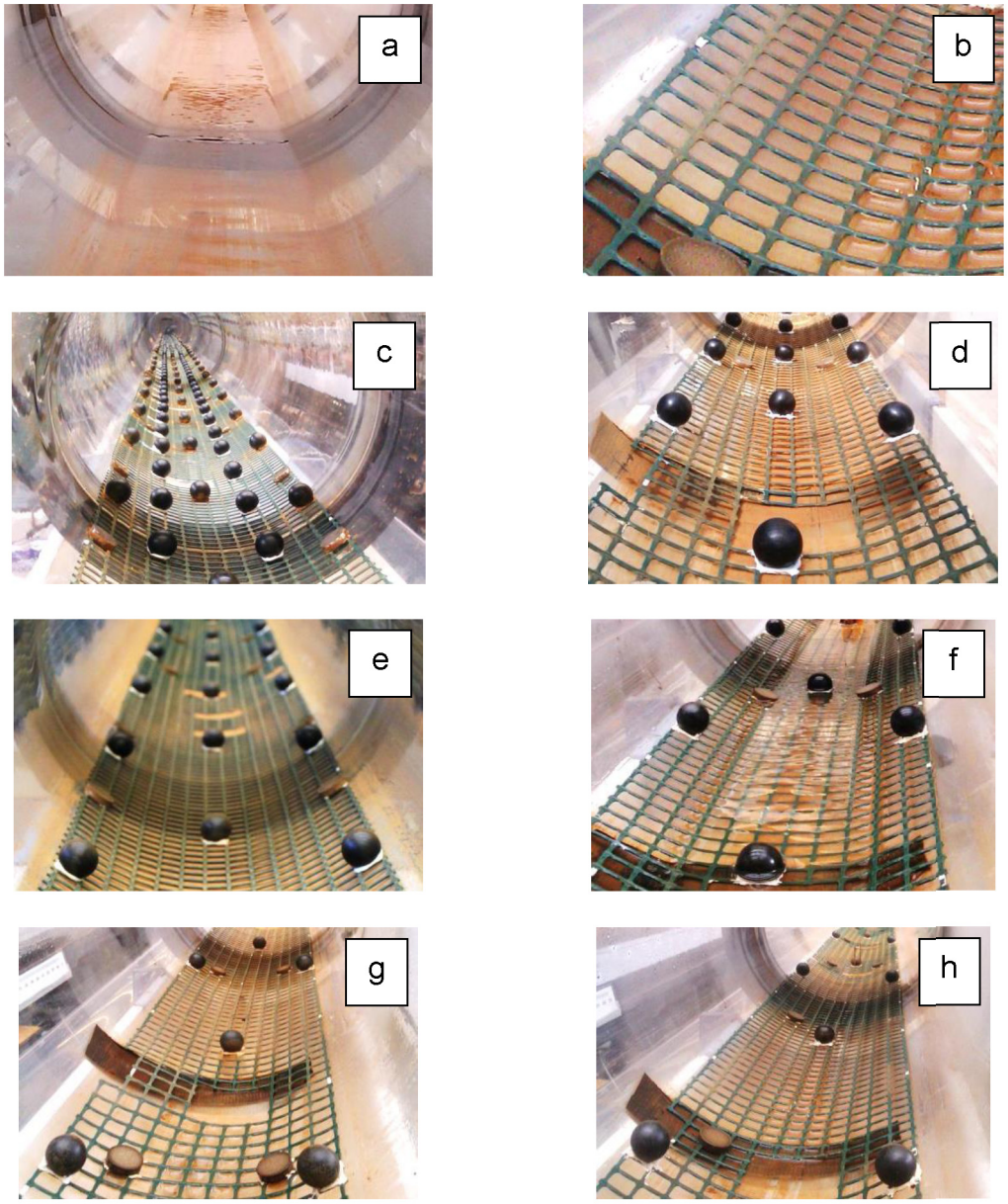

Figure 4.5 **Simulated continuous roughness in the perspex pipe: clean pipe (a), pipe with mesh (b), 4D spheres (c), 6D spheres (d), 8D spheres (e), 10D spheres (f), 12D spheres (g), 16D spheres (h).**

4.2 Water surface measurement - wave probes

A wave probe is composed of two thin wires which are stretched perpendicular to the water surface and partly submerged in the water. An electric current is generated using wave monitor module (for specifications see Appendix A) and the resultant voltage between these wires relates directly to the water level between the two wires. Original wave probes (e.g. those which are provided by Churchill Ltd) are stainless steel bars of approximately 2mm in diameter. These probes are appropriate for still water conditions or for conditions when the flow velocity is relatively low. However, applications whereby the flow velocity is relatively high (e.g. simulated dry weather flow in a 300mm sewer pipe) thinner wires are required to reduce the size of the vortices and increase the frequency at which these vortices are shed. This is necessary to ensure that the shed vortices do not impact significantly on the measurement of the water level fluctuations which are relatively low frequency. In these particular experiments, a thinner 0.25mm in diameter tinned copper wire was adopted.

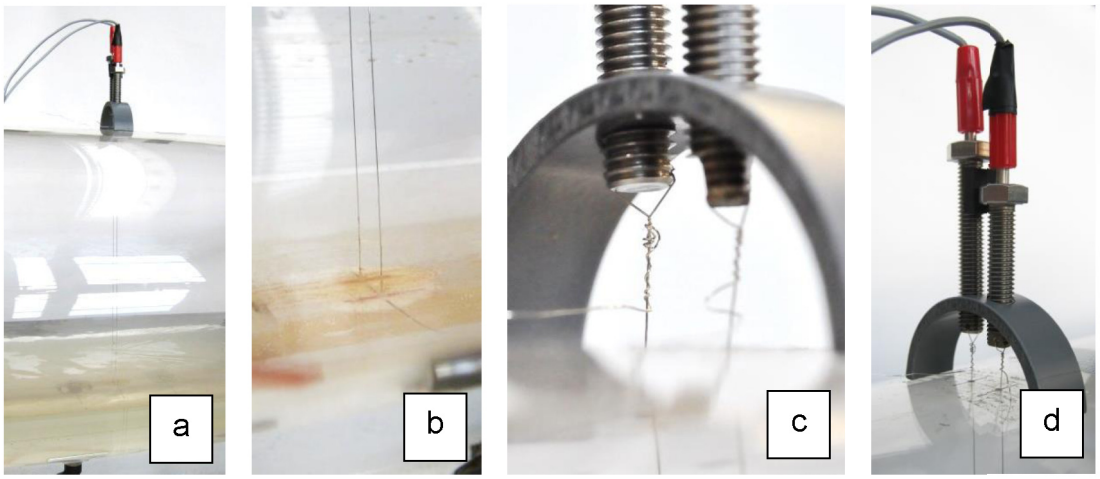

Figure 4.6 Single wave probe arrangement inside the pipe.

The wave probe (see Figure 4.6a) wires were inserted in the pipe through two 2mm diameter holes which were drilled at the top and bottom of the perspex

pipe. The distance between the centers of the two adjacent holes was 12.5mm. In order to work accurately, the wires have to be in tension under a small elastic deformation, so that they do not bend significantly or oscillate in the flow. In the reported experiments the probe wires were glued to the bottom of the pipe as shown in Figure 4.6b to stop them from moving and to prevent water from dripping from the pipe. At the top of the pipe, the wires were fed through the holes which were sealed. Outside the pipe these wires were attached to the 6mm diameter stainless steel screws which were mounted in a plastic arch (see Figure 4.6c). By carefully turning the screw the wire was put in the required state of tension so that the whole setup was stable enough not to move during the experiment. The wave probe wires were connected to the wave monitor module. The electrical signals generated by the wave probe monitor were digitized and stored using a National Instrument system.

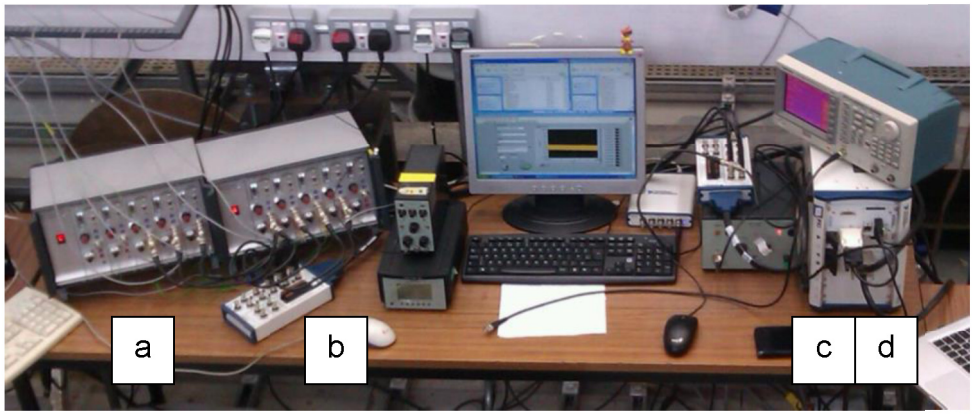

Figure 4.7 Wave monitor module (a), BNC adapter (b), DAC (c) and PC (d) set up.

The wave monitor module produced by Churchill Controls (2001) was used to measure the flow depth fluctuations (see Figure 4.7a and Appendix A3). One wave probe wire probe was energised with a 5kHz frequency square wave. This enabled a current to flow between the wires to be sensed by the wave probe circuit board and transformed into voltage output that was proportional to the

immersion depth (i.e. instantaneous water level). The wave monitor data (see Figure 4.7a) were sent to the BNC adapter (see Figure 4.7b and Appendix A4) which was connected to a National Instrument PIXe-1082 PC unit (see Figure 4.7c and 4.7d, and Appendix A4 and A5).

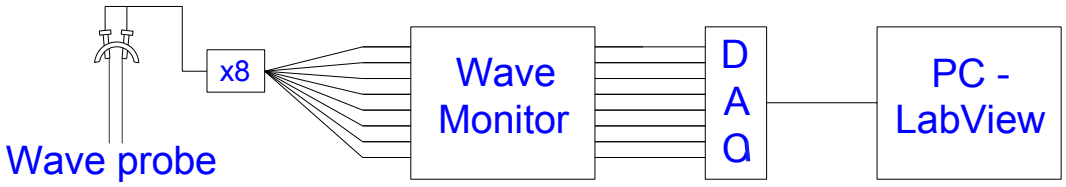

Figure 4.8 Laboratory wave probe equipment schematics.

This DAQ device can record simultaneously 8 analog channels at 10 MS/s with 16-bit resolution (National Instruments 2011). Figure 4.8 demonstrates the connection of the above devices (for specifications see Appendix A3 - A5).

4.2.1 Data collection

The process of wave probe data collection was controlled from the PC, by the use of a specially created LabView program. The data was recorded in real time, so that to capture accurately the temporal behavior of the water surface, which was presented in terms of voltage as a function of time. The wave probe readings were obtained for a period of 500s which was split into 20s long files recorded sequentially. In all experiments a maximum of 500s of data was collected, which gave a water surface reading time series of more than 8 minutes. The LabView program was used to record the wave probe data at a sampling rate of 22.1kHz. It should be noted that acoustic and hydraulic data were recorded simultaneously.

4.2.2 Calibration

All wave probes were calibrated simultaneously and an individual calibration coefficient was applied to each of these wave probes. The procedure of calibration was as follows. The pipe end gate was set at a fixed position. The pipe was then filled with water up to the end gate level. When the water settled down, so that it was still and the water surface horizontal, the voltage readings of the water probes were recorded at 45Hz for 200s. From the gate height position, pipe slope and streamwise location of the wave probe along the pipe the exact flow depth at a point of the wave probe is calculated.

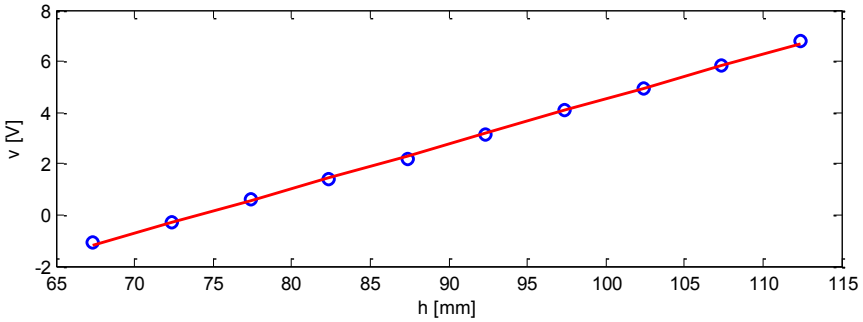

Figure 4.9 Wave probe voltage to flow depth calibration.

The flow depth was then related to the time averaged voltage recorded by the wave probe at each position. The following procedure was repeated for at least five gate positions so that a linear relationship between the voltage and flow depth could be obtained for each individual wave probe (see Figure 4.9).

For each of the wave probes a calibration relationship was obtained and used to convert the measured voltage to the actual flow depth (for Matlab code see Appendix B). On average, the standard deviation (STD) of the wave probe voltage reading for the flat water was 0.0035V, which suggested that the

accuracy of the flow depth reading was approximately 28μm. The wave probe calibration was repeated each day before the start of experiments.

4.2.3 Wave probe data

An example of the calibrated wave probe data continuous reading for seven wave probes is presented in Figures 4.10 and 4.11. Figure 4.10 shows the actual flow depth for seven wave probes for 20s interval, and Figure 4.11 shows the water level fluctuations above the mean for same wave probes and time series of 4 - 6s interval. Here the wave probes (WP) 1 - 7 were located at 9.60m, 11.55m, 11.62m, 11.67m, 11.70m, 12.80m and 13.80m respectively. The presented graphs are for clean pipe condition at a uniform depth of 87mm and flow velocity of 0.32m/s.

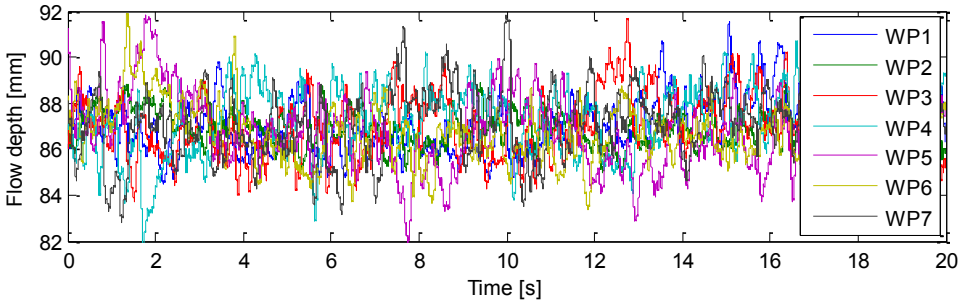

Figure 4.10 Example of flow depth data for 7 wave probes for clean pipe at velocity of 0.32m/s and mean flow depth of 87mm.

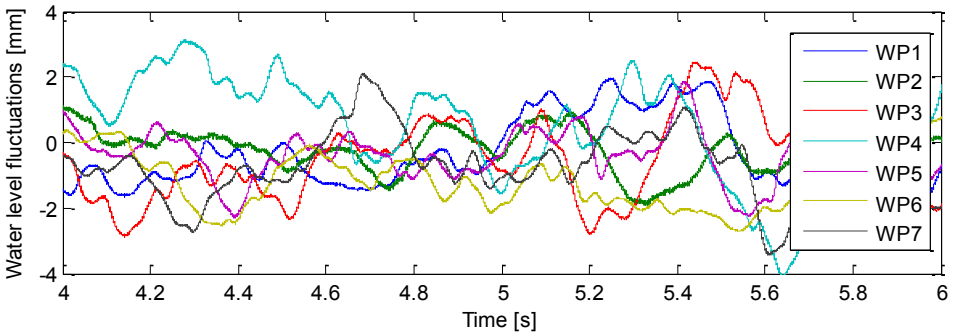

Figure 4.11 Example of water level fluctuation data for 7 wave probes for clean pipe at velocity of 0.32m/s and mean flow depth of 87mm.

4.2.4 Data analysis

The wave probe data were statistically analysed to extract information about the pattern of the water surface fluctuations. The mean (time-averaged) flow depth (h_m) recorded on a wave probe was obtained from equation (4.1), where m is the wave probe number, w is the calibrated, digitised signal from the wave probe, n is the sample number in the wave probe data file and N is the total length of the signal time series.

$$h_m = \frac{1}{N}\sum_{n=1}^{N} w_m(n) \quad \textbf{(4.1)}$$

Secondly, the mean (time-averaged) flow depth (h) between all wave probes, where M is the total number of wave probes, for a time series of length (N) was obtained for wave probe signal:

$$h = \frac{1}{M}\sum_{m=1}^{M} h_m \quad \textbf{(4.2)}$$

Thirdly, the wave probe signals were processed so that the fluctuations from the mean for each individual probe were obtained:

$$\bar{w}_m(n) = w_m - h_m \quad \textbf{(4.3)}$$

Further, the standard deviation (STD) of flow depth fluctuations was obtained for each individual wave probe:

$$\sigma_m = \sqrt{\frac{1}{N}\sum_{n=1}^{N} \bar{w}_m^2} \quad \textbf{(4.4)}$$

Next, the mean of the STD between all wave probes was found for each of the recorded signals (which effectively indicated mean wave roughness height):

$$\sigma = \frac{1}{M}\sum_{m=1}^{M} \sigma_m \quad \textbf{(4.5)}$$

Lastly, the mean peak to peak flow depth variation (amplitude) was determined for each of the wave probes and averaged. The total 500s sample was split into non-overlapping 5s time intervals for which a peak to peak wave height is found. The mean of the peak to peak flow depth variation was obtained for all the wave probes:

$$W = \frac{1}{M}\sum_{m=1}^{M}(max\{\overline{w}_m\} - min\{\overline{w}_m\}) \quad \textbf{(4.6)}$$

The spectrogram characteristic, which is a signal spectral density variation in time, was used to study the power spectral density (PSD), or the probability density function (PDF) of the flow depth variation:

$$\widetilde{w}_m(t_0, F_j) = \frac{\Delta t}{2\pi}\left|\sum_{T_s=t_0}^{t_0+K_F}\overline{w}_m(T_s)e^{2i\pi(T_s-1)(F_j-1)/K_F}\right|^2 \quad \textbf{(4.7)}$$

where Δt is the time step, K_F is the length of the Fourier transform and t_0 is the index in the time series from which the Fourier analysis is carried out, T_s and F_j are the time shift and frequency indices, respectively.

The correlation function which estimates the similarity between two random variables or sets of data at two different points in space or time was used in the wave probe analysis. The higher the value of the correlation function, the greater the similarity between the signals recorded on two different wave probes. The basic expression for the correlation function is:

$$CF(1,2) = corr(w_1, w_2) = \frac{E_j[(w_1 - \mu_1)(w_2 - \mu_2)]}{\sigma_1\sigma_2} \quad \textbf{(4.8)}$$

where, w_1 and w_2 are two different wave probe data sets recorded at the same time (random variables), E_j is the expected value operator (average of all

values), $\mu_{1,2}$ is the mean and $\sigma_{1,2}$ is the standard deviation of the wave probes data w_1 and w_2. The same analysis can be applied to the data of the same wave probe w_1 and w_1 which will result in the autocorrelation.

See Appendix B for the relevant Matlab codes of the above data analysis.

4.3 Acoustic instrumentation

The theoretical models of Morse and Ingard (1968) and Attenborough and Taherzadeh (1995) suggest that the level of the surface roughness results in an apparent increase in the acoustic reflection (scattering) of that surface in the directions other than specular. A change in the roughness height results in the change in the acoustic pressure measured in an acoustic pulse which propagates above the rough water surface. Acoustic instrumentation was developed that measures the propagating sound over the water surface fluctuations in a pipe. This acoustic instrumentation consisted of a speaker, microphone array, amplifiers, DAQ and a PC with LabView code.

4.3.1 Acoustic Sensor

The acoustic sensor consisted of four Brüel & Kjær 4190-C-001 (Appendix A6) 1/2-inch 50mV/Pa sensitivity microphones which can measure sound pressure in the frequency range of 3Hz - 20kHz and a powerful Visaton TI100 8Ohm speaker (Impactaudio 2006, see Appendix A7) with the diameter of the diaphragm of 100mm and frequency response in the range of 1Hz - 20kHz (see Figure 4.12). The microphones were connected to Brüel & Kjær Type 2669-C preamplifiers.

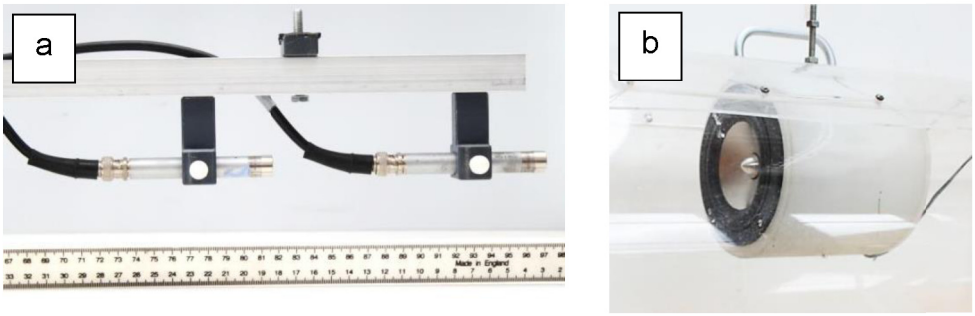

Figure 4.12 Microphone array (a) and speaker (b).

The microphone array was installed on an aluminum bracket which was attached to the top of the pipe as shown in Figure 4.12. These microphones were arranged in a linear array and separated at 160mm, 320mm and 480mm. The microphones were oriented to face the speaker which was located at 9.25m from the upstream end of the pipe. This arrangement resulted in a 5.69m separation between the speaker and microphone 1 (located at 14.94m) (see Figure 4.13 and Appendices A8 - A10).

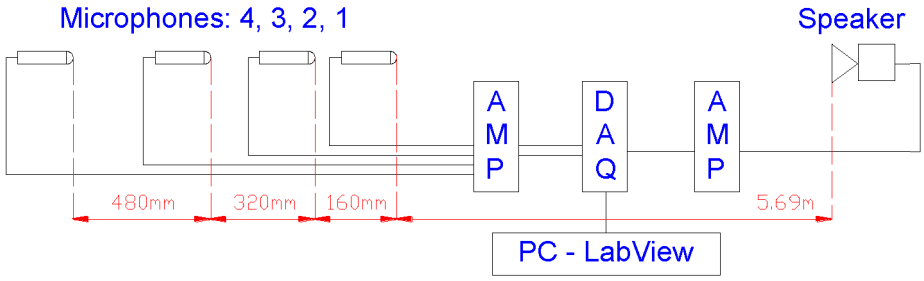

Figure 4.13 Microphone and speaker hardware set up diagram.

The acoustic signal was emitted from the speaker, which was connected to the amplifier, and DAQ. The signal propagated along the pipe and was recorded on the four microphones. The microphones were connected to the conditioning amplifier and the signals were digitized by the DAQ and stored on the PC. A LabView program was used to generate the signal and record the acoustic data at a sampling rate of 22.1kHz.

4.3.2 Acoustic signals

Two types of signals were selected for this application: a Gaussian pulse and continuous sinusoidal wave. The Gaussian pulse was chosen because it is short and has a well-defined spectrum. It is assumed that the presence of a dynamically rough water surface would result in the variation of the acoustic pulse pressure which could be statistically analysed and compared against the surface roughness data obtained with the 8 wave probes. Some previous works (e.g. Qin et al. 2008, Sharp 2001, Umnova et al. 2002) have established that the pulse scattering can be a good indicator of statically rough surface height.

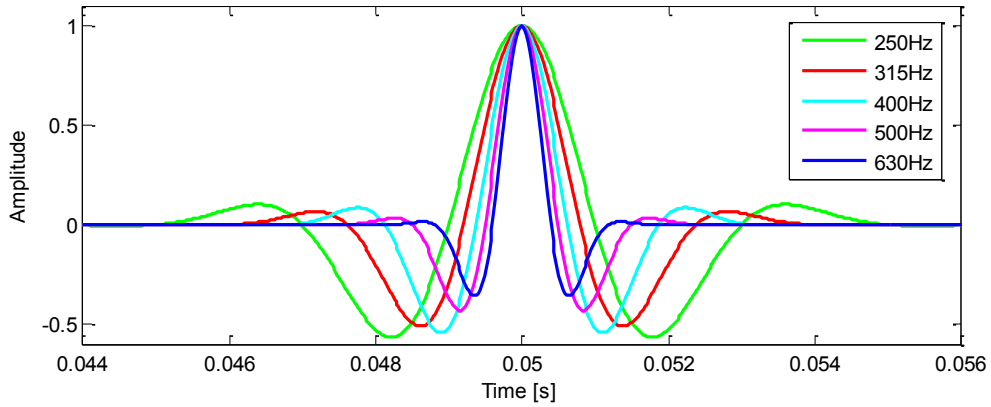

Figure 4.14 Relative amplitude of electronically generated Gaussian pulses of 250, 315, 400, 500 and 630Hz.

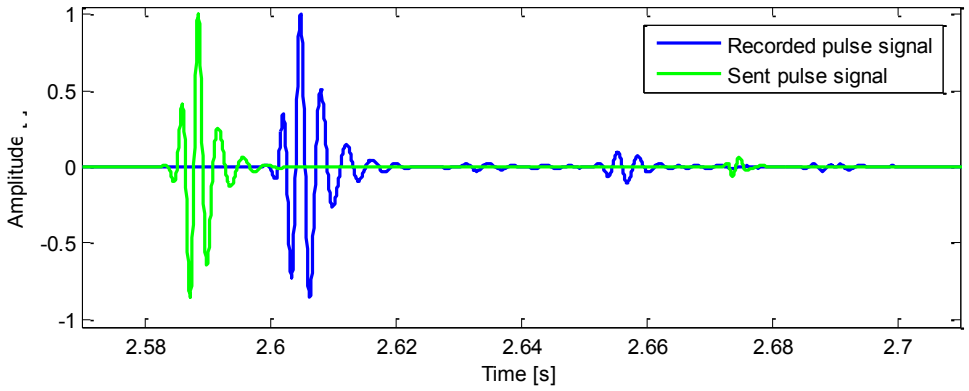

Figure 4.15 Relative amplitude of sent and recorded Gaussian pulses of 315Hz, which shape is induced by speaker and pipe properties.

Gaussian pulses with the center frequency of 250Hz, 315Hz, 400Hz, 500Hz and 630Hz were chosen. At frequencies below the 1st cut-on frequency (f_c) the acoustic field in the pipe can be approximated with a plane wave travelling in the axial direction. In the case of the 300mm pipe this frequency is f_c = 664Hz. The shape of the pulse used in these experiments is shown in Figure 4.14 for five different frequency bands.

The results of some preliminary experiments suggested that the pulse reflections from the pipe ends significantly reduce after 1s. Hence, it was suggested to emit a pulse every 2 seconds and the sound pressure was recorded in a 20 second long packet. This means that 10 pulses were captured in a single packet. It takes 0.018s for the pulse to reach the microphone from the speaker. Figure 4.15 shows the send and received pulse signal of 315Hz.

Continuous sinusoidal wave signal was also used to determine the effect of the water surface statistics on the amplitude of the continuous wave envelope. The plane sinusoidal continuous waves were generated with a signal generator Tektronix AFG3020B. Continuous waves of 315Hz, 500Hz, 630Hz and 800Hz were initially considered (see Figure 4.16).

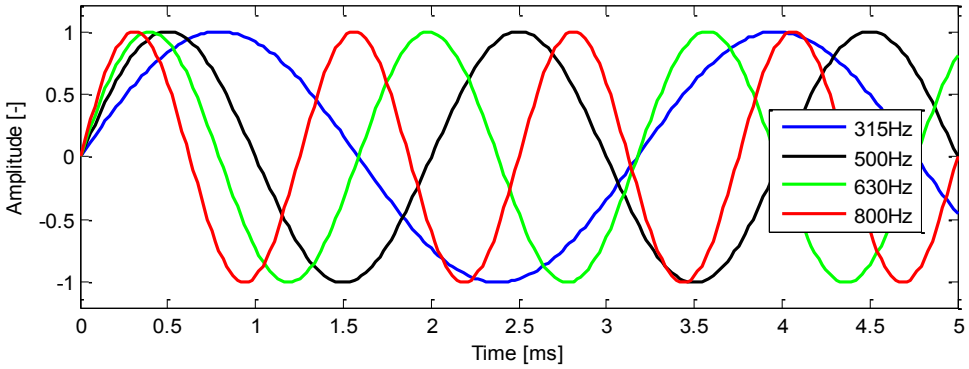

Figure 4.16 Relative amplitude of electronically generated continuous sinusoidal wave signal of 315, 500, 630 and 800Hz.

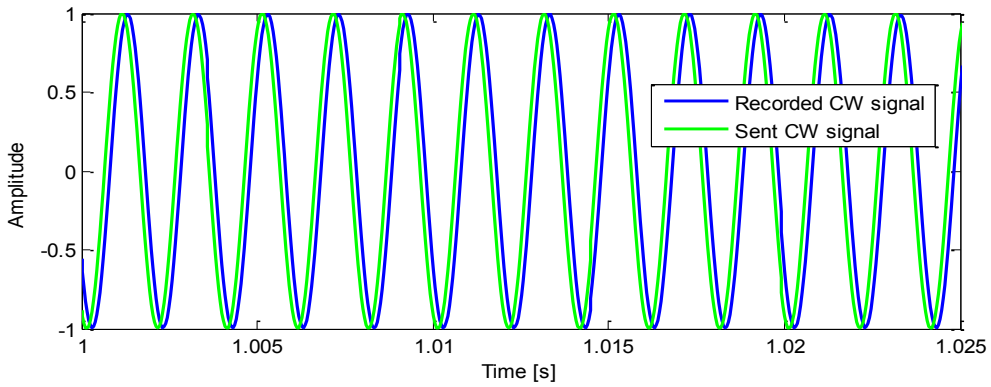

Figure 4.17 Relative amplitude of sent and recorded continuous sinusoidal wave signal of 500Hz.

In these experiments a signal was played and the sound pressure in the pipe was recorded simultaneously with the wave probe data reading. For the statistical characteristics the STD of the continuous wave due to the water fluctuations was examined as a function of time. Figure 4.17 shows the send and received 500Hz continuous sine wave signals.

4.3.3 Data analysis

The pulse data were analysed in the following manner. Firstly, the recorded pulse pressure (g), as a function of time (t) and pulse sequential number (y_i), was filtered using the Butterwort filter of the 3rd kind in the frequency range of 250 - 850Hz. Filtering helped to remove any noise and bias in received signal.

$$\widetilde{g_{y_i}}(t) = iir\{g_{y_i}(t)\} \quad \textbf{(4.9)}$$

Further, a specific time window was selected to extract the pulse tail response of the water surface. The maximum value ($\|g\|$) for each of the recorded pulses was found and used to normalise (find relative) the acoustic pressure data:

$$\widetilde{g_{y_i}}(t) = \frac{\widetilde{g_{y_i}}(t)}{\|g\|} \quad \textbf{(4.10)}$$

Figure 4.18 shows examples of pulse maximum peak and first tail peak for recorded pulse pressure, which was normalised by maximum pressure, and absolute value of that.

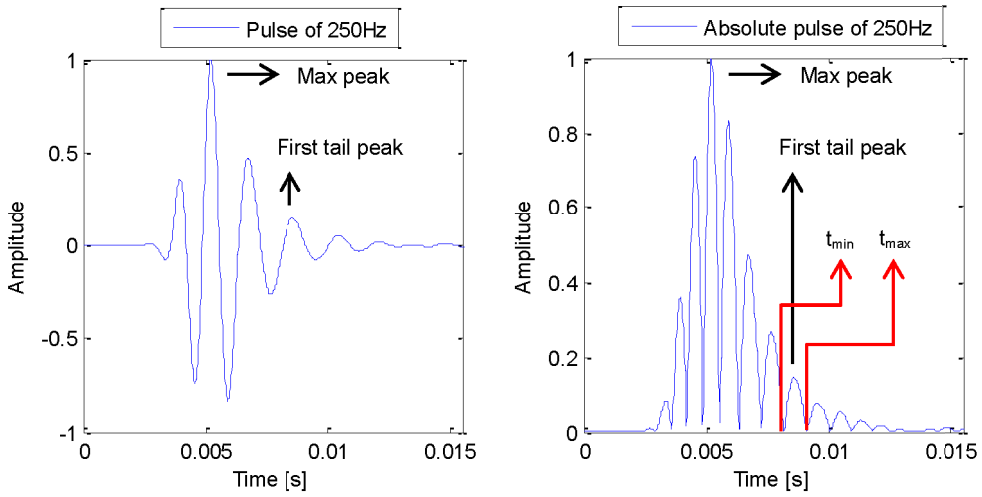

Figure 4.18 Example of 250Hz pulse relative pressure and absolute pulse relative pressure recorded reflection in empty pipe, with maximum peak and first tail peak.

The mean absolute relative pulse signal was found for the tail region of all pulses, where Y is the total number of pulses used in the analysis:

$$\langle g \rangle = \frac{1}{Y} \sum_{y_i=1}^{Y} \frac{1}{T_w} \int_{t_{min}}^{t_{max}} |\widetilde{g_{y_i}}(t)|\, dt \qquad \textbf{(4.11)}$$

where t_{min} and t_{max} define the bounds of the time window used for the integration as shown in Figure 4.18, and $T_w = t_{max} - t_{min}$. The standard deviation in the modulus of the acoustic relative pressure in the tail of all of the pulses between all of the 4 microphones (x_i), where X is the total number of microphones, was calculated as:

$$\sigma_g = \frac{1}{X} \sum_{x_i=1}^{X} \sqrt{\frac{1}{T_w} \int_{t_{min}}^{t_{max}} \left(\widetilde{g_{x_i}}\right)^2 dt} \qquad \textbf{(4.12)}$$

The correlation function (CF) was obtained using the six microphone pairs:

$$CF(x_i, x_j) = corr\left(\widetilde{g_{x_i}}, \widetilde{g_{x_j}}\right) = \frac{E_j\left[\left(\widetilde{g_{x_i}} - \mu_{\widetilde{g_{x_i}}}\right)\left(\widetilde{g_{x_j}} - \mu_{\widetilde{g_{x_j}}}\right)\right]}{\sigma_{\widetilde{g_{x_i}}}\sigma_{\widetilde{g_{x_j}}}}, i \neq j \quad \textbf{(4.13)}$$

where, x_i and x_j are two different microphone data sets of pulse tail recorded at the same time, i and j are microphone index numbers that can take values of 1 to 4, such that $i \neq j$, i.e. for $x_{i=1}$, $x_{j=2}$ data from microphones 1 and 2 is considered, respectively. Further, in equation (4.13) E_j is the expected value operator (average of all values), $\mu_{\widetilde{g_{x_{i,j}}}}$ is the microphones mean pressure and $\sigma_{\widetilde{g_{x_{i,j}}}}$ is the standard deviation between the recorded data x_i and x_j.

The maximum value of the CF was then found from:

$$\|CF(x_i, x_j)\| = max\left\{corr\left(\widetilde{g_{x_i}}, \widetilde{g_{x_j}}\right)\right\} \quad \textbf{(4.14)}$$

From the following the mean of 6 CF maxima among all the data was calculated, where x_i, x_j represents a microphone pair:

$$CF = \frac{1}{6}\sum_{i \neq j}^{X}\|CF(x_i, x_j)\| \quad \textbf{(4.15)}$$

For the continuous sine wave (CW) data (c_w) the filtering was performed using a Butterworth filter of the 3rd kind in 250 - 850Hz frequency range:

$$c_w(t) = iir\{c_w(t)\} \quad \textbf{(4.16)}$$

The Hilbert transform was then used to represent the recorded data as analytic signals from which the signal envelope can be extracted. The Hilbert transform of a signal is defined as:

$$\widehat{c_w}(t) = \Pr\frac{1}{\pi}\int_{-\infty}^{\infty}\frac{c_w(\tau)}{t-\tau}d\tau \quad \textbf{(4.17)}$$

where Pr stands for the principal value of this integral. Practically, for a discrete time series $c_w(t)$, the Hilbert transform is implemented using the Fourier transform and convolution theorem.

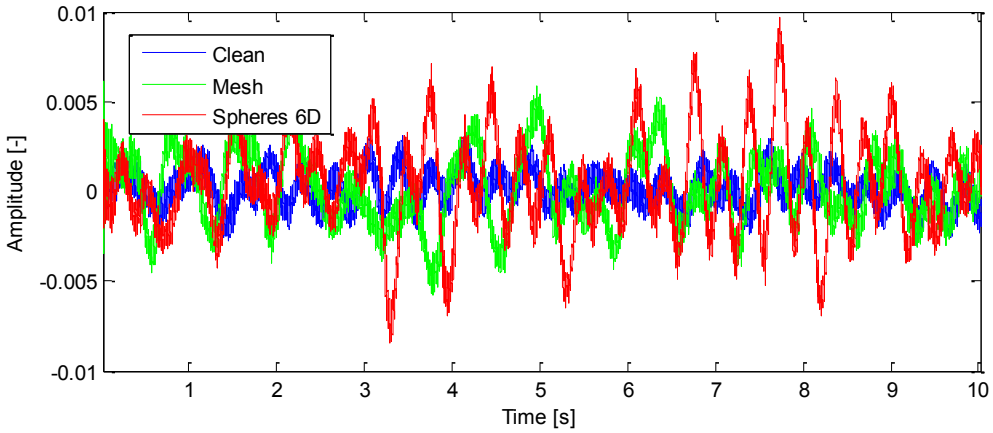

Figure 4.19 Example of filtered and normalised by mean 500Hz continuous wave envelope in clean pipe, pipe with mesh and pipe with 6D spheres at mean flow depth of 79mm and velocities of 0.29m/s, 0.26m/s and 0.24m/s, respectively.

The above enables to represent a signal from the microphone, $c_w(t) = \tilde{A}(t)\,cos(\omega_0 t)$, with $\tilde{A}(t)$ being the envelope of $c_w(t)$ in its analytic form

$$c_{w_a}(t) = c_w(t) + \mathrm{i}\widehat{c_w}(t) = \tilde{A}(t)e^{\mathrm{i}\omega_0 t}\,, \qquad \mathrm{i} = \sqrt{-1} \tag{4.18}$$

The Hilbert transform can be implemented using the 'hilbert' command in Matlab. It enables to determine easily the amplitude, i.e. envelope ($\mathrm{s}_{x_i}(t)$) of a continuous sine wave for each of the four microphones (x_i) from

$$\mathrm{s}_{x_i}(t) = e^{\mathrm{Re}\{\log c_{w_a}(t)\}} \tag{4.19}$$

Here Re is the real part of the natural logarithm of the analytic signal, $c_{w_a}(t)$. The signal to noise ratio for the extracted envelope of this signal was better than 32.7dB. Figure 4.19 shows an extracted CW envelope for the clean pipe, pipe with the mesh and pipe with 6D spheres.

Once the envelope was extracted, the mean amplitude of the continuous sound pressure envelope, between all microphones (X), in a specified time window ($T_e = 500s$) can be found from:

$$s = \frac{1}{X}\sum_{x_i=1}^{X}\frac{1}{T_e}\int_0^{T_e} s_{x_i}(t)\,dt \qquad \textbf{(4.20)}$$

Next, the mean standard deviation in the acoustic signal envelope ($s_{x_i}(t)$) for all the four microphones (X) is obtained:

$$\sigma_s = \frac{1}{X}\sum_{x_i=1}^{X}\sqrt{\frac{1}{T_e}\int_0^{T_e}\left(s_{x_i}(t) - \overline{s_{x_i}}\right)^2 dt} \qquad \textbf{(4.21)}$$

where $\overline{s_{x_i}}$ is the mean value of $s_{x_i}(t)$ in the time interval T_e.

Then the probability density function of the envelope data ($s_{x_i}(t)$) was calculated as the probability where $P(B \le \left(s_{x_i}(t) - \overline{s_{x_i}}\right) \le B + \Delta B)$ for a given amplitude limit of B and bin width ΔB.

See Appendix B for relevant Matlab codes of the above data analysis.

4.4 Preliminary experiments

Preliminary measurements of the water surface fluctuations were carried out in clean pipe, pipe with mesh and when the pipe had the 6D sphere arrangement. The aim of these experiments was to establish whether the wave probes are able to capture accurately the water surface fluctuations in the absence and in the presence of different wall roughness. The results of these experiments were helpful to determine the optimal positions of the wave probes in the pipe in the streamwise and cross-sectional directions. The pipe's cross-sectional pattern and the correlation between the adjacent wave probes were measured. Also

during these experiments different acoustic signals were tested and based on these results the best signals selected for use in the major experiments.

4.4.1 Wave probe noise elimination

Initial testing of the equipment showed wave probe data spectra with repetitive peaks at certain frequency. It was suspected that the wave probe wires and monitor could interfere to generate some unwanted noise which affected the recorded wave probe signal. In order to check whether there was any noise generated by the wires and the wave monitor, analogue external filters were used. RC filters with cut-off frequencies of 321Hz (filter 1) and 32Hz (filter 2), respectively, were fitted between wave monitor and the BNC adapter (see Figure 4.7).

A signal from one wave probe sample was recorded via three channels simultaneously: a channel with no filter; channel with filter 1; and channel with filter 2. The result of filtering is shown in Figure 4.20. The wave probe sample was recorded in running water for clean pipe for three flow regimes 0.16m/s, 0.18m/s and 0.21m/s which resulted in time-averaged flow depth (h) of 52mm, 62mm and 79mm, respectively.

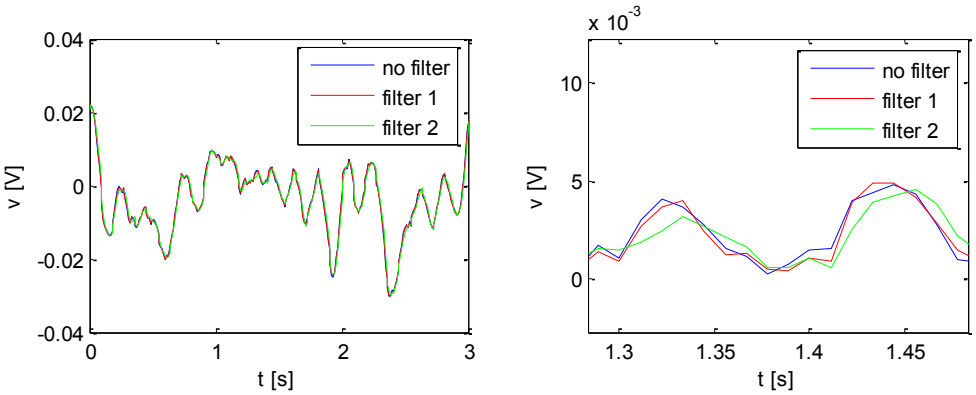

Figure 4.20 Filter effect on the wave probe reading for clean pipe at 0.18m/s.

Figure 4.20 shows three recorded readings on top of each other, each for different filter condition. The recorded signals overlay each other. However, when zoomed in (bottom left Figure), a small discrepancy can be spotted between the samples. If zoomed even closer, it can be noted that filters have a small effect and there is some difference between the raw (no filter) and filtered data. Effect of Filter 1 is milder (1% RMS change) than of Filter 2 (3% RMS change), so it was decided to use Filter 1 in all of the experiments to reduce random noise and aliasing effects, and not to affect the wave reading.

4.4.2 Wave probe equipment checks

Further, it is investigated whether the wave monitor cable adaptor and the data acquisition are working consistently. One wave probe sample was recorded with current equipment (Figure 4.8) and similar equipment in the lab, which consisted of Churchill Ltd 8 unit Wave Monitor, NI Corp BNC-2110 connector, and DAQ located in the NI Corp PIXe-1082 PC control unit (Appendix A).

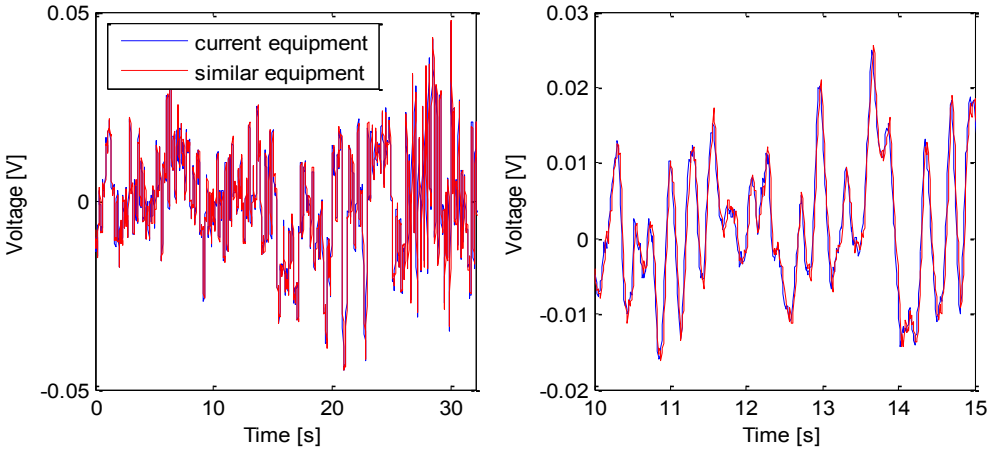

Figure 4.21 Normalised by mean and zoomed wave probe data recorded with two equipment sets for clean pipe at 0.18m/s.

As for section 4.4.1, here the experiments were repeated for clean pipe at three flow regimes at time-averaged velocity of 0.16m/s, 0.18m/s and 0.21m/s. The result from this test is presented in Figure 4.21, where the data from current and similar equipment is normalised by the mean and zoomed. The samples voltage amplitude RMS had a maximum difference in range of 0.5 - 0.75% for all three flow regimes. The above shows that both of the systems, record exactly the same data, providing consistent and reliable results.

4.4.3 Hydraulic experimental conditions

Preliminary measurements of water surface waves and acoustics, under steady flow conditions for a clean pipe, pipe with the presence of mesh, and spheres of 6D arrangement were taken at 3 flow discharges for each wall roughness pattern (Table 4.2). The hydraulic conditions presented in Table 4.2 cover some range of flow conditions that will be used in main series of tests (section 4.5), so that any information learned from the preliminary tests will be applicable over the range of flow conditions used in the main tests.

Table 4.2 Preliminary experimental conditions.

No.	Pipe condition	h	Q	V	k_s
	-	[mm]	[l/s]	[m/s]	[mm]
a	Clean pipe	52	1.29	0.16	1.15
b	Clean pipe	62	1.90	0.18	1.11
c	Clean pipe	79	3.13	0.21	0.96
d	Mesh	63	1.90	0.18	1.69
e	Mesh	79	3.08	0.21	1.21
f	Mesh	93	4.36	0.24	0.81
g	6D Spheres	66	2.01	0.18	2.06
h	6D Spheres	79	2.98	0.20	1.76
i	6D Spheres	91	4.09	0.23	1.05

The pipe contained 150mm x 1m fiberglass absorbent brackets which were placed at the inlet and outlet of the pipe (Figures 4.22a). Additionally, the inlet

and outlet tanks top were sealed with 60mm absorbent fiberglass layers (Figure 4.22b and 4.22c), and the manhole lids through which the microphone bracket and speaker were inserted into the pipe (Figure 4.22d and 4.22e). All of the mentioned above was carried out to increase the signal to noise ratio. The only external noise present during the experiments was the falling water from the pipe outlet noise.

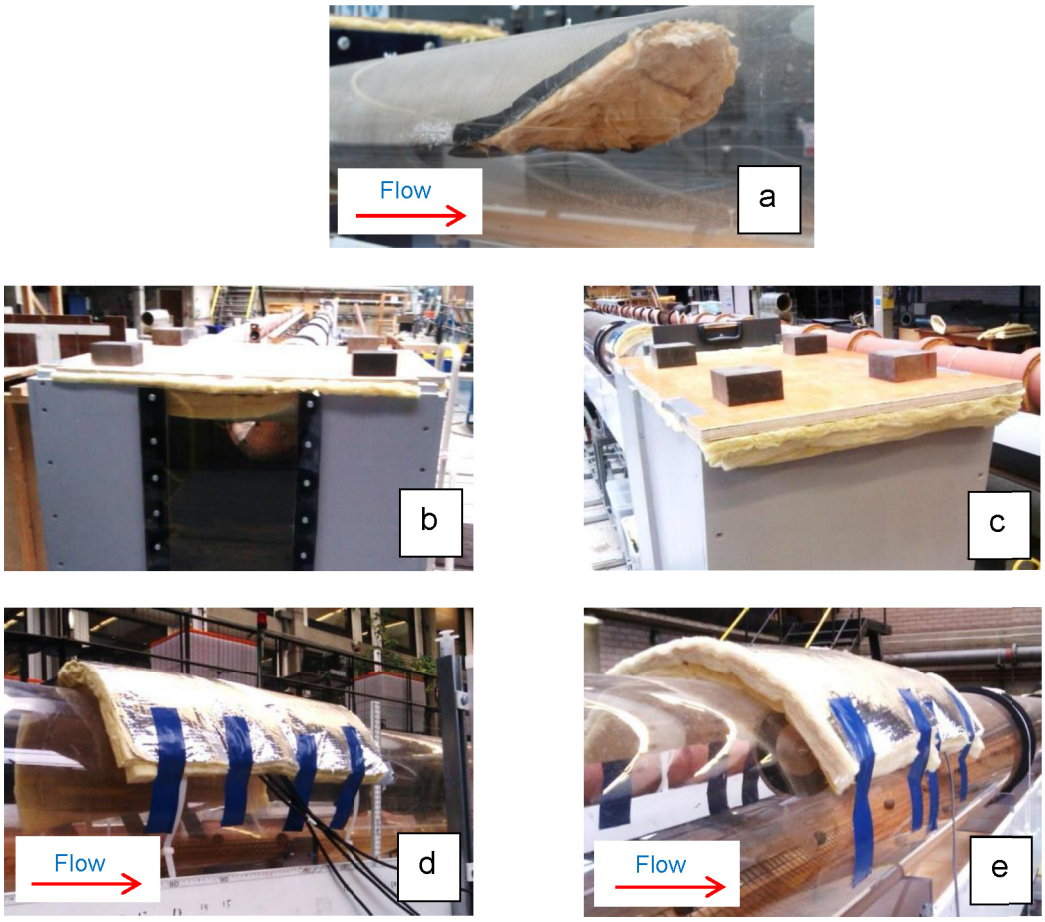

Figure 4.22 Pipe inlet internal fiberglass absorbent at 0 - 1m, same as at outlet at 19 - 20m (a), inlet tank top cover (b), outlet tank top cover (c), microphone cover at 8.5 - 9.5m (d), speaker cover at 14.7 - 15.3m.

All of the experiments were run in 'quiet' conditions. This involved running experiments after the general building ventilation was switched off. Also, the water pumps were switched off during wave probe and acoustic measurements. After the required flow regime was achieved the water flow was driven by the

head loss from the 30 tonne water tank located four stories above the Hydraulic Laboratory. The flow rate and flow depth were measured to be stable (when the flow rate or flow depth dropped by more than 3% or 1.5mm, respectively, the flow condition was regarded to become unstable) at least for 550s for the highest flow velocity of 0.5m/s with mean flow depth of 128mm for clean pipe condition, after 550s the flow velocity and depth started to decrease. For all experiments, the wave probe and acoustic data was recorded simultaneously for continuous 500s and the flow regime was set to appear in subcritical zone.

4.4.4 Wave probe streamwise and cross-sectional pattern

Twenty four wave probes were installed in the pipe and used to measure the flow depth fluctuations at streamwise and cross-sectional locations of the pipe. The probes were positioned at 8 streamwise locations and 3 cross-sectional locations for each streamwise position.

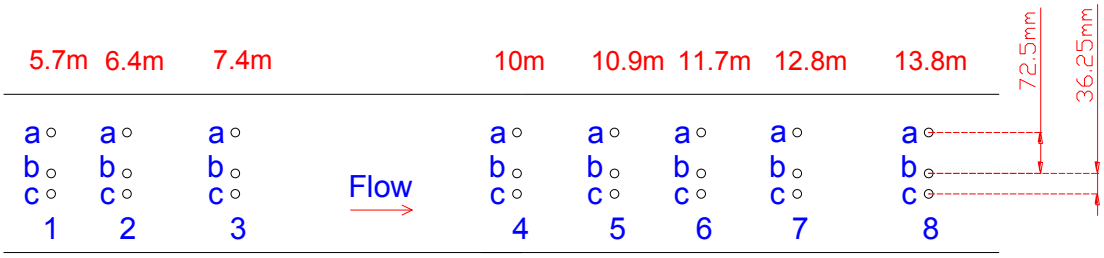

Figure 4.23 Wave probe arrangement in streamwise direction and cross-section.

Figure 4.23 demonstrates that the wave probes were located at 5.7m, 6.4m, 7.4m, 10m, 10.9m, 11.7m, 12.8m, and 13.8m in streamwise direction, where the time averaged flow depth was measured to be uniform for all test conditions. At each streamwise location three wave probes were installed across the pipes cross-section, one in the pipe center (centerline location) at 145mm from the edge of the pipe (b) and two adjacent wave probes were offset to the ½ (a) and

¾ (c) of the pipe radius, at 72.5mm and 36.25mm respectively from the pipe centerline. Figure 4.24 shows the photograph of the cross-sectional arrangement of three wave probes at 11.7m in streamwise location, attached at the top of the pipe with the use of plastic brackets (Figure 4.24a) and sealed from the outside at the bottom of the pipe (Figure 4.24b).

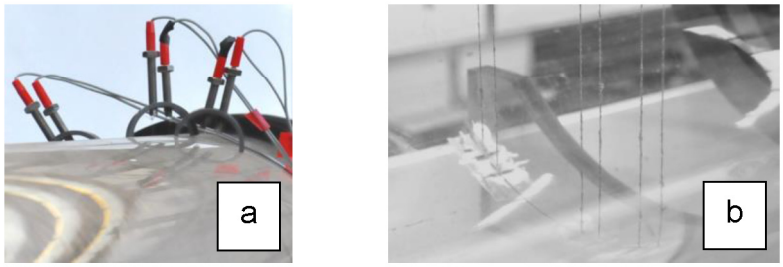

Figure 4.24 The cross-sectional arrangement of three wave probes at 11.7m in streamwise location. Top (a) and inside the pipe (b) view.

Experimental conditions and measurement results are summarised in Table 4.3, where columns left to right show experiment number, pipe wall roughness condition, time-averaged flow depth, flow velocity, hydraulic roughness, mean streamwise (longitudinal) wave STD (σ_l), uniform mean streamwise wave STD ($\overline{\sigma_l}$), with last two found from equation (4.5), uniform mean cross-sectional wave peak-to-peak amplitude ($\overline{W_c}$) found from equation (4.6) and uniform mean cross-sectional wave STD ($\overline{\sigma_c}$) found from equation (4.5).

Table 4.3 Experimental results for streamwise and cross-sectional wave probes.

No.	Pipe condition	h	V	k_s	σ_l	$\overline{\sigma_l}$	$\overline{W_c}$	$\overline{\sigma_c}$
	-	[mm]	[m/s]	[mm]	[mm]	[mm]	[mm]	[mm]
a	Clean pipe	52	0.16	1.15	0.21	0.03	1.18	0.03
b	Clean pipe	62	0.18	1.11	0.28	0.07	1.47	0.08
c	Clean pipe	79	0.21	0.96	0.48	0.10	1.91	0.11
d	Mesh	63	0.18	1.69	0.25	0.15	2.39	0.14
e	Mesh	79	0.21	1.21	0.52	0.11	2.38	0.10
f	Mesh	93	0.24	0.81	0.83	0.16	3.12	0.16
g	6D Spheres	66	0.18	2.06	0.74	0.30	4.14	0.29
h	6D Spheres	79	0.20	1.76	1.23	0.69	10.68	0.67
i	6D Spheres	91	0.23	1.05	1.08	0.61	9.48	0.60

Firstly, the mean water surface wave STD data (σ_l) for the wave probes located at three pipe cross-sectional positions in streamwise directions a, b and c was calculated. The water surface wave STD in wave probes located at 1a, 2a, 3a, 4a, 5a, 6a, 7a and 8a was compared to those of b and c, which was found to be within 3% range (see Figure 4.25). However, the data also revealed that the wave probes located at 5.7m, 6.4m, and 7.4m had on average much larger wave STD (Figure 4.25). It is believed that the flow at these positions is not fully established or completely uniform, as such the mean statistics of the wave probes a, b and c located between 9.5m and 14m will be considered in the further analysis, which will be denoted with an overhead bar, i.e. $\overline{\sigma_l}$, $\overline{W_c}$ and $\overline{\sigma_c}$.

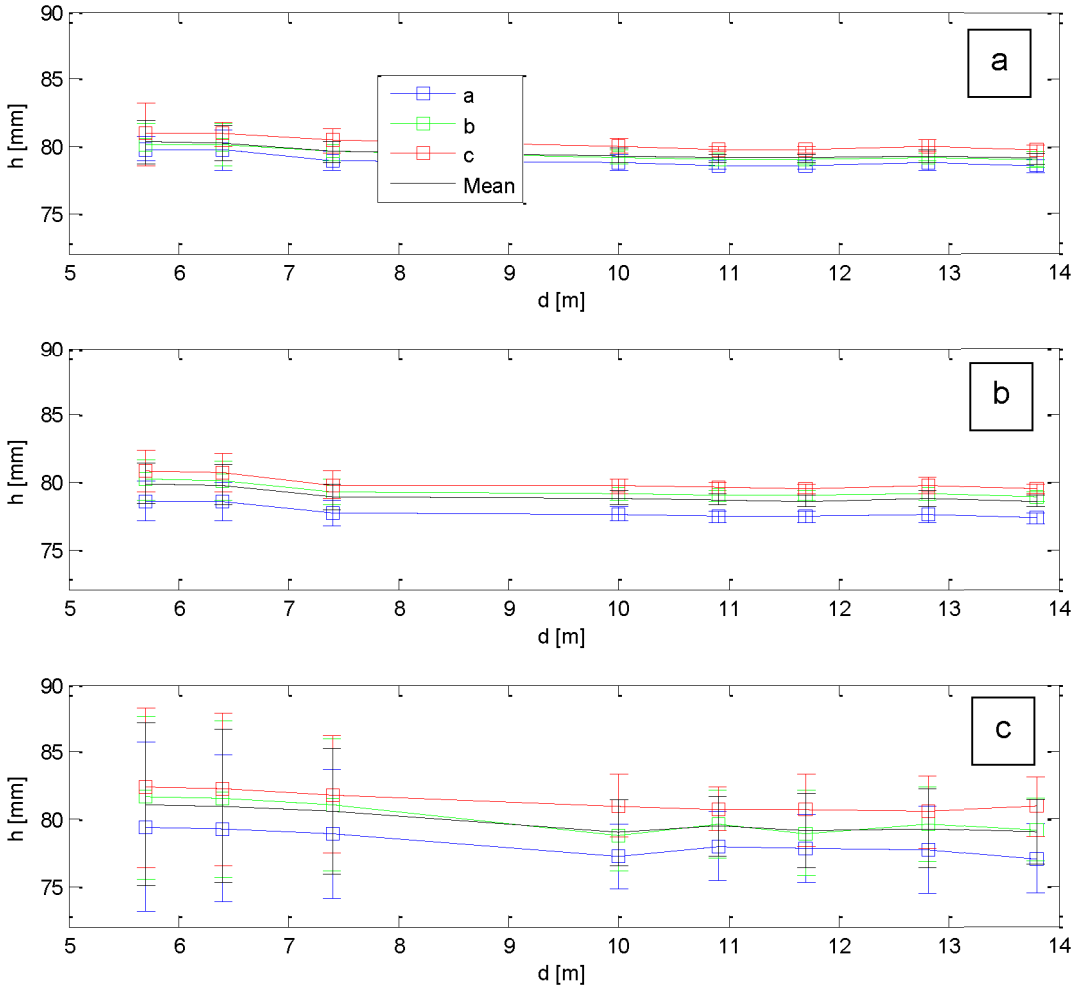

Figure 4.25 An example of streamwise flow depth pattern for wave probes (see Figure 4.23) at cross-sectional locations a, b, c and their mean with wave data STD error bars (σ_l) for test c (a), e (b) and h (c) from Table 4.3.

Second, the wave probe data at the established uniform flow streamwise locations (10m, 10.9m, 11.7m, 12.8m, 13.8m) was used to examine the flow depth cross-sectional pattern for three pipe wall conditions at all discharges. Here, experimentally three points were measured at each streamwise position and mean STD ($\overline{\sigma_c}$) found (for points 4a, 4b and 4c, and same for probes, 5, 6, 7 and 8) and two were assumed to be symmetrical (4a and 4b, same for probes, 5, 6, 7 and 8) and hence transformed along the middle of pipe diameter (D_c). Figure 4.26 illustrates an example of the typical pattern for three tests with different roughness conditions (Table 4.3), where the mean of probes a, b and c identified the 'M-shaped' water surface pattern in the pipe's cross-section.

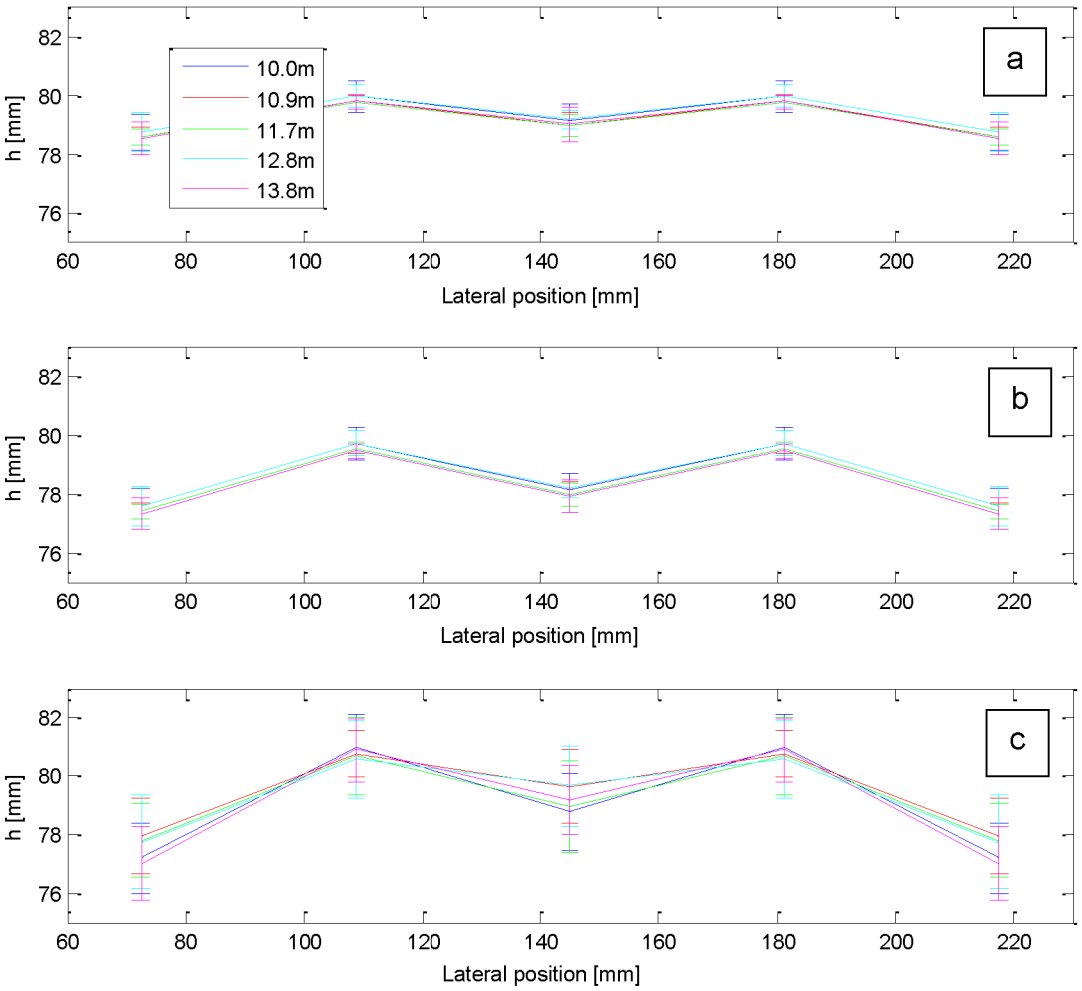

Figure 4.26 An example of mean cross-sectional flow depth pattern between probes a, b and c located at five streamwise positions (see Figure 4.23) with wave STD error bars ($\overline{\sigma_c}$) for test c (a), e (b) and h (c) from Table 4.3.

Same pattern, as shown in Figure 4.26, was observed for all experiments. It was found that, the statistics for the wave probes ($\overline{\sigma_l}$ and $\overline{\sigma_c}$), located in flow uniform area, despite the position, are similar (see Table 4.3). This eliminates the further need of three wave probe positioning in the pipe's cross-section, and in future experiments (section 4.5) the statistics of the wave probes located only in the centerline of the pipe (location b) will be considered.

4.4.5 Wave probe frequency spectrum

The 500s wave probe data from experiments listed in section 4.4.3 was used to obtain the frequency spectrum of the water surface waves for the wave probes 4b, 5b, 6b and 7b (see Figure 4.23) for conditions listed in Table 4.3. For each 500s long flow depth readings the length of the time window in frequency spectrum analysis was defined as 11.3s with an overlapping segment of 1.1s.

Figure 4.27 demonstrates the frequency spectrum of the flow depth fluctuation extracted from a single wave probe 4b, in clean pipe (a), pipe with mesh (b) and pipe with 6D sphere arrangement (c), for same mean flow depth of 79mm and velocities of 0.215m/s, 0.211m/s and 0.203m/s, respectively. The frequency spectrum is a representation of frequencies at which the flow depth fluctuation occurs at any given time. From Figure 4.27 it is visible, that the boost of frequency occurrence is only regular at 1 - 3Hz. Some of the frequency peaks, which seem to be irregularly repetitive, bounce up to 3 - 10Hz. All of them have long appearance time of 50 - 100s. Assessment of all flow depth fluctuation data, from all conditions (Table 4.3), gave result with similar patterns of frequency distribution.

The above spectral data suggests that there are significant variations in the spectral composition of the wave probe signal recorded in the pipe. The signal is non-stationary as occasional bursts of energy are clearly visible in the signal spectrogram. These bursts occur regularly at 20 - 30 second intervals.

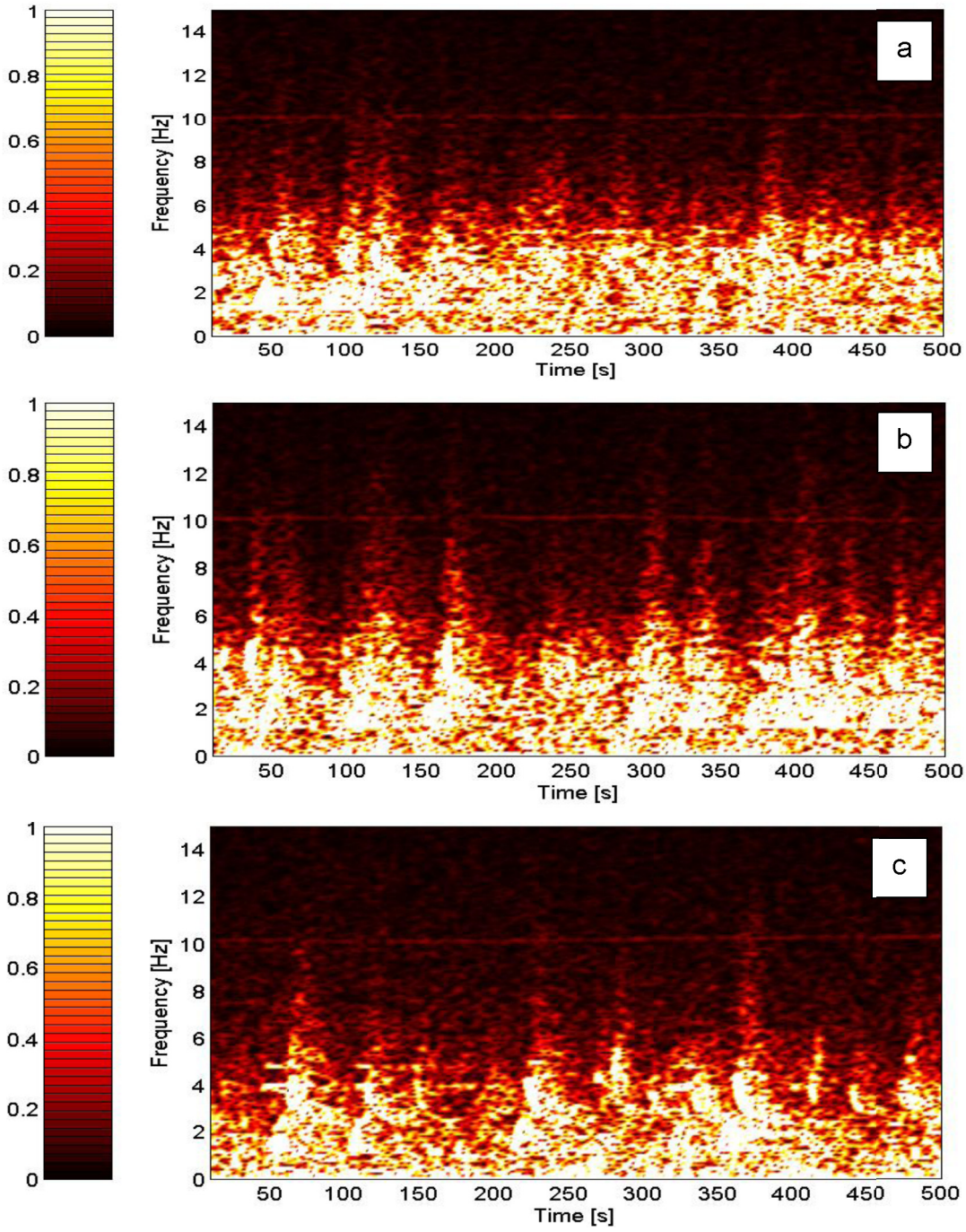

Figure 4.27 Frequency spectrum for 500s long flow depth fluctuation sample in clean pipe at 0.215m/s (a), pipe with mesh at 0.211m/s (b) and pipe with spheres at 0.203m/s (c).

4.4.6 Wave probe moving correlation

A similar procedure to cross-correlation (equation 4.8) was used to estimate the moving correlation between the signals recorded on single wave probe. The length of the time window in cross-correlation analysis was defined as 11.3s with an overlapping segment of 1.1s.

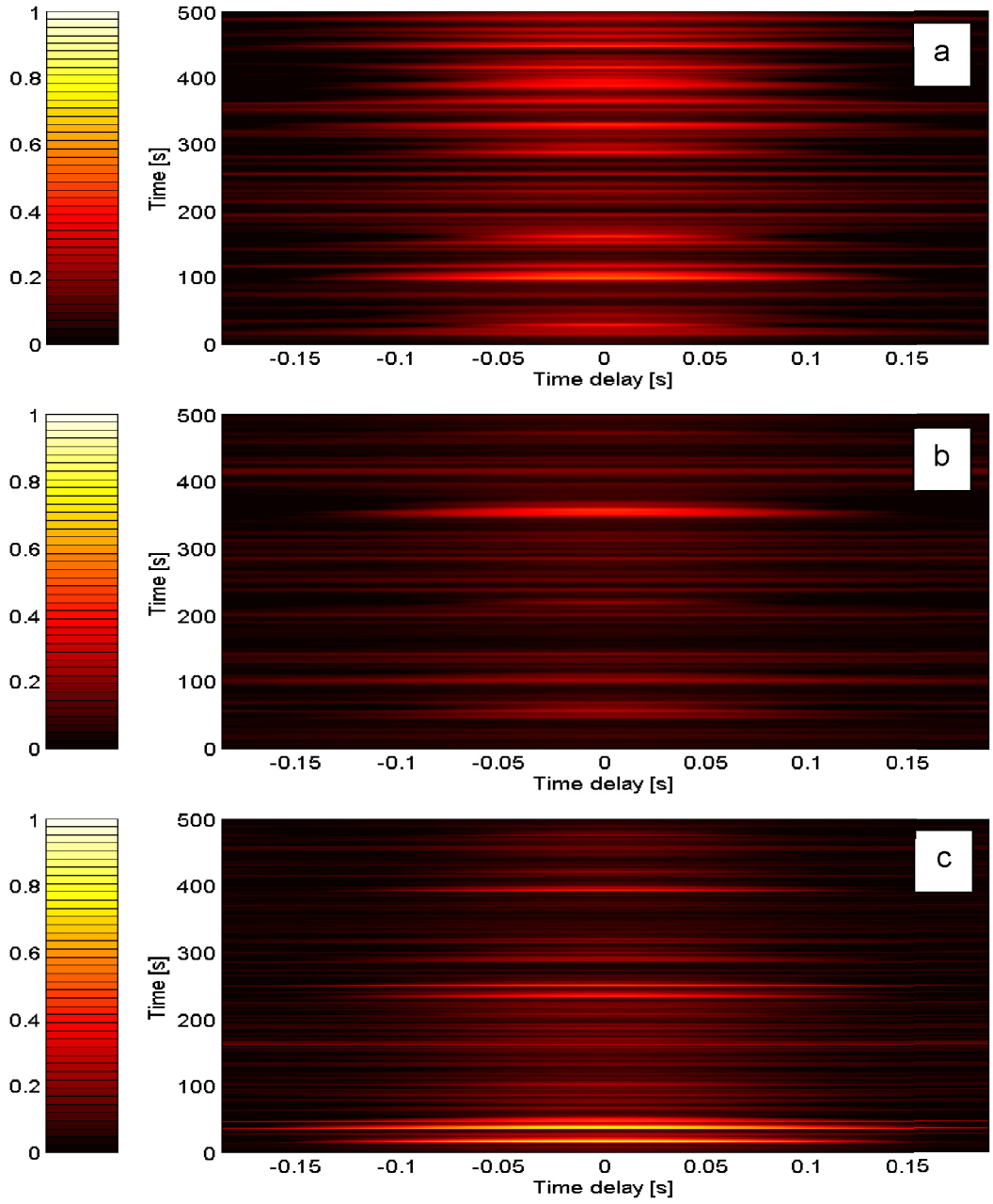

Figure 4.28 Moving correlation for 500s long flow depth fluctuation sample in clean pipe at 0.215m/s (a), pipe with mesh at 0.211m/s (b) and pipe with spheres at 0.203m/s (c).

The moving auto-correlation function for three pipe wall conditions, with mean flow depth of 79mm and velocities of 0.215m/s (a), 0.211m/s (b) and 0.203m/s (c), for wave probe 4b are presented on Figure 4.28 as a function of the time delay. The data shows that the variance measured over a period of 500s changes significantly. A change of 4 - 5 fold can be observed within a 20 - 30 second interval. This suggests that the process is non-stationary. The same results were obtained for all conditions listed in Table 4.3.

4.4.7 Wave probe cross and auto correlation

Additional streamwise (A, B, C) and cross-sectional (1, 2, 3, 4) closely spaced wave probes were installed into the pipe at locations of 11.55m, 11.58m, 11.63m and 11.70m (Figure 4.29). As described in section 4.4.4, probes B were installed in the pipe centre. The moving auto-correlation on individual wave probes has shown that there is little correlation of the water surface pattern within 1.1s time interval (section 4.4.6). Whereas, closely spaced wave probes should provide information on how quickly the correlation of the water surface waves at different points fall apart. The cross and auto correlation was performed for wave probes 1, 2, 3 and 4 for A, B, C sets.

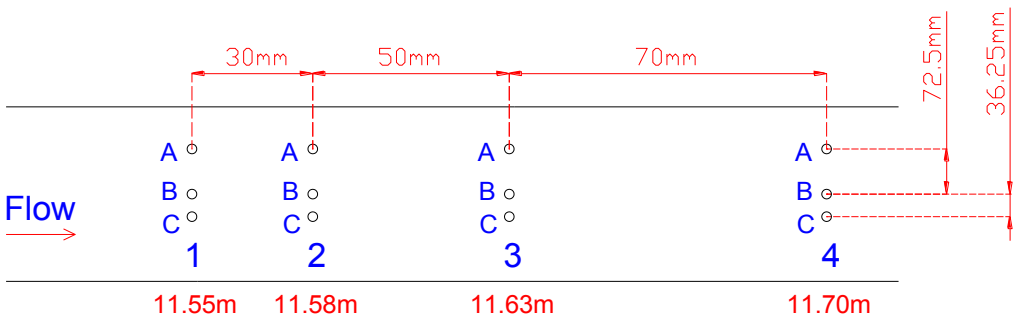

Figure 4.29 Closely spaced additional wave probe arrangement in streamwise direction and cross-section.

Figure 4.29 shows the correlation and auto-correlation functions for streamwise wave probe locations A, B and C, between positions 1-1 (auto correlation), 1-2, 1-3 and 1-4 (cross-correlation) for three pipe wall conditions, with mean flow depth of 79mm and velocities of 0.215m/s (row a), 0.211m/s (row b) and 0.203m/s (row c) from Table 4.3. The position of CF maximum corresponds to the temporal delay which is required for the water surface roughness pattern to propagate the distance separating the probes.

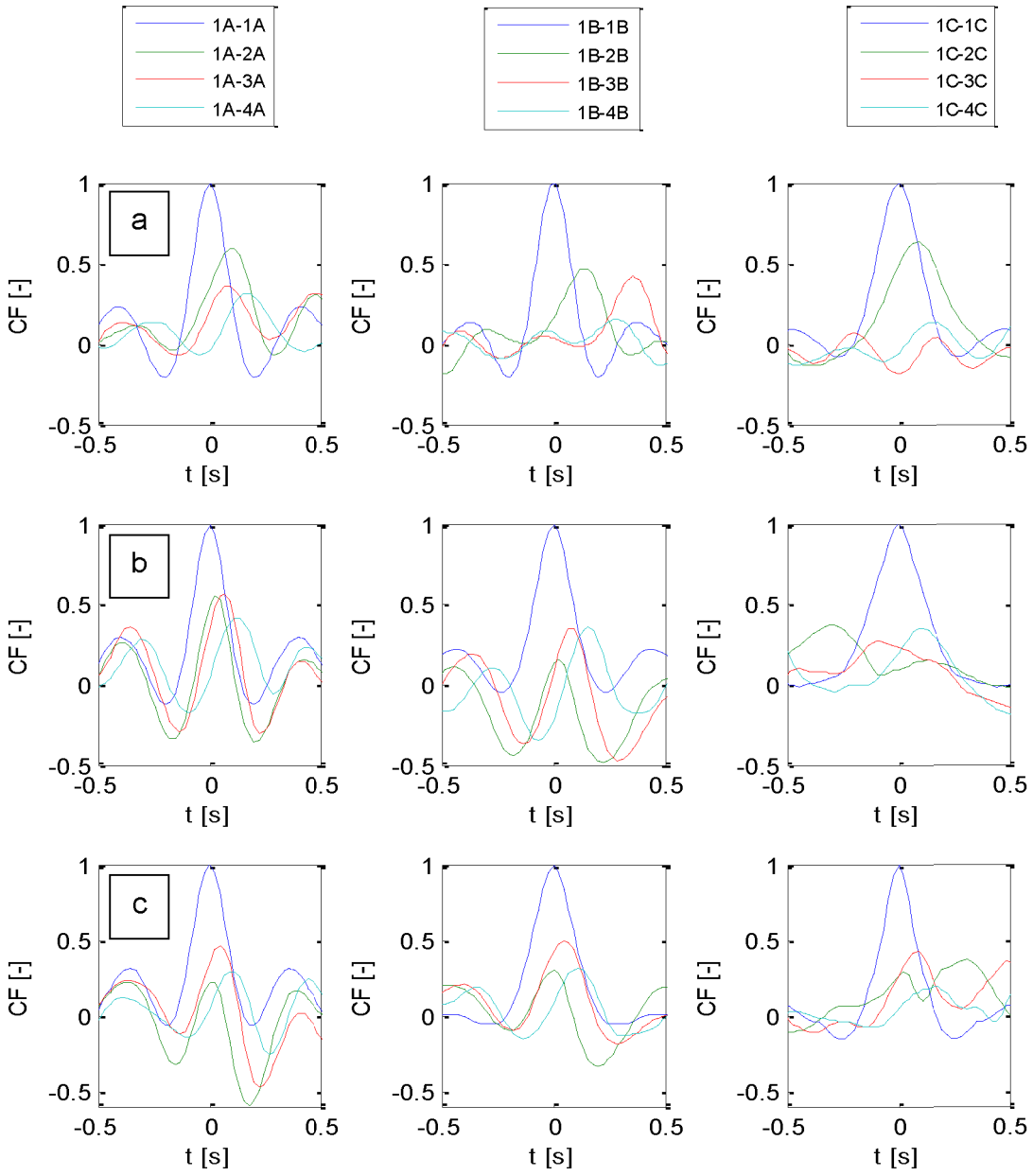

Figure 4.30 Correlation and auto-correlation function for streamwise wave probe locations of A, B and C (see Figure 4.29) for clean pipe at 0.215m/s (row a), pipe with mesh at 0.211m/s (row b) and pipe with spheres at 0.203m/s (row c).

From Figure 4.30 it can be seen that for all regimes and streamwise probe location the auto-correlation is equal to 1, which is expected. The data shown in row (a) suggest that for this regime the spatial correlation length in the roughness water surface pattern is approximately the spacing between probe rows 1 and 2, i.e. 30mm. The data shown in rows (b) and (c) suggest that there is better correlation between the signals recorded on those probes which were placed more close to the pipe wall. In general Figure 4.30, shows that for all three regimes, the correlation between the probes in streamwise location A are higher and fall apart slower than for those in B and C, this was also detected in the rest of the test summarised in Table 4.3. This could be related to the fact that the water surface waves measured at location A are influenced by the pipe wall. Generally, the correlation between adjacent wave probes is higher for clean pipe condition rather than pipe with mesh or spheres.

Also, the auto and cross-correlation were performed in cross-sectional direction for the wave probe locations as per Figure 4.30. Figure 4.31 shows the correlation function for cross-sectional wave probe locations of A, B and C (see Figure 4.29) for clean pipe at 0.215m/s (row a), pipe with mesh at 0.211m/s (row b) and pipe with spheres at 0.203m/s (row c). From the presented data it can be noted that the signals recorded on these probes are factually uncorrelated. The same conclusion can be made for the other flow regimes listed in Table 4.3, for which the signals from the probes in the lateral direction to the flow were found as uncorrelated.

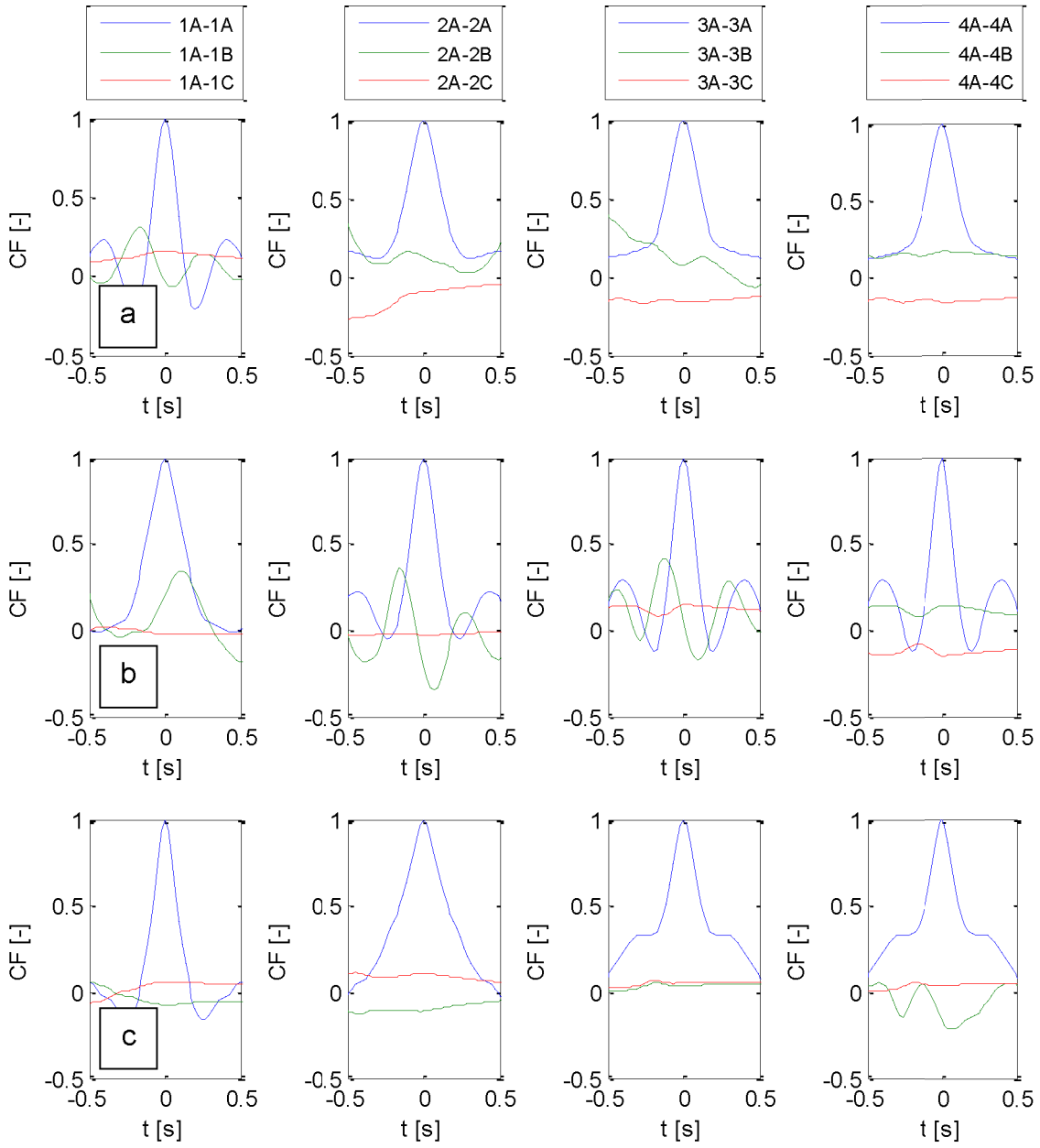

Figure 4.31 Correlation and auto-correlation function for cross-sectional wave probe locations of A, B and C (see Figure 4.29) for clean pipe at 0.215m/s (a), pipe with mesh at 0.211m/s (b) and pipe with spheres at 0.203m/s (c).

4.4.8 Acoustic signal tests

Both for the pulse and the continuous wave at all the frequencies preliminary experiments (full hydraulic conditions are listed in Table 4.2) were carried out to establish those frequencies at which the effect of the rough water surface was particularly pronounced in terms of the standard deviation in the signal

amplitude (see Table 4.4). The acoustic equipment in these experiments was arranged as described in section 4.3.1.

Table 4.4 Experimental data for pulse and continuous sine wave STD sensitivity (of different signal frequencies) of the water wave STD.

No.	h	V	$\bar{\sigma}_l$	Pulse					Continuous wave			
				σ_g [-]					σ_s[V]			
	[mm]	[m/s]	[mm]	250Hz	315Hz	400Hz	500Hz	630Hz	315Hz	500Hz	630Hz	800Hz
a	52	0.16	0.03	0.168	0.217	0.176	0.128	0.183	0.122	0.051	0.049	0.115
b	62	0.18	0.07	0.181	0.213	0.19	0.158	0.102	0.136	0.067	0.078	0.096
c	79	0.21	0.10	0.195	0.207	0.115	0.13	0.016	0.149	0.072	0.063	0.072
d	63	0.18	0.15	0.15	0.241	0.169	0.164	0.083	0.117	0.082	0.075	0.142
e	79	0.21	0.11	0.159	0.233	0.128	0.176	0.107	0.105	0.076	0.068	0.079
f	93	0.24	0.16	0.17	0.243	0.171	0.152	0.09	0.111	0.084	0.071	0.085
g	66	0.18	0.30	0.182	0.271	0.203	0.189	0.112	0.137	0.113	0.073	0.127
h	79	0.20	0.69	0.173	0.348	0.251	0.175	0.127	0.125	0.131	0.089	0.146
i	91	0.23	0.61	0.204	0.342	0.224	0.163	0.168	0.173	0.126	0.074	0.132

In Table 4.4, where columns from left to right indicate experiment number, mean flow depth, velocity, established uniform wave STD, followed by five columns of pulse tail peak maximum mean standard deviation (σ_g) for 250Hz, 315Hz, 400Hz, 500Hz and 630Hz, with last four columns showing the mean (between all microphones) standard deviation in the amplitude of the continuous wave envelope (σ_s) for 315Hz, 500Hz, 630Hz and 800Hz.

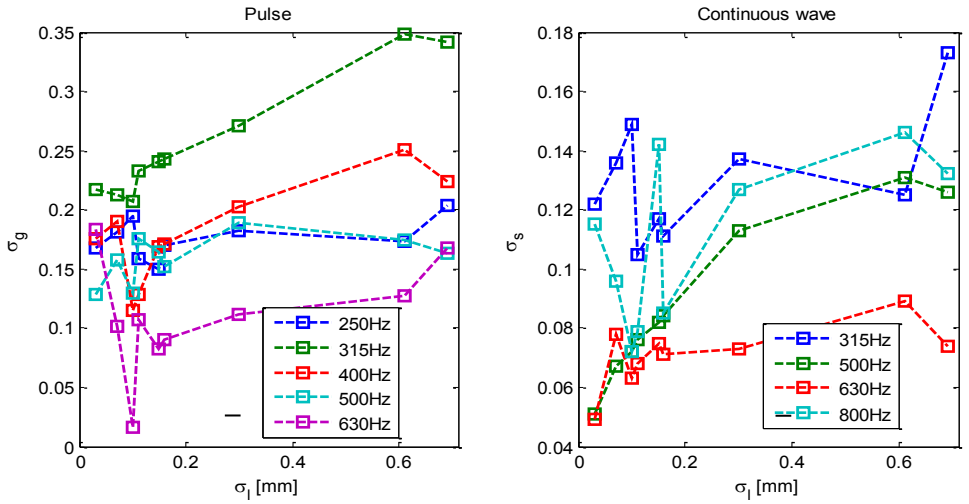

Figure 4.32 Pulse and continuous sinusoidal wave different frequency signal STD comparison to surface water waves STD for all conditions.

These results are illustrated graphically in Figure 4.32. From which it can be seen that for the pulse at the frequency of 315Hz the signal STD demonstrates positive relation with the increasing water surface roughness, whereas other appear to be more random for the presented range of conditions. Hence, pulse of 315Hz will be used in further experiments.

For the continuous wave signals, signal of 500Hz demonstrates positive relation with increasing mean roughness height, for the presented range of flow conditions. As such, a continuous wave of 500Hz will be used for further experiments. It should be noted that these results are general and may be considered true for the presented range of experimental conditions and the wave probe and acoustic data analysis methodology.

4.4.9 Conclusions

With the preliminary experiments described in the above section, it was possible to establish that: (i) the uniform, turbulent flow in the pipe is a complex process which is non-stationary; (ii) the zone between 10 - 13.8m was found to have well established uniform water flow conditions; (iii) flow depth STD in uniform flow is the same in lateral or cross-sectional position of the pipe; (iv) there is little correlation between the signals recorded on the adjacent wave probes for experiments with greater water surface roughness; (v) standard deviations of Gaussian pulse signal of 315Hz and continuous wave envelope of 500Hz (with acoustic equipment located at 9.25m and 14.94m for microphones and speaker, respectively) are sensitive to standard deviation in water surface waves recorded by the wave probes for the range of tested hydraulic conditions.

Considering the above, for the tests in the next section (section 4.5), the acoustic arrangement as presented in this section will be use. Whereas, in the experiments described in section 4.5, the wave probes will be spaced between 9.6m and 13.8m, which will be located only in the pipe centerline. This should allow to collect representative data of the water surface wave pattern, and reduce the time between different experimental condition setup.

4.5 Hydraulic roughness experiment

In each of the experiments a steady, uniform flow was achieved through a calibrated discharge which was measured with a volumetric tank, and by changing the end gate position. The flow regime settings were chosen to provide flow of cross-section at areas, close to those which are generally observed in combined sewer pipes, during dry and low wet weather flow.

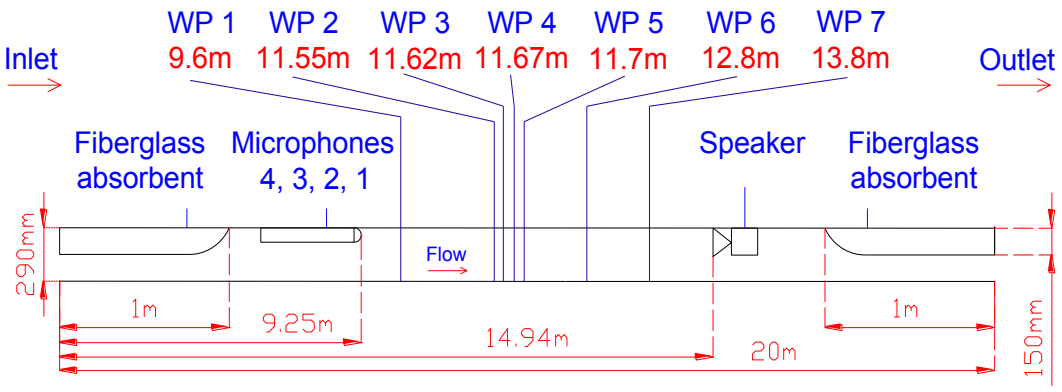

Figure 4.33 The schematics of 290mm PVC pipe experimental rig setup.

Based on the conclusion of the preliminary experiments (section 4.4), for the acoustic equipment and the wave probes the middle section of the pipe (8-15m) was chosen as an experimental section, so that experimental flow regime

conditions were stable and not affected by the pipe inlet or outlet conditions. During all experiments the pipe was set at a gradient of 1:2000. Seven wave probes were located in the centerline of the pipe from 9.6 - 13.8m (see Figure 4.33). The wave probes recorded the flow depth fluctuation on the center line of the pipe's cross-section. The microphones and the speaker were placed at the ends of the section that contained the wave probes. The separation between the speaker and the microphone array (the separation of the microphones in array is presented in section 4.4.1) was 5.69m as they were located at 9.25m and 14.94m. The sound was emitted in the direction opposite to the flow.

Table 4.5 Experimental conditions for distributed roughness in 290mm pipe.

Roughness RC	Uniform flow depth range h [mm]	Uniform flow occupation range a_h [%]	Uniform flow discharge range Q [l/s]	Uniform flow velocity range V [m/s]
C	52 – 106	12 - 33	1.3 - 5.6	0.16 - 0.26
M	63 - 106	16 - 33	1.9 - 5.7	0.18 - 0.26
4D	72 - 113	19 - 36	2.4 - 6.4	0.19 - 0.27
6D	66 - 112	17 - 36	2.0 - 6.3	0.18 - 0.27
8D	77 - 122	21 - 40	2.7 - 7.4	0.20 - 0.28
10D	71 - 120	19 - 39	2.3 - 7.2	0.18 - 0.28
12D	74 - 124	20 - 41	2.5 - 7.5	0.19 - 0.28
16D	71 - 111	19 - 35	2.2 - 6.2	0.18 - 0.27

For this final experimental set up a number of pipe bed roughness patterns (description is presented in section 4.1.1) and flow regimes were examined. A total number of 61 experiments were performed for the pipe with running flow. Table 4.5 shows roughness types and other experimental conditions. Both the acoustic and wave probe data was recorded for a total of continuous 500s for each flow condition, which was repeated only once.

4.6 Experimental results

A total of 61 experiments with various bed roughness conditions (RC), flow depths and discharges were undertaken. A summary of the hydraulic flow conditions and water surface wave statistics measured by the wave probes are presented in Table 4.6.

For each pipe bed roughness condition, Table 4.6 shows the mean water depth (h) which was obtained from the wave probe data collected at 7 centerline locations between 9.6 - 13.8m in the pipe's streamwise direction. The average pipe's cross-sectional area occupied by the flow (a_h) in percentage was calculated from the mean water depth data. The flow discharge (Q) was measured by observing the time for a volumetric tank filling up to a certain level. The mean flow velocity (V) was calculated from the knowledge of the discharge and cross-sectional area occupied by the flow.

In these experiments the Froude's number (Fr) ranged from 0.21 - 0.26 and hence all experiments were in the subcritical flow regime. The Reynolds number (Re) was in the range of 4460 - 16020, indicating that a fully developed turbulent flow in the pipe was always observed. The friction factor (f) was in the range of 0.032 - 0.051. The roughness value (k_s), which was calculated using the Colebrook-White equation showed values of 0.69 - 2.8mm.

Further Table 4.6 presents ratio of hydraulic roughness height to water depth (k_s/h). Next to last column shows wave peak-to-peak amplitude or maximum wave height (W) measured as an average of all wave probes. Last column shows mean wave standard deviation height (σ) measured as an average of all wave probes.

Table 4.6 Measured hydraulic parameters and ratios for all experiments.

No.	RC	h [mm]	a_h [%]	Q [l/s]	V [m/s]	Fr [-]	Re [-]	f [-]	k_s [mm]	k_s/h [-]	W [mm]	σ [mm]
1	C	52	12	1.29	0.162	0.227	4458	0.0474	1.15	0.0221	1.29	0.03
2		62	16	1.90	0.183	0.234	5964	0.0436	1.11	0.0179	1.90	0.07
3		70	19	2.46	0.199	0.240	7224	0.0409	1.01	0.0145	2.46	0.09
4		79	22	3.13	0.215	0.244	8615	0.0388	0.96	0.0122	3.13	0.10
5		89	26	3.98	0.232	0.248	10246	0.0369	0.92	0.0103	3.98	0.14
6		106	33	5.62	0.258	0.254	13106	0.0340	0.78	0.0074	5.62	0.17
7	M	63	16	1.90	0.178	0.225	5897	0.0471	1.69	0.0269	1.90	0.15
8		70	19	2.36	0.192	0.232	6947	0.0437	1.41	0.0202	2.36	0.22
9		74	20	2.69	0.201	0.236	7656	0.0420	1.30	0.0176	2.69	0.13
10		79	22	3.08	0.211	0.239	8468	0.0404	1.21	0.0153	3.08	0.11
11		83	24	3.45	0.219	0.243	9210	0.0390	1.11	0.0133	3.45	0.12
12		93	28	4.36	0.240	0.251	10970	0.0357	0.81	0.0087	4.36	0.16
13		106	33	5.68	0.259	0.254	13198	0.0340	0.78	0.0074	5.68	0.15
14	4D	72	19	2.36	0.185	0.220	6845	0.0486	2.33	0.0324	2.36	0.29
15		81	23	3.07	0.204	0.228	8337	0.0442	1.91	0.0235	3.07	0.36
16		90	26	3.93	0.225	0.239	10052	0.0395	1.35	0.0150	3.93	0.43
17		93	28	4.23	0.231	0.242	10609	0.0384	1.24	0.0133	4.23	0.47
18		97	29	4.66	0.241	0.247	11419	0.0367	1.04	0.0108	4.66	0.40
19		100	31	4.96	0.246	0.248	11950	0.0360	0.99	0.0099	4.96	0.39
20		104	32	5.38	0.253	0.250	12668	0.0351	0.92	0.0089	5.38	0.38
21		108	34	5.82	0.259	0.252	13389	0.0343	0.86	0.0080	5.82	0.36
22		113	36	6.39	0.268	0.255	14312	0.0333	0.77	0.0068	6.39	0.33
23	6D	66	17	2.01	0.178	0.221	6114	0.0487	2.06	0.0313	2.01	0.30
24		79	22	2.98	0.203	0.230	8175	0.0437	1.76	0.0223	2.98	0.69
25		84	24	3.41	0.215	0.237	9074	0.0409	1.43	0.0170	3.41	0.63
26		91	27	4.09	0.232	0.245	10412	0.0375	1.05	0.0115	4.09	0.61
27		99	30	4.92	0.247	0.250	11901	0.0355	0.90	0.0091	4.92	0.50
28		104	32	5.40	0.254	0.252	12721	0.0346	0.83	0.0080	5.40	0.49
29		112	36	6.29	0.267	0.255	14171	0.0332	0.75	0.0067	6.29	0.47
30	8D	77	21	2.74	0.195	0.224	7648	0.0462	2.12	0.0275	2.74	0.58
31		86	25	3.60	0.220	0.239	9446	0.0400	1.33	0.0155	3.60	0.96
32		103	32	5.22	0.248	0.247	12354	0.0361	1.07	0.0103	5.22	0.76
33		109	34	5.90	0.260	0.251	13514	0.0344	0.89	0.0082	5.90	0.72
34		118	38	6.93	0.275	0.255	15142	0.0327	0.75	0.0064	6.93	0.66
35		122	40	7.41	0.281	0.257	15863	0.0321	0.70	0.0057	7.41	0.62
36	10D	71	19	2.27	0.180	0.215	6612	0.0508	2.71	0.0381	2.27	0.41
37		76	21	2.61	0.191	0.222	7374	0.0473	2.25	0.0296	2.61	0.44
38		87	25	3.59	0.217	0.235	9384	0.0413	1.58	0.0181	3.59	0.56
39		94	28	4.35	0.235	0.244	10850	0.0376	1.13	0.0120	4.35	0.61
40		99	30	4.96	0.248	0.251	11982	0.0353	0.88	0.0088	4.96	0.76
41		105	32	5.47	0.255	0.252	12833	0.0347	0.86	0.0082	5.47	0.64
42		114	37	6.53	0.270	0.255	14533	0.0331	0.76	0.0067	6.53	0.53
43		120	39	7.18	0.278	0.257	15532	0.0322	0.70	0.0058	7.18	0.50
44	12D	74	20	2.47	0.185	0.217	7034	0.0495	2.61	0.0352	2.47	0.49
45		80	22	3.05	0.206	0.232	8325	0.0429	1.65	0.0206	3.05	0.56
46		88	26	3.77	0.223	0.240	9760	0.0396	1.33	0.0151	3.77	0.60
47		95	28	4.43	0.237	0.246	11019	0.0371	1.06	0.0112	4.43	0.73
48		97	29	4.70	0.242	0.248	11506	0.0364	1.00	0.0103	4.70	0.78
49		101	31	5.10	0.249	0.250	12211	0.0353	0.91	0.0090	5.10	0.66
50		107	34	5.74	0.258	0.252	13265	0.0344	0.87	0.0081	5.74	0.60
51		111	35	6.18	0.265	0.254	13985	0.0336	0.80	0.0072	6.18	0.56
52		118	38	6.94	0.274	0.255	15139	0.0328	0.77	0.0065	6.94	0.55
53		124	41	7.54	0.281	0.255	16017	0.0324	0.76	0.0061	7.54	0.49

No.	RC	h [mm]	a_h [%]	Q [l/s]	V [m/s]	Fr [-]	Re [-]	f [-]	k_s [mm]	k_s/h [-]	W [mm]	σ [mm]
54	16D	71	19	2.21	0.178	0.214	6483	0.0515	2.80	0.0395	4.18	0.53
55		77	21	2.75	0.195	0.224	7654	0.0464	2.16	0.0281	5.47	0.63
56		86	25	3.59	0.218	0.237	9401	0.0405	1.43	0.0166	6.06	0.68
57		89	26	3.95	0.228	0.244	10141	0.0382	1.13	0.0127	6.22	0.77
58		94	28	4.46	0.239	0.248	11095	0.0364	0.95	0.0101	6.35	0.83
59		103	32	5.28	0.252	0.251	12519	0.0349	0.87	0.0084	5.58	0.70
60		108	34	5.86	0.261	0.254	13483	0.0339	0.80	0.0074	5.24	0.63
61		111	35	6.23	0.267	0.255	14088	0.0332	0.74	0.0066	4.93	0.59

Figure 4.34 shows the relation between the mean water depth and flow discharge for all of the pipe bed roughness conditions. The time averaged discharge increases with the increase in flow depth, and can be expressed by the following equation

$$h = 47Q^{0.47} \tag{4.22}$$

with a line of best fit (red line on the graph) of R^2 = 0.99. This form of relationship was expected given the circular shape of the conjugate. It demonstrates that the flow in the pipe behaves as anticipated.

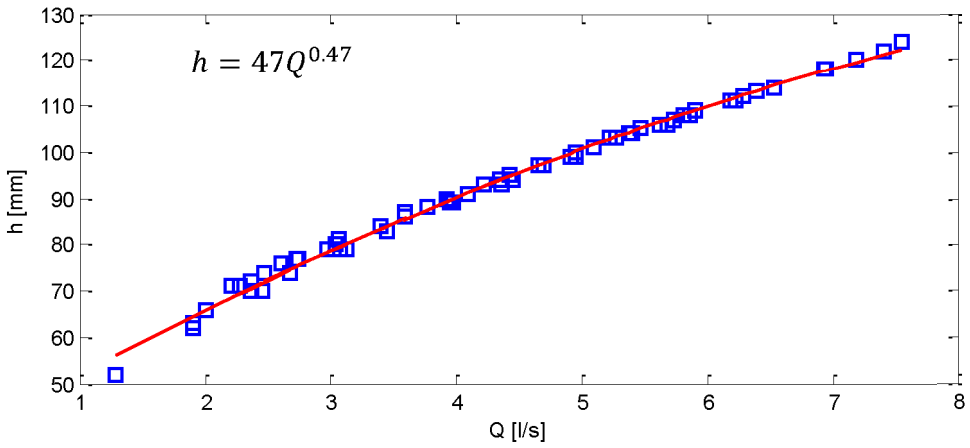

Figure 4.34 Water depth as a function of flow discharge for all pipe conditions, with R^2 = 0.99.

Figure 4.35 shows the time averaged mean flow velocity as a function of friction factor, where a power relation with a fit of R^2 = 0.95 can be expressed as

$$V = 0.0077f^{-1} \tag{4.23}$$

For all of the conditions it can be seen that the velocity values decrease as the friction factor increases. As expected, the values of friction factor increase as the flow velocity decreases. The values for the clean pipe are below the fit line. It seems that as the clean pipe condition pattern is different from other distinct pipe roughness condition patterns it does not follow the general trend for the velocity as a function of friction factor. If the clean pipe data is excluded from the analysis, for the distinct roughness data a power relation with a fit of R2 = 0.98 can be expressed as $V = 0.0089f^{-1}$.

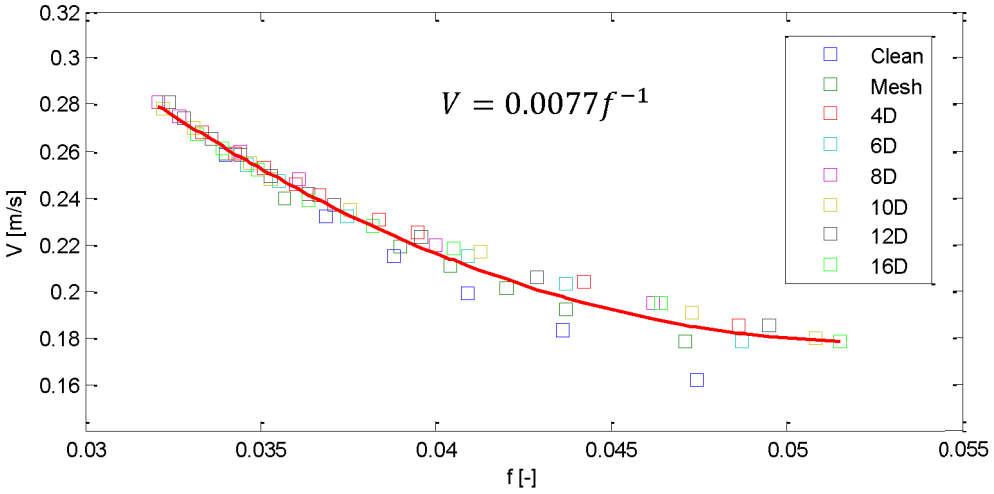

Figure 4.35 Mean flow velocity as a function of friction factor for all pipe conditions, with $R^2 = 0.95$.

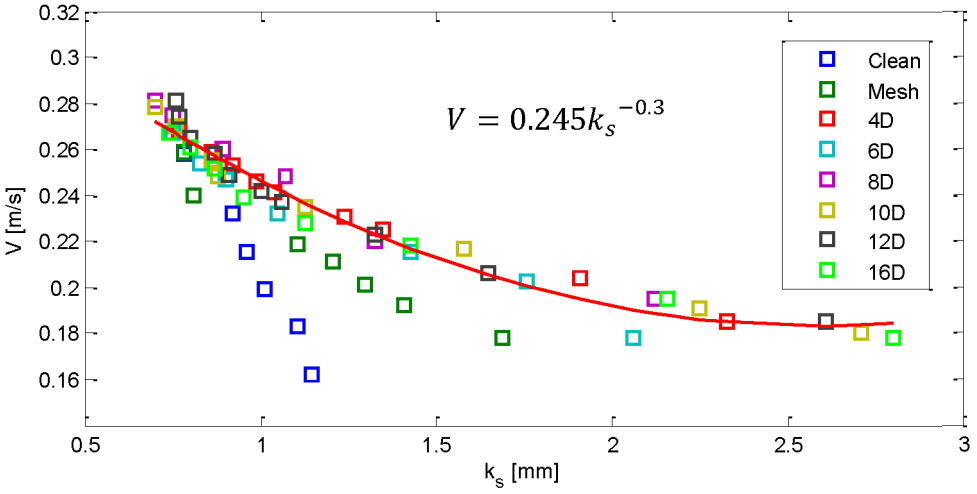

Figure 4.36 Mean flow velocity as a function of roughness for pipe roughness conditions with spheres, with $R^2 = 0.97$.

Further, Figure 4.36 shows a similar relation to that illustrated in Figure 4.35, where time averaged mean flow velocity is presented as a function of hydraulic roughness. A power equation for pipe roughness condition data simulated with spheres with a fit of R^2 = 0.97 can be expressed as:

$$V = 0.245{k_s}^{-0.3} \quad \textbf{(4.24)}$$

Figure 4.36 demonstrates that all of the data follow the same trend, where with the decreasing velocity values, the hydraulic roughness increases. However, the data for clean pipe and pipe with mesh deviate from the trend observed for the spheres. If only the data with distinct roughness will be considered, then equation (4.24) transforms to $V = 0.242{k_s}^{-0.33}$ with R^2 = 0.90, and for all conditions the equation becomes $V = 0.238{k_s}^{-0.32}$ with R^2 = 0.73. On their own, the relation for the clean pipe RC can be expressed as $V = 0.2{k_s}^{-1.17}$, and for mesh RC $V = 0.236{k_s}^{-0.45}$.

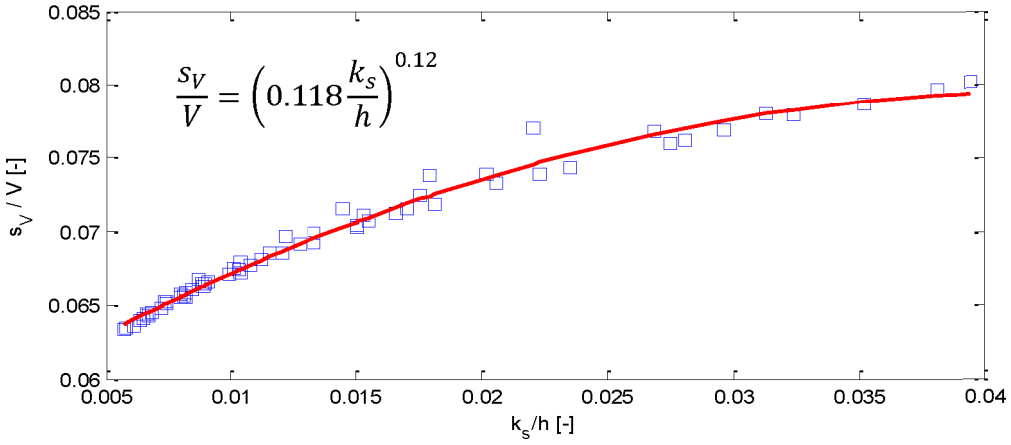

Figure 4.37 Shear velocity to mean flow velocity ratio as a function of roughness to flow depth ratio for all pipe conditions, with R^2 = 0.98.

Figure 4.37 shows the relation of shear velocity (s_V) to mean flow velocity as a function of calculated hydraulic roughness to flow depth ratio for all tests. A power equation with a fit of R^2 = 0.98 demonstrating this relation can be expressed as:

$$\frac{s_V}{V} = \left(0.118\frac{k_s}{h}\right)^{0.12} \quad \textbf{(4.25)}$$

where shear velocity was calculated as $s_V = \sqrt{S_0 g_a R}$. Figure 4.37 demonstrates that with the increase in shear velocity to velocity ratio the hydraulic roughness to flow depth ratio also increases.

The wave probe data values are presented in Table 4.6 (it should be noted that to reflect the current arrangement of the wave probes in the uniform flow area, the notation was changed from those used in preliminary experiments, section 4.4). The peak-to-peak wave amplitude or maximum wave height (W) measured on all wave probes, has values of 0.37 - 10.70mm. The mean wave standard deviation (σ) measured on all wave probes has values of 0.03 - 0.96mm.

The peak-to-peak wave amplitude (W) of all wave probes, measured from wave peak to peak over the whole length of data series was compared against the standard deviation of the flow depth (σ) for all of the experiments (see Figure 4.38). The relation between these two characteristics is close to linear with R^2 = 0.83. It can be seen that more variance or scatter in the data is present at 8D and 10D roughness conditions.

Also, in Figure 4.38 two groups of wave amplitude to wave STD may be identified based on roughness pattern, group (1) consists of C, M, 4D, 6D and 8D (with long dashed red line of best fit) and group (2) consists of 10D, 12D and 16D (with short dashed red line of best fit) roughness conditions. This suggests that different types of physical water surface wave behavior exist for different pipe bed roughness spacing. Two linear relations, $W(1)$ with fit of R^2 =

0.95 and $W(2)$ with fit of R^2 = 0.86 are proposed for groups (1) and (2), respectively, as shown in equations below.

$$W(1) = 13.92\sigma - 0.0065 \quad \textbf{(4.26)}$$

$$W(2) = 8.18\sigma + 0.12 \quad \textbf{(4.27)}$$

Equations (4.26) and (4.27) show a small error (0.0065 and 0.12) in wave amplitude estimation, as it is expected that if the wave STD equals to zero, the wave amplitude should also be equal to zero. The error may be induced by the method of water wave amplitude estimation (equation 4.6).

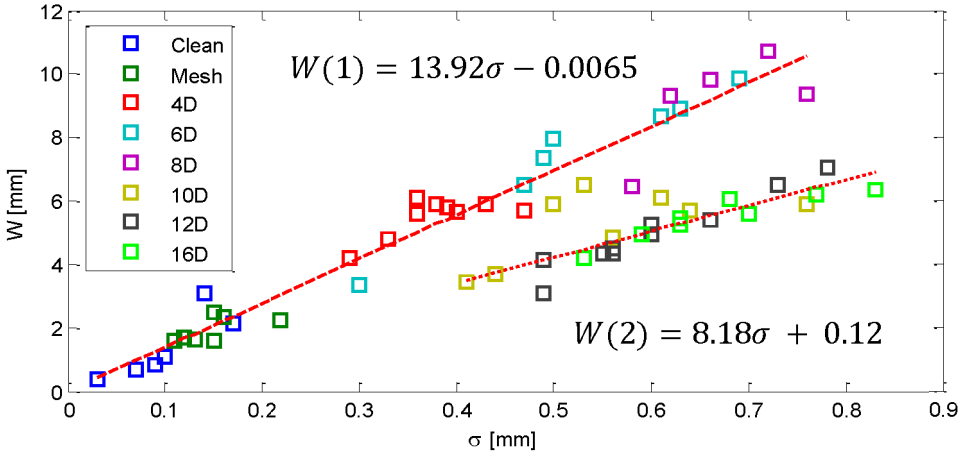

Figure 4.38 Wave amplitude as a function of wave STD height for all experiments, with two subgroups, with a fit of R^2 = 0.95 for group (1) and fit of R^2 = 0.86 for group (2).

The obtained Gaussian relative flow depth distribution (Figure 4.39) was used to calculate the theoretical wave probe standard deviation $\sigma(PDF)$ using equation (4.7). Figure 4.39 shows an example of relative flow depth distribution for three pipe conditions, clean pipe at 0.183m/s, pipe with mesh at 0.178m/s and pipe with 6D sphere arrangement at 0.176m/s. To demonstrate Gaussian distribution these three regimes were chosen as they show similar water depth of 62mm, 63mm and 66mm respectively.

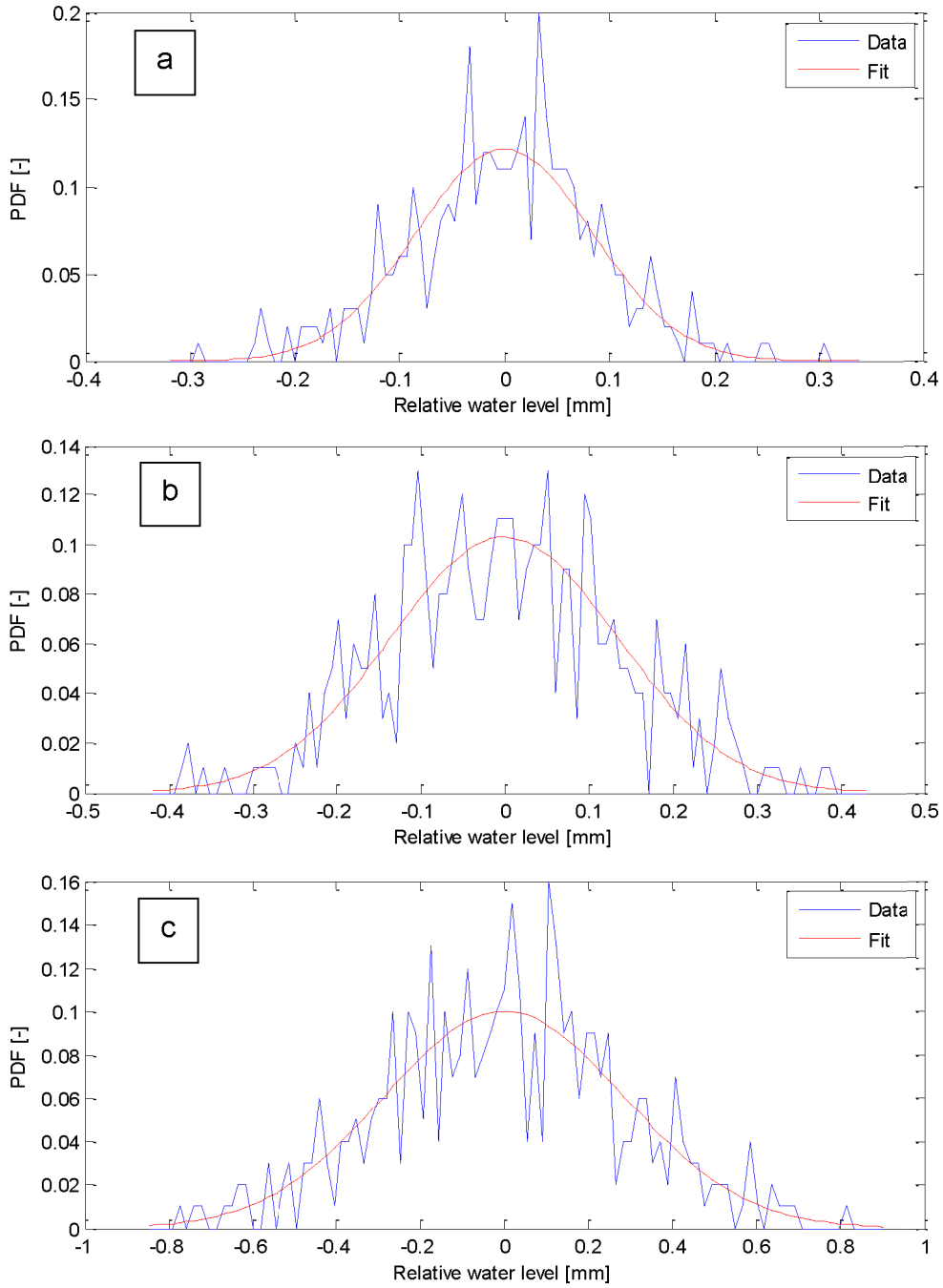

Figure 4.39 Gaussian distribution for the detrended water surface waves, mean of all wave probes, for clean pipe at 0.183m/s and h = 62mm (a), pipe with mesh at 0.178m/s and h = 63mm (b) and pipe with 6D spheres arrangement at 0.176m/s and h = 66mm (c).

The standard deviation values of the water surface wave distribution obtained with the PDF (example shown in Figure 4.39) were compared to the original values of wave standard deviation determined from equation (4.5). These are illustrated in Figure 4.40.

The relation of the PDF obtained surface wave STD and the surface wave STD obtained from the wave probe statistics (Figure 4.40) can be expressed as:

$$\sigma(PDF) = 0.95\sigma + 0.0136 \quad \textbf{(4.28)}$$

where the data set has a linear trend, with a fit value of R^2 = 0.98. A value of 0.0136 could be addressed to the systematic error of data approximation using the probability density function (PDF).

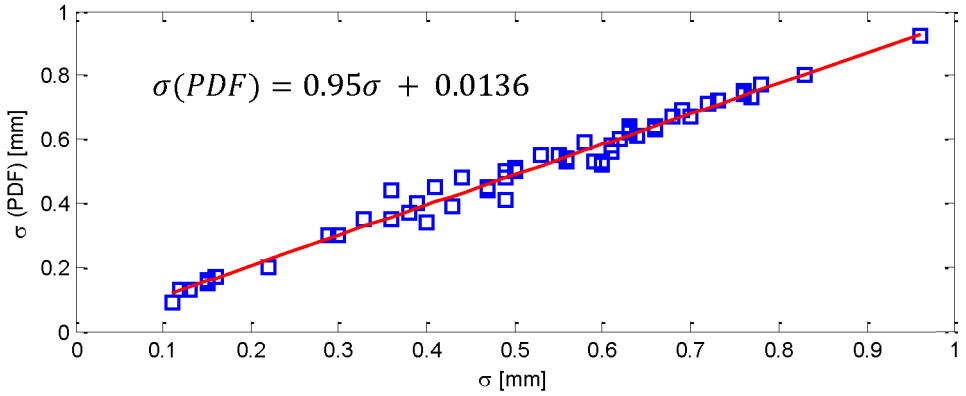

Figure 4.40 **Wave standard deviation obtained from Gaussian distribution as a function of wave standard deviation, with R^2 = 0.98.**

The above indicates that the flow depth fluctuations have a normal Gaussian distribution which can be implemented in the models of predicting wave STD for different flow conditions. However, for further analysis calculated raw value of the water surface waves standard deviation (σ) will be used.

4.7 Hydraulic parameters and bed pattern relation

The influence of the pipe wall roughness pattern on the water surface fluctuations of the flow was studied and relations obtained in this section. The statistics of the wave STD height (σ), extracted from the wave probes, with

relation to flow depth, velocity, hydraulic roughness, friction factor and wall roughness conditions are presented below (for values see Table 4.6).

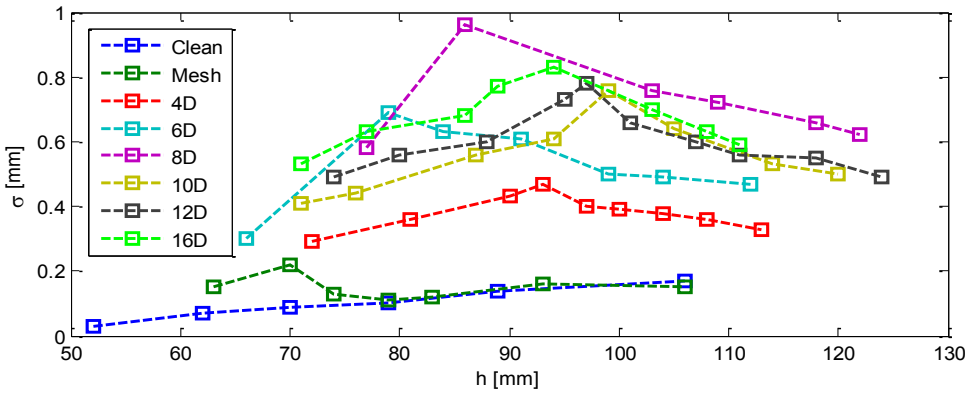

Figure 4.41 Wave STD as a function of flow depth for all pipe conditions.

First of all, Figure 4.41 shows the relation between the mean wave standard deviation and the mean flow depth for all pipe conditions. Here, the trend seems to show that the σ rises to a peak value for each distinct pipe wall roughness condition and then reduced. The maximum wave standard deviation value occurs at a different water depth for different wall roughness conditions. For the clean pipe condition the wave standard deviation follows a different trend which gradually increases with increase in flow depth. Here, as the pipe roughness is negligible and considered smooth the water surface wave STD are only governed by the increase in flow depth and velocity. This means that the clean pipe condition cannot be assessed in the same group as rough pipe conditions and will be excluded from further analysis, as this work concentrates on pipes with the presence of roughness.

Figure 4.42 illustrates the data that is the same as on Figure 4.41, only the curves for different pipe wall roughness concentration conditions are color coded. The coding is related to three main Schlichting's roughness concentration types (see section 2.2.5).

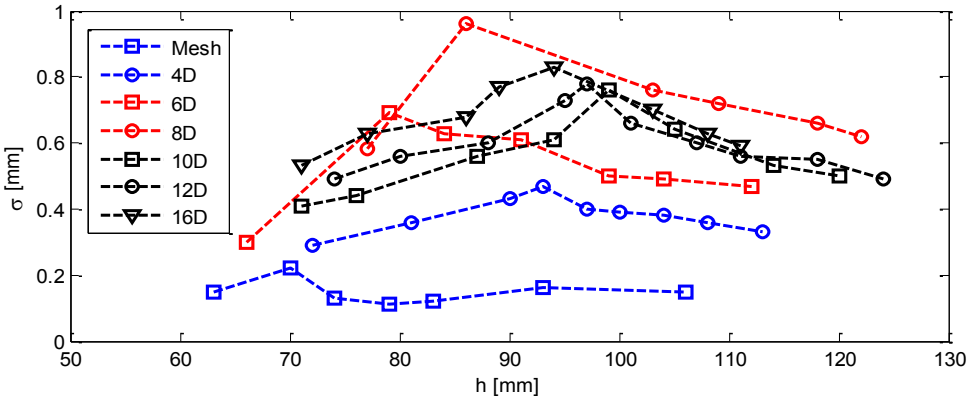

Figure 4.42 Color coded wave STD as a function of flow depth for all pipe conditions.

Originally Schlichting's roughness concentration catergorisation comes from 2D elements on flat plates. In presented experiments the exact same Schlichting's roughness concentration definition was applied to pipes (curved surfaces) with distinct elements, where the value range of the roughness coefficient (λ_r) that describes the three classes have been changed according to the presented experimental range (Table 4.1).

From Figure 4.42, the adopted Schlichting's roughness concentration is defined as: (i) blue - closely packed or continuous roughness with range of $[0.0001 < \lambda_r \leq 0.008 \; and \; \lambda_r \geq 0.044]$ or 'd-type' roughness. Roughness of this type is considered to be a very rough bed with minimal element separation so that the flow which occurs between the elements does not have a strong effect on the flow above the roughness elements. In some cases this roughness is closely packed and tends towards smooth roughness condition, i.e. pipe with mesh and 4D roughness; (ii) red - roughness elements in this type of bed are separated by such a distance that the flow which is generated between the roughness elements has a protruding effect on the flow layer above the roughness elements. Here roughness concentration has a small range $\lambda_r = [0.0027 - 0.0033]$ or can be defined as 'transitional' roughness; (iii) black - the 'k-type'

roughness, where the roughness elements of the distributed roughness act as individuals. At the location of this type of roughness element the flow is effected for a short distance however returns to uniform condition before reaching next roughness element. Here roughness concentration has a small range $\lambda_r = [0.012 - 0.0023]$.

Further, Figure 4.43 shows the relation between the mean wave standard deviation and the mean time averaged flow velocity for all pipe conditions. The general pattern of the data is similar to that observed in Figures 4.41 and 4.42. Here, the wave STD height reaches its maximum at different velocities for different roughness conditions. The maximum wave STD for mesh, 6D and 8D spheres is achieved at lower velocities.

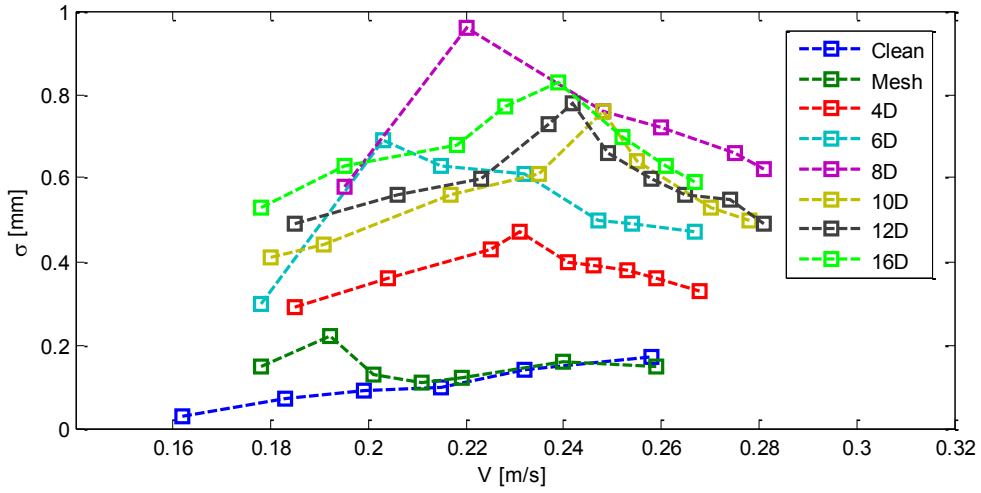

Figure 4.43 Wave STD as a function of mean flow velocity for all pipe conditions.

Figures 4.44 and 4.45 show the relation between wave STD height and the hydraulic roughness and the friction factor, respectively. The pattern of these relations is similar to that shown in Figure 4.43, with the only difference that the trend of wave STD height maximum occurrence has changed. The maximum

values of wave STD for 6D and 8D roughness conditions appear at higher hydraulic roughness and friction factor than for those of 10D, 12D and 16D.

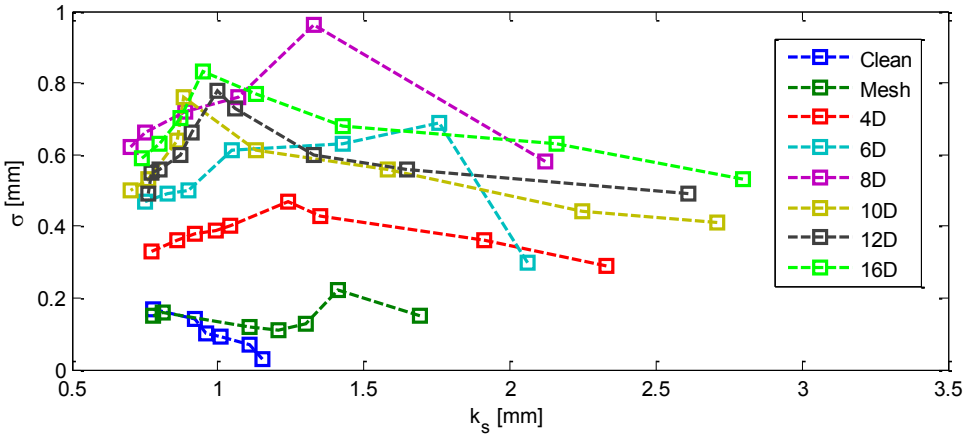

Figure 4.44 Wave STD as a function of hydraulic roughness for all pipe conditions.

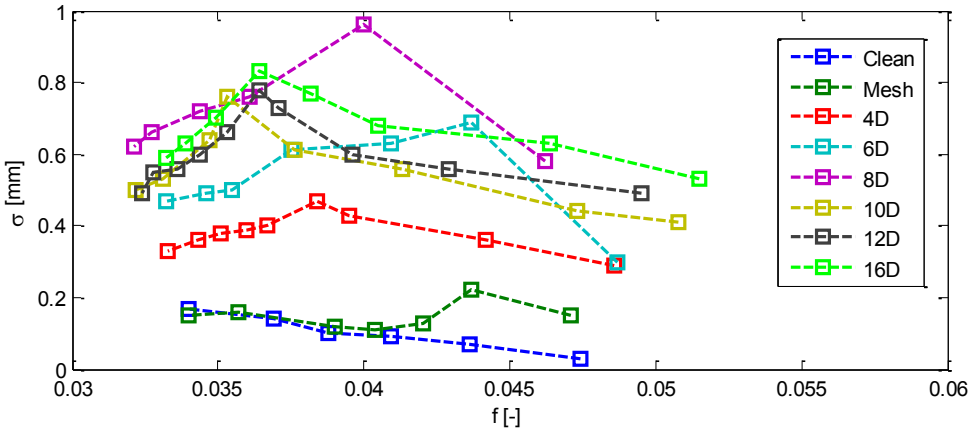

Figure 4.45 Wave STD height to roughness ratio as a function of friction factor.

Form the above it can be concluded that the height of wave standard deviation is dependent up on the roughness condition (pattern) of the pipe bed. As such, in further figures, the pipe bed conditions with distinct roughness (Mesh, 4D, 6D, 8D, 10D, 12D and 16D) will only be considered.

Figure 4.46 demonstrates a power relation between the wave STD height and the flow depth to streamwise spacing between roughness (L_s) ratio for the rough pipe conditions. The streamwise spacing between roughness elements is

expressed in mm (see Table 4.1), it was chosen as it is a simple method to account for pipe bed roughness pattern.

$$\sigma = \left(0.36\frac{h}{L_s}\right)^{-\frac{1}{2}} \tag{4.29}$$

The relation shown in Figure 4.46 can be expressed as shown in equation (4.29), which has a fit R^2 = 0.77. From Figure 4.46 it can be seen that the wave STD height decreases with increase in flow depth to roughness element streamwise separation ratio.

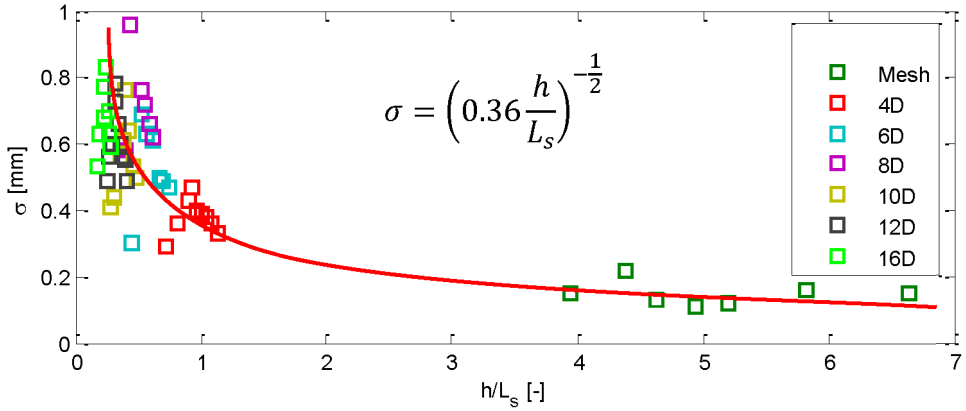

Figure 4.46 Wave STD height as a function of flow depth to roughness streamwise spacing ratio for rough pipe conditions, with R^2 = 0.77.

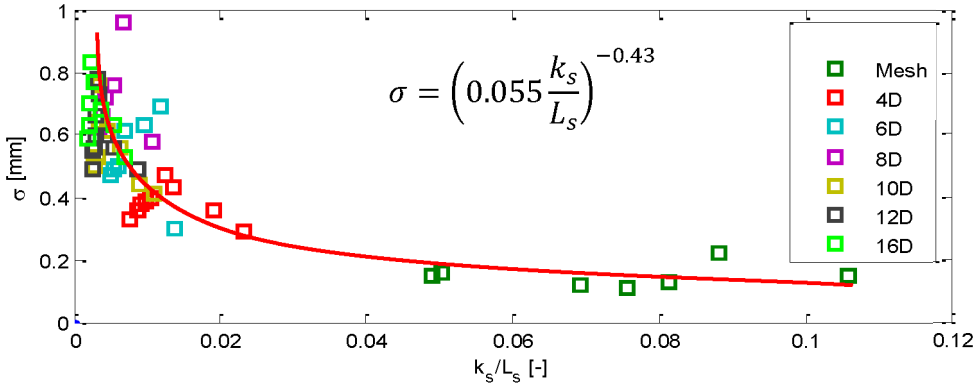

Figure 4.47 Wave STD height as a function of hydraulic roughness to roughness streamwise spacing ratio for rough pipe conditions, with R^2 = 0.78.

Figure 4.47 demonstrates a power relation between the wave STD height and hydraulic roughness to streamwise spacing between roughness (L_s) ratio for the

rough pipe conditions. The trend observed in figure 4.47 is similar to that in Figure 4.46. Which can be expressed as per equation (4.30) with R^2 = 0.78.

$$\sigma = \left(0.055\frac{k_s}{L_s}\right)^{-0.43} \quad \textbf{(4.30)}$$

Figure 4.47 shows that the wave STD height decreases with increase in hydraulic roughness to roughness element separation ratio.

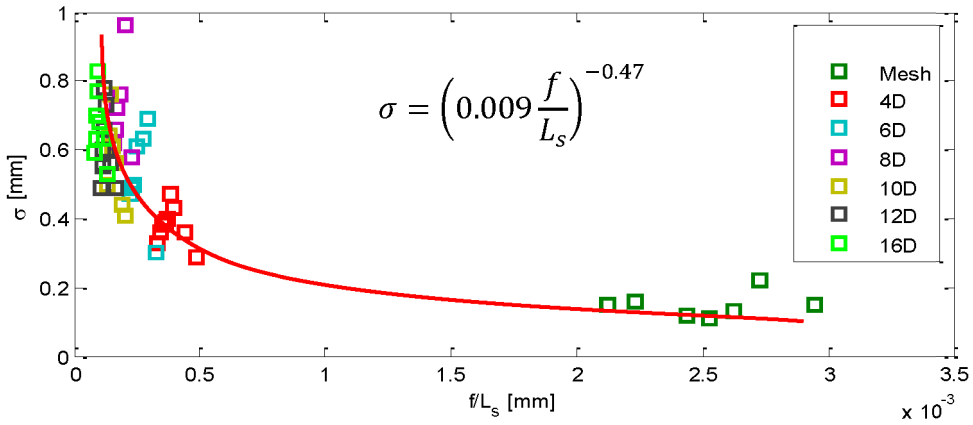

Figure 4.48 Wave STD height as a function of friction factor to roughness streamwise spacing ratio for rough pipe conditions, with R^2 = 0.84.

Further, Figure 4.48 shows a power relation, similar to those as in Figures 4.46 and 4.47, between wave STD height and friction factor to streamwise spacing between roughness elements ratio.

$$\sigma = \left(0.009\frac{f}{L_s}\right)^{-0.47} \quad \textbf{(4.31)}$$

Equation (4.31) shows an expression for data in Figure 4.48 with R^2 = 0.84.

Considering the above it can be concluded that wave standard deviation height for rough pipe bed conditions is dependent in combination up on the parameters of flow depth, hydraulic roughness, friction factor and also velocity. As such, a non-dimensional relation of wave STD to flow factors can be proposed.

Figure 4.49 shows the dependence of the dimensionless ratio of shear velocity to velocity multiplied by flow depth to roughness separation as a function of wave STD height.

$$\frac{s_V}{V} * \frac{h}{L_s} = 0.0093\sigma^{-1.6} \qquad \textbf{(4.32)}$$

For this data, the power expression (equation 4.32) has a fit of R^2 = 0.80. From Figure (4.49) it is seen that the dimensionless parameter decreases with increasing wave standard deviation height.

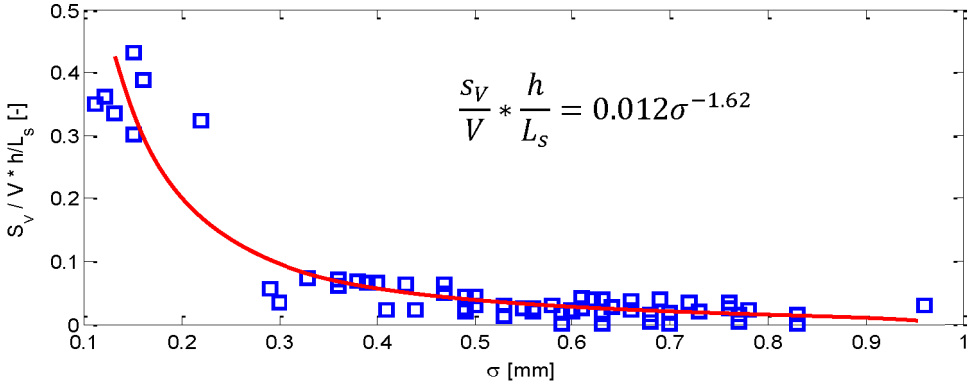

Figure 4.49 Shear velocity to velocity ratio multiplied by flow depth to roughness separation ratio as a function of wave STD for rough pipe conditions, with R^2 = 0.80.

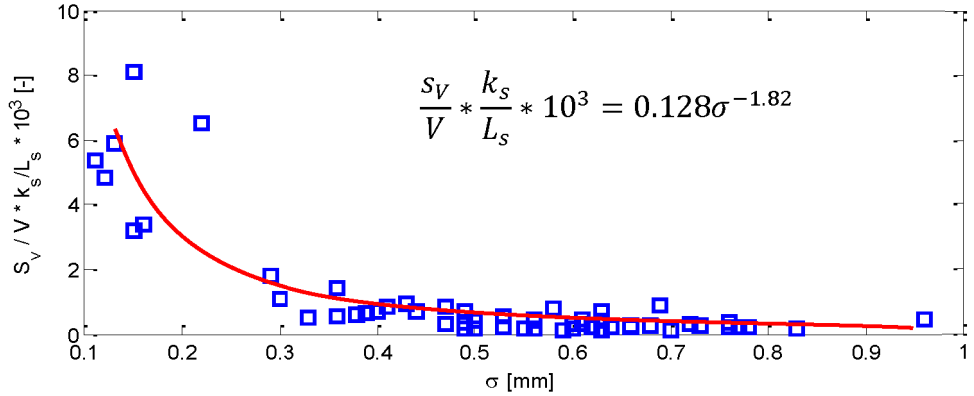

Figure 4.50 Dimensionless ratio of shear velocity to velocity multiplied by roughness to roughness separation as a function of wave STD height for rough pipe conditions, with R^2 = 0.75.

Figure 4.50 demonstrates similar trend to that in Figure 4.49. However, this power relation has a fit of only R^2 = 0.75 and can be expressed as:

$$\frac{s_V}{V} * \frac{k_s}{L_s} * 10^3 = 0.0001\sigma^{-1.82} \quad \textbf{(4.33)}$$

For a better fit, a non-dimensional expression between ratio of shear velocity to velocity multiplied by friction factor to roughness separation divided by roughness diameter (for the mesh the sum of mesh grid side width, 16mm, was used) as a function of wave STD height to hydraulic roughness ratio (Figure 4.51) can be characterised as shown in equation (4.34) with a fit of R^2 = 0.81.

$$\frac{s_V}{V} * \frac{f}{(L_s/\mathrm{D})} * 10^3 = 0.124\sigma^{-1.54} \quad \textbf{(4.34)}$$

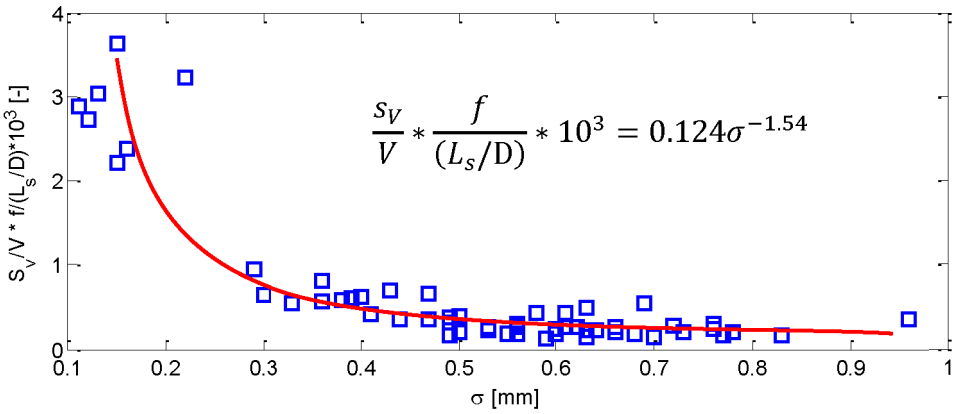

Figure 4.51 Dimensionless ratio of shear velocity to velocity multiplied by friction factor to roughness separation as a function of wave STD height for rough pipe conditions, with R^2 = 0.81.

The relations illustrated in Figures 4.49 and 4.51 indicate that the for the rough pipe conditions (considered in the experimental range of this study) the information of the wave STD height could be a good indicator of roughness element spacing in a repetitive hexagonal pattern. The following section (section 4.8) will reveal the method of non-invasive acoustic detection of water surface wave standard deviation height.

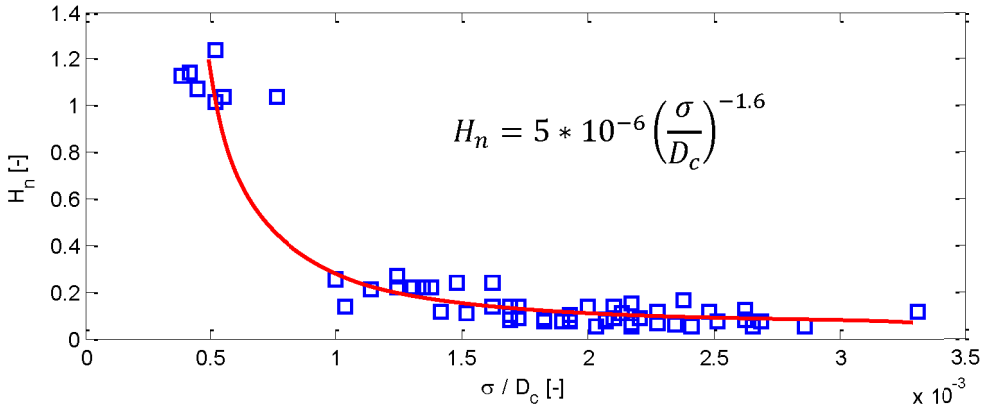

Figure 4.52 Dimensionless hydraulic parameter as a function of wave STD height to pipe diameter ratio to for rough pipe conditions, with R^2 = 0.85.

Considering the results presented in Figures 4.49 and 4.51 a general relation between a dimensionless hydraulic parameter (H_n), which corresponds to the governing pipe flow parameters and the roughness element separation (equation 4.35), and the wave roughness height normalised by pipe diameter was proposed (equation 4.36).

$$H_n = \left(\frac{s_V}{V} * \frac{k_s}{L_s} * \frac{Re}{f}\right)/10^3 \quad \textbf{(4.35)}$$

$$H_n = 0.124\left(\frac{\sigma}{D_c}\right)^{-1.6} \quad \textbf{(4.36)}$$

Figure 4.52 demonstrates a down sloping power relation expressed in equation (4.36) which has a fit of R^2 = 0.85. The dimensionless hydraulic parameter was developed to depend upon shear velocity, velocity, hydraulic roughness, Reynolds number, friction factor and roughness element separation, so that the parameter would be unique for a given flow regime and roughness condition. Such that the relation presented in equation (4.36) could be applicable for a wide range of problems outside the experimental range reported in this section.

4.8 Acoustic detection of surface waves

Together with the wave probe analysis for different pipe conditions, the analysis of the recorded acoustic signal was performed.

After the series of preliminary tests, the Gaussian shape pulse of 315Hz and the continuous sinusoidal sine wave of 500Hz were shown to have the best sensitivity to the pipe surface water variations. This choice of frequencies is not accidental. At frequencies below these, the acoustic wavelength is too large. As a result, the ratio of the wavelength to the roughness height STD is too small to have a measurable effect. At frequencies higher than these, the acoustic field in the pipe becomes modal (see section 4.4.3) and highly sensitive to the flow depth in the pipe. In these conditions case, the effect of flow depth becomes similar or greater than that of the water surface roughness.

Therefore, the adopted frequencies provide a reasonable compromise between the sensitivity of the proposed acoustic method and the complexity for data interpretation required in the case when the acoustic field in the pipe becomes modal. The detailed acoustic analysis is presented in section 4.2.3. In this final section, the obtained acoustic data is related to water surface wave probe data for the same pipe conditions.

Table 4.7 presents the obtained acoustic data, for all experiments, considered to be most relevant in detecting water surface fluctuations. In the Table 4.7, first and second columns list the experiment number and pipe bed condition, respectively, as per Table 4.6. Further, mean flow depth and normalised by pipe geometry the wave standard deviation parameter, i.e. wave standard deviation

multiplied by a ratio of flow depth to flow surface width in pipe's cross-section (L_w), $[\sigma]^* = \sigma(h/L_w)$ is shown. This was done so that the water surface wave STD can be comparable between pipes of different flow depths and diameters. The above is followed by $\langle g \rangle$, which is the mean absolute pulse tail peak relative pressure (normalised by the maximum pressure as calculated from equation 4.11), and same value normalised by pipe geometry, $[\langle g \rangle]^{**} = \langle g \rangle (L_w/P_a)$, where P_a is the dry perimeter of air in pipe's cross-section. Next column shows the pulse average value of the maxima in the correlation function between 6 microphones pairs (CF), which is followed by the normalised correlation function, $[CF]^{**} = CF(L_w/P_a)$. Then a standard deviation of the maximum of the correlation function of 6 microphone pairs is presented as σ_{CF}, followed by the normalised standard deviation in the correlation function, $[\sigma_{CF}]^{**} = \sigma_{CF}(L_w/P_a)$. Next columns shows the mean amplitude in the envelope of the continuous sine wave (s), followed by its normalised value $[s]^{**} = s(L_w/P_a)$. Next to the last column shows the STD of continuous sinusoidal wave envelope (σ_s, which was calculated using equation 4.21). The last column presents the normalized values of the standard deviation in the continuous wave envelope $[\sigma_s]^{***} = \sigma_s(A_a/A_p)$, where A_p is the dry cross-sectional area of the partially filled pipe and A_a is the cross-section of the pipe. The above acoustic quantities were normalised by the available air gap in the pipe due to pipe and flow geometry in pipe's cross-section. This was done as the acoustic signal amplitude is sensitive to the dry area in the pipe in which the acoustic signal is emitted by the speaker and propagates to the receiver. This normalisation allows to account for the difference in the cross-sectional area of the pipe in the experiments with the variable flow depth, that could in principle be applied to pipes of different diameters with different internal conditions.

Table 4.7 Measured acoustic parameters and ratios for all experiments.

No.	RC	h [mm]	$[\sigma]^*$ [mm]	$\langle g \rangle$ 10^2 [-]	$[\langle g \rangle]^{**}$ 10^2 [-]	CF [-]	$[CF]^{**}$ [-]	$[\sigma_{CF}]^{**}$ 10^2 [-]	s 10^2 [V]	$[s]^{**}$ 10^2 [V]	σ_s 10^3 [V]	$[\sigma_s]^{***}$ 10^3 [V]
1	C	52	0.007	19.20	6.47	0.9896	0.33	0.49	65.04	21.92	0.003	0.003
2		62	0.018	20.84	7.85	0.9880	0.37	0.59	70.54	26.57	0.05	0.042
3		70	0.025	21.47	8.71	0.9864	0.40	0.61	73.84	29.95	0.13	0.106
4		79	0.031	22.15	9.65	0.9852	0.43	0.67	74.35	32.39	0.23	0.179
5		89	0.047	23.85	11.18	0.9846	0.46	0.77	75.71	35.49	0.23	0.170
6		106	0.065	24.93	13.00	0.9826	0.51	0.90	85.9	44.79	0.35	0.235
7	M	63	0.039	19.77	7.54	0.9895	0.38	0.56	68.94	26.30	0.07	0.059
8		70	0.062	21.21	8.58	0.9874	0.40	0.54	70.81	28.63	0.15	0.122
9		74	0.038	21.64	9.08	0.9859	0.41	0.58	72.21	30.29	0.07	0.056
10		79	0.034	21.83	9.52	0.9838	0.43	0.61	74.02	32.29	0.06	0.047
11		83	0.038	22.49	10.13	0.9828	0.44	0.58	75.26	33.91	0.11	0.084
12		93	0.055	22.84	10.99	0.9808	0.47	0.68	79.33	38.16	0.27	0.196
13		106	0.057	24.52	12.83	0.9782	0.51	0.77	87.89	45.99	0.41	0.274
14	4D	72	0.083	20.38	8.39	0.9901	0.41	0.68	74.19	30.55	0.51	0.411
15		81	0.112	21.86	9.67	0.9886	0.44	0.83	74.5	32.96	0.78	0.602
16		90	0.144	22.18	10.47	0.9876	0.47	1.02	79.52	37.54	1.89	1.390
17		93	0.161	23.85	11.49	0.9836	0.47	0.99	82.83	39.91	1.98	1.432
18		97	0.142	24.16	11.95	0.9829	0.49	1.10	83.19	41.14	1.71	1.209
19		100	0.141	24.97	12.58	0.9820	0.49	1.29	85.87	43.27	1.61	1.118
20		104	0.142	25.52	13.18	0.9805	0.51	1.13	87.99	45.44	1.54	1.043
21		108	0.139	26.13	13.81	0.9788	0.52	1.15	89.09	47.10	1.50	0.991
22		113	0.132	26.51	14.42	0.9779	0.53	1.22	91.02	49.50	1.10	0.703
23	6D	66	0.081	21.05	8.23	0.9877	0.39	0.90	72.45	28.31	0.49	0.406
24		79	0.211	22.50	9.83	0.9857	0.43	1.23	77.65	33.94	3.63	2.824
25		84	0.201	22.77	10.31	0.9855	0.45	1.25	79.37	35.92	3.82	2.901
26		91	0.206	23.89	11.33	0.9847	0.47	1.28	82.39	39.09	4.59	3.363
27		99	0.180	24.63	12.34	0.9831	0.49	1.32	86.45	43.31	3.43	2.395
28		104	0.183	25.41	13.10	0.9827	0.51	1.32	88.26	45.49	3.47	2.356
29		112	0.186	26.15	14.14	0.9807	0.53	1.36	91.89	49.68	3.54	2.279
30	8D	77	0.174	21.11	9.06	0.9891	0.42	1.07	74.23	31.84	3.79	2.984
31		86	0.312	21.51	9.87	0.9880	0.45	1.11	80.27	36.85	8.96	6.735
32		103	0.282	23.41	12.02	0.9863	0.51	1.41	83.02	42.61	5.86	3.995
33		109	0.279	24.67	13.12	0.9859	0.52	1.28	84.63	45.00	5.22	3.427
34		118	0.273	25.59	14.30	0.9847	0.55	1.52	88.72	49.58	4.76	2.941
35		122	0.264	26.77	15.28	0.9838	0.56	1.37	92.15	52.59	4.56	2.739
36	10D	71	0.117	21.38	8.75	0.9881	0.40	0.83	72.13	29.53	0.81	0.655
37		76	0.131	21.81	9.24	0.9862	0.42	0.90	72.4	30.69	1.14	0.904
38		87	0.183	22.46	10.36	0.9853	0.45	0.94	77.4	35.71	2.14	1.603
39		94	0.211	23.68	11.48	0.9836	0.48	1.03	80.72	39.13	3.77	2.713
40		99	0.273	23.97	12.04	0.9831	0.49	1.17	82.76	41.56	5.79	4.034
41		105	0.241	24.91	12.91	0.9816	0.51	1.28	85.49	44.30	4.20	2.836
42		114	0.213	26.16	14.33	0.9802	0.54	1.28	91.7	50.23	4.02	2.548
43		120	0.210	27.37	15.45	0.9795	0.55	1.21	92.86	52.43	3.37	2.054
44	12D	74	0.143	21.29	8.92	0.9912	0.42	1.05	74.91	31.39	0.67	0.535
45		80	0.173	21.61	9.49	0.9894	0.43	0.96	72.95	32.03	2.01	1.559
46		88	0.198	21.93	10.21	0.9881	0.46	0.92	75.64	35.22	2.42	1.800
47		95	0.255	22.49	10.95	0.9867	0.48	1.07	78.32	38.13	2.97	2.129
48		97	0.276	22.90	11.34	0.9866	0.49	1.19	80.08	39.66	4.26	3.007
49		101	0.241	23.51	11.92	0.9860	0.50	1.30	81.93	41.55	3.38	2.332
50		107	0.229	24.57	12.94	0.9847	0.52	1.33	84.28	44.38	3.17	2.104
51		111	0.220	24.89	13.40	0.9846	0.53	1.17	86.58	46.62	4.42	2.860
52		118	0.228	25.97	14.53	0.9840	0.55	1.19	89.65	50.14	3.78	2.333
53		124	0.212	26.81	15.43	0.9845	0.57	1.20	92.62	53.29	4.37	2.594

No.	RC	h [mm]	$[\sigma]^*$ [mm]	$\langle g \rangle$ 10^2 [-]	$[\langle g \rangle]^{**}$ 10^2 [-]	CF [-]	$[CF]^{**}$ [-]	$[\sigma_{CF}]^{**}$ 10^2 [-]	s 10^2 [V]	$[s]^{**}$ 10^2 [V]	σ_s 10^3 [V]	$[\sigma_s]^{***}$ 10^3 [V]
54	16D	71	0.151	20.55	8.36	0.9893	0.40	0.93	72.05	29.32	0.97	0.787
55		77	0.189	21.05	9.04	0.9885	0.42	1.00	73.25	31.47	2.39	1.880
56		86	0.221	22.13	10.17	0.9870	0.45	1.10	77.51	35.62	4.09	3.072
57		89	0.256	22.85	10.75	0.9871	0.46	1.16	78.98	37.15	4.87	3.593
58		94	0.287	23.56	11.46	0.9867	0.48	1.17	81.77	39.76	6.14	4.406
59		103	0.260	24.61	12.61	0.9861	0.51	1.31	85.79	43.95	5.56	3.799
60		108	0.243	25.26	13.36	0.9852	0.52	1.36	88.61	46.88	4.12	2.720
61		111	0.232	25.73	13.86	0.9854	0.53	1.38	90.53	48.78	4.72	3.052

Second row in the table heading shows the multiplication value for the data (next to the data units), which is not shown in according figure labels and equations.

Below are presented the relations between the acoustic parameters (from Table 4.7) plotted as a function of hydraulic parameters (presented in Table 4.6). First the results for the pulse signal will be shown.

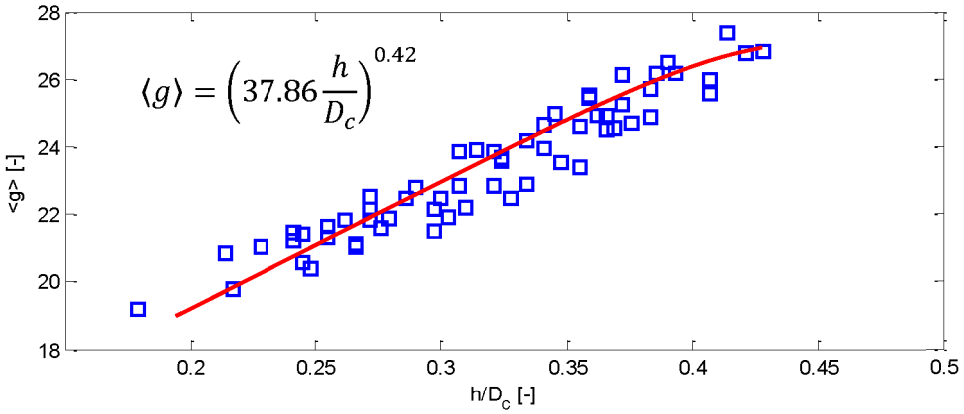

Figure 4.53 Mean pulse tail relative pressure between all microphones as a function of flow depth to pipe diameter ratio for all experiments, with R^2 = 0.90.

Figure 4.53 demonstrates a power relationship between mean pulse tail relative pressure and flow depth to pipe diameter ratio, with a fit of R^2 = 0.90. This indicates that with the increase in flow depth the received pulse relative amplitude also increases, which is expected as the same amount of sound energy propagates through a space with decreased area. The above relation can be expressed as:

$$\langle g \rangle = \left(37.86 \frac{h}{D_c}\right)^{0.42} \quad \textbf{(4.37)}$$

where from the pulse amplitude the flow depth can be easily obtained, given that the pipe diameter is known. The flow depth was divided by the pipe diameter to get an expression suitable for a range of pipe diameters with different water flow depths.

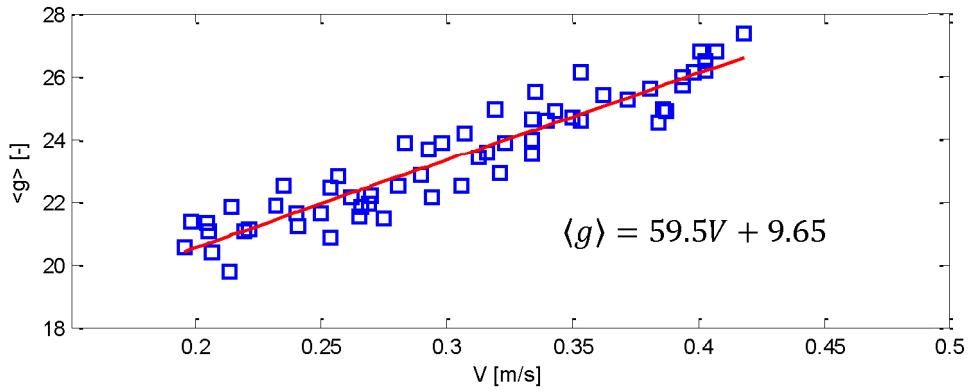

Figure 4.54 Mean pulse tail relative pressure between all microphones as a function of mean flow velocity for all experiments, with R^2 = 0.91.

Figure 4.54 shows a linear relation (equation 4.38) between the mean pulse tail relative pressure and time-averaged mean flow velocity, with fit of R^2 = 0.91.

$$\langle g \rangle = 59.5V + 9.65 \qquad \textbf{(4.38)}$$

This equation (4.38) enables of obtaining acoustically an approximate value of mean water flow velocity.

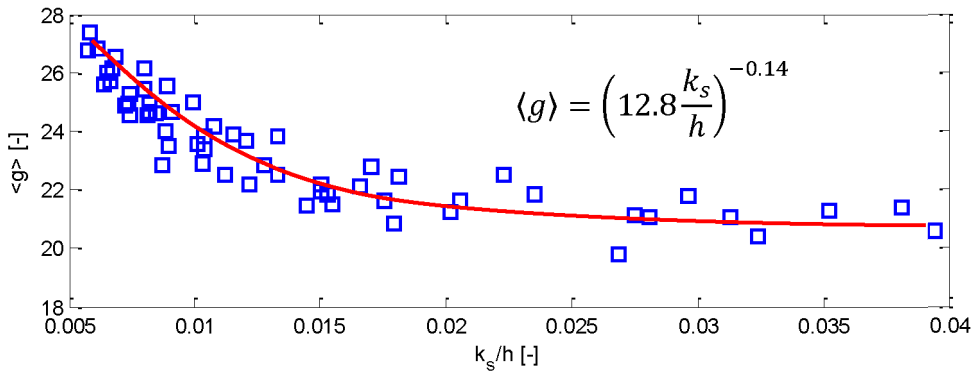

Figure 4.55 Mean pulse tail relative pressure between all microphones as a function of hydraulic roughness to flow depth ratio for all experiments, with R^2 = 0.82.

Figure 4.55 shows a power relation between the mean pulse tail relative pressure and hydraulic roughness to flow depth ratio, with fit of R^2 = 0.82, that can be approximated with the following expression:

$$\langle g \rangle = \left(12.8\frac{k_s}{h}\right)^{-0.14} \quad \textbf{(4.39)}$$

This demonstrates that from the pulse data a relative to flow depth value of hydraulic roughness can be calculated.

A better approximation for estimating the hydraulic roughness from acoustics can be achieved, if the mean pulse tail relative pressure is normalised by the ratio of water surface width (L_w) to dry perimeter of air (P_a) both in pipes cross-section ($[\langle g \rangle]^{**}$), which is shown in Figure 4.56.

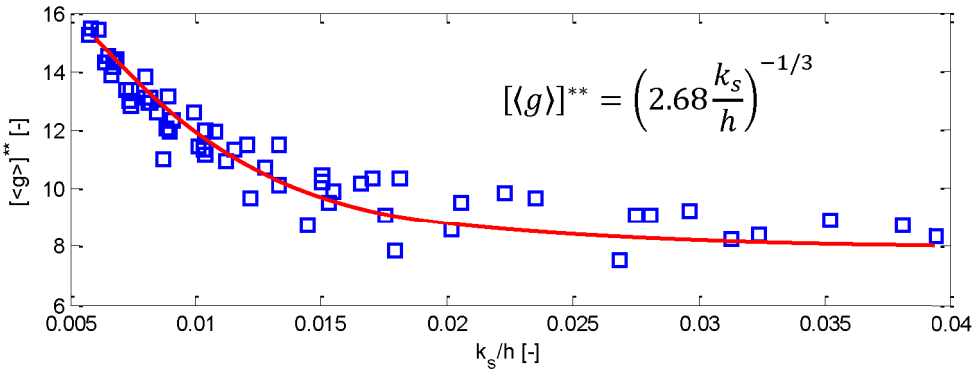

Figure 4.56 Pulse tail mean relative pressure between all microphones normalised by pipe geometry as a function of hydraulic roughness to flow depth ratio for all experiments, with R^2 = 0.85.

Here the normalisation parameters L_w and P_a can be calculated using the values of pipe diameter and flow depth, where the last can be acoustically found from equation (4.37). The obtained improved empirical relation has an attractive fit of R^2 = 0.85, and can be expressed as:

$$[\langle g \rangle]^{**} = \left(2.68\frac{k_s}{h}\right)^{-1/3} \quad \textbf{(4.40)}$$

which is an inverse power equation, where the increase in hydraulic roughness to flow depth ratio causes the normalised pulse power amplitude to decrease. This is an important finding which enables in few simple steps to be used to obtain the overall hydraulic roughness of the pipe via acoustic measurement.

From the above it can be concluded that the mean pulse tail relative roughness (either normalised by pipe and flow geometry or not) may be used to non-invasively estimate the flow depth, mean flow velocity and pipe hydraulic roughness. Although, to estimate the water surface wave fluctuation statistics a standard deviation of the pulse tail peak should be considered.

Figure 4.57 illustrates a relation between the normalised STD of the pulse maximum mean correlation function and normalised surface wave mean STD. These data shows that the standard deviation in the correlation coefficient increases with the increased value of the effective surface roughness.

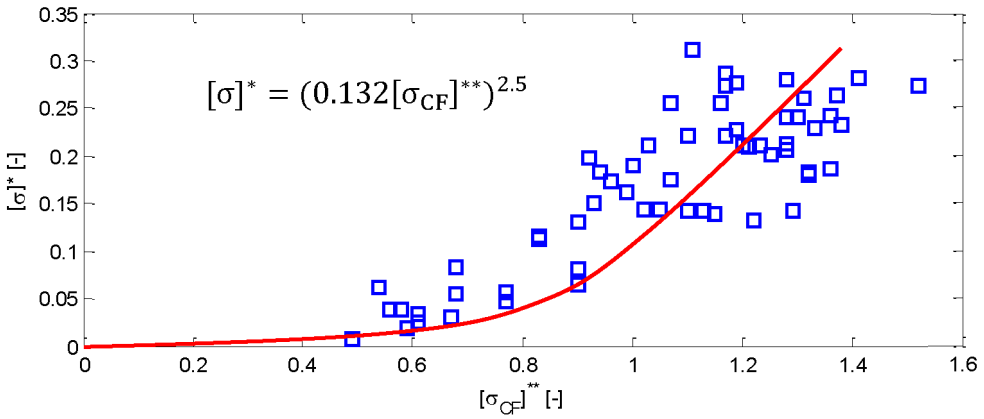

Figure 4.57 Surface waves mean standard deviation normalised by pipe geometry as a function of normalised standard deviation of pulse tail peak maximum mean correlation function for all experiments, with R^2 = 0.80.

This finding makes good physical sense as it suggests that the fluctuation in the acoustic pulse is greater for greater values of σ^* and L_w. As the level of water in the pipe increases, the width of the free, rough boundary increases as well. For a given value of the mean wave roughness height, a wider free boundary will result in a stronger scattering of the acoustic wave. For a given flow depth, the higher value of $[\sigma]^*$ will also result in a stronger scattering of the acoustic signal as there would be stronger interaction between the incident acoustic wave and the rough water surface interface.

The data shown in Figure 4.57 can be used to derive an approximate relation, with R^2 = 0.80 between the intensity in the scattered acoustic wave and the mean wave roughness height (equation 4.41).

$$[\sigma]^* = (0.132[\sigma_{CF}]^{**})^{2.5} \quad \textbf{(4.41)}$$

The above relationship accuracy could be related to the fact that the pulse readings were taken every 2 seconds and that had eliminated the pulse from detecting the full range of water perturbations during experiment times (it should be considered here that the water surface experiments have revealed that the water flow in a pipe is a non-stationary process). This means that the pulse readings were short time-dependent selections of water surface fluctuations. However, the above demonstrates that in general the pulse MAX mean CF is sensible to pipe's hydraulic changes with regards to water surface.

The relationship between the continuous sine wave envelope parameters (from Table 4.7) plotted as a function of hydraulic parameters (shown in Table 4.6) are presented in the following sections.

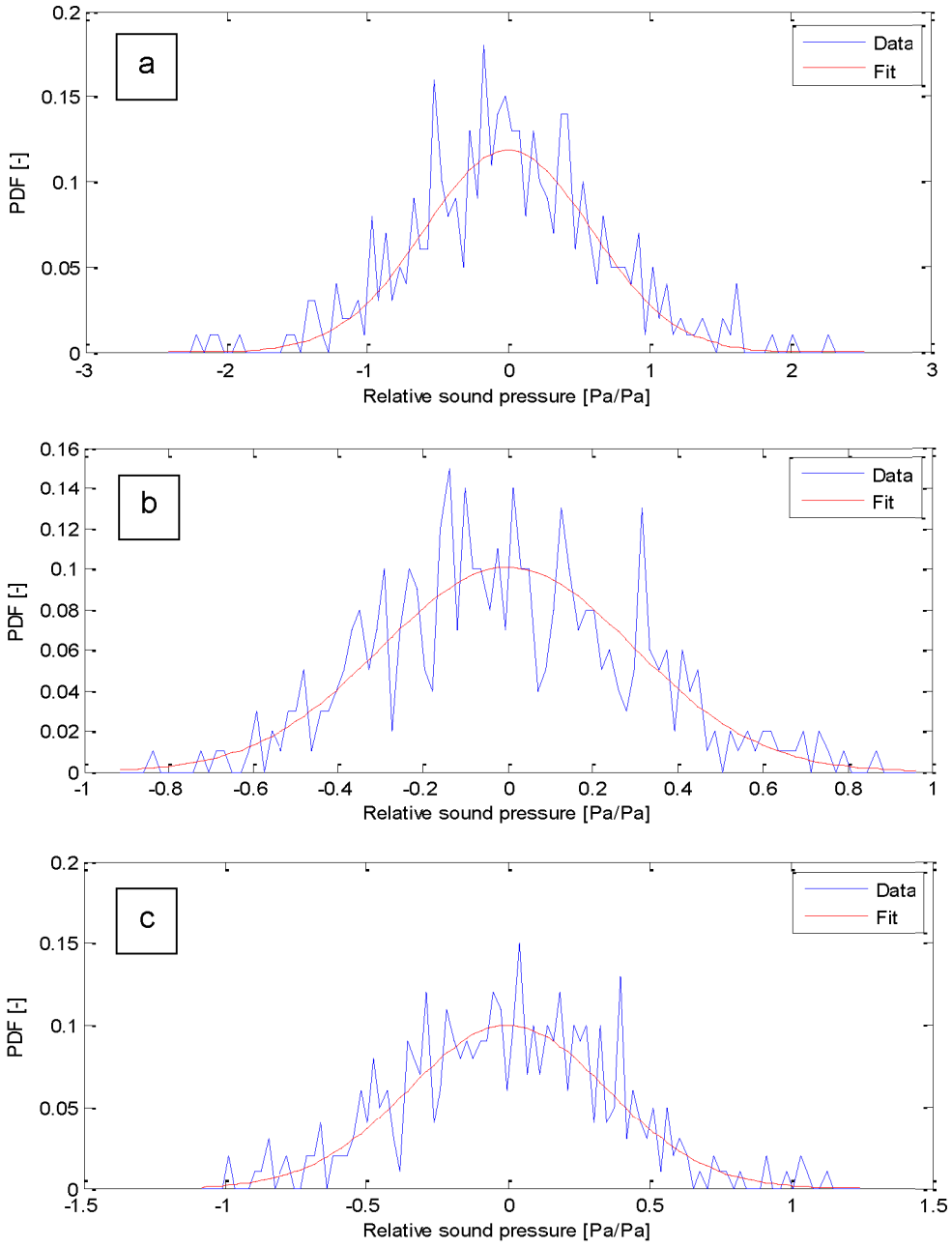

Figure 4.58 Gaussian distribution for the continuous sine wave envelope, mean of all microphones, for clean pipe at 0.183m/s and h = 62mm (a), pipe with mesh at 0.178m/s and h = 63mm (b) and pipe with 6D spheres arrangement at 0.176m/s and h = 66mm (c).

As it was confirmed that the water surface wave standard deviation has a Gaussian distribution (equation 4.29), the same check was undertaken for the acoustic amplitude envelope of the continuous sine wave. Figure 4.58 illustrates that the probability density function (PDF) for the continuous sound wave envelope is close to Gaussian distribution. These figures present the average results calculated by averaging the envelopes recorded on all the four

microphones. The hydraulic regimes for which the data is presented were: clean pipe with flow velocity of 0.183m/s, pipe with mesh with flow velocity of 0.178m/s and pipe with 6D spheres arrangement and flow velocity of 0.176m/s. Figure 4.58 clearly demonstrates that the distribution of the sine wave envelope relative sound pressure can be approximated with the Gaussian distribution for a range of the pipe conditions.

Figure 4.59 shows the linear relationship between the standard deviation values of the continuous sine wave envelope obtained with the PDF and those determined statistically from equation (4.21). The relation of the above has a fit of R^2 = 0.95 and can be expressed as:

$$\sigma_s(PDF) = 1.76\sigma_s - 0.02 \quad \textbf{(4.42)}$$

This assumption enables us to assign a mathematical model that can predict the sound pressure fluctuations, however this activity is not covered in this work, but may be considered in future.

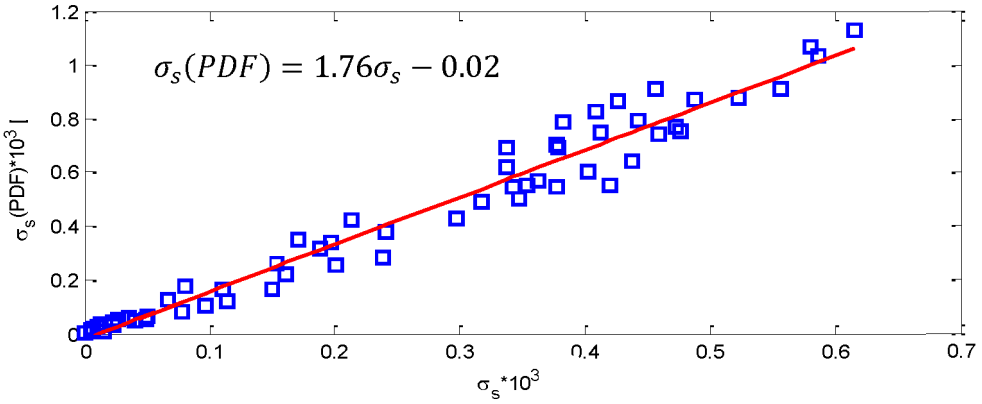

Figure 4.59 Gaussian distribution for the continuous sine wave envelope as a function of relative sound pressure standard deviation, with R^2 = 0.95.

Figure 4.60 demonstrates a power relation between the mean amplitude in the continuous sine wave and flow depth to pipe diameter ratio, which has a fit of R^2 = 0.92. This relation can be approximated by the following equation:

$$s = \left(134\frac{h}{D_c}\right)^{0.44} \quad \textbf{(4.43)}$$

Same as per pulse relative pressure (Figure 4.53), the continuous wave envelope relative amplitude increases with the increase in flow depth as the sound propagates through a duct of smaller area.

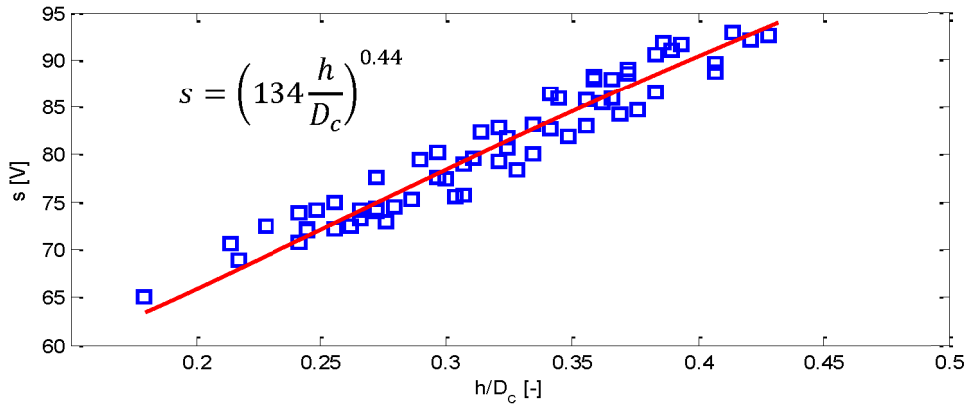

Figure 4.60 Continuous sine wave mean relative amplitude between all microphones as a function of flow depth to pipe diameter ratio for all experiments, with R^2 = 0.92.

The above result is expected, as the relative change in sound pressure wave envelope (s) is also linked to the variation of dry cross-sectional area of the pipe (A_a). This is achieved by assuming that the force attained by the speaker (F_s) is constant in all studied regimes. To maintain the displacement of air in the pipe the force $A_a p_{n_i}$ should be applied that gives:

$$F_s = \mathrm{A}_{a,n_i} p_{n_i} \quad \textbf{(4.44)}$$

where p_{n_i} is the measured acoustic pressure in the dry area of pipe and index n_i refers to the number of flow regime in Table 4.7. The dry cross-sectional area is defined by the radius of pipe (r) and the mean water depth (h) that results in:

$$\mathrm{A}_a = \pi r^2 \left\{1 - \frac{1}{\pi}\left[\cos^{-1}\frac{r-h}{r} - \frac{1}{2}\sin\left(2\cos^{-1}\frac{r-h}{r}\right)\right]\right\} \quad \textbf{(4.45)}$$

By assuming that the mean water depth is relatively close to the radius of the pipe, i.e. $\frac{r-h}{r} \ll 1$, the cross-sectional area of the dry pipe can be simplified to:

$$\mathrm{A}_a \approx \pi r^2 \left[\frac{1}{2} + \frac{2}{\pi}\left(\frac{r-h}{r}\right) - \frac{1}{3\pi}\left(\frac{r-h}{r}\right)^3\right]$$
$$= \pi r^2 \left(\frac{1}{2} + \frac{5}{3\pi}\right) - hr\left(1 + \frac{h}{r} - \frac{h^2}{3r^2}\right) \quad \textbf{(4.46)}$$

By relating the change in sound pressure with the first flow regime, second Newton's law shown in equation (4.44) can be employed to derive:

$$\frac{\mathrm{s}_{,n_i}}{\mathrm{s}_{,1}} = \frac{\mathrm{A}_{a,1}}{A_{a,n_i}} \quad \textbf{(4.47)}$$

where wave envelope is related to the acoustic pressure as:

$$s_{,n_i} = |p_{n_i}| \quad \textbf{(4.48)}$$

Hence, as it is observed in Figure 4.60, the relative increase in wave envelopes depends on flow depth that is consistent with the approximated cross-sectional area obtained in equation (4.46).

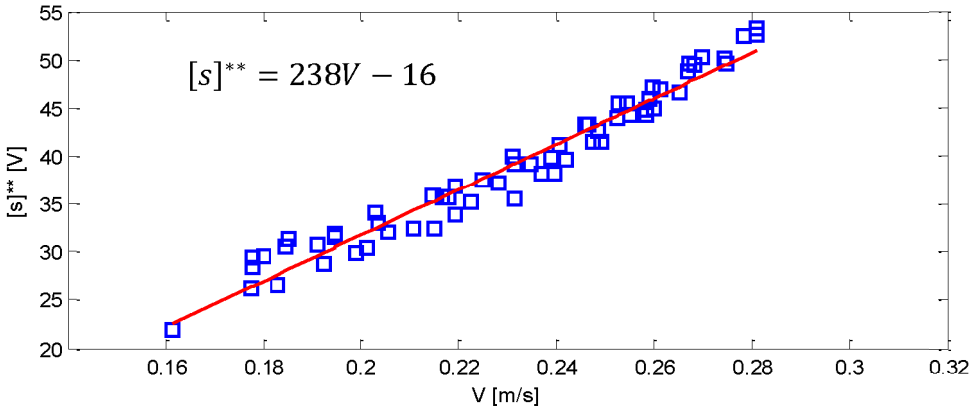

Figure 4.61 Continuous sine wave mean relative amplitude between all microphones normalised by pipe geometry as a function of mean flow velocity for experiments with distinct roughness, with R^2 = 0.96.

Figure 4.61 presents an attractive linear relation between the normalised by pipe geometry continuous wave envelope mean relative amplitude and mean flow velocity for experiments with distinct roughness, with fit of R^2 = 0.96, that can be expressed as:

$$[s]^{**} = 238V - 16 \quad \textbf{(4.49)}$$

The above suggest that after the flow depth value was acoustically obtained from equation (4.43), the wave envelope relative pressure can be normalised and the mean flow velocity can be calculated using equation (4.49).

In Figure 4.62 and onwards the relations for experiments with distinct roughness will be only used, as it was confirmed in section 4.6 that the hydraulic pattern for the clean pipe is different from those with distinct roughness. Unlike the pulse signal, the continuous wave signal was found to be more sensible to the changes in the hydraulic and physical parameters of the tested flow regimes.

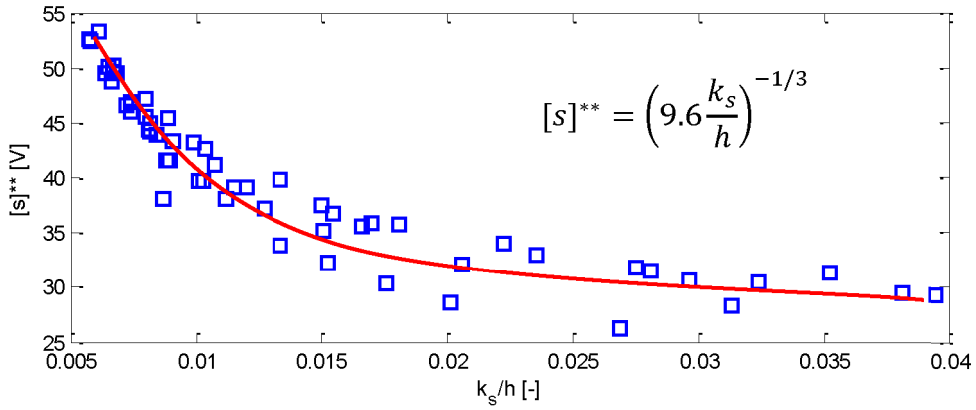

Figure 4.62 Continuous sine wave mean relative amplitude between all microphones normalised by pipe geometry as a function of hydraulic roughness to flow depth ratio for experiments with distinct roughness, with R^2 = 0.90.

Figure 4.62 presents a down-sloping power relation between the normalised by pipe geometry continuous wave envelope mean relative amplitude and hydraulic roughness to flow depth ratio.

$$[s]^{**} = \left(9.6\frac{k_s}{h}\right)^{-1/3} \quad \textbf{(4.50)}$$

Relation in Figure 4.62 that can be expressed as shown in equation (4.50) which has a fit of R^2 = 0.90. It should be noted that just for the roughness with spheres this relation has a fit of R^2 = 0.95, with $[s]^{**} = 10.44k_s/h^{-0.3}$.

Figure 4.63 demonstrates the relation between the normalised standard deviation in the acoustic wave envelope and the normalized RMS wave height. Similarly, to the result obtained in the case of the impulsive acoustic excitation (see Figure 4.57), the fluctuations in the acoustic wave envelope increase with the increased value of $[\sigma]^*$ (Figure 4.63).

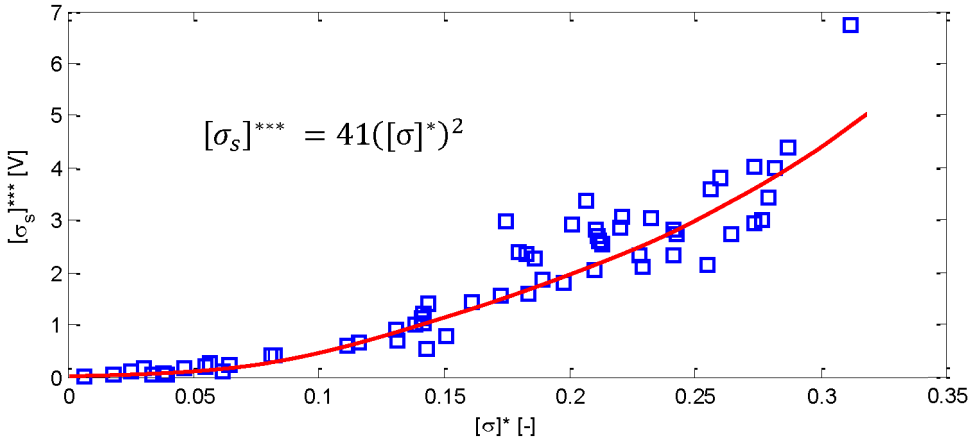

Figure 4.63 Continuous sinusoidal wave envelope standard deviation normalised by pipe geometry as a function of normalised surface waves mean standard deviation for experiments with distinct roughness, with R^2 = 0.96.

It is suggested in (Morse and Ingard 1968, p.512) that the change in the acoustic pressure in the fundamental mode in a circular pipe is directly proportional to the change in the wall admittance (β), i.e:

$$\Psi_{00} \propto \beta \tag{4.51}$$

Bass and Fuks (1979) suggested that the effective impedance of a rigid, rough boundary is expressed as:

$$\beta \propto k\sigma^2 \tag{4.52}$$

i.e. that the amplitude of the observed fluctuations in the wave envelope should be proportional to the squared wave roughness height. Here k is the wavenumber in air. The analysis of the behavior of the standard deviation in the acoustic wave envelope suggests that it can be fitted closely, R^2 = 0.96, with the following approximation:

$$[\sigma_s]^{***} = 41([\sigma]^{*})^2 \quad \textbf{(4.53)}$$

which contains a quadratic term. The following proposed relation using sinusoidal wave seems more attractive than that obtained using the impulsive method of excitation. It has a good physical sense. Being continuous the sinusoidal wave proactively responds to the instant changes in pipe surface wave variations which are instantly reflected in the acoustic wave envelope. This relation can be explained theoretically using the notion of the effective surface admittance derived in (Morse and Ingard 1968, Attenborough and Taherzadeh 1995).

4.9 Conclusions

The following chapter presented a number of controlled hydraulic and acoustic laboratory experiments conducted at full scale, 290mm diameter perspex pipe with the presence of equally distributed roughness. The roughness was simulated by the use of a plastic square mesh and a systematic arrangement of uniform spheres on the mesh. In total, 8 different pipe wall conditions were examined, including clean pipe, pipe with mesh and six different sphere patterns and flow conditions were used with each wall condition summing to 61 tests all together.

The following work was influenced by the hypothesis that the fluctuations of the water surface are governed by the pipe wall roughness condition. Hence, this theory was tested. The specially designed wave probes were used to measure the water surface fluctuations and wave statistics. Also, a novel acoustic instrumentation was proposed to measure the in-pipe conditions to relate the acoustic statistics to those of the wave probes influenced by hydraulic wall roughness. During this research a number of interesting facts and relations were discovered:

(i) Flow inside the pipe with a free surface under uniform conditions is a non-stationary or cyclo-stationary process;

(ii) Wave peak-to-peak height or amplitude has a positive linear relation with the wave height standard deviation;

(iii) The wave height standard deviation follows the normal Gaussian distribution and can be predicted for shallow water regimes;

(iv) Three different roughness concentration types, ‘k, ‘t’ and ‘d’ may be defined with improved concentration parameter for pipe with mesh and hexagonal sphere arrangement. Although more data is required to validate this finding;

(v) The wave standard deviation as a function of flow depth or velocity demonstrates a deviation in patterns between different pipe bed roughness separation types. Although, for each type, at some critical water depth the wave standard deviation has a pronounced peak;

(vi) Water surface wave standard deviation due to pipe mesh and sphere roughness element separation may be expressed using hydraulic parameters of water depth (equation 4.29), hydraulic roughness

(equation 4.30) and friction factor (equation 4.31) with a R^2 fit of 0.77, 0.78 and 0.84, respectively;

(vii) An empirical relation between water surface wave standard deviation to pipe diameter ratio and dimensionless hydraulic parameter (which depends on shear velocity, velocity, hydraulic roughness, Reynolds number, friction factor and roughness element streamwise separation) was proposed, which has a R^2 fit of 0.85 (equation 4.35);

(viii) Normalised pulse relative amplitude empirical relation to mean flow depth to pipe diameter ratio (equation 4.37), flow velocity (equation 4.38) and hydraulic roughness to pipe flow depth (equation 4.39) with a R^2 fit of 0.90, 0.91 and 0.82 was found, respectively;

(ix) Correlation function for pulse tail can be used to predict standard deviation in the wave height (equation 4.41) with a R^2 fit of 0.80;

(x) The continuous wave envelope standard deviation follows the normal Gaussian distribution;

(xi) Continuous sinusoidal wave envelope amplitude empirical relations to mean flow depth to pipe diameter ratio (equation 4.43), flow velocity (4.49) and hydraulic roughness to flow depth ratio (equation 4.50) with a R^2 fit of 0.92, 0.96 and 0.90 was found, respectively;

(xii) The normalised standard deviation of the continuous sinusoidal wave envelope was found to have a pronounced power relation with the normalised wave standard deviation (equation 4.53) with a close fit of $R^2 = 0.96$.

The above study has confirmed that the hydraulic behavior due to different pipe bed roughness patterns is complex and by far little information is known.

However, non-dimensional relations between the water surface wave standard deviation (considering the flow mean depth, velocity and hydraulic roughness) and the streamwise spacing between the roughness elements (mesh and spheres) was proposed.

Further, a novel acoustic instrumentation was developed which is capable of measuring in-pipe flow depth, mean flow velocity, hydraulic roughness and most importantly wave standard deviation for pipes with uniform free surface flow. A number of simple empirical relations were proposed to conduct the above. As a result, the water surface wave standard deviation obtained from the acoustic data can be substituted in to the equations proposed for the rough pipe conditions and as such the roughness pattern for a given pipe condition may be obtained.

Chapter 5 Field experiments

In the UK the majority of sewer pipe inspections are carried out using conventional CCTV technology (Hao et al. 2012, Rogers et al. 2012). CCTV method provides detailed in-sewer imaging, from which the pipe condition and overall roughness coefficient is estimated via inspection of the collected images. Most conventional methods such as CCTV, laser profiling and Zoom Cameras are slow and expensive as they require the inspection device to move through the pipe. Generally, to cut expenses, companies avoid costly automated sewer analysis software's (RVI by Maverick Inspection 2010) and rely up on operators' visual estimate of sewer roughness condition (Dirksen et al. 2011), which in the UK is performed according to the WRc Manual of Sewer Condition Classification (2004). The current sewer inspection market lacks a reliable method to measure the pipe wall roughness in-situ. This chapter describes the field experiments carried out with acoustic equipment described before. The collected acoustic data was then related to the estimated pipe hydraulic roughness values obtained from CCTV reports for the same pipe sections. As a result, a new acoustic method to detect pipe wall roughness in dry pipe conditions was proposed.

5.1 Acoustic equipment field trials

The acoustic equipment (described in section 3.2) was tested in the field in several live sewers. In these field trials sewer pipes with no or little flow were inspected.

The trials were carried out together with the University of Natural Resources and Life Science (Vienna) and with the support of LINZ AG in Pashing and IKB in Innsbruck (Austria). Sewers of variable construction materials such as clay, PVC and concrete were tested, as well as circular pipes with different diameters from 225 - 400mm were covered. In total 33 sewer sections, or just over 1km of sewers were investigated during the trials.

The recordings of the CCTV data (reports / images / videos), for the sewer sections where the acoustic instrument was tested, was made available by the local water management companies, from which the estimated roughness values of individual pipe sections were obtained using a standard classification method - WRc Manual of Sewer Condition Classification (2004).

5.1.1 Experimental methodology

The acoustic inspection equipment used in the field experiments is described in section 3.2. It consists of an acoustic source and microphones, connected via an adapted coaxial cable and powered from a laptop.

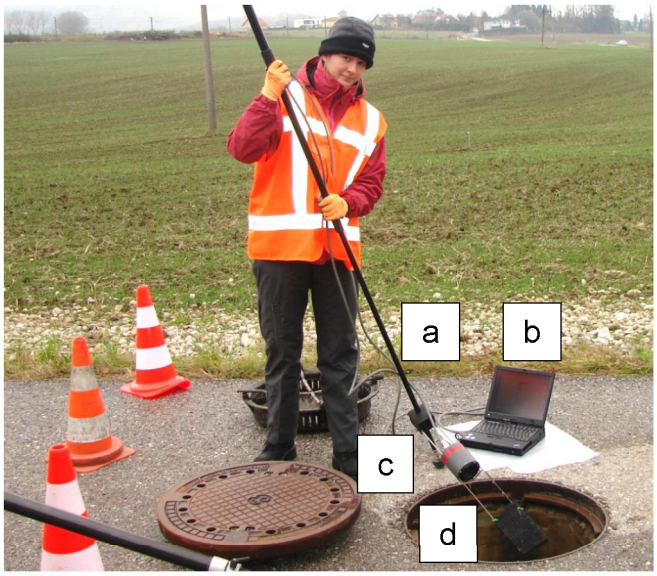

Figure 5.1 Acoustic equipment, which consisted of an extendable pole (a), laptop (b), acoustic sensor with speaker (c) and covered in foam microphones (d).

The acoustic sensor (Figure 5.1c and d) was attached to a telescopic pole (Figure 5.1b) so that the sensor can be lowered in to a manhole chamber. Such pole enables measurement in pipes which are buried up to 5.5m below the ground surface (the majority of pipes were 1 - 3m below the ground surface), with the operator controlling the process from ground level.

Once the sensor is lowered into the manhole (Figure 5.2a), it is inserted into the pipe as shown in Figure 5.2b. The vertical sensor position can be adjusted to keep the sensor very close to the soffit of the pipe and above the flow surface as it is shown in Figure 5.2b.

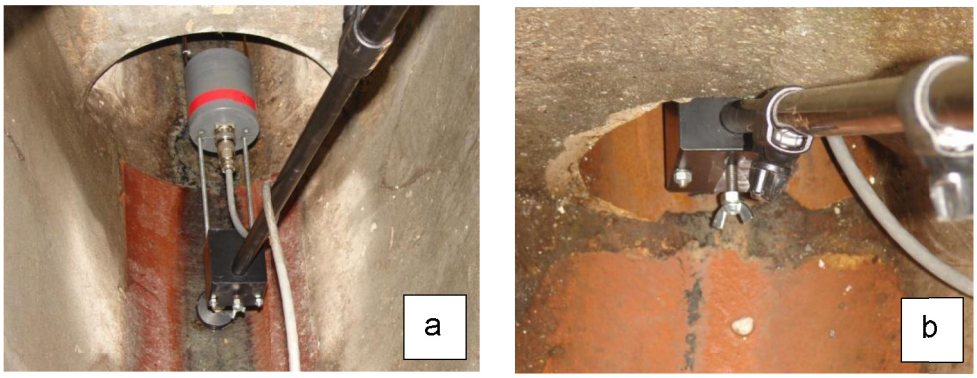

Figure 5.2 Acoustic sensor inside the manhole (a) and soffit (b) of a pipe.

Once the acoustic sensor was inserted into the pipe and touching the soffit, it was kept stationary, so that the measurement can be performed. The sensor emitted a 10-second long sinusoidal chirp covering frequencies from 200Hz - 20kHz. The signals reflected from the pipe discontinuities such as blockages, pipe deformations, partial wall collapses, poor joints, root infiltration, cracks, encrustation, and adjacent pipe connections (Bin Ali 2010). The recorded signals were deconvoluted in order to determine the acoustic impulse response of the pipe. Here, the standard deconvolution algorithm based on the Fourier

transform method (Bin Ali 2010) was used. Further, the obtained impulse responses was filtered and conditioned. The filtered impulse responses recorded on a microphone pair were combined coherently to determine the acoustic intensity. The total reflected acoustic energy was calculated and presented as a function of frequency and distance along the pipe length in terms of a spectogram in accordance with the procedure detailed in section 3.2.2. To calculate accurately the speed of sound in the pipe, a thermocouple was lowered into the manhole. The sound speed was calculated from the temperature data and its value was used to determine the exact locations of the discontinuities detected in the pipe. The laboratory and field experiments in 150 - 650mm diameter, 5 - 85m long pipes (Romanova 2009, Romanova et al. 2010) have shown that an accuracy of ±10mm in distance measurements could be achieved with this method.

The acoustic equipment software (Bin Ali 2010) had an embedded automated pipe condition classification unit, which is based on cross-correlation between the recorded acoustic signature for an unknown condition and signatures for some known conditions which are stored in a database. Since each of the conditions has a unique acoustic signature in a pipe of given diameter, it is possible to classify with a high degree of probability 79% of the conditions detected acoustically in the surveyed sewer pipes (Bin Ali 2010, Romanova et al. 2012). This methodology was able to identify most common in-sewer conditions such as: connections (CN), obstructions / blockages (OBX), joints (JD) cracks (C) and manhole chambers / junctions (JN), which were referenced according to standard in-sewer condition classification coding in the UK, WRc Manual of Sewer Condition Classification (WRc, 2004). These condition

notations are displayed in acoustic analysis window, above their energy spectrum reflections straight after the test signal was recorded as shown in Figure 5.3.

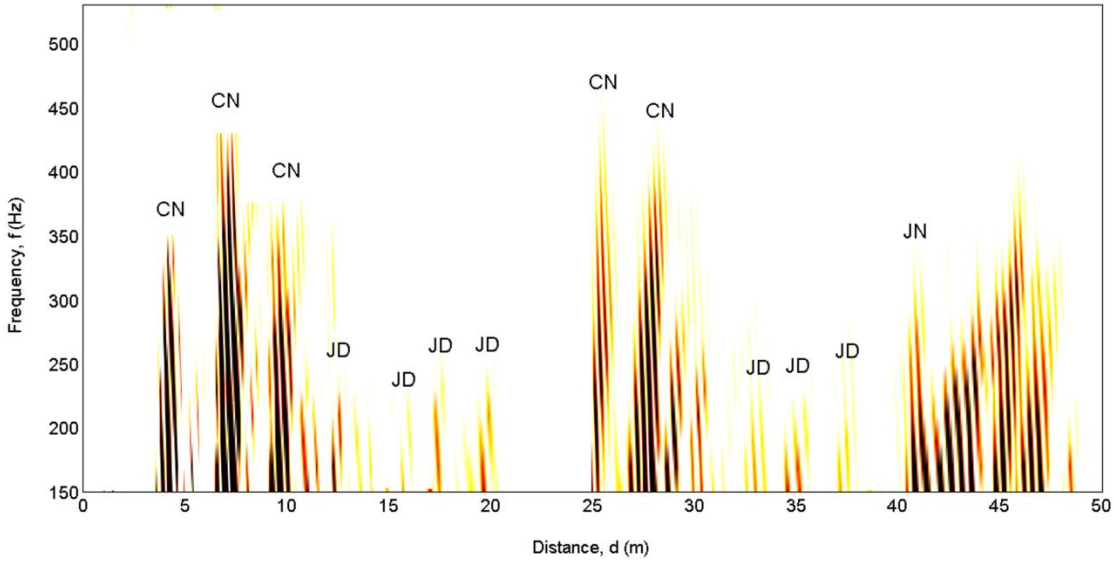

Figure 5.3 Acoustic intensity reflection spectogram from 300mm diameter concrete sewer with the presence of multiple obstructions.

Figure 5.3 demonstrates a typical acoustic defect classification recorded in a 40.5m long and 300mm diameter concrete pipe section. Here the reflected acoustic intensity is presented as a function of the frequency and distance along the pipe. Each detected defect inside the pipe is clearly visible as a yellow-to-black colored mark corresponding to the acoustic reflection. Marks with more intense color shading correspond to greater rate of sound reflection, i.e. caused from larger discontinuity. This particular sewer pipe section has 5 lateral connections (at 3m, 7m, 9m, 25m and 27m). CCTV taken image of lateral connection at 3m is presented in Figure 5.4a, which is actually a protruding connection. Also, this pipe has 7 worn out or displaced joints (at 13m, 15m, 17m, 20m, 33m, 35m, and 37m). A well pronounced pipe next junction is visible at 41m. All of these pipe defects were also detected by CCTV. Acoustic

spectogram reveals two reflections at 28m and 30m, which were not classified by acoustic defect detection methodology, or revealed in CCTV report.

Figure 5.4 Images of sewer conditions recorded by the CCTV: protruding pipe connection (a), hard compacted solid or obstruction (b) and wall crack (c).

Another typical example of pipe conditions detected with acoustic means is shown in Figure 5.5, where at 15.5m a hard compacted solid that rest beneath the lateral connection was identified. This condition is also visible in the CCTV image shown in Figure 5.4b. Also, this pipe section has a wall crack at 35m, for which the CCTV image is presented in Figure 5.4c. Overall this section of the pipe was 47.5m long where the acoustics identified the next junction (JN).

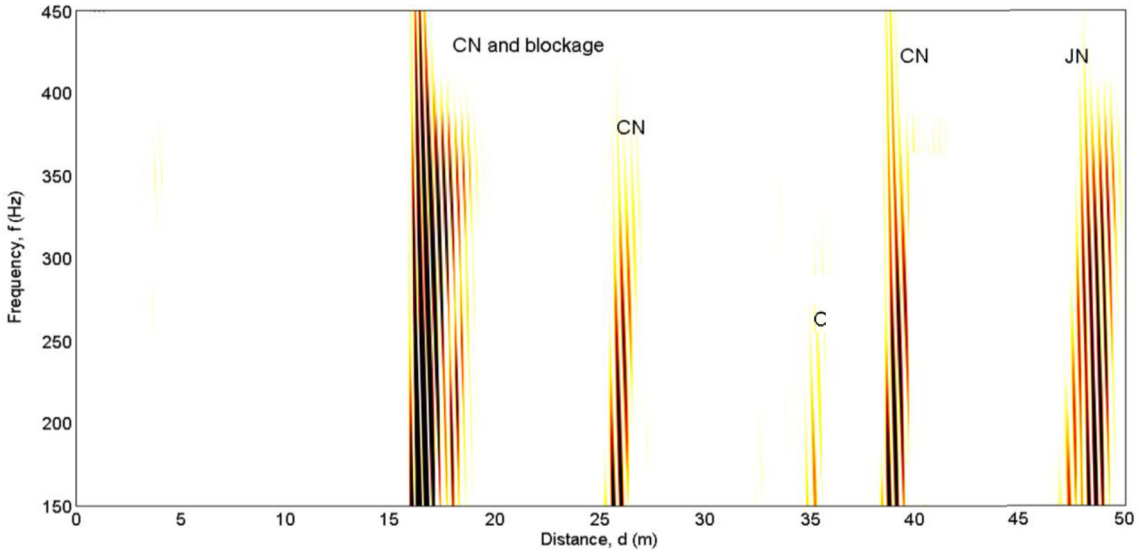

Figure 5.5 Acoustic reflection from 300mm, concrete, sewer with the presence of blockage formed from protruding sediments at 15.5m.

5.1.2 Acoustic estimation of the hydraulic roughness

From the above examples (Figures 5.3 and 5.5), it can be seen that each discontinuity in the pipe causes acoustic energy reflection, which may be either classified by the acoustic defect detection system or not. The total energy content (see equation 3.3) due to all pipe defects, deformations and pipe wall roughness in a single section can be acoustically quantified and related to the estimated pipe section roughness (k_s^r) obtained from CCTV report.

In order to study the capability of the acoustic roughness detection method, 33 sewer sections with the total length of 1315m were selected. The selected sections had 5 blockages, 22 bad joints and 67 cracks (either longitudinal or circumferential) and 68 other defects which were detected but not classified with the acoustic defect classification software. These were likely to be sediments, wall encrustation, wall general wear out and poor joints. The reflected acoustic energy was calculated from the instantaneous intensity data in accordance to the method detailed in section 3.2.2. In these calculations the whole length of the pipe section was used. The reflections from the house or lateral connections and pipe-end manholes were excluded because these do not contribute directly to the overall pipe hydraulic roughness. The overall estimated hydraulic roughness coefficient (k_s^r) for each pipe section provided in CCTV reports was estimated visually according to the CEN standard (2002), which are similar to the WRc document (2004). In these standards the value of estimated hydraulic roughness coefficient is assumed for a pipe running full form the in-pipe images for the whole pipe section considering the pipe wall material roughness, roughness due to defect number, type, severity and pipes cross-section deformation (see examples of pipe estimated roughness values in Appendix C).

Hence, estimated roughness coefficient (k_s^r) is generalised for the pipe section running full, where the values are assigned by a trained operator based on in-pipe images and guidelines provided in the according standards (WRc 2004, 2010 is used in the UK).

Table 5.1 Pipe conditions and estimated roughness.

No.	Material	D_c	d	Blockage	Joint	Crack	Other	All defects	k_s^r	ET	ET_d
		[mm]	[m]	No.	No.	No.	No.	No.	[mm]	[-]	[-]
1		225	36	0	0	1	1	2	0.5	0.479	0.058
2		225	34	0	0	2	2	4	1.5	0.546	0.067
3		250	41	0	0	2	0	2	1.0	0.614	0.057
4	Clay	250	34	1	0	0	2	3	2.4	0.438	0.052
5		250	58	0	1	3	0	4	3.0	1.107	0.076
6		250	43	0	2	10	1	13	4.7	1.692	0.157
7		250	42	1	0	2	2	5	6.0	1.951	0.177
8		250	48	0	0	2	1	3	2.0	1.028	0.086
9		250	45	0	2	1	3	6	3.2	1.054	0.094
10		250	55	0	2	2	3	7	4.3	2.049	0.149
11		250	36	0	0	8	1	9	5.8	1.862	0.207
12		300	28	0	0	0	1	1	1.0	0.593	0.071
13		300	24	0	0	0	2	2	1.5	0.524	0.073
14		300	33	0	1	0	2	3	2.0	0.741	0.075
15		300	32	0	0	3	1	4	2.4	0.736	0.077
16		300	30	0	0	2	1	3	2.0	0.743	0.083
17	Concrete	300	40	1	1	0	1	3	5.6	1.951	0.163
18		300	40	0	1	4	2	7	6.3	2.015	0.168
19		300	38	1	7	4	2	14	10.0	5.173	0.454
20		350	36	0	0	1	1	2	1.2	0.512	0.041
21		350	33	0	0	0	4	4	3.4	1.285	0.111
22		350	29	0	0	3	2	5	5.1	1.859	0.183
23		350	58	0	0	7	3	10	6.2	3.947	0.194
24		400	60	0	2	0	1	3	1.8	1.244	0.052
25		400	64	0	0	2	8	10	8.0	6.593	0.258
26		400	72	0	0	2	11	13	9.0	9.231	0.321
27		225	40	0	0	0	0	0	0.2	0.274	0.030
28		225	28	0	0	0	1	1	0.5	0.437	0.069
29		225	35	0	0	0	1	1	0.5	0.385	0.049
30	PVC	250	48	0	0	0	1	1	0.3	0.428	0.036
31		250	25	0	0	0	2	2	0.8	0.372	0.060
32		250	36	1	3	6	3	13	6.6	2.241	0.249
33		250	14	0	0	0	2	2	0.8	0.248	0.071
Total		-	1315	5	22	67	68	162	-	-	-

The characteristics of the surveyed pipes are summarised in Table 5.1. First, Table 5.1 provides section number, information on the pipe wall material, pipe diameter (D_c) and section length (d). Further, a total number of different pipe

defects for each section are summarised, these include blockages, displaced joints, cracks and others, followed by a total of all defects in given pipe section. Further column shows the estimated values of the pipe section roughness (k_s^r), obtained from CCTV reports. The last two columns in Table 5.1 show the acoustic energy content (ET) and normalised acoustic energy content (ET_d) for a given length of pipe section. Other defects appear in acoustic spectograms as unidentified reflections which are also included in analysis of obtaining the normalised reflected acoustic energy content over a given pipe section of length d. The quoted value of the energy in the acoustic reflections was normalised by the ratio of pipe section length to pipe diameter

$$ET_d = \frac{ET}{d/D_c} \tag{5.1}$$

so that the reflections from different pipe geometries could be compared.

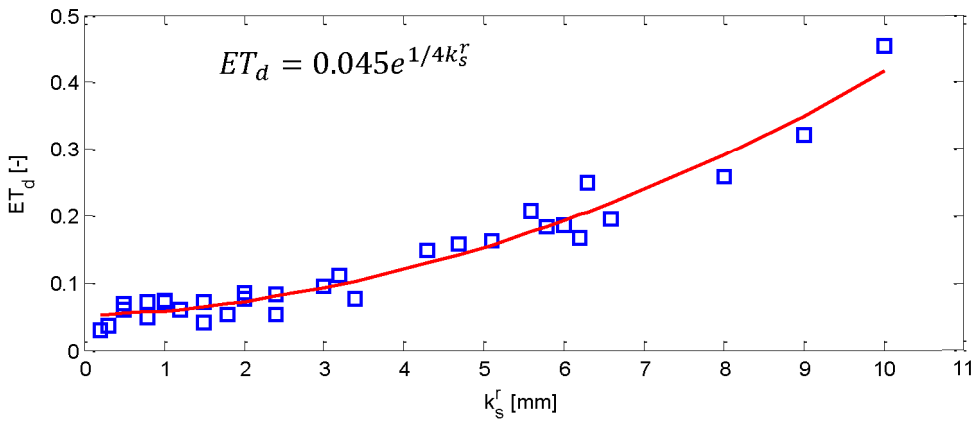

Figure 5.6 Acoustic energy content normalised by pipe geometry as a function of estimated hydraulic roughness, for field data with dry pipe conditions with R^2 = 0.91.

Figure 5.6 demonstrates the relation between the weighted acoustic response (ET_d) and the estimated pipe hydraulic roughness (k_s^r). This relation can be approximated with the following expression

$$ET_d = 0.045e^{1/4k_s^r} \tag{5.2}$$

which is accurate with R^2 = 0.91. Clearly, an increase in the overall pipe roughness causes an increase in the acoustic reflection strength, which has a good physical sense. This result is a novel finding as it suggests that the normalised acoustic reflection can be used to predict the estimated pipe wall roughness (defined by WRc 2004 standard) for a given pipe section assumed it is running full, where the roughness from pipe wall material, defects type, number and severity are considered.

5.2 Conclusions

An acoustic method based on signal reflectometry was used to investigate the estimated pipe section roughness in live sewers. The field trials took place in Austria, where more than 1km of sewers of various pipe diameter and material were investigated. A majority of these pipes were dry or with very little flow during the tests, so the methodology developed in the laboratory (section 3.2.2) was used to obtain pipe section overall acoustic energy content, which was related to the estimated roughness value of the same pipe section (defined by WRc 2004 standard).

It was found that the normalized acoustic energy reflected from the sewer defects increases exponentially with the estimated pipe roughness coefficient. An empirical relationship (equation 5.2) was proposed which enables automated roughness detection via acoustic means. This result corresponds to that obtained in laboratory work presented in section 3.5, where the hydraulic roughness due to pipe with block was found to increase with the increase in the acoustic energy (equation 3.18). However, the relation types and accuracy

obtained in this chapter and chapter 3 are different as: (i) this chapter was concerned with the estimated hydraulic roughness obtained for the whole pipe section assumed running full, where the roughness values were assigned by the operator based on WRc 2004 standard - the proposed relation may incur human factor errors; (ii) the data presented in chapter 3 was concerned with the hydraulic roughness caused by the blockage within a pipe running partially full, where the roughness was accurately calculated from the obtained hydraulic flow data in the controlled laboratory environment.

The proposed acoustic method is non-invasive, quick and can be easily automated. In the case, when a detailed pipe wall survey is required, the conventional survey techniques can be used together with automated acoustic roughness estimation to perform detailed and integrated pipe wall analysis. As a result of this strategy, a larger proportion of pipes may be surveyed in a shorter period, using the proposed acoustic method. In this way the problematic sections can be timely revealed to prevent sewer performance failure which may lead to flooding.

Chapter 6 Conclusions

6.1 Achievements and discussion

This thesis has been concerned with the problems associated with the development of airborne acoustic measurement of the hydraulic conditions in circular pipes with free surface flow over a local or distributed pipe wall roughness. Novel acoustic methods have been developed to predict: (i) the hydraulic roughness and the hydraulic energy losses due to the local obstruction in the pipe with a steady, non-uniform flow (chapter 3); (ii) overall hydraulic roughness of a pipe with distributed roughness (chapter 4); (iii) overall estimated hydraulic roughness for sewer pipes with little or no flow (chapter 5). The performance of these methods has been studied under a range of controlled flow and acoustic conditions in the laboratory and in the field.

The results of the experiments carried out in a laboratory pipes with local roughness suggest that:

(i) The hydraulic roughness conditions in the pipe with a local roughness can be studied using the acoustic reflectometry technique. This method enables the acoustic reflections from any discontinuities in the pipe to be recorded with a microphone array and subsequently analysed;

(ii) The instantaneous acoustic intensity reflected from any local discontinuities is an important characteristic which carries information about the defect nature, location and extent. It can be

used to calculate the reflected acoustic energy which can then be non-dimensionally related to the pipes cross-sectional area occupied by blockage, hydraulic head loss and hydraulic roughness caused by this blockage;

(iii) An empirical relation has been suggested which links the hydraulic head loss with the acoustic energy content in a pipe with a local blockage.

The local roughness results were obtained from two pipe sizes (150mm and 290mm) with different wall roughness under controlled laboratory conditions. In general, the local blockage height and the uniform flow depth did not exceed 41% and 34% of pipe's cross-sectional area, respectively, where the mean time - averaged flow discharges of 0.4 - 32l/s were achieved. The above indicates the boundary conditions for the achieved results. It should be noted that in all of the tests there was an air gap above the blockage for the sound to propagate. In the case of higher blockage and discharge, where the air gap may disappear, the effect of the acoustic reflection is expected to be similar to the reflection of the pipe end. In this case, the results of local blockage study will be impractical to implement. However, to prove this argument further investigations are required. Furthermore, in this study a blockage of fixed length $\approx D_c/1.5$ was used. It is suspected that the length of the blockage will only influence the length of the water deviation from the uniform flow condition upstream of the blockage, which will result in a demand for a longer laboratory pipe. Lastly, in this study, a range of two acoustic sensors was used (small and large), where in combination both sensors cover the pipe range of 120 - 650mm. The laboratory results were non-dimensionalised by the pipe diameter (for 150mm and 290mm

pipes), and it is assumed that the same principle will work for the full range of pipe sizes covered by the two acoustic sensors. Due to the sensor size, pipes smaller than 120mm are impractical to survey, as well as for the pipes larger than 650mm a sensor with much greater power should be used.

The results of the experiments with the distributed roughness suggest:

(i) The spectral and statistical characteristics of the free water surface roughness relate to the nature of the distributed bed roughness and its size;

(ii) A novel acoustic instrumentation has been developed to detect water surface characteristics by analyzing the airborne acoustic field. This equipment is based on the transmission of airborne acoustic pulses or continuous signals through the pipe from a speaker to microphone array which are separated by a sufficiently long distance;

(iii) An apparent change in surface roughness and its pattern results in a detectable change in the received acoustic signal characteristics;

(iv) Specifically, the standard deviation in the flow depth in a pipe with distributed wall roughness has been found to increase with the increasing mean flow depth and flow rate up to a certain peak point which was found to be different for different roughness conditions. Beyond this point the dependence between the flow depth and standard deviation in flow depth reverses;

(v) In the case of the clean pipe, the standard deviation in the flow depth has increased progressively with the increasing mean flow depth and flow velocity. This is different from pipes with distinct roughness elements;

(vi) The statistical distribution in the flow depth fluctuations has been found to be close to the Gaussian distribution;

(vii) A non-dimensional relation between the surface water wave standard deviation and hydraulic parameters (flow depth, roughness, and friction) to pipe roughness element streamwise separation has been proposed;

(viii) The mean amplitude of the tail part of the acoustic pulse propagated over the rough water surface was empirically related to the flow depth, mean flow velocity and normalised hydraulic roughness. Whereas the standard deviation in the correlation function of the pulse tail peak relative amplitude was related to water surface waves standard deviation;

(ix) It has been found that the dynamically rough water/air interface results in the dynamic fluctuations of the envelope of the continuous acoustic wave transmitted through the pipe. The statistical distribution in the amplitude of the continuous wave envelope has been found to be Gaussian;

(x) Empirical relations between the mean amplitude of the envelope of the acoustic sine wave and flow depth, velocity and the normalised hydraulic roughness have been proposed. The standard deviation of the envelope of the acoustic sine wave was

related to water surface wave standard deviation (standard deviation in mean flow depth).

The distributed roughness results were obtained from a 290mm pipe under controlled laboratory conditions with pipe roughness composed of mesh and spheres arranged in a hexagonal pattern with fixed cross-sectional and different streamwise spacing. In general, during the tests uniform flow depth did not exceed 41% of the pipe's cross-sectional area where the mean flow velocity of 0.19 - 0.42m/s was achieved. In nature, a bed pattern close to hexagonal seems to appear quite often, hence an idealized hexagonal pattern was chosen for the laboratory work. As roughness elements, spheres were selected, as in nature most of the bed elements are rounded. In the presented experiments, regular roughness elements in regular patterns were used, in the case of an irregular or random wall roughness patterns, it is expected that the results patterns would be similar, as the increase in water surface roughness height should results in the increase in signal standard deviation. However the curves normalised by the pattern geometry might shift (the above should be validated in further tests). The results from distributed roughness experiments were non-dimensionalised by the pipe's cross-sectional characteristics and flow conditions (diameter, flow width and depth, flow and air area). This should allow the obtained general relations to be applied to pipes of different diameters and flow conditions. However, as the experiments were carried out in a pipe of one size, the above assumption needs to be validated. Furthermore, for distributed roughness experiments the novel acoustic equipment which was developed also was not tested in pipes of different sizes and material. It is suspected, that for different pipe sizes the acoustic signal power and operational signal

frequency should be scaled accordingly to meet the criteria of the pipe diameter. For pipes of larger diameter more power is required to be emitted. Whereas, this study revealed that the standard deviation of the signal of frequency just below the first cut-on frequency of pipe (which is individual for different pipe diameters) corresponds best to the water surface wave variations. The above can be only validated via further laboratory and filed testing in a range of pipes and conditions.

The results of the acoustic field experiments in the pipe sections with little or no flow have suggested that:

(i) The acoustic response recorded in real sewers, which was analysed in terms of acoustic energy content, can be used to determine the overall estimated hydraulic roughness of pipe section. An empirical relation was proposed to relate the acoustic energy reflected from in-sewer defects and the estimated hydraulic roughness suggested by the WRc 2004 standard.

The above results were obtained in the field tests for a range of pipe sizes and materials in conditions with little or no flow. As such, the obtained non-dimensionalised results will be applicable for the pipe sizes of 120 - 650mm, which is the pipe sizes range of the current acoustic equipment.

Overall, the results of this study have demonstrated that there is a simple and attractive acoustic way of detecting the pipes hydraulic roughness in the presence of free water surface. The acoustics instrumentation used in local

roughness experiments and in the field, is the same, and it is already used by a number of water companies for pipeline survey and defect location and identification. The results obtained in this study can be synchronised with the already existing software which will allow automated acoustic roughness estimation due to blockages and in pipe with low flow or no flow conditions. Further, a novel acoustic instrumentation which should be inserted in to the pipe via two openings was proposed that is able of identifying hydraulic roughness due to distributed pipe wall roughness and relating that to roughness pattern.

6.2 Recommendations for future work

Currently the proposed method of local roughness detection is limited to pipes where the blockages are separated by a large enough distance to allow the water to return to uniform flow conditions. For further work, experiments with few blockages of different size and separation in a range of pipes are suggested to be carried out. Based on the obtained experimental data a new model can be developed to understand better the effects of the dynamic roughness on the airborne acoustic field in the pipe. It can also be recommended to validate the results of the laboratory experiments on the hydraulic roughness and head loss with a carefully instrumented live sewer.

In this work the distributed roughness experiments were limited to one mesh and six sphere patterns. It is recommended to carry out experiments in pipes of different diameters, with a more realistic wall roughness patterns covering more density ratios and height roughness spectra. This will allow to obtain more extended data to validate the proposed hydraulic relations for different

roughness concentration boundary values based on roughness type ('k', transitional or 'd'). Also, the extended range of experiments will improve the method used in acoustic analysis and perhaps suggest variation in signal power, wavelength and frequency based on pipe sizes.

The proposed experimental equipment, for detecting distributed roughness, is bulky and suitable for the laboratory use only due to its adaptability and mains power supply. A more compact field prototype of the acoustic instrument could be developed and build. This prototype should include special software to enable the automated analysis of the hydraulic characteristics in live pipes. The tests in live sewers in a range of pipes with distributed roughness of various patterns would supplement validation of the novel findings on distributed roughness of this thesis.

The results obtained in the field trials are suitable for a range of pipe sizes and the novel relation can be implemented in the already developed and used software code. This would attractively supplement the existing acoustic pipe survey sensor and provide an option of automated pipe estimated roughness detection via rapid, non-intrusive acoustic pipe survey.

References

Antonopoulos-Domis, M. (1980) Frequency dependence of acoustic resonances on blockage Position in a fast reactor subassembly wrapper. *Journal of Sound and Vibration*, 72, pp. 443-450.

Arthur, S., Crow, H., Pedezert, L. (2008) Understanding Blockage Formation in Combined Sewer Networks, *Water Management*, 161, pp. 215-221.

Attenborough, K. and Taherzadeh, S. (1995) Propagation from a point source over a rough finite impedance boundary. *Journal of Acoustical Society of America*, 98(3), pp. 1717-1722.

Barr, D.I.H. (1981) Solutions for Colebrook-White function for resistance to uniform turbulent flow, *Proceeding of Institution of Civil Engineers*, 71 (2,) pp. 529.

Barr, D.I.H. and Wallingford, H.R. (1998) *Additional tables for the hydraulic design of pipes, sewers and channel*s. Thomas Telford, London.

Bass, F.G. and Fuks, I.M. (1972) *Scattering of Waves by Statistically Rough Surface*. (original: *Rassejanie Voln na Statisticheski Nerovnoj Poverhnosti*), Moscow: Nauka, pp. 69-75, (in Russian). [Available online]: http://bookre. org/reader?file=504219&pg=3.

Bass, F.G. and Fuks, I.M. (1979) *Chapter 5, Wave scattering from statistically rough surfaces*. Oxford, New York, Pergamon Press.

Baur, R. and Herz, R. (2002) Selective inspection planning with aging forecast for sewer types (*2nd World Water Congress of the International-Water-Association, Berlin, Germany), Water Science and Technology*, 46 (6-7), pp. 389-396.

Berlamont, J.E., Trouw, K. and Luyckx, G. (2003) Shear stress distribution in partially filled pipes. *Journal of Hydraulic Engineering, ACSE*, 129 (9), pp. 697-705.

Bin Ali, M.T. (2010) *Development of Acoustic Sensor and Signal Processing Technique*. PhD Thesis, University of Bradford, UK.

Bin Ali, M.T., Horoshenkov, K.V. and Tait, S.J. (2010) Rapid Detection of Sewer Defects and Blockages Using Acoustic Based Instrumentation. *Proceedings of 7th International Conference on Sustainable Techniques and Strategies in Urban Water Management*. Lyon, France.

Blanksby, J., Khan, A. and Jack, A. (2002) Assessment of cause of blockage of small diameter sewers. Proc. Int. Conf. On Sewer Operation and Maintenance. ISBN 1 851 432 132.

Boulanger, P., Attenborough, K., Qin, Q. and Linton C.M. (2005) Reflection of sound from random distributions of semi-cylinders on a hard plane: models and data. *Journal of Applied Physics*, 38, pp. 3480-3490.

Boulanger, P., Attenborough, K., Taherzadeh, S., Waters-Fuller, T. and Li, K.M. (1998) Ground effect over hard rough surfaces. *Journal of Acoustical Society of America*, 104(3), pp. 1474-1482, DOI: 10.1121/1.424358.

Brüel & Kjær's (2011) Free-field Microphone 4190-C-001 [Online] Available at: http://www.bksv.com/Products/TransducersConditioning/acoustic-transducers /microphones/microphone-preamplifier-combinations/4190-C-1.aspx?sortOrder = [Accessed: 16/07/2012].

Brüel & Kjær's (2011) Free-field Microphone 4190-C-001 Specifications [Online] Available at: http://www.bksv.com/Products/Transducers Conditioning/ acoustic-transducers/microphones/microphone-preamplifier-combination s/4190-C-1.aspx?tab=specifications [Accessed: 04/08/2012].

Brüel & Kjær's (2011) Microphone Preamplifier 2669-C [Online] Available at: http://www.bksv.com/Products/TransducersConditioning/acoustic-transducers /microphones/preamplifiers/2669-C.aspx [Accessed: 03/08/2012].

CAHE (2002) *Computer Application in Hydraulic Engineering, Connecting Theory to Practice,* 5th edn. Haestad press, US.

CEN (European Committee for Standardization). EN 13508-2: *Conditions of drain and sewer systems outside buildings* - Part 2: Visual inspection coding system. November. 2002.

Chow, V.C. (1959) Open-Channel Hydraulics. McGraw-Hill Book Co., New York, USA.

Churchill Contrils Limited (2001) Wave monitor manual. [Online] Available at: http://www.churchill-controls.co.uk/downloads/wmman.pdf [Accessed: 24 Mar 2011].

Cieslik, A.R. (2009) *Three-dimensionality of shallow flows*. PhD Thesis: Delft Technical University, Eidenhoven, Netherlands.

Colebrook, C.F. (February 1939) Turbulent flow in pipes, with particular reference to the transition region between smooth and rough pipe laws. *Journal of Institution of Civil Engineers*, London. 11, pp. 133-156.

Cooper, J.R., Tait, S.J. and Horoshenkov, K.V. (2006) Determining hydraulic resistance in gravel-bed rivers from the dynamics of their water surfaces. Earth surface processes and landforms, *Wiley InterScience*, 31, pp. 1839-1848.

Darcy, H. (1857) *Recherches Experimentales Relatives au Mouvement de l'Eau dans les Tuyaux*. Mallet-Bachelier, Paris, France. (In French).

Deane, A. (1986) *Time domain work on brass instruments*. PhD thesis, University of Surrey, UK.

DeSalis, M.H.F. and Oldham, D.J. (1999) Determination of the blockage area function of a finite duct from a single pressure response measurement. *Journal of Sound and Vibration*, 221(1), pp. 180-186.

Dhanalakshmi, P., Palanivel, S. and Ramalingam, V. (2011) Pattern classification models for classifying and indexing audio signals. *Journal of Engineering applications and of Artificial Intelligence, ELSEVIER*, 24, pp. 350-357.

Dirksen, J., Clemens, F.H.L.R., Korving, H., Cherqui, F., Le Gauffre, P. and Snaterse, C. (2011 - accepted, not yet published) The consistency of visual sewer inspection data.

Dirksen, J., Goldina, A., Veldhuis, J.A.E. and Clemens F. (2007) The role of uncertainty in urban drainage decisions: uncertainty in inspection data and their impact on rehabilitation decisions. *LESAM, 2nd International Conference on Strategic Asset Management*, IWA, Portugal.

Djenidi, L., Elavarasan, R. and Antonia, R.A. (1999) The turbulent boundary layer over transverse square cavities. *Journal of Fluid Mechanics*, 395, pp. 271-294.

Duffield, A. (1984) Problems encountered when making simple impulse measurements. *Proceedings of the Institute of Acoustics*, pp. 21-28.

Duran, O. (2007) Automated pipe defect detection and categorization using camera/laser-based profiler and artificial neural network. IEEE Transactions on Automated Science and Engineering, 4(1), pp. 118-126.

Eguchi, M., Hara, T. and Manabe, T. (1997) Acoustic inspection systems for telecommunication conduits. *Proceedings of the 15th International Conference No-Dig '97*. Taipei, Taiwan.

El-Ghamry, M.H., Reuben, R.L. and Steel, J.A. (2003) The development of automated pattern recognition and statistical feature isolation techniques for the diagnosis of reciprocating machinery faults using acoustic emission. *Journal of Mechanical Systems and Signal Processing*, 17(4), pp. 805-823.

Fahy, F.J. (1995) *Sound Intensity*, 2nd edn., Taylor and Francis (CRC Press), ISBN 10: 0419198105.

Fischer, B., Hunger, W., Lehmann, T.M., Muller, K. and Schafer, T. (2007) Objective condition establishment of sewer systems. *Proceedings of 2nd Conference on Sewer Operation and Maintenance* (Ertl T., Pressel A, Kretschmer F, Haberl R. (eds)), pp. 207-215.

Fuchs, H.V. and Riehle, R. (1991) 10 years of experience with leak detection by acoustic-signal analysis. *Journal of Applied Acoustics,* 33, pp. 1-19.

Gill, M.A. (1971) Height of sand dunes in open channel flows, American *Society of Civil Engineers. Prorocеedings. Journal. Hydraulics Division,* 97(HY12), pp. 2067-2074.

Goodwin, J. (1981) *Relations between the geometry and acoustics of brass instruments*. PhD thesis, University of Surrey.

Great Britain. House of Commons, Committee of Public Accounts. *Out of sight – not out of mind: Ofwat and the public sewer network in England and Wales, Thirtieth report of session 2003-0*4 (HC 463, May 2004) London: The Stationery Office.

Hao, T., Rogers, C.D.F., Metje, N., Chapman, D.N. et al (2012) Condition assessment of the surface and buried infrastructure. *Tunnelling and Underground Space Technology*, 28, pp. 331-334.

Heyser, R.C. (1986) *81st Audio Engineering Society Convention*, Los Angeles, Paper 23969, pp. 12-16.

Horoshenkov, K.V., Tait, S.J., Bin Ali M.T. and Long, R. (August 2008) Patent Application: *Improvements in and relating to apparatus for the airborne acoustic inspection of pipes*. GB081519905.

Horoshenkov, K.V., Tolstoy, A., Bin Ali, M. T. (April 2009). Detecting pipe changes via acoustic matched field processing. *Applied Acoustics*, Elsevier, doi: 10.1016/j.apacoust.2008.08.007.

Horoshenkov, K.V., Yin, Y.A., Schellart, A., Ashley, R.M. and. Blanksby J.R (2004) The acoustic attenuation and hydraulic roughness in a large section sewer pipe with periodical obstacles*. Journal of Water Science and Technology*, 50(11), pp. 97–104.

IKB (2009). *Linz, Pashing CCTV reports*. Zit, B. private correspondence from Jun 2011. Kundencenter, Innsbruck, Austria.

Impactaudio (2006) Loudspeaker Visaton TI100 [Online] Available at: http://www.impactaudio.co.uk/product.asp?ref=522&session=a4191e51ac8c9a44d446748094baf774 [Accessed: 07/02/2011].

Iseley, T. (1999) Development of a new Sewer Scanning Technology - SSET, No-Dig, America. [Online] Available at: http://rebar.ecn.purdue.edu/ect/links/technologies/civil/sset.aspx [Accessed: 01 Nov 2011].

Ishimary, A. (1978) Rough surface scattering. In: *Wave propagation and scattering in random media*. Vol.2. London, Academic Press, pp. 463-483.

Jackson, A.C., Butler, J.P., Millet, E.J., Hoppin, F.G. and Davson, S.V. (1977) Airway geometry by analysis of acoustic pulse response measurements. *Journal of Applied Physics*, 43, pp. 523-536.

Jimenez, J. (2004) Turbulent flows over rough walls. *Annual Review of Fluid Mechanics*, 36, pp. 173–96.

Julien, P.Y., Friesen, N. Duan, J.G. and Eykholt, R. (2010) Celerity and amplification of supercritical surface waves. *ASCE, Journal of Hydraulic Engineering*, 136 (9), pp. 656-661.

Kleijwegt, R.A. (1992) *On sediment transport in circular sewer with non-cohesive deposit*. PhD thesis, Delft Technical University, Netherlands.

Knight, D.W. and Sterling, M. (2000) Boundary shear in circular pipes running partially full. *Journal of Hydraulic Engineering, ASCE*, 126 (4), pp. 263-275, DOI: 10.1061/(ASCE)0733-9429.

Knowles Acoustics (2012) Microphone SPM0208HE5 data sheet [Online] https://www1.elfa.se/data1/wwwroot/assets/datasheets/03010469.pdf [Acces sed: 03 Aug 2012].

Korving, H. and Clemens, F. (2005) Impact of dimension uncertainty and model calibration on sewer system assessment, *Water Science and Technology*, 52 (5), pp. 35-42.

Krogstad, P. (1991) Modification of the Van Driest damping function to include the effects of surface roughness. AIAA Journal, 29, pp. 888-894.

Krogstad, P.A., and Antonia, R.A. (1999) Surface roughness effects in turbulent boundary layers. *Experiments in Fluids*, 27, pp. 450-460.

Kryazhev, F.I. and Kudryashov, V.M. (1978) Spatial and temporal correlation function of the sound field in a waveguide with rough boundaries. *Soviet Physics of Acoustics*, 24(2), Mar-Apr, pp. 118-121.

Kryazhev, F.I. and Kudryashov, V.M. (1984) Array in a waveguide with a statically rough boundary. *Soviet Physics of Acoustics*, 30(6), Nov-Dec, pp. 469-472.

Kryazhev, F.I. and Kudryashov, V.M. (1984) Sound field in a waveguide with a statically rough admittance boundary. *Soviet Physics of Acoustics*, 30(5), Sept-Oct, pp. 391-393.

Kryazhev, F.I., Kudryashov, V.M., Petrov, N.A. (1976) Propagation of low-frequency sound waves in a waveguide with irregular boundaries. *Soviet Physics of Acoustics*, 22(3), May-June, pp. 211- 216.

Lyn, D.A. (1993) Turbulence measurements in open-channel flows over artificial bed forms. *Journal of Hydraulic Engineering*, 119 (3), pp. 306–326.

Manes, C., Pokrajac, D., McEwan, I. and Nikora, V. (2009) Turbulence structure of open channel flows over permeable and impermeable beds: A comparative study. *Journal of Physics of Fluids*, 21(12), Article number: 125109, DOI: 10.1063/1.3276292.

Maverick Inspection Ltd. (2010) Laser profiling (RPI) technology overview. [online] Available at: http://maverickinspection.com/Services/LaserProfiling/tabid/135/ Default.aspx [Accessed: 25/05/2010].

Mermelstein, P. (1967) Determination of the vocal-tract shape from measured formant frequencies. *Journal of the Acoustical Society of Am*erica, 41, pp. 1283-1294.

MiniCam Ltd. (2010) Zoom camera technology overview. [online] Available at: http://www. minicam2000.co.uk/index.php?id=17 [Accessed: 25/05/ 2010].

Moody, L.F. (1944) Friction Factors for Pipe Flow. *Transactions of the ASME*, 66 (8), pp. 671–684.

Morse, P.M. and Ingard, K.U. (1968) *Theoretical acoustics*. New York, London: McGraw-Hill.

Morvan, H., Knight, D., Wright, N., Tang, X.N., Crossley, A (2008) The concept of roughness in fluvial hydraulics and its formulation in 1D, 2D and 3D numerical simulation models. *Journal of Hydraulic Research,* 46(2), pp. 191-208.

National Instruments (2011) NI USB-6356, X Series Data Acquisition. [Online] Available at: http://sine.ni.com/nips/cds/view/p/lang/en/nid/209075 [Accessed: 10/07/2012].

National Instruments (2011) USB Data Acquisition. [Online] Available at: http://www.ni.com/dataacquisition/usb [Accessed: 10 Jun 2012].

National Instruments (2011) X series USB Data Acquisition. [Online] Available at: http://zone.ni.com/devzone/cda/tut/p/id/11556 [Accessed: 3/07/2012].

Nelson, J.M., McLean, S.R. and Wolfe, S.R. (1993) Mean flow and turbulence fields over two-dimensional bed forms. *Water Resources Research,* 29(12), pp. 3935-3953.

Nikko Kyodo Co Ltd (1993) Patent Application: *Surface acoustic wave device*. JP0057124.

Nikora, V., Koll, K., McEwan, I., McLean, S. and Dittrich, A. (2004) Velocity distribution in the roughness layer of rough-bed flows. *Journal of Hydrauic Engineering,* 130(10), pp. 1-7.

Nikora, V.I., Goring, D.G., McEwan, I. and Griffiths, G. (2001) Spatially averaged openchannel flow over rough bed. *Journal of Hydrauic Engineering*, 127(2), pp. 123-133.

Nikuradse, J. (1933) Stroemungsgeserze in rauhen Rohren'. *Ver. Dtsch. Ing. Forschungs Heft*, p. 361. (In German).

O'Loughlin, E.M. and MacDonald, E.G. (1964) Some roughness concentration effects on boundary resistance. *La Houille Blanche,* 7, pp. 773-782.

OFWAT (2004). The AMP4 Change Protocol. Version 1 – final determination: December.

OFWAT (2010). Water Services Regulation Authority, Annual report 2009-10. Controller of Her Majesty's Stationery Office, UK, ISBN: 9780102965995.

OurProperty (2012) Drain and sewer clearance services. [online] Available at: http://www.ourproperty.co.uk/guides/drain_sewer_clearance_services-p2.html [Accessed 27/08/2012].

Patel, V.C. (1998) Perspective: flow at high Reynolds number and over rough surfaces - Achilles heel of CFD, *ASME, Journal of Fluids Engineering*, 120, pp. 434-444.

Perry, A.E., Schofield, W.H. and Joubert, P. (1969) Rough wall turbulent boundary layers. *Journal of Fluid Mechanics*, 37, pp. 383–413.

Pokrajac, D. (2010) An Experimental Study of Turbulent Flow in the Vicinity of Transverse Square Bars. IUTAM symposium on the physics of wall-bounded turbulent flows on rough walls, Book Series: IUTAM, Nickels, TB, 22, pp. 21-26, DOI: 10.1007/978-90-481-9631-9_3.

Pokrajac, D. and Manes, C. (2009) Velocity Measurements of a Free-Surface Turbulent Flow Penetrating a Porous Medium Composed of Uniform-Size Spheres. *Transport in Porous Media*, 78(3) pp. 367-383, DOI: 10. 1007/s11242-009-9339-8.

Pokrajac, D., Campbell, L. J., Manes, C., Nikora, V. I. and McEwan, I. K. (2002) Spatially-averaged flow over ribbed roughness: A new application of quadrant analysis. *XXX IAHR Congress*, AUTh, Thessaloniki, Greece, Theme C: Turbulence-1, pp. 103-110.

Polatel, C. (2006) *Large-scale roughness effect on free-surface and bulk flow characteristics in open-channel flows*, PhD thesis, The University of Iowa, USA.

Qin, Q., Lukaschuk, S. and Attenborough, K. (2008) Laboratory studies of near-grazing impulsive sound propagation over rough water. *Journal of Acoustical Society of America*, 124(2), pp. EL40-EL44.

Qunli, W. and Fricke, F. (1989) Estimation of blockage dimensions in a duct using measured eigen frequency shifts. *Journal of Sound and Vibration*, 133, pp. 289-301.

Qunli, W. and Fricke, F. (1990) Determination of blocking locations and cross- sectional area in a duct by eigenfrequency shifts. *Journal of the Acoustical Society of America*, 87, pp. 67-75.

Raupach, M.R., Antonia, R.A. and Rajagopalan, S. (1991) Rough wall turbulent boundary layers. *Applied Mechanics Review,* 44(1), pp. 1-25.

Rogers, C.D.F., Hao, T., Burrow, M.P.N., Costello, S.B. et al (2012) Condition assessment of the surface and buried infrastructure - A proposal for integration. *Tunnelling and Underground Space Technology*, 28, pp. 202-211.

Romanova, A. (2009) *Hydraulic flows and acoustic response analysis*. BEng Dissertation, University of Bradford, UK.

Scanprobe (2001) Products - Scanprobe Camera Systems. [online] Available at: http://www.scanprobe.com/products_scanprobe.shtml [Accessed 27/08/2012].

Schichting, H. (1936) Experimentelle Untersuchungen zum Rauhigkeitsproblem. Ingenieur Archiv, 7, pp. 1-34. (In German).

Schlichting, H. (1936) Experimentelle Untersuchungen zum Rauhigkeitsproblem *Ing. Arch*. 7, pp. 1–34. (English: Experimental investigation of the problem of surface roughness. NACA TM 823, 1937).

Sharp, D.B. (2001) Acoustic pulse reflectometry: A review of the technique and some future possibilities. *Proceedings of the 8th International Congress on Sound and Vibration*, Hong Kong, China, pp.1067-1074.

Sharp, D.B. and Campbell, D.M. (1997) Leak detection in pipes using acoustic pulse reflectometry. *Acoustica,* 83, pp. 560-566.

Sharshar, N., Halfawy, M.R. and Hengmeechai, J. (2009) Video processing techniques for assisted CCTV inspection and condition rating of sewers. *NRCC*-50451.

Shenderov, E.L. (1989) *Radiation and Scattering of Sound*, (original: *Izluchenie i Rassejanie Zvuka*), St.Petersbourg: Sudostroenije, pp. 51-52, (in Russian).

Smith, J.D. and McLean, S.R. (1977) Spatially averaged flow over a wavy surface. *Journal of Geophysics Research*, 82, pp. 1735-1746.

Smith, A.A. (2004) *Miduss version 2: Reference manual / Theory of Hydraulics*. Canada: Alan A. Smith Inc., pp. 284-286.

Softpedia (2012) Moody Diagram. [online] Available at: http://webscripts. softpedia.com/scriptScreenshots/Moody-Diagram-Screenshots-33418 .html [Accessed: 16 /04/2012].

Sondhi, M.M. and Gopinath, B (1971) Determination of vocal-tract shape from impulse response at the lips. *Journal of the Acoustical Society of Am*erica, 49, pp. 1867-1873.

Sterling, M. and Knight, D.W. (2000) Resistance and boundary shear in circular conduits with flat beds running part full. *Proceeding of the Institute of Civil Engineers - Water Maritime and Energy*, 142(4), pp. 229-240.

Twersky, V. (1983) Multiple scattering of sound by correlated monolayers. *Journal of Acoustical Society of America*, 73, pp. 68-84.

Twersky, V. (1983) Reflection and scattering of sound by correlated rough surfaces. *Journal of Acoustical Society of America*, 73, pp. 85-94.

Twersky, V. (1996) Scattering and reflection by elliptically striated surfaces. *Journal of Acoustical Society of America,* 40, pp. 883-895.

Ugarelli, R. and Di Federico, V. (2010) Optimal Scheduling of Replacement and Rehabilitation in Wastewater Pipeline Networks. *Journal of Water Resource Planning and Management*, 136(3), pp. 348-356.

Ugarelli, R., Di Federico, V., and Sægrov, S. (2007) Risk based asset management for wastewater systems. *7th International Conference - Sustainable techniques and strategies in urban water management, Lyon,* pp. 917-924.

Ugarelli, R., Kristensen, S.M., Rostum, J., Sægrov, S. and Di Federico, V. (2008) Statistical analysis and definition of blockages-prediction formulae for the wastewater netweork of Oslo by evolutionary computing. *11th International Conference on Urban Drainage*, Edinburgh, Scotland, UK.

Umnova, O., Attenborough, K. and Cummings, A. (2002) High amplitude pulse propagation and reflection from a rigid porous layer. *Journal of Noise Control Engineering*, 50(6), pp. 204-210.

Van Rijn, L.C. (1984) Sediment transport, part III: Bed forms and alluvial roughness, *Journal of Hydraulic Engineering*, 110(12), pp. 1733-1754.

Weisbach, J. (1845) *Lehrbuch der Ingenieur und Maschinen-Mechanik*, *Theoretische Mechanik, Vieweg und Sohn, Braunschweig*. Vol. 1 (in German).

White, F. M. (2006) Chapter 6 – Viscous flow in ducts, Fluid mechanics, McGraw-Hill Higher Education.

Wood, D.H. and Antonia, R.A. (1975) Measurements in a turbulent boundary layer over a d-type surface roughness. *Journal of Applied Mechanics*, September, pp. 591-597.

WRc (2004) *The Manual of Sewer Condition Classification* - Edition 4, Water Research Centre Plc, Swindon, ISBN 9781-8989-20502.

WRc (2010) *Sewerage Rehabilitation Manual*, WRC, Swindon. [online] Available at: http://srm.wrcplc.co.uk/ for further details. [Accessed 30/03/2011].

Yalin, M.S. (1992) *River mechanics*. Pergamon Press Ltd, Oxford, UK, p. 219.

Yin, Y.A. and Horoshenkov, K.V. (2006) Remote characterisation of the acoustic properties of porous sediments in a multi-modal round pipe, *Proceeding of Institute of Acoustics*, 28(1).

Yoon, J.Y. and Patel. V.C. (1999) Numerical model of turbulent flow over sand dune. *Journal of Hydraulic Engineering*, 122, pp. 10-18.

Appendix

A. Equipment specification sheets

A1. Loudspeaker used in the small acoustic sensor

Waterproof Speaker - Visaton K 64 WP 8Ohm, 2.5 Inch. IP 65 rated. 6,4 cm (2.5") full-range speaker with a plastic basket and plastic diaphragm was used in small acoustic sensor presented in chapter 3. This speaker provides a broad frequency response and good voice reproduction. Particularly well suited to outdoor applications.

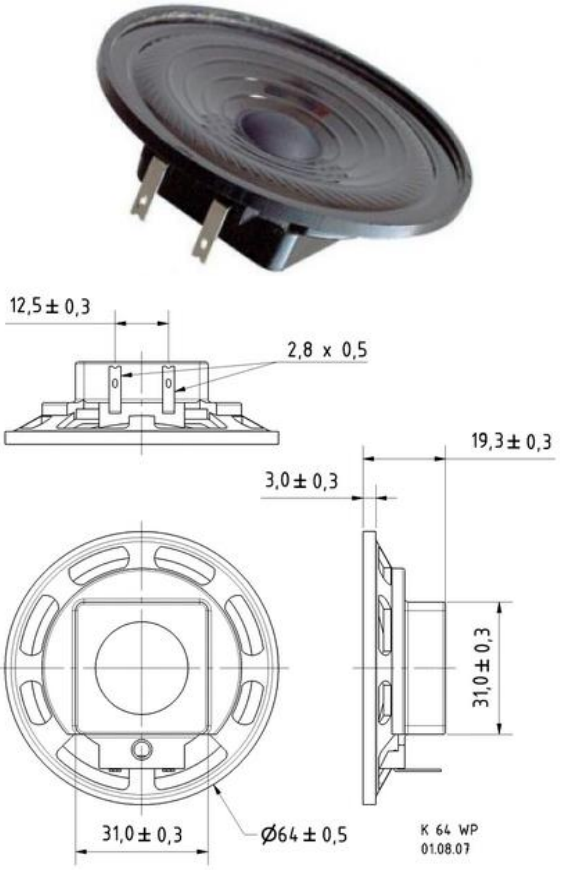

Technical Data:

Rated power	2 W
Maximum power	3 W
Nominal impedance Z	8 Ohm
Frequency response	200–15000 Hz
Mean sound pressure level	86 dB (1 W/1 m)
Resonance frequency fs	300 Hz
Magnetic induction	0,7 T
Magnetic flux	45 µWb
Height of front pole-plate	2 mm
Voice coil diameter	10 mm
Height of winding	2,5 mm
Cutout diameter	60 mm
Net weight	0,05 kg
Protective system	IP 65
Heat resistance	−25 ... 60 °C

Reference: Impactaudio (2006). Loudspeaker Visaton K64WP [Online] Available at: http://www.impactaudio.co.uk/index.php?route=product/product&product_id=452 [Accessed: 03 Aug 2012]

A2. Loudspeaker used in a large acoustic sensor

Visaton loudspeaker RF8, with nominal power handling of 10W to peak power handling of 15W, impedance of 4ohm, and diameter of 75mm was used in large acoustic sensor presented in chapter 3. This speaker has a frequency response of 130Hz - 20kHz and mean sound pressure of 86dB. The speaker measurements are presented below.

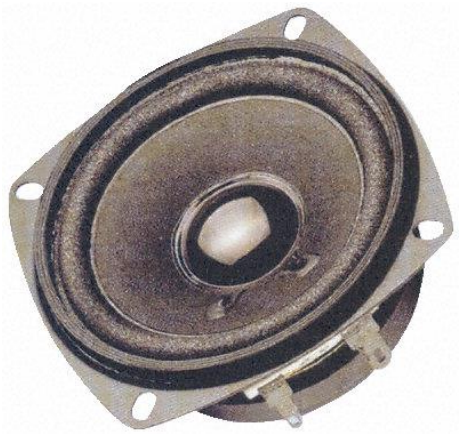

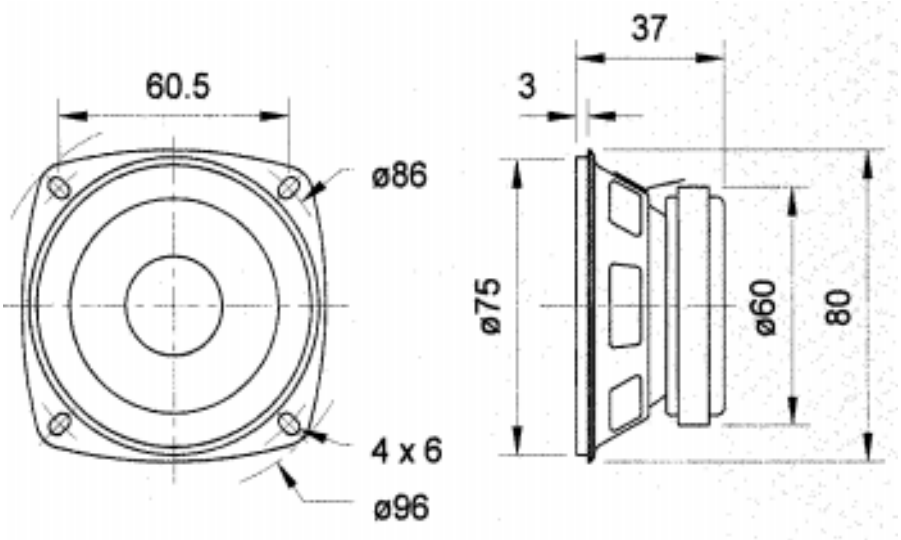

Reference: RS-online (2012). Loudspeaker Visaton RF8 [Online] Available at: http://uk.rs-online.com/web/p/loudspeaker-drive-units/3643313/ [Accessed: 03 Aug 2012]

A3. Wave monitor module

The wave probe monitor module (see picture below) is produced by the Churchill Controls Limited. The monitor consists of several wave probe modules and one power supply module. This wave monitor was used in experiments presented in chapter 4.

The instrument is a simple robust device for the measurement and recording of water waves in hydraulic models and ship tanks. It works on the principle of measuring the current flowing in a probe which consists of a pair of parallel conducting wires. The probe is energised with a high frequency square wave voltage to avoid polarization effects at the wire surfaces. The wires dip into the water and the current that flows between them is proportional to the depth of immersion. The current is sensed by an electronic circuit providing an output voltage proportional to the instantaneous depth of immersion, i.e. wave height, and can be used to drive a high speed chart recorder and/or data logger. The wave probe drive amplifier circuit diagram is presented below:

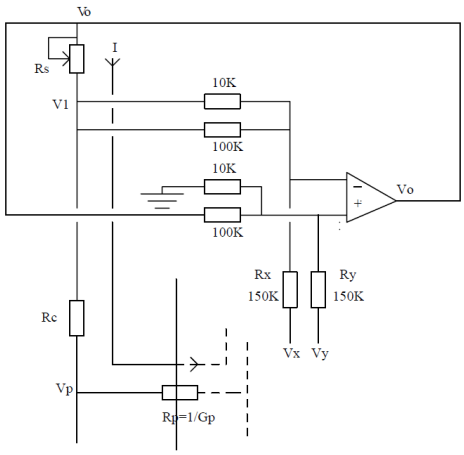

Reference: Churchill Controls Limited (2001). Wave monitor manual. [Online] Available at: http://www.churchill-controls.co.uk/downloads/wmman.pdf

A4. BNC connector block for wave probes and microphones

The BNC-2110 is shielded connector blocks with signal-labeled BNC connectors for easy connectivity of analog input, analog output, digital I/O and counter/timer signals to multifunction DAQ device, including analog output devices. The BNC-2110 works with all E Series and Basic multifunction DAQ devices. Dimensions – 20.3 by 11.2 by 5.5 cm. This device is used to transfer data from the wave monitor and the amplifier of the microphones to the DAQ located in the NI PIXe-1082.

The PXI chassis contains an embedded controllers which include integrated CPU, hard drive, memory, Ethernet, video, serial, USB, and other peripherals, such that it acts as a PC itself. The NI PIXe 1082 was used with X Series devices to synchronize the analog, digital, and counter subsystems. The PIXe 1082 has 8 slots 3U PXI, 4 hybrid slots, 3 PXI express slots, 1 PXI express system timing slot, with dedicated bandwidth performance of up to 1 GB/s per slot and 7 GB/s system bandwidth.

References: National Instruments Corporation (2012). Multifunction DAQ Accessories [Online] Available at: http://www.ni.com/pdf/products/us/4daqsc214.pdf
National Instruments Corporation (2012). NI BNC-2110 [Online] Available at: http://sine.ni.com/nips/cds/view/p/lang/en/nid/1865
National Instruments Corporation (2012). Control with X Series [Online] Available at: http://www.ni.com/white-paper/9382/en
National Instruments Corporation (2012). NI PIXe-1082 [Online] Available at: http://sine.ni.com/nips/cds/view/p/lang/en/nid/207346

A5. Data acquisition device for the wave probes and microphones

To process the data from the wave probes and microphones the National Instrument data acquisition (DAQ) device was used, model NI USB-6356 (see picture below), which was built into the NI PIXe - 1082:

The above DAQ has the following specifications: 8 simultaneous analog inputs at 1.25 MS/s/ch with 16-bit resolution; 10 MS/s total AI throughput; Deep onboard memory (32 or 64 MS) to ensure finite acquisitions, even with competing USB traffic; Two analog outputs, 3.33 MS/s, 16-bit resolution, ±10 V; 24 digital I/O lines (8 hardware-timed up to 10 MHz); Four 32-bit counter/timers for PWM, encoder, frequency, event counting, and more; Advanced timing and triggering with NI-STC3 timing and synchronization technology. The device is compatible with LabView, Visual Basic and Measurement Studio. Below is the schematic of the device analog and digital ports that can be used.

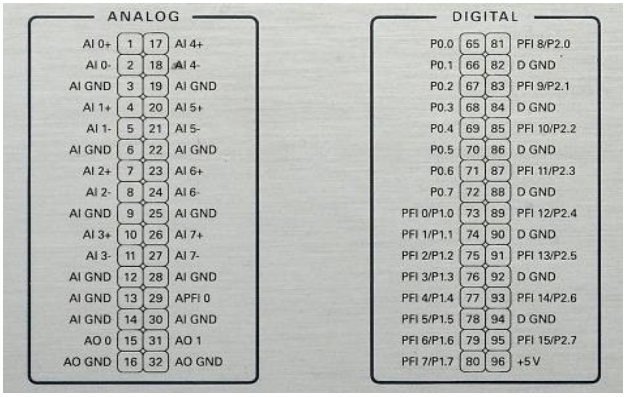

References: National Instruments (2011). USB Data Acquisition. [Online] Available at: http://www.ni.com/dataacquisition/usb/
National Instruments (2011). X series USB Data Acquisition. [Online] Available at: http://zone.ni.com/devzone/cda/tut/p/id/11556
National Instruments (2011). NI USB-6356, X Series Data Acquisition. [Online] Available at: http://sine.ni.com/nips/cds/view/p/lang/en/nid/209075

A6. Microphone used in distributed roughness experiments

Microphone and preamplifier are produced by the Brüel & Kjær company. The microphone is a: 4190-C-001 1/2-inch free-field microphone, 3 Hz to 20 kHz, 200 V Polarization. And the preamplifier is a: 2669-C. Both, in combination were used in distributed roughness experiments presented in chapter 4.

The microphone is designed for high-precision and high-frequency measurements, it is also geared to withstand rough handling and high temperatures, as well as the microphone can be used in high humidity environments. The microphone specifications are as follows: sensitivity 50mV/Pa, dyn. range 15-148dB, inherent noise 15dB A, lower limiting frequency 3dB, 3.15Hz, optimised free field, ext. polarized at voltage 200V, pressure coefficient -0.01dB/kPa, temperature coefficient -0.0012dB/ºC, temperature range of -30/+100 ºC, venting system at the rear.

The pre-amplifier is made completely out of stainless steel and has a 2 m fixed cable terminated with a LEMO 1B, 7-pin connector for input at the instrument end. It is compact and operates over a wide range of temperature, humidity and other environmental conditions. The specifications are as follows: supply voltage +/- 14-60V, oax output 55V and 20mA, frequency range 3Hz-20kHz, attenuation <0.36dB.

References: Brüel & Kjær's (2011). Free-field Microphone 4190-C-001 [Online] Available at: http://www.bksv.com/Products/TransducersConditioning/acoustic-transducers/microphones/microphone-preamplifier-combinations/4190-C-1.aspx?sortOrder=

Brüel & Kjær's (2011). Free-field Microphone 4190-C-001 Specifications [Online] Available at: http://www.bksv.com/Products/TransducersConditioning/acoustic-transducers/microphones/microphone-preamplifier-combinations/4190-C-1.aspx?tab=specifications

Brüel & Kjær's (2011). Microphone Preamplifier 2669-C [Online] Available at: http://www.bksv.com/Products/TransducersConditioning/acoustic-transducers/microphones/preamplifiers/2669-C.aspx

A7. Loudspeaker used in distributed roughness experiments

Loudspeaker producer: Visaton, model: TI100, 8 Ohm - 10cm, High-End low-midrange driver, which was used in distributed roughness experiments presented in chapter 4. The following uses a very strong and lightweight cone in pure titanium, the device produces very fast and detailed sound with great attack, as well as combines well with MHT 12 ribbon tweeter.

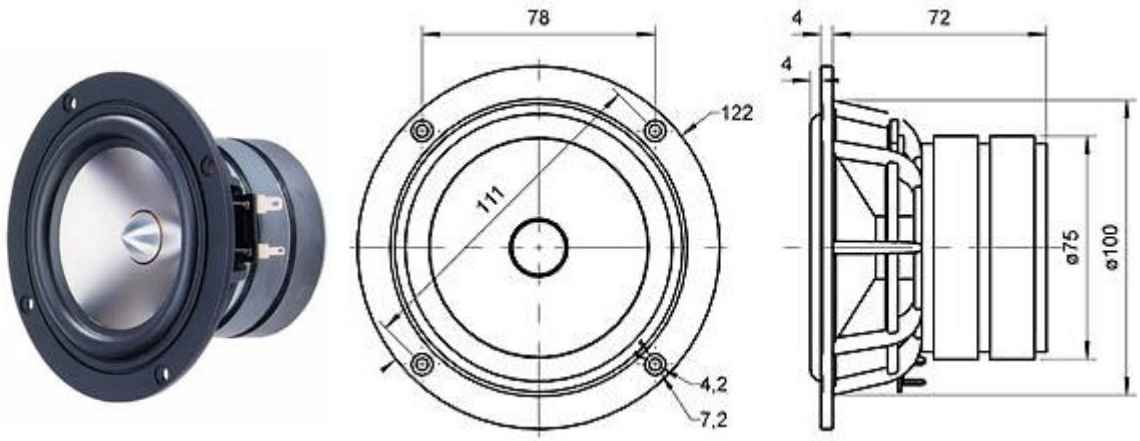

As a result of the construction using double magnets the TI 100 is also magnetically shielded. The TI 100 is ideal as a mid-bass unit in smaller high end shelf speakers or as a mid-range unit in high-end multiway speakers. The list of the speaker specifications is presented below:

Rated Power	40 Watt
Maximum power	60 Watt
Impedance	8 Ohm
Frequency response (-10 dB)	10- 20000 Hz
Mean sound pressure level	86 dB (1 W / 1 m)
Maximum cone displacement	4,5 mm
Resonance frequency	62 Hz
Magnetic induction	1,2 Tesla
Magnetic flux	300 micro Weber
Net Weight	1,05 kg

Reference: Impactaudio (2006). Loudspeaker Visaton TI100 [Online] Available at: http://www.impactaudio.co.uk/product.asp?ref=522&session=a4191e51ac8c9a44d446748094baf774 [Accessed: 07 Feb 2011]

A8. Microphone conditioning amplifier

Microphone conditioning amplifier, 4-channel NEXUS 2692-D for very high levels (100nC) with integration filters, was used in experiments presented in chapter 4. This conditioning amplifier is equally suited for laboratory and field use. 2692-D is compact and self-contained with an optional rechargeable battery, lightweight too (app. 3kg). Rack-mounting fittings are available for in-vehicle testing purposes as well as for stationary use.

A reference generator is included in the hardware and can be used as an excitation signal for your measurement setup. The output signal is sinusoidal at 159.2 Hz (± 1%) with a level of 1 V RMS. A 159.2 Hz (± 1%) sinusoidal test tone is also available. It is applied in parallel with the charge input signal. The level depends on the selected output sensitivities.

A number of filters are provided with NEXUS. The filters are low-pass filters with – 1 dB (– 10%) cut-off frequencies of 0.1, 1, 3, 10, 22.4, 30 and 100 kHz (40 dB/decade, 2-pole) and – 1 dB (– 10%) high-pass filters with 0.1, 1, 10 and 20 Hz cut-off frequencies (10, 20 Hz/80 dB/decade).

Reference: Brüel & Kjær's (2011). 2692-D 4-channel NEXUS Conditioning Amplifier for Very High Levels (100nC) with Integration Filters [Online] Available at: http://www.bksv.com/products/transducersconditioning/conditioningandamps/chargeconditioningamplifiers/2692d.aspx

A9. Continuous wave signal generator

Tektronix AFG3020B general purpose generators that was used to generate the sinusoidal continuous wave (chapter 4). Based on Generator on a Chip (GoC) technology, the AFG3020B offers unprecedented performance.

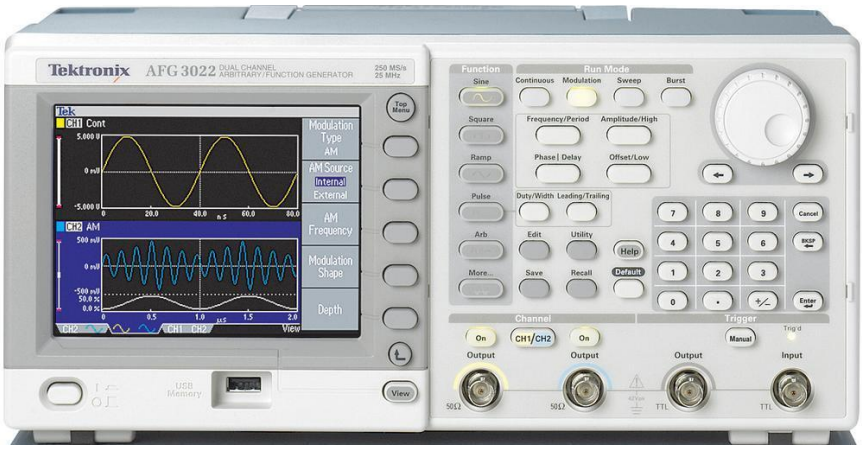

The general specification of the Tektronix AFG3020B signal generator are presented in the table below:

Bandwidth	Analog 34 MHz
Frequency, Output	25 MHz
Impedance, Output	50 Ω
Includes	Quick-start user manual, power cord, USB cable, CD-ROM with programmer manual, service manual, LabView™ and IVI drivers, CD-ROM with ArbExpressÂ® software, NIST-traceable calibration certificate.
Memory	Non-Volatile 4 Waveforms; Memory sample rate 2 to 128 K: 250 MS/s
Resolution	Vertical 14 bits, 1 mV
Time, Rise	and fall ≤20 ns
Waveform	1 µHz to 250 kHz, Arbitary waveforms 1 mHz to 12.5 MHz

Reference: Tequipment (2012). Tektronix AFG3021B Arbitrary / Function Generator 25 MHz 2 Channel [Online] Available at: http://www.tequipment.net/TektronixAFG3022B.html
Allied Electronics (2012). Tektronix AFG3022B [Online] Available at: http://www.alliedelec.com/search/productdetail.aspx?sku=70136865

A10. Power amplifier for the signal generator

Bruel and Kjaer power amplifier of type 2706 has been used to amplify the generated sound (chapter 4). The amplifier was designed to drive small vibration exciters. For this application, the maximum output current should be limited to 1.8A.

The power amplifier has a flat frequency response from 10Hz to 20 kHz (± 0.5dB). The power output capability is 75VA into a 3W exciter or resistive load and the maximum voltage gain is 40 dB. This enables the power amplifier to be used in acoustical measurement set-ups, even when third-octave narrow band noise is employed.

The use of a transformerless power output stage and high negative feedback results in very low harmonic distortion. A balanced preamplifier and rugged solid-state design results in a stable instrument which can tolerate temperature fluctuations and supply line variations.

References: Lab – Aparaty (2012). Urzadzenia [Online] Available at: http://www.labaparaty.pl/produkty.php5?id=3986
TekNet Electronics (2012). Bruel - Kjaer 2706 [Online] Available at: http://www.teknetelectronics.com/Search.asp?p_ID=1226&pDo=DETAIL
TekNet Electronics (2012). Product Data. Power Amplifier - Type 2706 [Online] http://www.teknetelectronics.com/DataSheet/BRUEL_KJAE/BRUEL_270624044.pdf

B. Matlab program codes

B1. Program list and description

No.	Program name	Description
B2	Filtering the reflected acoustic data	The intensity for 6 pairs of microphones is obtained for the chirp signal and total filtered intensity is saved in 'TheLast.m'.
B3	Calculating the energy content in the reflected acoustic data	Calculating the energy content for the obtained filtered chirp signal in any given distance period.
B4	Spectogram plot	Plotting the spectogram of the energy content obtained via 'Energy content for chirp signal'.
B5	Removing header from text files and converting them to Matlab	Removes the header from the 'txt' file recorded via LabView, assigns actual time, and saves new file in 'raw_x.m' format. Where 'x' is the file sequential number.
B6	Derivation of coefficients for wave probe calibration	The program reads data files for still water depths at different gate positions and produces a linear equation relating the water depth according to the output voltage. Output file 'coeffs_wp.txt' with equation coefficients for each wave probe is produced.
B7	Wave probe calibration	All wave probe calibration coefficient saved in 'coeffs_wp.txt' are applied to each 'raw_x.m', and as an output, new files with calibrated to mm wave probe readings are saved in 'rawcalib_x.m'.
B8	Wave probe and microphone data filtering	Input files 'rawcalib_x.m'. are used to be filtered. As an outcome, 'fil_x.m' file area produced.
B9	Wave probe statistics	The program calculates the mean flow depth, wave amplitude and wave rms.
B10	Gaussian pulse alignment	This program splits pulse series (using 'fil_x.m' files) from all 4 microphones into 1s long pulses, aligns and transposes on top of each other and saves as 'all_pulses.m'
B11	Gaussian pulse correlation function statistical analysis	Finds the mean and std of the temporal cross-correlation function for 4 microphones, moving from pulse to pulse. For the input 'all_pulses.m' are used.
B12	Continuous wave envelope and detrended wave probe	Finds the reshaped continuous wave envelope and the reshaped detrended wave probe data, so that it could be compared and statistics as mean value and std are found.
B13	Probability density function	Finds the std coefficient of the probability density functions for both the data of the continuous wave and the wave probes. Data variables obtained from 'Continuous wave envelope and detrended wave probe' are used.

B2. Filtering the reflected acoustic data

```
function [f, d, Intc] = FilterIntensity6MicPairs(FileName)

% for 150mm pipe: fstart – 150, up till 750;
% for 290mm pipe: fstart – 50, up till 375;

load(FileName)
if length(gTemperature) == 0,
   gTemperature = 11;
end
c = 343.2*sqrt((gTemperature+273.15)/293);
% cut-off frequency for individual pipe diameter (Hz):
Cf=(0.8*((0.56*c)/gPipeDia_mm))*1000;
% Start analysis from (Hz):
fstart = 150;
% Filter frequency increment (window) (Hz):
Wf = 100;
% Filter step shift from Wf (Hz):
Df = 20;
% Number of steps in filter analysis:
N = (((Cf-fstart-Wf)/Df)+(Wf/Df))-1;
% N=30;
Nd = length(gdAv);
gdTs = (0:Nd-1)/44100;
ca = 343.2;
d = gdTs/2*ca;

gdAv(:,3) = -gdAv(:,3);
gdAv(:,4) = -gdAv(:,4);
[B,A] = butter(3, 15000/44100);
gdAv = filter(B,A,gdAv);

s1 = 1; s2 = 2; xm12 = 27.5/2/1000;
for m = 1:N
    f(m) = fstart + (m-1)*Df;
    [b,a] = butter(3, [f(m) - Wf f(m) + Wf]/22050);
    Int12(:,m) = cumsum(filter(b,a,gdAv(:,s1))-
filter(b,a,gdAv(:,s2))).*(filter(b,a,gdAv(:,s1))+filter(b,a,gdAv(:,s2)
));
    mI = max(-Int12(:,m));
    Int12(:,m) = Int12(:,m)/mI;
end
s1 = 1; s2 = 3;xm13 = (27.5+17.5)/2/1000;
for m = 1:N
    f(m) = fstart + (m-1)*Df;
    [b,a] = butter(3, [f(m) - Wf f(m) + Wf]/22050);
    Int13(:,m) = cumsum(filter(b,a,gdAv(:,s1))-
filter(b,a,gdAv(:,s2))).*(filter(b,a,gdAv(:,s1))+filter(b,a,gdAv(:,s2)
));
    mI = max(-Int13(:,m));
    Int13(:,m) = Int13(:,m)/mI;
    Int13c(:,m) = spline(gdTs, Int13(:,m), gdTs + (xm13 - xm12)/ca);
end
s1 = 1; s2 = 4;xm14 = (27.5+17.5+12.5)/2/1000;
for m = 1:N
    f(m) = fstart + (m-1)*Df;
    [b,a] = butter(3, [f(m) - Wf f(m) + Wf]/22050);
    Int14(:,m) = cumsum(filter(b,a,gdAv(:,s1))-
filter(b,a,gdAv(:,s2))).*(filter(b,a,gdAv(:,s1))+filter(b,a,gdAv(:,s2)
));
```

```
    mI = max(-Int14(:,m));
    Int14(:,m) = Int14(:,m)/mI;
    Int14c(:,m) = spline(gdTs, Int14(:,m), gdTs + (xm14 - xm12)/ca);
end
s1 = 2; s2 = 3;xm23=(27.5+17.5/2)/1000;
for m = 1:N
    f(m) = fstart + (m-1)*Df;
    [b,a] = butter(3, [f(m) - Wf f(m) + Wf]/22050);
    Int23(:,m) = cumsum(filter(b,a,gdAv(:,s1))-
filter(b,a,gdAv(:,s2))).*(filter(b,a,gdAv(:,s1))+filter(b,a,gdAv(:,s2)
));
    mI = max(-Int23(:,m));
    Int23(:,m) = Int23(:,m)/mI;
    Int23c(:,m) = spline(gdTs, Int23(:,m), gdTs + (xm23 - xm12)/ca);
end
s1 = 2; s2 = 4;xm24 = (27.5+(17.5+12.5)/2)/1000;
for m = 1:N
    f(m) = fstart + (m-1)*Df;
    [b,a] = butter(3, [f(m) - Wf f(m) + Wf]/22050);
    Int24(:,m) = cumsum(filter(b,a,gdAv(:,s1))-
filter(b,a,gdAv(:,s2))).*(filter(b,a,gdAv(:,s1))+filter(b,a,gdAv(:,s2)
));
    mI = max(-Int24(:,m));
    Int24(:,m) = Int24(:,m)/mI;
    Int24c(:,m) = spline(gdTs, Int24(:,m), gdTs + (xm24 - xm12)/ca);
end
s1 = 3; s2 = 4;xm34 = (27.5+17.5+12.5/2)/1000;
for m = 1:N
    f(m) = fstart + (m-1)*Df;
    [b,a] = butter(3, [f(m) - Wf f(m) + Wf]/22050);
    Int34(:,m) = cumsum(filter(b,a,gdAv(:,s1))-
filter(b,a,gdAv(:,s2))).*(filter(b,a,gdAv(:,s1))+filter(b,a,gdAv(:,s2)
));
    mI = max(-Int34(:,m));
    Int34(:,m) = Int34(:,m)/mI;
    Int34c(:,m) = spline(gdTs, Int34(:,m), gdTs + (xm34 - xm12)/ca);
end
Int = Int12 + Int23c+Int34c+Int13c+Int24c+Int14c;
L = max(d); F = 1.5;
comp = 1+2.^(d/L*F);
for m =1:N,
%     m=1:30,
Intc(:,m) = Int(:,m).*comp';
Thresh = 0.01;
mx = max(abs(Intc(:,m))+Intc(:,m)); n = find(abs(Intc(:,m))+Intc(:,m)
< Thresh*mx);
Intc = Intc*1.1;
Intc(n,m) = 1e-6*mx;
end

save TheLast
```

B3. Calculating the energy content in the reflected acoustic data

```
function [Intc, IntA, IntR, IntT, ER, EA, ET] = EnergyAnyMicPairs
(FileName, FreqBand, d1,d2, s1,s2)

% On ENTRY:
% FileName = name of a valid MAT file with CHIRP data
% FreqBand = specify the frequency band [FreqStart FreqFinish]
% s1, s2   = use 6 6 for the sum of all
% d1, d2   = define the distance for energy analysis
% N        = number of frequency bands to analyse (1)
% On EXIT:
% Intc  = intensity array compensated
% ET    = energy total

load(FileName)
N = 1;
if length(gTemperature) == 0,
    gTemperature = 11;
end
c = 343.2*sqrt((gTemperature+273.15)/293);
Nd = length(gdAv);
dt = 1/44100;
time = (0:Nd-1)*dt;
d = c*time/2;
dr = dt*c/2;
ca = 343.2;
gdTs = time;
sd1=(d1*6428)/25;
sd2=(d2*6428)/25;
Channel=[s1 s2];
gdAv(:,3) = -gdAv(:,3); gdAv(:,4) = -gdAv(:,4);

xm12 = 27.5/2/1000;
xm13 = (27.5+17.5)/2/1000;
xm14 = (27.5+17.5+12.5)/2/1000;
xm23 =(27.5+17.5/2)/1000;
xm24 = (27.5+(17.5+12.5)/2)/1000;
xm34 = (27.5+17.5+12.5/2)/1000;

for m = 1:N
    if Channel==[6 6];
    [b,a] = butter(3, FreqBand/22050);
    Int12(:,m) = cumsum(filter(b,a,gdAv(:,1))-
filter(b,a,gdAv(:,2))).*(filter(b,a,gdAv(:,1))+filter(b,a,gdAv(:,2)));
    mI = max(-Int12(:,m));
    Int12(:,m) = Int12(:,m)/mI;
    Int12c(:,m)=Int12(:,m);
    u12=cumsum(filter(b,a,gdAv(:,2))-filter(b,a,gdAv(:,1))./(xm12);
    p12=(filter(b,a,gdAv(:,1))+filter(b,a,gdAv(:,2)));
    Int13(:,m) = cumsum(filter(b,a,gdAv(:,1))-
filter(b,a,gdAv(:,3))).*(filter(b,a,gdAv(:,1))+filter(b,a,gdAv(:,3)));
    mI = max(-Int13(:,m));
    Int13(:,m) = Int13(:,m)/mI;
    Int13c(:,m) = spline(gdTs, Int13(:,m), gdTs + (xm13 - xm12)/ca);
    p13(:,m) = (filter(b,a,gdAv(:,1))+filter(b,a,gdAv(:,3)));
    p13c(:,m) = spline(gdTs, p13(:,m), gdTs + (xm13 - xm12)/ca);
    u13(:,m) = cumsum(filter(b,a,gdAv(:,1))-filter(b,a,gdAv(:,3)));
    u13c(:,m) = spline(gdTs, u13(:,m), gdTs + (xm13 - xm12)/ca);
    Int14(:,m) = cumsum(filter(b,a,gdAv(:,1))-
filter(b,a,gdAv(:,4))).*(filter(b,a,gdAv(:,1))+filter(b,a,gdAv(:,4)));
    mI = max(-Int14(:,m));
```

```
    Int14(:,m) = Int14(:,m)/mI;
    Int14c(:,m) = spline(gdTs, Int14(:,m), gdTs + (xm14 - xm12)/ca);
    p14(:,m) = (filter(b,a,gdAv(:,1))+filter(b,a,gdAv(:,4)));
    p14c(:,m) = spline(gdTs, p14(:,m), gdTs + (xm14 - xm12)/ca);
    u14(:,m) = cumsum(filter(b,a,gdAv(:,1))-filter(b,a,gdAv(:,4)));
    u14c(:,m) = spline(gdTs, u14(:,m), gdTs + (xm14 - xm12)/ca);
    Int23(:,m) = cumsum(filter(b,a,gdAv(:,2))-
filter(b,a,gdAv(:,3))).*(filter(b,a,gdAv(:,2))+filter(b,a,gdAv(:,3)));
    mI = max(-Int23(:,m));
    Int23(:,m) = Int23(:,m)/mI;
    Int23c(:,m) = spline(gdTs, Int23(:,m), gdTs + (xm23 - xm12)/ca);
    p23(:,m) = (filter(b,a,gdAv(:,2))+filter(b,a,gdAv(:,3)));
    p23c(:,m) = spline(gdTs, p23(:,m), gdTs + (xm23 - xm12)/ca);
    u23(:,m) = cumsum(filter(b,a,gdAv(:,2))-filter(b,a,gdAv(:,3)));
    u23c(:,m) = spline(gdTs, u23(:,m), gdTs + (xm23 - xm12)/ca);
    Int24(:,m) = cumsum(filter(b,a,gdAv(:,2))-
filter(b,a,gdAv(:,4))).*(filter(b,a,gdAv(:,2))+filter(b,a,gdAv(:,4)));
    mI = max(-Int24(:,m));
    Int24(:,m) = Int24(:,m)/mI;
    Int24c(:,m) = spline(gdTs, Int24(:,m), gdTs + (xm24 - xm12)/ca);
    p24(:,m) = (filter(b,a,gdAv(:,2))+filter(b,a,gdAv(:,4)));
    p24c(:,m) = spline(gdTs, p24(:,m), gdTs + (xm24 - xm12)/ca);
    u24(:,m) = cumsum(filter(b,a,gdAv(:,2))-filter(b,a,gdAv(:,4)));
    u24c(:,m) = spline(gdTs, u24(:,m), gdTs + (xm24 - xm12)/ca);
    Int34(:,m) = cumsum(filter(b,a,gdAv(:,3))-
filter(b,a,gdAv(:,4))).*(filter(b,a,gdAv(:,3))+filter(b,a,gdAv(:,4)));
    mI = max(-Int34(:,m));
    Int34(:,m) = Int34(:,m)/mI;
    Int34c(:,m) = spline(gdTs, Int34(:,m), gdTs + (xm34 - xm12)/ca);
    p34(:,m) = (filter(b,a,gdAv(:,3))+filter(b,a,gdAv(:,4)));
    p34c(:,m) = spline(gdTs, p34(:,m), gdTs + (xm34 - xm12)/ca);
    u34(:,m) = cumsum(filter(b,a,gdAv(:,3))-filter(b,a,gdAv(:,4)));
    u34c(:,m) = spline(gdTs, u34(:,m), gdTs + (xm34 - xm12)/ca);
    Intc= (Int12c + Int13c + Int14c + Int23c + Int24c + Int34c)/6;
    Intc=(abs(Intc)+Intc)/2;
    p= p12+p13c+p14c+p23c+p24c+p34c;
    u= u12+u13c+u14c+u23c+u24c+u34c;
    end
 end
p_h=hilbert(p);
u_h=hilbert(u);

IntR=0.5*(p_h.*u - p.*u_h);
IntR=(imag(IntR));
mIR=max(IntR(:,m));
IntR(:,m) = IntR(:,m)/mIR;
IntR=((abs(IntR)+IntR)/2)*dr;

IntA=0.5*(p.*u + p_h.*u_h);
IntA=(real(IntA));
mIA=max(IntA(:,m));
IntA(:,m) = IntA(:,m)/mIA;
IntA=((abs(IntA)+IntA)/2)*dr;

IntRPos=0.5*((IntR(sd1:sd2))+abs(IntR(sd1:sd2)));
ER=sum(IntRPos);
IntAPos=0.5*((IntA(sd1:sd2))+abs(IntA(sd1:sd2)));
EA=sum(IntAPos);

IntT=Intc;
IntTPos=0.5*((IntT(sd1:sd2))+abs(IntT(sd1:sd2)));
ET=sum(IntTPos);
save TheLast
```

B4. Spectogram plot

```
function col_show_inv(x, y, z, zmin, zmax, Ncol, lb)

% Used to produce a color psuedocolor plot of matrix z.
% x and y are vectors with the coordinates for the elements
% of matrix z.
% zmin and zmax are scalars setting the limits for
% the selected colourmap.
% lb is the label for the colormap scale plot
% Ncol is the number of levels in the colourmap


font = 14;
corr = 1.15;
subplot(121)
split = 5;
pos = get(gca, 'position');
pos(3) = pos(3)/split;
delta = pos(3);
pos(1) = pos(1) - pos(3)/corr;
set(gca, 'position', pos);

% Make z start from 0:
dz = (zmax - zmin)/(Ncol+1);
%scale = zmin:dz:zmax;
scale = zmax:-dz:zmin;
%colormap(hot);
pcolor((1:2), scale, 1-[scale;scale]');
caxis([zmin zmax]);
set(gca, 'xtick', []);
set(gca, 'fontsize', font);
ylabel(lb);
% shading interp

subplot(122)
pos = get(gca, 'position');
pos(1) = pos(1) - split*delta;
pos(3) = pos(3) + split*delta*corr;
set(gca, 'position', pos);
pcolor(x, y, z), shading interp;
caxis([zmin zmax]);
set(gca, 'fontsize', font);
xlabel('Distance, d (m)');
ylabel('Frequency, f (Hz)');
hold off
colormap(bone)

% colormap(colorcube)
```

B5. Removing header from text files and converting them to Matlab

```
function RemovingHeader(Folder)

% Reads all TXT files in 'Folder' saved from LabView with header
containing start time.
% Removes the header from the data and constructs a time vector.
% Output creates new RAW.m files.

MyFolder = pwd;
eval(['cd ' Folder]);
FileNameStr = dir;
FileNameCell = {FileNameStr.name};
Nf = length(FileNameCell);

for m = 1:Nf-2,
    m
    FileName = cell2mat(FileNameCell(m+2));

[data, header] = hdrload(FileName);

t0 =
str2double(header(17,6:7))*60*60+str2double(header(17,9:10))*60+str2do
uble(header(17,12:19));
L = length(data(:,1));
fs = 22100;
T = 1/fs;
t = t0+(0:L-1)*T;

data = [t' data];
eval(['save raw_' num2str(m) '.mat data -mat']);
% eval(['save run_' num2str(m) '.txt data -ascii']);
end
end

function [data, header] = hdrload(FileName)


% HDRLOAD Load data from an ASCII FileName containing a text header.
%     [header, data] = HDRLOAD('FileNamename.ext') reads a data
FileName
%     called 'FileNamename.ext', which contains a text header.  There
%     is no default extension; any extensions must be explicitly
%     supplied.
%
%     The first output, HEADER, is the header information,
%     returned as a text array.
%     The second output, DATA, is the data matrix.  This data
%     matrix has the same dimensions as the data in the FileName, one
%     row per line of ASCII data in the FileName.  If the data is not
%     regularly spaced (i.e., each line of ASCII data does not
%     contain the same number of points), the data is returned as
%     a column vector.
%
%     Limitations:  No line of the text header can begin with
%     a number.  Only one header and data set will be read,
%     and the header must come before the data.
%
%     See also LOAD, SAVE, SPCONVERT, FSCANF, FPRINTF, STR2MAT.
%     See also the IOFUN directory.
```

```
% check number and type of arguments
if nargin < 1
  error('Function requires one input argument');
elseif ~isstr(FileName)
  error('Input must be a string representing a FileNamename');
end

% Open the FileName.  If this returns a -1, we did not open the
FileName
% successfully.
fid = fopen(FileName);
if fid==-1
  error('FileName not found or permission denied');
  end

% Initialize loop variables
% We store the number of lines in the header, and the maximum
% length of any one line in the header.  These are used later
% in assigning the 'header' output variable.
no_lines = 0;
max_line = 0;

% We also store the number of columns in the data we read.
ncols = 0;

% Finally, we initialize the data to [].
data = [];

% Start processing.
line = fgetl(fid);
if ~isstr(line)
  disp('Warning: FileName contains no header and no data')
  end;
[data, ncols, errmsg, nxtindex] = sscanf(line, '%f');

while isempty(data)|(nxtindex==1)
  no_lines = no_lines+1;
  max_line = max([max_line, length(line)]);
  % Create unique variable to hold this line of text information.
  % Store the last-read line in this variable.
  eval(['line', num2str(no_lines), '=line;']);
  line = fgetl(fid);
  if ~isstr(line)
    disp('Warning: FileName contains no data')
    break
    end;
  [data, ncols, errmsg, nxtindex] = sscanf(line, '%f');
  end % while

data = [data; fscanf(fid, '%f')];
fclose(fid);

header = setstr(' '*ones(no_lines, max_line));
for i = 1:no_lines
  varname = ['line' num2str(i)];
  eval(['header(i, 1:length(' varname ')) = ' varname ';']);
  end

eval('data = reshape(data, ncols, length(data)/ncols)'';', '');
end
```

B6. Derivation of coefficients for wave probe calibration

```
function  WP_calib_coeff

% Input- recorded flat water data at different heights of pipe end
gate.
% Output- file containing the calibration constants for each wave
probe.

depths = [80;
          90;
          105;
          120]; % Input pipe end gate position, note that each file
name should have this position as well.

L = length(depths);
l = [10.43; 11.56; 11.62; 11.68; 11.71; 12.81; 13.79]; % Wave probe
location

for g = 1:L
depthG = (((depths(g)/0.002)-((20.1 - l(:,1)))*1000)*0.002)';
hG(g,:) = depthG(:,:);
end
allV = zeros(L,7);
for d=1:L
    d
    depth = depths(d);
    %data=load(['GateCal' num2str(depth) 'mm.txt']);   % --- for .txt
    load(['raw_' num2str(depth) 'mm.mat']);    % --- for .mat
    data = data(:,3:9);
    allV(d,:)=mean(data(:,:));
    clear data
end
coeffs = zeros(7,2);

for probe = 1:7
    y = allV(:,probe);
    coeffs(probe,:) = polyfit(y,hG(:,probe),1);
figure
plot(hG(:,probe),allV(:,probe),'o');
hold on
y =(hG(:,probe)-coeffs(probe,2))./coeffs(probe,1);
plot(hG(:,probe),y);
end

save coeffs_wp.txt coeffs -ascii
```

B7. Wave probe calibration

```
function DataWPcalib(Folder)

% This file applies calibration coefficients (produced by
WP_calib_coeff) to WP data and creates new files.

c = load('coeffs_wp.txt');

% i.e: c = [6.2371724e+000  8.4941164e+001
%     1.4247437e+001  1.7306691e+002
%     6.6765318e+000  8.4477251e+001
%     5.9905547e+000  7.7075550e+001
%     5.7336333e+000  7.4391313e+001
%     6.2447726e+000  7.8200401e+001
%     6.0420338e+000  7.6047704e+001];

MyFolder = pwd;
eval(['cd ' Folder]);
FileNameStr = dir;
FileNameCell = {FileNameStr.name};
Nf = length(FileNameCell);

for m = 1:Nf-2,
    m
    FileName = cell2mat(FileNameCell(m+2));

load(FileName);
wp = data(:,3:9);

for k=1:7
wpc(:,k) = (wp(:,k)*c(k,1))+c(k,2);
end

data = [data(:,1:2) wpc data(:,10:15)];
eval(['save rawcalib_' num2str(m) '.mat data -mat']);
end
end
```

B8. Wave probe and microphone data filtering

```
function DataFilter(Folder)

% This file filters all the data
% For input files rawcalib_x.m should be used.

MyFolder = pwd;
eval(['cd ' Folder]);
FileNameStr = dir;
FileNameCell = {FileNameStr.name};
Nf = length(FileNameCell);

fs = 22100;
[b,a] = butter(3, [250 850]/(fs/2));

for m = 1:Nf-2,
    m
    FileName = cell2mat(FileNameCell(m+2));

load(FileName);
fil = filter(b,a,data(:,11:15));

data = [data(:,1:10) fil];
eval(['save fil_' num2str(m) '.mat data -mat']);
end
end
```

B9. Wave probe statistics

```
function [all]=WaveProbeStats(Folder)

% This program calculates the Wave Probe statistics.
% Use calibrated wave probe data.

MyFolder = pwd;
eval(['cd ' Folder]);
FileNameStr = dir;
FileNameCell = {FileNameStr.name};
Nf = length(FileNameCell);

for m = 1:Nf-2,
    m
    FileName = cell2mat(FileNameCell(m+2));
    load(FileName);
    wp = data(:,3:9);
    wp_mean(m,:) = mean(wp);
    wp_detrend = detrend(wp);
    wp_diff(m,:) = max(wp_detrend)-min(wp_detrend);
    wp_rms(m,:) = sqrt(mean(wp_detrend.^2));
end
wp_d = mean(mean(wp_diff));
wp_r = mean(mean(wp_rms));
wp_m = mean(mean(wp_mean));
all = [wp_d, wp_m, wp_r];
end
```

B10. Gaussian pulse alignment

```
% This program splits pulse series from ALL microphone into 1s long
pulses, aligns and transposes on top of each other.

MyFolder = pwd;
eval(['cd ' Folder]);
FileNameStr = dir;
FileNameCell = {FileNameStr.name};
Nf = length(FileNameCell);

    p=1:44200:442000;
for m = 1:Nf-2,
    m
    FileName = cell2mat(FileNameCell(m+2));
    load(FileName);
    pu1 = data(:,12);
    pu2 = data(:,13);
    pu3 = data(:,14);
    pu4 = data(:,15);
for k=2:8                                   % number of pulses-1 in a
file to analyse
    pressure1(k,:) = pu1(p(k):p(k+1)-1);
    pressure2(k,:) = pu2(p(k):p(k+1)-1);
    pressure3(k,:) = pu3(p(k):p(k+1)-1);
    pressure4(k,:) = pu4(p(k):p(k+1)-1);
    [pumax,nmax] = max(pressure1(k,:));     % find the maximum value (y)
    w = (nmax-250):(nmax+773);              % identify the pulse
analysis window (x) for ALL pulse
    pulses1(:,k) = pressure1(k, w);
    pulses2(:,k) = pressure2(k, w);
    pulses3(:,k) = pressure3(k, w);
    pulses4(:,k) = pressure4(k, w);
end
eval(['pulses1_' num2str(m) '=pulses1;' ]);
eval(['pulses2_' num2str(m) '=pulses2;' ]);
eval(['pulses3_' num2str(m) '=pulses3;' ]);
eval(['pulses4_' num2str(m) '=pulses4;' ]);
end
data1 = [pulses1_1, pulses1_2, pulses1_3, pulses1_4, pulses1_5,
pulses1_6, pulses1_7];
data2 = [pulses2_1, pulses2_2, pulses2_3, pulses2_4, pulses2_5,
pulses2_6, pulses2_7];
data3 = [pulses3_1, pulses3_2, pulses3_3, pulses3_4, pulses3_5,
pulses3_6, pulses3_7];
data4 = [pulses4_1, pulses4_2, pulses4_3, pulses4_4, pulses4_5,
pulses4_6, pulses4_7];
data = [data1 data2 data3 data4];
data(:, find(sum(abs(data)) == 0)) = [];
eval(['save all_pulses.mat data -mat']);

% figure;
hold on; plot(data1, '--k');
hold on; plot(data2, '--k');
hold on; plot(data3, '--k');
hold on; plot(data4, '--k');
end
```

B11. Gaussian pulse correlation function statistical analysis

```
% Finds the STD of temporal cross-correlation function for 4
microphones, moving from pulse to pulse.

% Load i.e. all_pulses.mat, where a number of pulses are transposed on
top of each other and aligned

load(FileName);
dt = data;
dt(:, find(sum(abs(dt)) == 0)) = [];
d = [0, 160, 320, 480, 480, 800, 960]; % distance between the
microphones

% For extrema no.7 (or any other time window):
nst = 392;  nl = 440; % w7- 392:440
dn1 = 9; dn2 = 20+dn1; dn3 = 31+dn2;

for k=1:49
m1 = dt(nst-1:nl-1,k)';
m2 = dt(nst+dn1:nl+dn1,k+49)';
m3 = dt(nst+dn2:nl+dn2,k+98)';
m4 = dt(nst+dn3:nl+dn3,k+147)';

[c11,lags] = xcorr(m1, m1, 'coeff');
[c12,lags] = xcorr(m1, m2, 'coeff');
[c23,lags] = xcorr(m2, m3, 'coeff');
[c34,lags] = xcorr(m3, m4, 'coeff');
[c13,lags] = xcorr(m1, m3, 'coeff');
[c24,lags] = xcorr(m2, m4, 'coeff');
[c14,lags] = xcorr(m1, m4, 'coeff');

c11=c11(:,:); mc11=max(c11); % find max point coordinate
c12=c12(:,:); mc12=max(c12);
c23=c23(:,:); mc23=max(c23);
c34=c34(:,:); mc34=max(c34);
c13=c13(:,:); mc13=max(c13);
c24=c24(:,:); mc24=max(c24);
c14=c14(:,:); mc14=max(c14);

mc_all(k,:) =  [mc12 mc23 mc13 mc24 mc14];
end

mx7 = mean(max(mc_all));
m7 = mean(mean(mc_all));
mm7 = (max(mean(mc_all))-min(mean(mc_all)));
st7 = mean(std(mc_all));
```

B12. Continuous wave envelope and detrended wave probe

```
function [cwn, wpd] = CW_envelopes_stats(Folder)

% The envelope of the continuous wave signal is obtained and the
statistical data of the envelope is calculated.

% Output:   cwn – normalised continuous wave data
            wpd – detrended wave probe data


MyFolder = pwd; % access the folder
eval(['cd ' Folder]);
FileNameStr = dir;
FileNameCell = {FileNameStr.name};
Nf = length(FileNameCell); % number of files in the folder


for m = 1:Nf-2,
    m
    FileName = cell2mat(FileNameCell(m+2));
    load(FileName); % load a single file from the folder
    for p = 1:7 % a number of 7 wave probes
    time = data(:,2)-data(1,2); % allocate time
    wp_data = data(:,p+2); % allocate data
    wpr(m,p,:) = mean(reshape(wp_data, 1105, 400)); % reshape all
WP's, and find mean value of all sample windows
    wpd(m,p,:) = detrend(wpr(m,p,:)); % detrend all WP's
    wm(m,p,:) = mean(wpr(m,p,:)); % MEAN, for a single WP in a file
over 10 files
    wr(m,p,:) = sqrt(mean(wpd(m,p,:).^2)); % RMS, for a single WP in a
file over 10 files
    wf(m,p,:) = fft(wpd(m,p,:)); % Spectrum
    ws(m,p,:) = (abs(wf(m,p,2:201))); % squeezed data of the spectrum
    end
    N = length(time);
    time_wp = time(1:1105:N);
    for c = 1:4
    x =  data(:,c+11);
    hx = hilbert(x);
    lhx = log(hx);
    cwe = (exp(real(lhx))); % envelope of the signal
    cwr = mean(reshape(cwe, 1105, 400)); % reshaped envelope
%    times = linspace(0, max(time), length(cwr));
    T = max(time_wp);
    nt = find(time_wp > .01*T);
    cwn(m,c,:) = cwr(nt); % data over all samples (380)
    cm(m,c,:) = mean(cwn(m,c,:)); % MEAN, for a single MIC in a file
over 10 files
    cr(m,c,:) = sqrt(mean(detrend(cwn(m,c,:)).^2)); % RMS, for a
single WP in a file over 10 files
    cf(m,c,:) = fft(cwn(m,c,:)); % Spectrum
    cs(m,c,:) = detrend((abs(cf(m,c,2:198)))); % squeezed data of the
spectrum
    end
    time_m = time_wp(nt);
end
```

B13. Probability density function

```
%    Finds the PDF for wave probe and continuous wave signal data.

z = wpd;
z1 = mean(z);
z2 = (squeeze(z1));
z3 = z2';

for p = 1:7
sp(p) = sqrt(mean(z3(:,p).^2));
end

plot(z3);

X = linspace(-1.5, 1.5, 100);
for p=1:7
F = hist(z3(:,p), X);
[spp(p), a(p)] = PDF_Gauss_Recover(1, 1, X, F);
end


X = linspace(-0.7, 0.7, 100);
F = hist(z3(:,4), X);
[spp, a] = PDF_Gauss_Recover(1, 1, X, F);


%    Finding PDF for CW

x = cwn;
x1 = mean(x);
x2 = detrend((squeeze(x1)'));

for m = 1:4
sm(m) = sqrt(mean(x2(:,m).^2));
end

X = linspace(-0.015, 0.015, 100);
for m = 1:4
F = hist(x2(:,m), X);
[smm(m), a(m)] = PDF_Gauss_Recover(1, 1, X, F);
End



%    Where, [1]:


function [s, a] = PDF_Gauss_Recover(s, a, X, F)

% function [param] = PDF_Gauss_Recover(s, a, X, N)
% Used to deduce two parameters in the function f(x) =
% a/sqrt(2*pi)*exp(-x^2/(2*s^2)) (Gaussian-ish) which fits the data F
with
% argument X. s being the standard deviation. a is a stupid
normalisation
% factor which we must select to fit the data.
% On Entry:
% s and a   =   pretty good guesses for the values of s and a
% X         =   is the array with the arguments for F (bin centres)
% F         =   are the measured PDF data (normalised!)

[param, data_opt] = RecoverGauss(s, a, X, F);
```

```
s = param(1); a = param(2);
Gauss = a/sqrt(2*pi)*exp(-X.^2/2/s.^2);
plot(X, F, X, Gauss, 'r');legend('Data', 'Fit');



%    Where, [2]:

function [param, opt] = RecoverGauss(s, a, X, N)

% Nelder-Mead simplex (direct search) method.

x(1) = s; x(2) = a;
option(1) = -1;option(2) = .1;option(14)=3000;
options = optimset('MaxFunEvals', 5000);
lb = [0 0]'; ub = [5 100]';
%[param,opt] = fminsearchbnd('RecoverDampingSub', x, lb, ub, options,
time, data);
[param,opt] = fminsearch('RecoverGaussSub', x, options, X, N);



%    Where, [3]:

function
[x,fval,exitflag,output]=fminsearchbnd(fun,x0,LB,UB,options,varargin)

% size checks
xsize = size(x0);
x0 = x0(:);
n=length(x0);

if (nargin<3) || isempty(LB)
  LB = repmat(-inf,n,1);
else
  LB = LB(:);
end
if (nargin<4) || isempty(UB)
  UB = repmat(inf,n,1);
else
  UB = UB(:);
end

if (n~=length(LB)) | (n~=length(UB))
  error 'x0 is incompatible in size with either LB or UB.'
end

% set default options if necessary
if (nargin<5)|isempty(options)
  options = optimset('fminsearch');
end

% stuff into a struct to pass around
params.args = varargin;
params.LB = LB;
params.UB = UB;
params.fun = fun;
params.n = n;

% 0 --> unconstrained variable
% 1 --> lower bound only
% 2 --> upper bound only
```

```
% 3 --> dual finite bounds
% 4 --> fixed variable

params.BoundClass = zeros(n,1);
for i=1:n
  k = isfinite(LB(i)) + 2*isfinite(UB(i));
  params.BoundClass(i) = k;
  if (k==3) & (LB(i)==UB(i))
    params.BoundClass(i) = 4;
  end
end

% transform starting values into their unconstrained
% surrogates. Check for infeasible starting guesses.
x0u = x0;
k=1;
for i = 1:n
  switch params.BoundClass(i)
    case 1
      % lower bound only
      if x0(i)<=LB(i)
        % infeasible starting value. Use bound.
        x0u(k) = 0;
      else
        x0u(k) = sqrt(x0(i) - LB(i));
      end

      % increment k
      k=k+1;
    case 2
      % upper bound only
      if x0(i)>=UB(i)
        % infeasible starting value. use bound.
        x0u(k) = 0;
      else
        x0u(k) = sqrt(UB(i) - x0(i));
      end

      % increment k
      k=k+1;
    case 3
      % lower and upper bounds
      if x0(i)<=LB(i)
        % infeasible starting value
        x0u(k) = -pi/2;
      elseif x0(i)>=UB(i)
        % infeasible starting value
        x0u(k) = pi/2;
      else
        x0u(k) = 2*(x0(i) - LB(i))/(UB(i)-LB(i)) - 1;
        % shift by 2*pi to avoid problems at zero in fminsearch
        % otherwise, the initial simplex is vanishingly small
        x0u(k) = 2*pi+asin(max(-1,min(1,x0u(i))));
      end

      % increment k
      k=k+1;
    case 0
      % unconstrained variable. x0u(i) is set.
      x0u(k) = x0(i);

      % increment k
      k=k+1;
```

```
    case 4
      % fixed variable. drop it before fminsearch sees it.
      % k is not incremented for this variable.
  end

end
% if any of the unknowns were fixed, then we need to shorten
% x0u now.
if k<=n
  x0u(k:n) = [];
end

% were all the variables fixed?
if isempty(x0u)
  % All variables were fixed. quit immediately, setting the
  % appropriate parameters, then return.

  % undo the variable transformations into the original space
  x = xtransform(x0u,params);

  % final reshape
  x = reshape(x,xsize);

  % stuff fval with the final value
  fval = feval(params.fun,x,params.args{:});

  % fminsearchbnd was not called
  exitflag = 0;

  output.iterations = 0;
  output.funcount = 1;
  output.algorithm = 'fminsearch';
  output.message = 'All variables were held fixed by the applied
bounds';

  % return with no call at all to fminsearch
  return
end

% now we can call fminsearch, but with our own
% intra-objective function.
[xu,fval,exitflag,output] = fminsearch(@intrafun,x0u,options,params);

% undo the variable transformations into the original space
x = xtransform(xu,params);

% final reshape
x = reshape(x,xsize);

% ===========================================
% ========= begin subfunctions =========
% ===========================================
function fval = intrafun(x,params);
% transform variables, then call original function

% transform
xtrans = xtransform(x,params);

% and call fun
fval = feval(params.fun,xtrans,params.args{:});
```

```
% ======================================
function xtrans = xtransform(x,params);
% converts unconstrained variables into their original domains

xtrans = zeros(1,params.n);
% k allows soem variables to be fixed, thus dropped from the
% optimization.
k=1;
for i = 1:params.n
  switch params.BoundClass(i)
    case 1
      % lower bound only
      xtrans(i) = params.LB(i) + x(k).^2;

      k=k+1;
    case 2
      % upper bound only
      xtrans(i) = params.UB(i) - x(k).^2;

      k=k+1;
    case 3
      % lower and upper bounds
      xtrans(i) = (sin(x(k))+1)/2;
      xtrans(i) = xtrans(i)*(params.UB(i) - params.LB(i)) +
params.LB(i);
      % just in case of any floating point problems
      xtrans(i) = max(params.LB(i),min(params.UB(i),xtrans(i)));

      k=k+1;
    case 4
      % fixed variable, bounds are equal, set it at either bound
      xtrans(i) = params.LB(i);
    case 0
      % unconstrained variable.
      xtrans(i) = x(k);

      k=k+1;
  end
end



%    Where, [4]:

function z = RecoverGaussSub(x, X, N)

s = x(1); a = x(2);

Gauss = a/sqrt(2*pi)*exp(-X.^2/2/s.^2);

z = sum(abs(N - Gauss));
```

C. Estimated hydraulic roughness values

C1. Table of estimated pipe full hydraulic roughness in used sewers for clay and concrete pipes (WRc 2004)

Typical condition	Suggested estimated hydraulic roughness * k_s^r [mm]
Virtually as new condition. Light coating of slime (<2mm maximum) to half depth. Free of silt/debris. Peak dwf velocity typically exceeds 1.5m/s.	0.3
Normal condition. Sliming of invert to 3mm maximum. No silt or debris. Peak dwf velocity typically exceeds 1.0m/s.	0.6
Normal condition. Normal sliming of invert (3 to 5mm). No silt or debris. Peak dwf velocity between 0.7 and 1.0m/s.	1.5
Normal condition. As above but with light and localised accumulation of silt or heavy sliming exceeding 5mm depth.	3.0
Normal condition. Mortar loss causing gaps at joints or loss of cross section, not more than 5% caused by root penetration, silt or slight encrustation at joints.	6.0
Poor condition. Longitudinal cracking/fracturing of pipe with marginal ovality of cross section. Normally slimed. No silt or debris.	6.0
Poor condition. Multiple fracturing with up to 10% loss of cross section, severe displacement at joints. Standing waves well developed at part full flow.	15.0
Poor condition. Structurally sound but with heavy encrustation at joints or debris/silt causing 15% loss of cross section.	15.0
Very poor condition. Multiple fracturing. Pronounced deformation/ovality, causing up to 20% loss of cross section.	30.0
Partial or total collapse of pipe.	30.0 to 150.0+

Renovation lining design range

* The suggested estimated hydraulic roughness values indicated in the above table are given for a pipe running full and assume good alignment of pipes. Any roughness due to joint eccentricity, reduction in cross-sectional area due to silt, encrustation or deformation must be separately assessed and allowed for in capacity determinations. The (k_s^r) values specified in this table take no account of changes in pipe dimensions.

Reference: WRc (2004) *The Manual of Sewer Condition Classification* - Edition 4, Water Research Centre Plc, Swindon, ISBN 9781-8989-20502.

C2. Visual image assessment of estimated roughness values (WRc 2004)

(1) Slight joint displacement free of slime and slit snup concrete pipe, 525mm diameter, k_s^r = 0.3mm.

(2) Slight joint displacement, lightly slimed to 1/3 depth, claywere pipe, 525mm diameter, k_s^r = 1.5mm.

(3) Infiltration at joint, minor encrustation, light to moderate sliming spun, concrete pipe, 600mm diameter, k_s^r = 2.4mm.

(4) Slight joint displacement, fine roots penetratingjoint gaps, slimed to 1/3 depth snup, concrete pipe, 450mm diameter, k_s^r = 3mm.

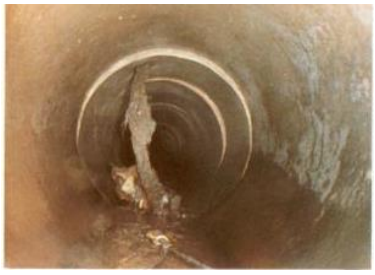

(5) Moderate joint displacemnt, lightly slimed, blockage, 450mm diameter, k_s^r = 4mm.

(6) Slight joint displacement, heavy encrustation, lightly slimed, clayware pipe, 450mm diameter, k_s^r = 6mm.

(7) Heavy joint displacemnt, lightly slimed, clayware pipe, 450mm diameter, k_s^r = 6mm.

(8) Opent joints, joint displacement, debris on invert 5% loss of diameter, clayware pipe, 305mm diameter, k_s^r = 6mm.

(9) Longitudinal cracks, ovality of cross section, heavy joint displacement, moderate sliming to 1/3 depth, clayware pipe, 525mm diameter, k_s^r = 15mm.

(10) Heavy encrustation at joints, medium debris, clayware pipe, 225mm diameter, k_s^r = 15mm.

(11) Longitudinal cracks, broken pipe pieces, heavy joint displacement, clayware pipe, 450mm diameter, k_s^r = 15mm.

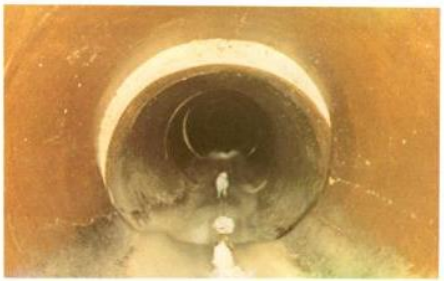

(12) Longitudinal cracks, ovality of cross section, heavy joint displacement, clayware pipe, 450mm diameter, k_s^r = 15mm.

(13) Longitudinal cracks, medium encrustation, root penetration, clayware pipe, 305mm diameter, k_s^r = 15mm.

(14) Loss of 15% of cross section, concrete pipe, 305mm diameter, k_s^r = 15mm.

(15) Severe encrustation, major debris on invert, clayware pipe, 305mm diameter, k_s^r = 30mm.

(16) Loss of 25% of cross section, broken pipe, concrete pipe, 450mm diameter, k_s^r = 150mm.

Reference: WRc (2004) *The Manual of Sewer Condition Classification* - Edition 4, Water Research Centre Plc, Swindon, ISBN 9781-8989-20502.